Doctoral theses at NTNU, 2022:351

Hervé Vicari

Investigation of debris flow entrainment and mitigation using flexible barriers

Physical and numerical modelling

Doctoral thesis

NTNU
Norwegian University of Science and Technology
Thesis for the Degree of
Philosophiae Doctor
Faculty of Engineering
Department of Civil and Environmental Engineering

NTNU
Norwegian University of
Science and Technology

Hervé Vicari

Investigation of debris flow entrainment and mitigation using flexible barriers

Thesis for the Degree of Philosophiae Doctor

Trondheim, November 2022

Norwegian University of Science and Technology
Faculty of Engineering
Department of Civil and Environmental Engineering

NTNU
Norwegian University of
Science and Technology

NTNU
Norwegian University of Science and Technology

Thesis for the Degree of Philosophiae Doctor

Faculty of Engineering
Department of Civil and Environmental Engineering

ISBN 978-82-326-5538-0 (printed ver.)
ISBN 978-82-326-5199-3 (electronic ver.)
ISSN 1503-8181 (printed ver.)
ISSN 2703-8084 (online ver.)

Doctoral theses at NTNU, 2022:351

Printed by NTNU Grafisk senter

Preface

This PhD study was conducted at the Department of Civil and Environmental Engineering at the Norwegian University of Science and Technology (NTNU). The research was made possible through the financial support from the project Klima2050, funded by the Research Council of Norway.

The thesis is organized as a paper-based thesis and comprises four published or accepted papers.

The PhD was conducted under the supervision of Professor Vikas Thakur and Professor Steinar Nordal. The evaluation committee consists of Professor Sabatino Cuomo (University of Salerno), Doctor Corinna Wendeler (Geobrugg AG) and Professor Yutao Pan (Norwegian University of Science and Technology).

The committee for the appraisal of this thesis comprises the following members:

Professor Sabatino Cuomo (first opponent)
University of Salerno, Italy

Dr. Corinna Wendeler (second opponent)
Geobrugg AG, Switzerland

Professor Yutao Pan (administrator)
Norwegian University of Science and Technology, Norway

The supervisors of this study are:

Professor Vikas Thakur (main supervisor)
Norwegian University of Science and Technology, Norway

Professor Steinar Nordal (co-supervisor)
Norwegian University of Science and Technology, Norway

Abstract

Debris flows typically increase in scale by entraining soil, fluid, and boulders along the flow channel. Entrainment is typically modelled according to semi-empirical formulations which do not allow to capture the physical mechanisms of interaction between the flow and the channel bed materials. A 28m-long large-scale flume physical model and the Material Point Method were therefore adopted to study the debris flow entrainment and its mitigation.

An instrumentation was developed to measure entrainment of a 6 m-long wet soil bed built at the end of the flume channel. Flow velocities, flow depths, and entrainment were measured for release debris flow volumes of 2.5 m^3 and 6 m^3. Flow mobility and entrainment were interpreted based on the measurements of the flow basal stresses, which resulted in an average flow basal apparent friction of 9°, suggesting a high degree of flow liquefaction.

The Material Point Method (MPM) was adopted to back-calculate the test results. A one-phase elasto-plastic model was used to model the debris flow and the erodible bed materials. A softening model was introduced for the erodible bed to capture the effect of increasing pore pressures on the decrease of the apparent friction of the erodible bed. The numerical results show that a debris flow entrains the erodible bed by shearing the soil bed (basal scour mechanism) and by pushing the soil bed on surfaces normal to the flow direction (ploughing mechanism). The progressive reduction of the bed shear strength was captured. Weaker beds cannot resist gravity and are therefore easily entrained through a self-propelled entrainment behavior. Entrainment of stronger beds is dominated by the ploughing action of the debris flow. The simulation of the flume tests points towards the ploughing-enabled type of entrainment where the bed residual apparent friction is back-calculated to be 22.5°.

A special entrainment case was studied in MPM, where a boulder resting in the channel is hit by the flow front. The frontal boulder entrainment is found to reduce the flow mobility, proportionally to the mass of the boulder.

Flexible barriers were finally examined to study the mitigation of debris flows through entrainment reduction. An additional flume test was performed with an initial flow volume of 6 m^3, where a compact flexible barrier was placed upstream of the erodible bed. In all the tests a terminal flexible barrier was also installed. The upstream barrier was observed to split the flow into two surges. The flow velocity after the barrier is reduced, and the smaller surges erode 70% less compared to the test without the upstream barrier. The impact on the terminal barrier is also reduced, resulting in a pile-up mechanism with a reduction of the impact force by 94% compared to the case without the upstream barrier. A run-up impact mechanism is instead observed for the compact upstream flexible barrier. A curvilinear overflow creates, which induces additional centrifugal forces normal to the slope and to the barrier. The multiple flexible barrier configuration examined in this work is found to be effective in reducing entrainment, flow velocity, and impact forces, as the flow propagates downstream.

Acknowledgments

I would like to express my sincere gratitude to my supervisors, Professor Vikas Thakur and Professor Steinar Nordal. Professor Vikas Thakur supported me during the whole PhD. Vikas contacted the research group of the Hong Kong University of Science and Technology to use their testing facility and always motivated me to carry out these challenging experiments. I would like to thank Professor Steinar Nordal for his continuous feedback and discussions on the research. He provided constructive criticism to my work and many useful suggestions to discuss the research results. I really enjoyed all the scientific discussions with my supervisors, which helped me to improve my research methodology. I am also thankful to Anders Solheim and Bjørn Kalsnes, from the Norwegian Geotechnical Institute, who provided useful ideas and comments during the PhD study.

I am grateful to Professor Charles W.W. Ng and Professor Clarence Choi for allowing me to stay four months at the Hong Kong University of Science and Technology and to use their large-scale flume facility. The "Saturday" lectures from Professor Ng gave me unvaluable teachings on research. Professor Choi kindly welcomed me in Hong Kong and was always available for discussions on the experiments. He also gave me useful suggestions on how to improve the writing of a scientific paper.

I am very grateful to the PhD students in Hong Kong, and in particular to Dr. Haiming Liu, Roanga De Silva and Sunil Poudyal. Their help was fundamental to carry out the flume experiments.

I would like to thank Dr. Quoc Anh Tran, who joined our geotechnical group in the end of 2020. His MPM code was essential to simulate the flume experiments. Q.A. was always available for discussions and to answer my doubts on MPM and to fix the code. I really enjoyed the discussions we had on the numerical modelling of debris flows and I hope to continue research collaborations with him.

The Geotechnical Group at NTNU provided great support during my PhD. Professors have always been available for discussions. The technical staff at NTNU (Frank Stæhli, Tage Westrum, Karl Ivar Volden Kvisvik, Espen Andersen and Per Asbjørn Østensen) was able to physically build my ideas and scratches for the flume tests and helped to perform some flume tests.

I would like to thank my PhD colleagues and friends for the nice moments spent together during the PhD. We shared many interesting discussions, lunches, salary beers and time together.

I am grateful to my family for their support even if I have been staying in Norway in the last four years. Foremost, thanks for bringing me out in the nature since I was a kid. Being out in the mountains has surely provided inspiration and motivation to carry out this research. Finally, I thank all my friends for the nice time spent together.

Hervé Vicari

Oslo, 19th May 2022

Table of contents

Table of figures

Table of tables

Chapter 1

1. Introduction

Mitigation measures for a debris flow in Jølster, Norway

1.1. Background and motivation

A debris flow is a very rapid to extremely rapid flow of saturated non-plastic debris in a steep channel (Hungr et al. 2001). Debris flows are typically mixtures of soil, fluid, rocks, and vegetation. Debris flows usually originate from minor landslides or from the erosion of sediments by water (Takahashi 2014). The initial debris flow volume may increase in scale by entraining bed material along the channel (Hungr et al. 2005). Entrainment can increase the volume of the flow by several orders of magnitude (Berger et al. 2011). Entrainment happens when a debris flow shears or collides an erodible bed (Hungr et al. 2005). A wet erodible bed may generate excess pore pressures (Sassa 1985, Iverson et al. 2011), which reduce the shear resistance of the bed and increase entrainment (Iverson 2012). A higher debris flow volume leads to longer runout (Rickenmann 1999, Yifru 2020) and higher impact forces on mitigation structures (Vicari et al. 2021a).

Figure 1.1 shows the Hunnedalen (Norway, 2016) debris flow, where the initial landslide volume was about 2000 m^3, which increased to 20000 m^3 following entrainment (Vicari et al. 2021b). Scenarios for climate change in Norway indicate an increase in precipitations which will lead to more frequent water-rich landslides and debris flows (Hanssen-Bauer et al. 2017). The Centre for Research-based Innovation Klima 2050 (Solheim et al. 2021) was created with the aim to reduce the risks associated with climate change and protect critical infrastructures from landslides in Norway.

To reduce the risk associated with debris flows, mitigation structures can be installed along debris flow channels, or towards their end. Check dams (Remaître et al. 2008) and terminal barriers have been applied in the past to stop debris flows. To stop bigger debris flow volumes, the use of multiple rigid barriers has been proposed (Kwan et al. 2015). In Norway, terminal walls (Figure 1.2) are among the most used mitigation techniques. Indeed, the steep Norwegian topography may often hinder the construction of heavy mitigation structures high up in the channel. However, when the terminal wall is built at the end of the channel, it cannot prevent the initial landslide to entrain channel bed material along the flow path and increase in volume. In this study, a lightweight net installed upstream in the debris flow channel is studied, aiming to prevent debris flow entrainment and minimize the runout.

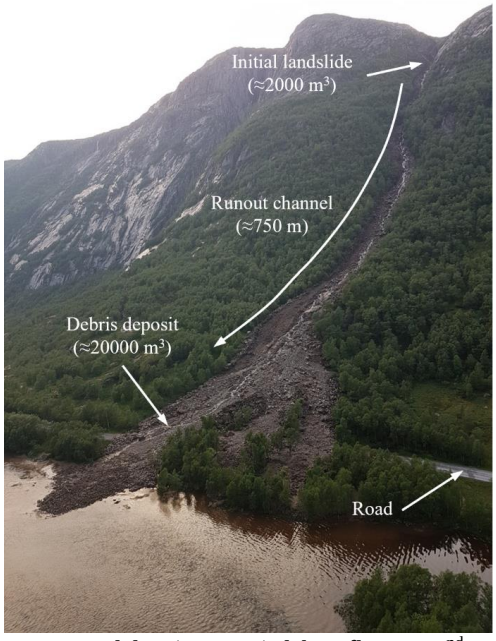

Figure 1.1 Hunnedalen (Norway) debris flow on 2nd June 2016

Figure 1.2 Terminal wall built in Hunnedalen after the debris flow event in June 2016 to protect the road against future debris flow events

Obviously, rigid barriers would be too massive to be built upstream in steep Norwegian channels. In recent years, flexible barriers have been introduced to mitigate debris flows (Wendeler

et al. 2008). Their compact and lightweight structure allows to install them upstream in debris flow channels. The bulk of existing literature has focused on modelling flexible barriers impacted by debris flows on fixed channel beds (Ng et al. 2017, Song et al. 2018). Indeed, the main aim of these previous studies was to identify loads on the flexible barrier and the influence of debris flow properties on the interaction mechanisms with the barrier. However, in nature, channels are typically erodible. In this study, multiple flexible barriers are studied in combination with an erodible bed, to determine the influence of an upstream flexible barrier on debris flow entrainment and impact on a terminal barrier.

In order to effectively design flexible barriers to reduce debris flow bulking, debris flow entrainment must be better understood. Existing numerical software typically model entrainment according to empirical formulations (e.g., Frank et al. 2015), which have limited applicability and do not replicate the physical processes observed in nature. At the same time, observations and measurements of erosion volumes and depths in nature are limited due to the poor temporal and spatial predictability of debris flows and to the inaccessibility of mountain channels. Physical controlled tests to study entrainment are therefore fundamental to understand the physical mechanisms leading to entrainment. Based on the results from these experiments, numerical methods with appropriate constitutive models can be calibrated, allowing for better simulations of the physical processes of entrainment.

1.2. Research objectives

To progress towards a more rational understanding of entrainment and of the influence of the flexible barriers on entrainment, field studies, physical flume modelling and numerical modelling are carried out in this work. The objectives of the research can be categorized as follows:

i. To understand the entrainment process and the factors influencing it. Therefore, compare and discuss the applicability of some empirical, analytical and numerical entrainment models.
ii. To design and perform experiments to study the entrainment behavior by debris flows. This will require to design a simple, cheap and effective technique to measure the spatial distribution of entrainment in an erodible bed, so that entrainment can be distinguished from debris flow deposition.

iii. To model debris flow and entrainment of a soil bed using the Material Point Method (MPM). Simulate the entrainment of large boulders typically observed in nature.

iv. Suggest innovative solutions for the mitigation of debris flows in Norway, by accounting for the typical topography and geological characteristics of channels, and to study the influence of these countermeasures on debris flow entrainment. The impact forces by the debris flow on the countermeasures (flexible barriers) should be examined.

1.3. Scientific challenges

To achieve the research objectives listed above, the following aspects of the debris flow and entrainment mechanics must be analyzed:

i. *Flow behavior*. What is the role of debris flow pore pressures on the flow mobility and on the temporal evolution of entrainment and deposition?

ii. *Flow-erodible bed interaction*. What are the driving mechanisms of entrainment and the influence of pore pressure in the erodible bed on the entrainment magnitude? How does the entrainment of soils and boulders affect the debris flow mobility?

iii. *Flow-barrier interaction.* What factors influence the impact load and runup height on flexible barriers? How is the impact load changing with the location and the dimensions of the flexible barrier?

iv. *Flow-erodible bed interaction with multiple flexible barriers*. An upstream flexible barrier is expected to modify the flow behavior downstream. Therefore, how does the upstream barrier affect downstream entrainment and the successive impact on a terminal flexible barrier?

1.4. Outline of the thesis

This study is organized as a paper-based thesis and is divided in nine chapters. The first part of the thesis presents an introduction and a literature study of debris flows, entrainment and mitigation barriers:

- *Chapter 1* introduces the background of the research, the objectives, and scientific challenges of the study. The list of publications and declarations of authorship are listed.

- *Chapter 2* provides a short literature study on debris flows. The physical principles of debris flow mechanics and entrainment are analyzed. The typical debris flow countermeasures are reviewed, with a particular focus on flexible barriers.

The second part of the thesis presents the publications that the author prepared. The results of the physical and numerical model are described and discussed in the papers:

- *Chapter 3* presents the numerical analysis with a depth-averaged model of a real debris flow event, with particular focus on simulating entrainment. *Paper I* discuss the Hunnedalen (Norway) debris flow in June 2016. A field study is carried out to collect information of the debris flow event, which is back-calculated using RAMMS software. To simulate entrainment, an empirical formulation is used. In the paper, it is shown, that different values of the empirical model parameters can significantly influence the simulation results. The shortcomings from *Paper I* suggest the need to carry out controlled physical tests to better study entrainment by a debris flow. Furthermore, physical observations are needed to understand the influence of flexible barriers on entrainment.
- *Chapter 4* presents the experimental work. Physical flume modelling is carried out to study the debris flow entrainment and the impact on flexible barriers. The design of the flume experiments is discussed. Small-scale flume tests were performed to design a technique to measure entrainment. *Paper II* describes the experiments carried out in a large-scale flume model in Hong Kong to study entrainment by debris flows and the interaction with flexible barriers. The entrainment measurements are interpreted based on an analytical formulation. The influence of the flow basal stress on the temporal evolution of entrainment is analyzed. Finally, the impact force measurements on the flexible barriers are presented. This work is done in close cooperation with the Hong Kong University of Science and Technology (HKUST).
- *Chapter 5* presents results from numerical modelling using the Material Point Method (MPM). To capture numerically both entrainment and debris flow interaction with the flexible barrier, a three-dimensional model is needed. *Chapter 5* introduces the MPM model used in this work. *Paper III* aims at back-calculating the flume experiments using MPM. A constitutive model is introduced for the erodible bed, which allows to simulate entrainment. The entrainment mechanisms by the debris flow are discussed and the importance of using a three-dimensional numerical model to simulate the runup mechanism

on the flexible barrier is highlighted. *Paper IV* covers a special but significant entrainment situation: the entrainment of a boulder by a debris flow is modelled explicitly using MPM. Two situations are analyzed: a large boulder resting in the flow channel and being hit by the front of a debris flow, and a boulder bouncing over an erodible soil bed. The flow mobility with the additional boulder is discussed. *Paper IV* is a first attempt to realistically simulate the complexity of entrainment by boulder-rich debris flows, as observed in Hunnedalen.

The third part of the thesis provides additional analysis and discussions of the papers:

- *Chapter 6* discusses the debris flow mobility on the fixed bed. The role of debris flow pore pressures on the mobility is discussed, based on the measurements from the flume experiments (*Paper II*), the computation using the MPM model (*Paper III*) and idealized block models.
- *Chapter 7* discusses entrainment. Three modelling techniques are discussed and compared: analytical solution (*Paper II*), MPM model (*Paper III*) and empirical model in RAMMS (*Paper I*). The advantages, drawbacks, and limits of applicability of each method are highlighted. A block model is used to back-analyze the flow mobility on an erodible bed. The role of an upstream flexible barrier on entrainment reduction is further discussed (based on *Paper II*). Finally, the entrainment of a boulder at the flow front is further discussed in relation to real debris flow events.
- *Chapter 8* discusses the impact dynamics on the flexible barriers. The impact loads and runup kinematics on the upstream vs. terminal flexible barrier are analyzed, considering the experimental results (*Paper II*), the MPM analysis (*Paper III*) and a block model.
- *Chapter 9* presents the summary, conclusions, and recommendations for future research.

1.5. List of papers and declaration of authorship

- *Paper I*: Vicari, H., Nordal, S., Thakur, V. (2021). The Significance of Entrainment on Debris Flow Modelling: The Case of Hunnedalen, Norway. In: Barla, M., Di Donna, A., Sterpi, D. (eds) Challenges and Innovations in Geomechanics. IACMAG 2021. Lecture Notes in Civil Engineering, vol 126. Springer, Cham. https://doi.org/10.1007/978-3-030-64518-2_60

The main idea of the paper was proposed by H. Vicari. H. Vicari carried out the numerical simulations and wrote the paper. S. Nordal and V. Thakur provided discussions and inputs.

- *Paper II*: Vicari, H., Ng, C.W.W., Nordal, S., Thakur, V., De Silva, W.A.R.K., Liu, H., Choi, C.E. 2021. The Effects of Upstream Flexible Barrier on the Debris Flow Entrainment and Impact Dynamics on a Terminal Barrier. Canadian Geotechnical Journal, Just-IN: 1–37. https://doi.org/10.1139/cgj-2021-0119.

  The main idea of the paper was proposed by H. Vicari. H. Vicari designed the erosion columns to measure entrainment. The large-scale flume model was made available by the Hong Kong University of Science and Technology and by the Hong Kong University. C.W.W. Ng, C.E. Choi, W.A.R.K. De Silva, H. Liu provided their support and experience to design the flume experiments. The experiments were carried out by H. Vicari, W.A.R.K. De Silva, H. Liu, S. Poudyal and with the help of laborers. The experimental results were analyzed by H. Vicari, with input and suggestions from W.A.R.K. De Silva and H. Liu. H. Vicari proposed the interpretation of entrainment, the influence of the upstream flexible barrier on the creation of multiple surges and the centrifugal force transmitted on the upstream flexible barrier. S. Nordal, C.E. Choi and W.A.R.K. De Silva provided suggestions on the interpretation of the tests. H. Vicari wrote the paper, based on input and discussions from all co-authors.

- *Paper III*: Vicari, H., Tran, Q.A., Nordal, S., and Thakur, V.K.S. 2022. MPM modelling of debris flow entrainment and interaction with an upstream flexible barrier. Landslides. doi:10.1007/s10346-022-01886-8.

  H. Vicari proposed the idea of studying both entrainment and impact on the flexible barrier using a three-dimensional model. H. Vicari proposed the constitutive model for the erodible bed. Q.A. Tran wrote the MPM code and implemented the constitutive model. H. Vicari carried out the simulations, with inputs and discussions from Q.A. Tran and S. Nordal. H. Vicari wrote the paper. All authors provided discussions and comments on the simulation results and on the paper.

- *Paper IV*: Vicari, H., Tran, Q.A., Nordal, S., Thakur, V. 2022. MPM simulations of debris flow entrainment, modelling boulders explicitly. Accepted at the conference Geohazards 8 (Québec city).

H. Vicari proposed the idea of modelling explicitly large boulders in MPM and study their entrainment by a debris flow. Q.A. Tran wrote the MPM code. H. Vicari carried out the numerical simulations. H. Vicari wrote the paper. All authors provided comments on the paper.

Chapter 2

2. Literature study

Eroded debris flow channel in the Alps

In this chapter, a short literature study on debris flow mechanics, entrainment and flexible barriers is presented.

2.1. Debris flows

Table 2.1 shows the classification of landslides by (Hungr et al. 2014), based on (Varnes 1978). Debris flow is a particular type of water rich landslide, with specific geological, kinematical and mechanical characteristics. The most comprehensive definition of debris flow is given by (Hungr et al. 2014), who revised the original landslide classification from (Varnes 1978): debris flow is a *"Very rapid to extremely rapid surging flow of saturated debris in a steep channel. Strong entrainment of material and water from the flow path"*. Debris flows occur on established channels. A debris flow may originate from a landslide falling on a loose soil deposit or from the progressive erosion of soil bed by runoff water. The debris flow then propagates in several surges downstream along the channel and it erodes soil, rocks and fluid from the channel bed and banks. Deposition occurs when the debris flow reaches a flatter unconfined fan. Boulder rich lateral and frontal levees are typically observed during this deposition stage, while finer and more liquefied material from the flow body may continue travelling downslope.

Debris flows can be qualitatively distinguished from other types of rapid mass movements, based on the classification from Coussot and Meunier (1996), which is established on the water content in the landslide and the granular and cohesive material contents (Figure 2.1). Debris flows contain both coarse and cohesive material and have quite high solid fraction. Mud flows, instead, are characterized by a dominance of cohesive material. Debris avalanches present similar material compositions as debris flows, but their movement is not confined in a channel. The absence of channelization may create dryer erodible beds, and therefore dryer debris flows (Koo et al. 2018). Finally, rock avalanches may be regarded as avalanches of fragmented rocks with very low water content (Hungr et al. 2014). These different types of landslides are therefore characterized by different geomaterials and water contents, which may exhibit different mechanical behaviors (Iverson 1997, 2015). This thesis focuses on debris flows.

Table 2.1 Classification of landslides (taken from Hungr et al. 2014)

Type of movement	Rock	Soil
Fall	1. Rock/ice fall	2. Boulder/debris/silt fall
Topple	3. Rock block topple	5. Gravel/sand/silt topple
	4. Rock flexural topple	
Slide	6. Rock rotational slide	11. Clay/silt rotational slide
	7. Rock planar slide	12. Clay/silt planar slide
	8. Rock wedge slide	13. Gravel/sand/debris slide
	9. Rock compound slide	14. Clay/silt compound slide
	10. Rock irregular slide	
Spread	15. Rock slope spread	16. Sand/silt liquefaction spread
		17. Sensitive clay spread
Flow	18. Rock/ice avalanche	19. Sand/silt/debris dry flow
		20. Sand/silt/debris flowslide
		21. Sensitive clay flowslide
		22. Debris flow
		23. Mud flow
		24. Debris flood
		25. Debris avalanche
		26. Earthflow
		27. Peat flow
Slope deformation	28. Mountain slope deformation	30. Soil slope deformation
	29. Rock slope deformation	31. Soil creep
		32. Solifluction

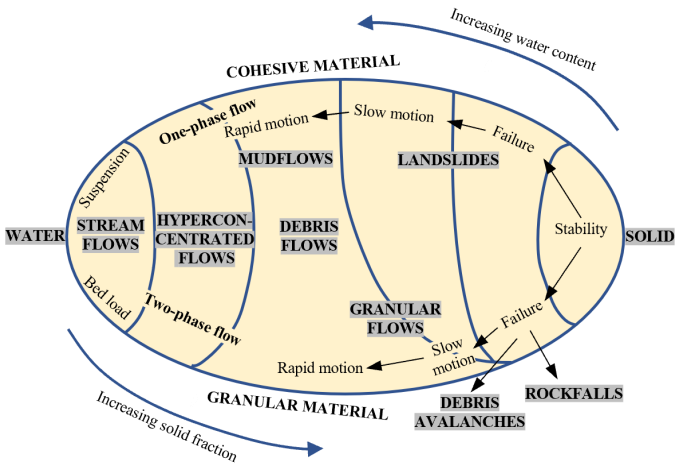

Figure 2.1 Classification of mass movements on steep slopes depending on the water content and material type (modified from Coussot and Meunier 1996)

2.2. Mechanisms in debris flows

A debris flow comprises water and normally well graded soil, ranging from clay to boulders. This diverse composition implies that aspects of fluid rheology interacting with solids need to be considered. The solid particles interact with each other by friction (enduring contacts), or by collisions (inertial contacts). Similarly, within the fluid, quasi-static viscous stresses, or inertial turbulent stresses may dominate. To identify which stress mechanisms are dominant during the debris flow motion, dimensionless numbers have been proposed (Iverson 1997).

The Savage number is the ratio between solid collisional and friction stresses (Iverson 1997):

$$N_{\mathrm{Sav}} = \frac{\rho_{\mathrm{s}} \delta^2 \dot{\gamma}^2}{(\rho_{\mathrm{s}} - \rho_{\mathrm{w}}) g \mu' h_{\mathrm{f}}} \qquad \textbf{2.1}$$

where g is the acceleration due to gravity, ρ_{s} is the density of the solid grains, ρ_{w} is the fluid density, δ is the average grain diameter in the flow, $\mu' = tan\varphi'$ is the effective friction coefficient of the soil, and $\dot{\gamma}$ is the shear rate of the flow. The numerator of the Savage number is proportional to the solid density and to the square of a velocity ($\delta\dot{\gamma}$). $\delta\dot{\gamma}$ represents the relative velocity (v_{rel}) of two particles in a sheared mixture before collision (Figure 2.2a). The numerator of N_{Sav} may therefore be interpreted as the fluctuation kinetic energy of a unit volume of solid particles. High kinetic energy of the solid particles give rise to frequent and intense collisions between the particles. Instead, the denominator of the Savage number is a Coulomb-type of stress, thus proportional to the vertical stress (Figure 2.2b). Hence, the denominator is proportional to the potential energy of the flow per unit volume. If the numerator prevails over the denominator, collisions between particles dominate over enduring contacts between the particles, which may create a dilated flow, almost like a gas. Vice versa, if the denominator prevails, solid particles are in continous quasi-static contact.

The shear rate is an important parameter to evaluate the Savage number. Within a debris mixture, the shear rate $\dot{\gamma}$ may vary quite significantly along the flow depth (Sanvitale and Bowman 2017). However, if the flow velocity is approximated to be linear along the flow depth (Figure 2.2c), $\dot{\gamma}$ can be expressed as:

$$\dot{\gamma} = \frac{v_{\mathrm{f,top}} - v_{\mathrm{f,bot}}}{h_{\mathrm{f}}} \qquad \textbf{2.2}$$

where $v_{f,top}$ is the flow velocity at the top and $v_{f,bot}$ is the flow velocity at the base of the flow. The experiments by (Johnson et al. 2012) suggested that $v_{f,bot}$ may be approximated as half the average flow velocity ($\bar{v}_f$). Hence, the shear rate can be expressed as (Iverson et al. 2010):

$$\dot{\gamma} = \frac{\bar{v}_f}{h_f} \qquad \textbf{2.3}$$

The Friction number is the ratio between frictional and viscous stresses (Iverson 1997):

$$N_{fric} = \frac{C_s}{1 - C_s} \frac{(\rho_s - \rho_w) g \mu' h_f}{\eta_w \dot{\gamma}} \qquad \textbf{2.4}$$

where C_s is the solid concentration of the flow and η_w is the viscosity of the fluid component. The denominator of the Friction number is proportional to the viscosity and to the shear rate, which therefore represents a viscous-type of stress of the fluid component. If the numerator of the Friction number prevails, enduring frictional contacts between solid particles are dominant. However, if the denominator prevails, viscous shearing within the fluid is dominant.

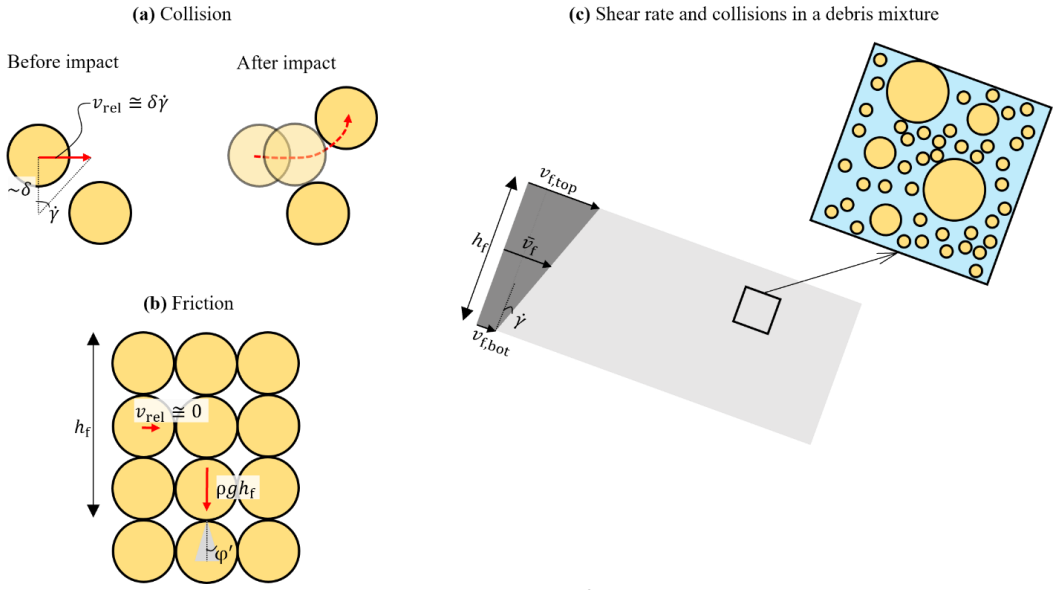

Figure 2.2 Interactions between solid grains in a debris flow: (a) Collision between two grains; (b) Friction between grains; (c) Shear rate and collisions within a debris flow mixture

Equations 2.1 and 2.4 not only depend on the material parameters but may also greatly change in function of the flow parameters, such as the flow depth and velocity and shear rate. A thin and fast flow made of larger particles is typically associated to collisional type dynamics, while a thick and slow flow is typically more frictional. Furthermore, the friction stresses in the debris flow are regulated by the generation and dissipation of excess pore pressures. High excess pore pressures may be generated during the triggering of a loose and wet soil, where high shearing is typically observed (Wang and Sassa 2003). The persistence of these excess pore pressures depends on the dynamic character of the debris flow and on pore pressure diffusion towards the free boundaries of the debris flow (Iverson and George 2014). The pore pressure number is the ratio between the timescale for debris flow motion and the timescale for slope-normal pore pressure diffusion (Iverson 2015):

$$N_{\mathrm{P}} = \frac{t_{\mathrm{Propagation}}}{t_{\mathrm{P_wDissipation}}} = \frac{\left(\frac{L}{g}\right)^{\frac{1}{2}}}{\frac{\eta_{\mathrm{w}} h_{\mathrm{f}}^2}{k_{\mathrm{f}} D_{\mathrm{f}}}} \qquad \textbf{2.5}$$

where L is the characteristic length of the debris flow, k_{f} is the intrinsic permeability of the water through the debris material and D_{f} is the drained elastic bulk modulus of the debris flow. $t_{\mathrm{Propagation}}$ represents the typical debris flow duration, obtained by normalizing L by the gravity acceleration which acts on the debris flow. $t_{\mathrm{P_wDissipation}}$ expresses the timescale for excess pore-pressure diffusion (dissipation), considering a one-way drainage towards the free surface of the flow, as exemplified in Figure 2.3. Notice that the excess pore-pressure distribution over the flow depth z is drawn qualitatively to respect the zero-flux basal boundary condition (an impermeable base is here assumed), $\frac{\partial p_{\mathrm{w}}}{\partial z}\Big|_{z=0} = -\rho_{\mathrm{w}} g cos\theta$, and the pressure-free surface boundary condition, $p_{\mathrm{w}}(z = h_{\mathrm{f}}) = 0$. Eq. 2.5 shows that excess pore pressures may be dissipated quickly in a thin debris flow. (Iverson 2015) therefore suggested using large testing facilities to better imitate the debris flow dynamics observed in nature. For this reason, a large-scale 28 m-long flume was used in this work to study the debris flow dynamics and entrainment.

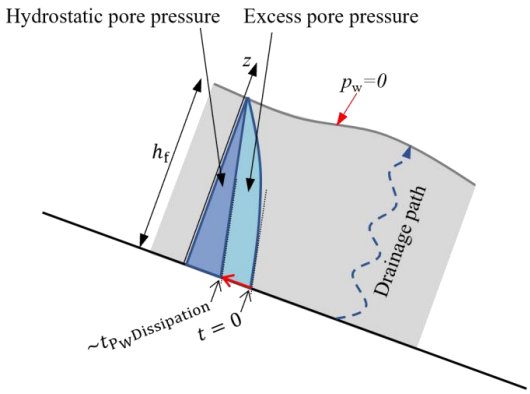

Figure 2.3 Pore pressure dissipation in a debris flow

2.3. Entrainment

Entrainment refers to the incorporation of channel bed material into the debris flow. The bed material, which is initially in a static position can be entrained by the flow at its base or from the destabilization of the lateral channel banks. Figure 2.4 shows a typical cross-section of a debris flow channel, where the debris flow (here indicated as Channel material) can entrain the colluvial blanket at the base; additionally, following this erosion, the lateral channel banks may become unstable and therefore be incorporated into the debris flow. This thesis will focus on the entrainment from the base of the channel, without considering the presence of erodible channel banks.

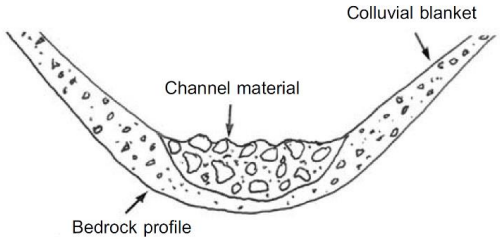

Figure 2.4 Cross section of a debris flow channel perpendicular to the flow direction (figure taken from Hungr et al. 2005)

When the debris flow overrides the channel bed sediments, it transmits basal stresses onto the bed. Different stresses may arise, depending on the surface where the flow impacts or rubs the erodible bed. Issler et al. (2000) postulated different erosion mechanisms in snow avalanches

(Figure 2.5). In particular, ploughing (Figure 2.5a) occurs at the front of dense avalanches; ripping (Figure 2.5b) occurs when a slab in the bed is incorporated into the flow; eruption occurs at the flow front (Figure 2.5c); continuous scour happens at the base of the avalanche (Figure 2.5d). In debris flows, a clear classification of entrainment mechanisms has not been established yet. However, some research suggest the dominance of frontal ploughing entrainment (Barbolini et al. 2005, Berger et al. 2011), while other research indicated the dominance of scour entrainment from the base of the flow (Iverson et al. 2011, Iverson 2012).

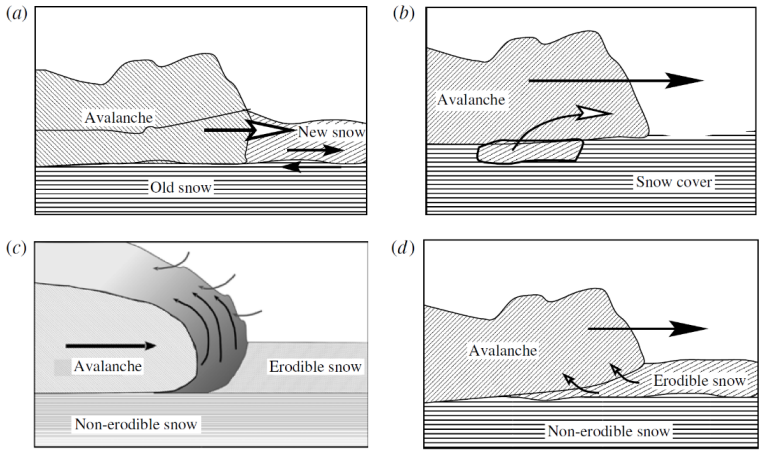

Figure 2.5 Schematic of the possible entrainment mechanisms in snow avalanches (Issler et al. 2000): (a) Ploughing; (b) Intermittent ripping; (c) Eruption; (d) Sustained scour. (figure taken from Issler 2014)

As the erodible bed is exposed to shear or collisions by the debris flow on top, it may still resist entrainment by internal stress. It is suggested to model the erodible bed as a Mohr-Coulomb frictional material (Iverson 2012). If the bed becomes sufficiently sheared by the debris flow, pore pressures inside the bed may arise, reduce the effective stresses, decrease the shear resistance inside the erodible bed and promote entrainment.

To understand the mechanism of excess pore pressure generation in an erodible bed, it is convenient to consider an element of the erodible bed near the surface (or near the evolving boundary between the debris flow and the erodible bed, if entrainment has happened on top). The

bed element is considered to be saturated (Figure 2.6a), which is common after periods of intense and prolonged rainfall. As the flow overrides the bed element, it transmits a normal stress σ onto the element (from the weight of the debris flow) and a shear stress τ, which causes a shear strain rate $\dot{\gamma} = \frac{d\gamma}{dt}$ in the bed element. The generation of excess pore pressures (p_{w}) in this element can be expressed as follows (Iverson 2012, Iverson and George 2014):

$$\frac{dp_{\mathrm{w}}}{dt} - \frac{k_{\mathrm{f}} D_{\mathrm{f}}}{\eta_{\mathrm{w}}} \frac{d^2 p_{\mathrm{w}}}{dz^2} = \frac{d\sigma}{dt} - D_{\mathrm{f}} \dot{\gamma} tan\psi \qquad \textbf{2.6}$$

where ψ is the dilatancy angle of the soil bed. The equation shows that pore pressures may generate by direct compression of pores ($\frac{d\sigma}{dt}$). Furthermore, if the bed material exhibits a contractive behaviour (i.e. $\psi < 0$), the shearing ($d\gamma$) would cause either a volumetric contraction ($d\varepsilon_{\mathrm{v}}$) of the bed (in drained conditions, Figure 2.6b) or an increase in pore pressures (in undrained conditions, Figure 2.6c). If the shearing is sufficiently high and the permeability of the bed sufficiently low, the increase of pore pressure dominates over the pore pressure dissipation (undrained condition). Erodible beds are most commonly in a loose state, as they were formed by colluvial processes or from deposition from previous debris flow events. Loose erodible beds are therefore expected to exhibit a contractive behaviour with development of excess pore pressures. The increase in pore pressures determines a decrease in effective stresses and therefore a decrease in the shear resistance of the bed. The case shown in Figure 2.6c may be captured by using a two-phase model, where both the solid and fluid phases are modelled explicitly. However, to model undrained conditions in a one-phase model (Figure 2.6d), a dilatancy angle equal to zero should be used to have no plastic volumetric deformation. At the same time, as pore pressures are not modelled explicitly, a constitutive law should be introduced to artificially reduce the shear strength of the material. This can be achieved by manipulating the apparent friction of the one-phase material, which can be made decrease with the shear strain. This tactic will be used and explained in *Papers III* and *IV*.

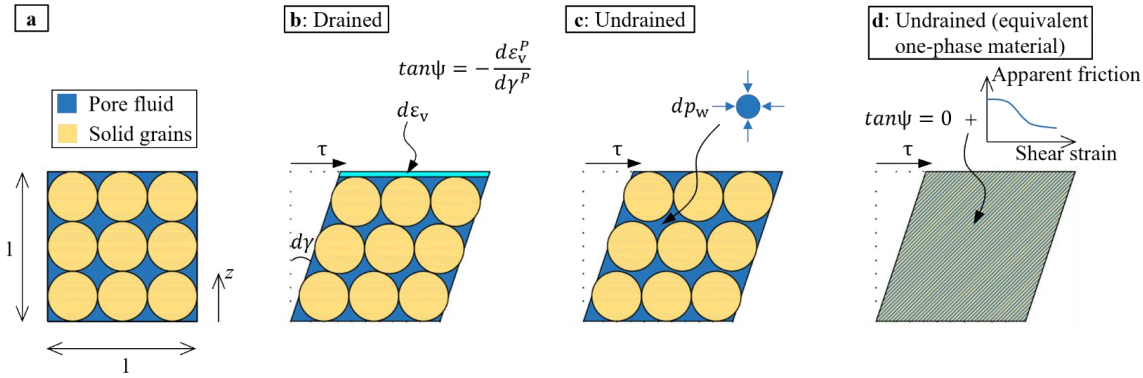

Figure 2.6 Mechanism of pore pressure generation in an erodible bed: (a) saturated erodible bed element in an initial loose state; (b) bed sheared ($d\gamma$) in drained conditions with creation of volumetric strain ($d\varepsilon_v$); the dilatancy angle is the ratio between the plastic strains: $tan\psi = -d\varepsilon_v^P / d\gamma^P$; (c) bed sheared in undrained conditions with generation of excess pore pressures (dp_w); (d) modelling bed shearing in undrained conditions for an equivalent one-phase material

2.3.1. Physical modelling of entrainment

Table 2.2 shows the main experimental and field works carried out to study the entrainment process, based on a literature study. The methodology used in each work is indicated. From each study, the typical observed flow depth and velocity and entrainment magnitude are highlighted. Finally, the table summarizes the main outcomes from each study. In summary, this previous research has shown that entrainment is a scale dependent process (i.e., dependent on the debris flow volume and flow depth), positively correlated to the bed water content. Both basal scour, ploughing and collisional stresses have been seen to influence the entrainment process.

Table 2.2 denotes some of the flume experiments (Iverson et al. 2011, Reid et al. 2011, Vicari et al. 2021a) as “large-scale”. Indeed, in these tests, high flow volumes were released, which created large flow depths (in the order of 0.5 m), similar to those observed in the field (in the order of 2 m). By idealizing the stresses at the base of the flow to be proportional to the thickness of the flow (Iverson et al. 2010), these flume experiments may therefore be regarded as “large-scale”, as they are expected to be characterized by large magnitudes of stresses, almost similar to stresses observed in full-scale debris flows (hereon also indicated as natural or field debris flows). The term large-scale flume tests will be used consistently in the rest of the thesis and in the papers.

Table 2.2 Experimental and field observations of the entrainment process. V_i denotes the initial debris flow volume; m_i denotes the initial debris mass; h_f denotes the flow depth; v_f denotes the flow velocity; V_E denotes the entrained volume; E denotes the entrainment rate; h_E denotes the erosion depth

Study	Methodology	h_f (m)	v_f (m/s)	Entrainment	Main outcome
(Rickenmann and Weber 2003)	Field tests. Debris flow is generated by water runoff (V_i=3600-40600 m^3)	1-4	2-8	V_E=9000-127000 m^3	Entrainment volume positively correlated to the released water volume
(Barbolini et al. 2005)	Small-scale flume experiments of dry granular material (m_i=25 kg)		2.2-3.1	E=0.42-0.54 m/s	- Predominant erosion mechanism is Ploughing - Erosion rate proportional to the flow velocity
(Breien et al. 2008)	Field observations at Fjærland (V_i=25000 m^3)	10	14	V_E=240000 m^3	Erosion process may be self-sustained by debris flow volume increase
(Berger et al. 2010, 2011)	Field observations at Illgraben (V_i=25000 m^3)	2	3-8	h_E=0.55 m	- Entrainment is larger at the flow front, probably driven by collisions - Deposition observed at the tail of the debris flow
(Mangeney et al. 2010)	Small-scale flume tests of granular material (dry glass beads)	0.01 (flow front)	1.5	h_E=3.5 mm	Erosion depths and runout distance increase with the channel inclination
(Bowman et al. 2010)	Centrifuge	-	-	-	Initially unsaturated bed can decrease debris flow runout compared to flow on a fixed bed
(Iverson et al. 2011, Reid et al. 2011)	Large-scale flume tests (V_i=6 m^3)	0.4	10	h_E=0-0.12 m	- Entrainment positively correlated to the initial bed water content - Flow momentum increase for debris flow overriding wet beds
(Schürch et al. 2011)	Field observations at Illgraben (V_i=10000 m^3)	1-3	-	h_E=0-5 m	- Flow depth controlling entrainment - Net erosion observed for higher flow depths; net deposition observed for smaller flow depths
(Mccoy et al. 2012)	Field observations (V_i=100-2800 m^3)	0.5-1.2	3-4.6	h_E=0.2-1.1 m	Entrainment positively correlated with bed water content and pore pressure increase in the bed
(Haas and Woerkom 2016)	Small-scale flume tests (V_i=3.4·10^{-3} m^3)	0.015-0.03	1.5 -3.5	h_E=5-40 mm	- Entrainment increases with channel slope, flow velocity, shear stress - Influence of debris flow composition is studied
Paper II	Large-scale flume tests (V_i=2.5-6 m^3)	0.3	5-7	h_E=0.01-0.12 m	- Entrainment rate depends on the flow basal shear stress - Entrainment positively correlated to the debris flow volume - An upstream flexible barrier can significantly decrease entrainment

2.3.2. Numerical modelling of entrainment

Numerical modelling of entrainment may be categorized based on the type of numerical method. Most of the previous research modelled the flow and erodible bed as continuum materials. The dynamic behaviour of such continuum materials can be described according to the mass and momentum conservation laws. A further classification can be made by distinguishing three-dimensional models, which solve the three-dimensional equations of motion, and depth-averaged models, which average the conservation equations over the flow depth (normal to the topography).

Traditionally, depth-averaged models have been most used, as they require a much shorter computation time, while providing sufficient accuracy to model long debris flow runouts. In a depth-averaged model, the mass conservation equation is expressed by Eq. 2.7. Reference is made to Figure 2.7, for simplicity derived on a two-dimensional topography, for an incompressible flow.

$$\frac{\partial h_f}{\partial t} + \frac{\partial (h_f \bar{v}_f)}{\partial x} = E \qquad \textbf{2.7}$$

where t is time, h_f is the flow depth, $\bar{v}_f$ is the flow velocity along x, depth-averaged over the z direction. E is the entrainment rate, which expresses the volume gained by the flow in a unit time per unit basal area:

$$E = -\frac{\partial z_b}{\partial t} \qquad \textbf{2.8}$$

where z_b is the evolving boundary between the flow and the erodible bed.

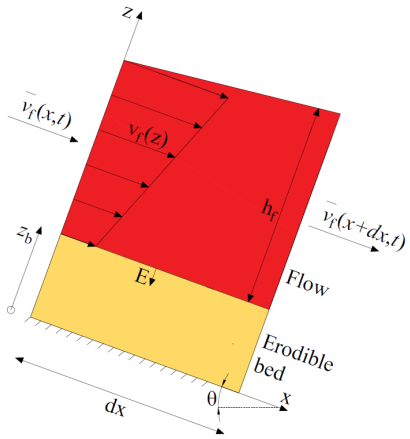

Figure 2.7 Illustration of the flow and erodible bed layers in a depth-averaged model

Different empirical and analytical formulations have been proposed in literature to evaluate the entrainment rate, as summarized in Table 2.3. Most of the formulations are empirical and they generally show that the entrainment rate is proportional to the flow depth and velocity.

(Frank et al. 2015) proposed an empirical formulation to calculate the entrainment rate and the maximum erosion depth by a debris flow, based on field measurements at Illgraben. This model is implemented in the software RAMMS::DF, which will be discussed later. The parameters of the model are shown in Figure 2.8. The entrainment rate is assumed constant as:

$$E = -dz/dt \tag{2.9}$$

where dz/dt is a constant value which is calibrated from observations. The maximum erosion depth is expressed as:

$$e_{\mathrm{m}} = \frac{dz}{d\tau}(\tau - \tau_{\mathrm{c}}) \tag{2.10}$$

where $\frac{dz}{d\tau}$ is an empirical parameter; τ is the slope-parallel stress due to gravity; τ_{c} is a critical shear stress. In the model, entrainment only occurs once τ exceeds τ_{c}.

(McDougall and Hungr 2005) proposed an empirical formulation for the entrainment rate, which is proportional to the flow depth and velocity:

$$E = \bar{E} h_{\mathrm{f}} \bar{v}_{\mathrm{f}} \tag{2.11}$$

where $\bar{E}$ is a user-specified parameter selected by trial and error.

(Sovilla et al. 2006) proposed a semi-empirical entrainment model for snow avalanches, where the entrainment rate is proportional to the flow velocity through a calibrated parameter K:

$$E = K \bar{v}_{\mathrm{f}} \tag{2.12}$$

The same model was then adopted by (Hussin et al. 2012) to model debris flows.

(Iverson 2012) derived an analytical formulation of the entrainment rate based on the conservation of momentum of the entrained bed layer in the case of a basal scour entrainment mechanism (i.e. the flow is considered to transmit eroding shear stresses onto the bed in a direction parallel to the flow velocity):

$$E = \frac{\tau_{\mathrm{f,bot}} - \tau_{\mathrm{b,top}}}{\rho_{\mathrm{b}} v_{\mathrm{f,bot}}} \tag{2.13}$$

where $\tau_{f,bot}$ is the flow basal shear stress and $\tau_{b,top}$ is the bed resisting shear stress; $v_{f,bot}$ is the velocity at the base of the flow.

Table 2.3 Entrainment rate formulations for depth-averaged models

Study	Comment
(Frank et al. 2015, 2017); *Paper I*	Direct field measurements of the entrainment rate at Illgraben (Berger et al. 2011)
(McDougall and Hungr 2005)	Empirical formulation
(Sovilla et al. 2006, Hussin et al. 2012)	Semi-empirical formulation
(Medina et al. 2008, Iverson 2012, Iverson and Ouyang 2015); *Paper II*	Analytical solution based on conservation of momentum for the entrained bed layer [refer to *Paper II* for the derivation]

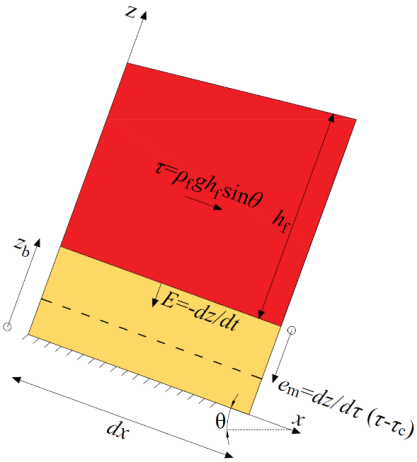

Figure 2.8 Sketch of the empirical entrainment model (Frank et al. 2015) used in RAMMS::DF

Contrary to depth-averaged models, full three-dimensional models do not require to introduce assumptions and a specific formulation to compute entrainment rate. Indeed, the bed can simply be modelled as a material with an appropriate constitutive law. Table 2.4 summarizes the different approaches used in literature.

Table 2.4 Constitutive models for the erodible bed in three-dimensional models

Study	Constitutive model for the erodible bed
(Lee and Jeong 2018)	Softening model transitioning from solid to viscous behaviour with increasing velocity
(Lee et al. 2019)	Softening model transitioning from solid to viscous behaviour with increasing deviatoric shear strain
(Nikooei and Manzari 2020)	Mohr-Coulomb yield criterion with constant friction
Papers III* and *IV	Mohr-Coulomb yield criterion with softening model to account for development of excess pore pressures with increasing distortional strain

2.4. Barriers for debris flow mitigation

Mitigation barriers are typically built in debris flow channels to retain debris flows. Check dams are small rigid structures positioned along rivers and streams. They have traditionally been applied on quite gentle slopes to stabilize the riverbeds, by reducing the flow velocity and therefore increase the deposition of the solid particles suspended in the water. Check dams have been for example applied in the Alps (e.g. Remaître et al. 2008) and in Japan (e.g. Maricar et al. 2011). Rigid barriers and slit structures have also been implemented to retain debris flows and dissipate their energy. Figure 2.9 shows rigid barriers installed in the field.

Figure 2.9 Examples of rigid barriers in Aosta Valley (Italian Alps) (**a**) Closed rigid barrier; (**b**) Slit sectional barrier

In 1994-1995, DeNatale et al. observed that a flexible net barrier, originally built to mitigate rockfalls, was able to stop several small debris flow events in California. This observation inspired DeNatale et al. (1999) to carry out a series of debris flow tests in the USGS flume facility to evaluate the performance of rockfall net barriers on debris flow retention. They concluded that flexible barriers could be effective in resisting the impact loading of small debris flows. To provide more systematic design of flexible barriers, the WSL group (Switzerland) initiated a research program consisting of field and small-scale tests (Wendeler et al. 2008, 2019). The key advantage is that flexible barriers can be more easily installed in remote and steep mountainous channels compared to traditional rigid structures (Wendeler et al. 2008). In parallel to the Swiss group, the Geotechnical Engineering Office in Hong Kong and the Hong Kong University of Science and Technology performed small- and large-scale flume tests and numerical simulations to improve the understanding and design of flexible barriers for debris flow mitigation (Kwan and Cheung 2012, Ng et al. 2017).

Figure 2.10a shows an example of flexible debris flow barrier installed in the field. The structural components of a flexible barrier can be identified as (Figure 2.10b): vertical posts to transfer the loads to the foundation; horizontal cables anchored on the sides of the channel; ring net retaining the debris flow and transferring the loads to posts and the cables. Brake elements (Castanon-Jano et al. 2017) can also be installed on the cables to absorb energy from the debris flow impact and reduce the forces on the other structural components of the barrier.

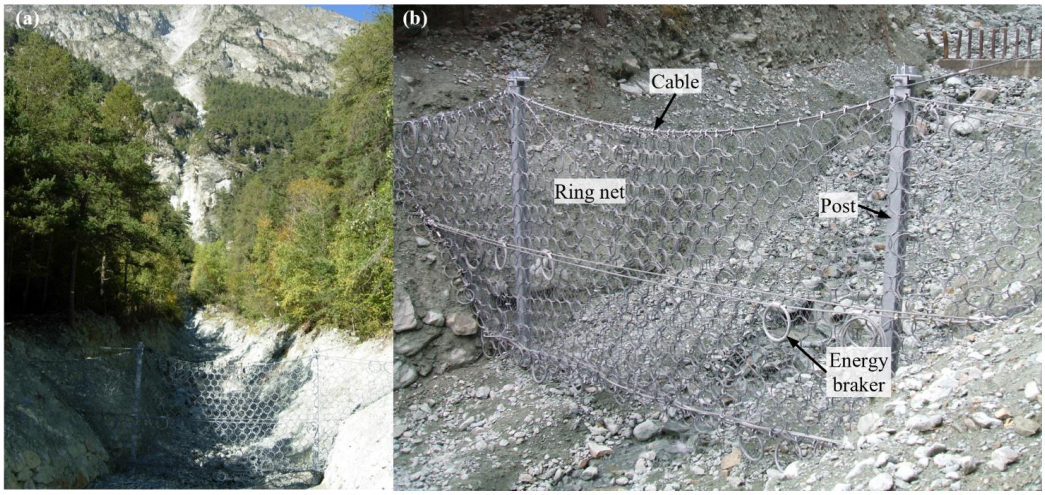

Figure 2.10 (**a**) Flexible barrier installed in a debris flow channel in Aosta Valley (Italian Alps); (**b**) details of the flexible barrier

2.4.1. Physical modelling of flexible debris flow barriers

Table 2.5 shows the main experimental and field studies regarding the debris flow-flexible barriers interaction, based on a literature study. These studies modelled the base of the flume as non-erodible (DeNatale et al. 1999, Wendeler et al. 2008, Canelli et al. 2012, Wendeler and Volkwein 2015, Ng et al. 2017, Song et al. 2018, 2019). Wendeler et al. (2019) tested flexible barriers in the field (Illgraben channel), where the bed was erodible; however, the debris flow-erodible bed interaction was not analysed. The main goal of these studies was indeed to define loading models for the impact of debris flows on a barrier. The shortcoming of not considering an erodible bed motivates the need to study the influence of a flexible barrier on the debris flow entrainment, which will be addressed in this thesis.

Furthermore, (Kwan et al. 2015, Ng et al. 2019, 2020a) proposed a design methodology for multiple rigid barriers, accounting for impact, overflow and landing models. Compared to the design of a single terminal barrier, multiple barriers can stop the flow progressively and in the upstream parts of the channel, which may reduce entrainment and therefore prevent the debris flow to increase in size. The multiple barrier framework has so far been evaluated for the case of debris flows on fixed beds impacting rigid barriers. In this study, the case of multiple (upstream + terminal) flexible barriers with an erodible bed will be modelled for the first time.

Table 2.5 Experimental and field observations of the debris flow-flexible barrier interaction

Study	Methodology	Main outcome
(DeNatale et al. 1999)	Large-scale flume tests ($V_i = 10\ m^3$) with terminal flexible barrier	First study of flexible debris flow barrier
(Wendeler et al. 2008)	Flexible barrier installed in Illgraben	Cable forces measured for several natural debris flow events
(Wendeler and Volkwein 2015)	Small-scale flume tests ($V_i = 0.15\ m^3$)	Retention capacity of the flexible barrier is dependent on the mesh opening size of the ring net
(Wendeler et al. 2019)	Small-scale flume tests and field observations (Illgraben)	- Run-up impact mechanism observed in the flume tests and pile-up mechanism observed in the field - Definition of a load model
(Canelli et al. 2012)	Small-scale flume tests ($V_i = 0.4\ m^3$)	Study on the impact kinematics
(Ng et al. 2017, Song et al. 2018, 2019)	Centrifuge tests	- Granular flows exhibit a pile-up impact mechanism on the barrier, while viscous flows exhibit a run-up type of impact - The total impact load on flexible barriers is lower than for rigid barriers, due to prolonged interaction promoting internal energy dissipation in the debris flow - Impact forces from granular flows are higher than the forces from viscous flows, because of higher internal energy dissipation by frictional shearing
(Ng et al. 2020a)	Large-scale flume tests	Study of the impact mechanisms of a debris flow on a flexible barrier
(Kwan et al. 2015, Ng et al. 2018, 2019, 2020a)	Small- and large-scale flume tests of multiple rigid barriers	Definition of a framework for the design of multiple rigid barriers
Paper II	Large-scale flume tests ($V_i = 2.5 - 6\ m^3$)	- Influence of an upstream flexible barrier on the debris flow entrainment - Multiple flexible barriers can reduce the impact load on a terminal flexible barrier

2.4.2. Analytical and numerical modelling of flexible debris flow barriers

The main goal of a flexible debris flow barrier is to take energy out of the flow and to retain a part of or the total debris flow volume. To achieve this goal, the flexible barrier should be designed to withstand the impact forces transmitted by the debris flow. The impact force by a debris flow can be evaluated by modelling the debris flow as a continuum equivalent fluid transmitting on the barrier a combination of hydrostatic and hydrodynamic loads (Ng et al. 2021):

$$F_{\mathrm{T}} = \frac{1}{2} K \rho_{\mathrm{f}} g h_{\mathrm{f}}^2 cos\theta W + \alpha \rho_{\mathrm{f}} v_{\mathrm{f}}^2 h_{\mathrm{f}} W \quad \textbf{2.14}$$

where F_T is the total peak impact force normal to the barrier; K is an earth pressure coefficient; ρ_{f} is the debris flow density; h_{f} is the flow depth before impact; θ is the slope angle; W is the width of the debris flow channel; v_{f} is the debris flow velocity before impact and α is a dynamic pressure coefficient. The value of K may be assumed equal to 1 according to design guidelines (Kwan and Cheung 2012), as the flow is fluidised. Values of K greater than 1, correspondent to a passive earth pressure, have also been reported (Song et al. 2018). The value of α may be assumed equal to 2 according to design guidelines (Kwan and Cheung 2012), although a range of values from 1 to 5 has been reported in the literature (Poudyal et al. 2019).

By dividing both sides of Eq. 2.14 by the term $\rho_{\mathrm{f}} v_{\mathrm{f}}^2 h_{\mathrm{f}} W$, one obtains the following dimensionless equation:

$$\frac{F_{\mathrm{T}}}{\rho_{\mathrm{f}} v_{\mathrm{f}}^2 h_{\mathrm{f}} W} = \frac{K}{2(Fr)^2} + \alpha \quad \textbf{2.15}$$

where Fr is the Froude number (corrected for the gravitational component):

$$Fr = \frac{v_{\mathrm{f}}}{\sqrt{g h_{\mathrm{f}} cos\theta}} \quad \textbf{2.16}$$

Eq. 2.15 shows that, for sufficiently high values of the Froude number (e.g. $Fr > 3$), the first term on the right hand side of Eq. 2.15 is negligible compared to the second term, equal to α. In this case, therefore, Eq. 2.14 reduces to:

$$F_{\mathrm{T}} = \alpha \rho_{\mathrm{f}} v_{\mathrm{f}}^2 h_{\mathrm{f}} W \quad \textbf{2.17}$$

Eq. 2.17 is used in design guidelines in Hong Kong (Kwan and Cheung 2012) to evaluate the dynamic impact load, with the recommended values $\rho_{\mathrm{f}} = 2200\ kg/m^3$ and $\alpha = 2.0$. The application of a hydrostatic load is instead recommended for static debris piling against the barrier (Kwan and Cheung 2012). A schematic of the design impact scenario is shown in Figure 2.11.

Eq. 2.17 will also be used in this thesis to interpret the experimental data (*Paper II*), as large values of the Froude number were observed. Furthermore, Eq. 2.17 may be considered to be applicable for the Norwegian debris flow conditions, as the steep topography is expected to promote very fast debris flow motion, as observed in Fjærland (Breien et al. 2008) and simulated for the Hunnedalen case by Vicari et al. (2021b).

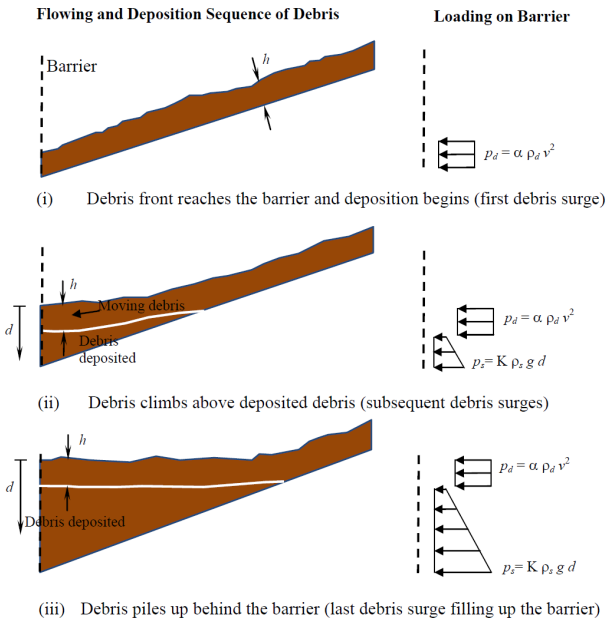

Figure 2.11 Design impact scenario on a flexible barrier (figure taken from Kwan and Cheung 2012). p_d and p_s denote the dynamic and hydrostatic pressures respectively

The application of Eq. 2.17 for the design of flexible barriers may be limited by the lack of knowledge of the debris flow characteristics such as the flow depth and velocity. Numerical methods, instead, can be used to evaluate the runout of the debris flow and its interaction mechanisms with a flexible barrier. To model the debris flow-flexible barrier interaction, a three-dimensional model needs to be used; indeed, the traditional depth-averaged models are unable to capture the vertical momentum redirection typical of the impact run-up mechanism on a barrier (Ng et al. 2020b). The development of three-dimensional numerical models has been hindered in the past by limited computational power. However, in recent years, three-dimensional modelling of the debris flow-flexible barrier interaction has advanced significantly. Table 2.6 shows a summary of some three-dimensional numerical models used to study the flow-flexible barrier interaction.

Table 2.6 Summary of three-dimensional numerical models to compute the debris flow-flexible barrier interaction. DEM indicates the Discrete Element Method; LB indicates Lattice Boltzmann method; FEM indicates the Finite Elements Method; ALE indicates the Arbitrary Lagrangian-Eulerian formulation; CFD indicates Computational Fluid Dynamics; MPM indicates the Material Point Method

Study	**Method to compute flow dynamics**	**Method to compute flexible barrier mechanics**	**Validation**	**Main outcomes**
(Leonardi et al. 2016)	DEM for grains + LB for fluid	FEM with equivalent net	Hypothetical case	Both solid and fluid components contribute to the impact force
(Cheung et al. 2018, Kwan et al. 2019)	ALE. Elastoplastic model yield criterion for the debris flow	FEM - ALE. Structural components modelled as beam elements as elastic materials	Illgraben field test (Wendeler et al. 2008) and Veltheim test	Debris flow friction influencing impact forces
(Li et al. 2020)	DEM for solid phase and CFD for fluid phase	DEM	Flexible barrier response calibrated on rockfall impact	Stresses on all structural components of the barrier can be evaluated
(Zhao et al. 2020)	ALE. Drucker-Prager yield criterion for the debris flow	ALE	Veltheim test	Debris flow with boulders in front is evaluated
Paper III	MPM. Mohr-Coulomb model for the debris flow	MPM	Large-scale tests (Vicari et al. 2021a)	Barrier is simplified in 2D as a curved rigid barrier

Chapter 3

3. Numerical modelling of debris flow entrainment applied to a real case

Channel in Hunnedalen (Norway) after the debris flow event

Entrainment is one of the most important phenomena influencing the debris flow dynamics, as it can significantly increase the debris flow volume and it may modify of the flow composition and basal stresses. The Hunnedalen (Norway) debris flow (2nd June 2016) is analyzed in this chapter. Indeed, this event was characterized by an initial volume of about 2000 m^3 which increased up to 20000 m^3 due to entrainment of soil, fluid, and boulders along the channel. Therefore, this debris flow event is chosen as a reference to illustrate the significance of entrainment in nature. The analysis of a real natural event may provide useful insights on the entrainment mechanics.

However, available data of a debris flow event are typically limited, as the flow dynamics cannot be directly observed or recorded. For instance, in the case of the Hunnedalen debris flow, only the final erosion and deposition along the channel were observed, but limited data are available about the flow depth and velocities for instance. Therefore, it may be useful to numerically back-calculate the debris flow event to simulate the debris flow dynamics and the entrainment process. Full three-dimensional simulations of the entire flow dynamics would require a very high computational power, because of the large scale of natural debris flow events (e.g., 750 m longitudinal extension for the Hunnedalen debris flow). Hence, depth-averaged simulations are usually adopted to simulate natural debris flows, which require a significantly lower computation time. As discussed previously in chapter 2.3.2, in depth-averaged models, entrainment is modelled through the entrainment rate, without modelling the internal mechanics of the erodible bed. Assumptions are therefore made to model the entrainment rate (e.g., Eqs. 2.9-2.13). In this chapter, RAMMS::DF (Rapid Mass Movement Simulation, ramms.slf.ch/ramms) depth-averaged software (Christen et al. 2010, Frank et al. 2015) is used to back-calculate the entrainment observed in the Hunnedalen debris flow. The influence of the model parameters on the simulation results is therefore discussed.

3.1. The depth-averaged numerical model RAMMS

Depth-averaged numerical models are based on the assumption that velocities and stresses along the flow thickness may be integrated (Pudasaini and Hutter 2007). The assumption is valid if the flow depth is small compared to the longitudinal extent of the flow. Therefore, the variations of velocities and stresses along the flow depth (perpendicular to the basal topography) are neglected. This assumption allows to simplify the mass and momentum conservation equations and reduce the computational cost.

The mass conservation in RAMMS is conceptually equivalent to Eq. 2.7 but extended in RAMMS to a three-dimensional basal topography. Eq. 2.9 is used for the entrainment rate (Frank et al. 2015, 2017) and Eq. 2.10 expresses the maximum (cap) entrainment depth (cf. Figure 2.8). Therefore, the parameters $\frac{dz}{dt}$, $\frac{dz}{d\tau}$, τ_c need to be assumed as input for the simulation in RAMMS. Their influence on the modelled entrainment volume will be discussed in *Paper I*.

Referring to the flow element dx in Figure 2.7, the depth-averaged momentum conservation equation in the x-direction can be expressed in a Eulerian reference frame as:

$$\frac{\partial(h_f \bar{v}_f)}{\partial t} + \frac{\partial\left(h_f \bar{v}_f^2\right)}{\partial x} = g h_f sin\theta - \frac{\partial\left(\frac{1}{2} K g cos\theta h_f^2\right)}{\partial x} - \frac{\tau_{f-b}}{\rho_f} \qquad \textbf{3.1}$$

where g is the acceleration due to gravity, θ is the slope angle, K is the earth-pressure coefficient, ρ_f is the density of the flow and τ_{f-b} is the shear resistance at the base of the flow. In RAMMS, Eq. 3.1 is extended to a three-dimensional topography.

To illustrate the physical meaning of the left-hand-side (LHS) of Eq. 3.1, it is useful to transform the LHS from the Eulerian form to its Lagrangian form. This is achieved by first expanding the derivatives in Eq. 3.1 and then using the mass conservation equation (Eq. 2.7):

$$\frac{\partial(h_f \bar{v}_f)}{\partial t} + \frac{\partial\left(h_f \bar{v}_f^2\right)}{\partial x} = h_f \frac{\partial \bar{v}_f}{\partial t} + \bar{v}_f \frac{\partial h_f}{\partial t} + h_f \bar{v}_f \frac{\partial \bar{v}_f}{\partial x} + \bar{v}_f \frac{\partial(h_f \bar{v}_f)}{\partial x} = h_f \frac{\partial \bar{v}_f}{\partial t} + h_f \bar{v}_f \frac{\partial \bar{v}_f}{\partial x} + \bar{v}_f E \qquad \textbf{3.2}$$

The right-hand-side of Eq. 3.2 can be rewritten by using the Lagrangian total derivative ($\frac{d}{dt} = \frac{\partial}{\partial t} + \bar{v}_f \frac{\partial}{\partial x}$) to obtain:

$$h_f \frac{d\bar{v}_f}{dt} + \bar{v}_f E \qquad \textbf{3.3}$$

which represents the x-momentum variation in time of a flow column of height h_f (per unity density and per unit basal area). The equation is valid for a Lagrangian reference system which is fixed with the flow column moving at a velocity $\bar{v}_f$ (e.g., DAN software, McDougall and Hungr 2005). A simple representation of this momentum variation is shown in Figure 3.1.

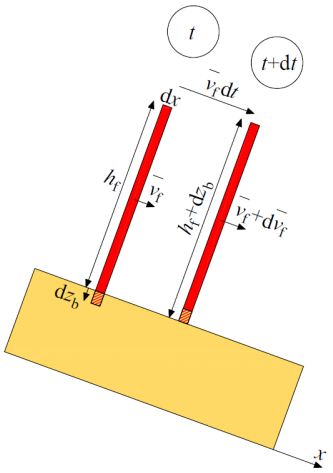

Momentum at time t: $h_f\bar{v}_f$
Momentum at time t+dt: $(h_f+dz_b)(\bar{v}_f+d\bar{v}_f)$
(where $dz_b=E\cdot dt$)

Momentum variation: $[(h_f+dz_b)(\bar{v}_f+d\bar{v}_f)-(h_f\bar{v}_f)]/dt \approx h_f d\bar{v}_f/dt+\bar{v}_f E$

Figure 3.1 Flow column movement observed in a Lagrangian reference system and variation of the flow momentum in a depth-averaged framework

The right-hand-side of Eq. 3.1 is the sum of the forces (per unit density and basal area) acting on the flow column, specifically the slope-parallel gravity force; the force due to longitudinal variations of the flow depth and normal stress; and the shear resistance at the base of the flow, which is modelled in RAMMS according to the Voellmy rheology:

$$\tau_{f-b} = \mu_{f-b}\rho_f g h_f cos\theta + \frac{\rho_f g \vec{v}_f^2}{\xi} \qquad \textbf{3.4}$$

where μ_{f-b} is the apparent friction coefficient at the base of the debris flow and ξ is the turbulence coefficient of the flow. These parameters need to be back-calculated to simulate the entrainment volumes and debris flow runout. The back-calculation of the model parameters is described in *Paper I*, which follows.

3.2. The Hunnedalen debris flow: geology and triggering factors

The Hunnedalen debris flow occurred in the Mjåland channel, Hunnedalen, Rogaland County in Norway (Figure 3.2a, b). Figure 3.2c shows the geological map of the Mjåland area, which is mainly constituted by gneiss. The bedrock is covered by a thin layer of soil in the upper part of the channel, while glaciofluvial deposits are found in the alluvial fan at the base of the channel (Figure 3.2d).

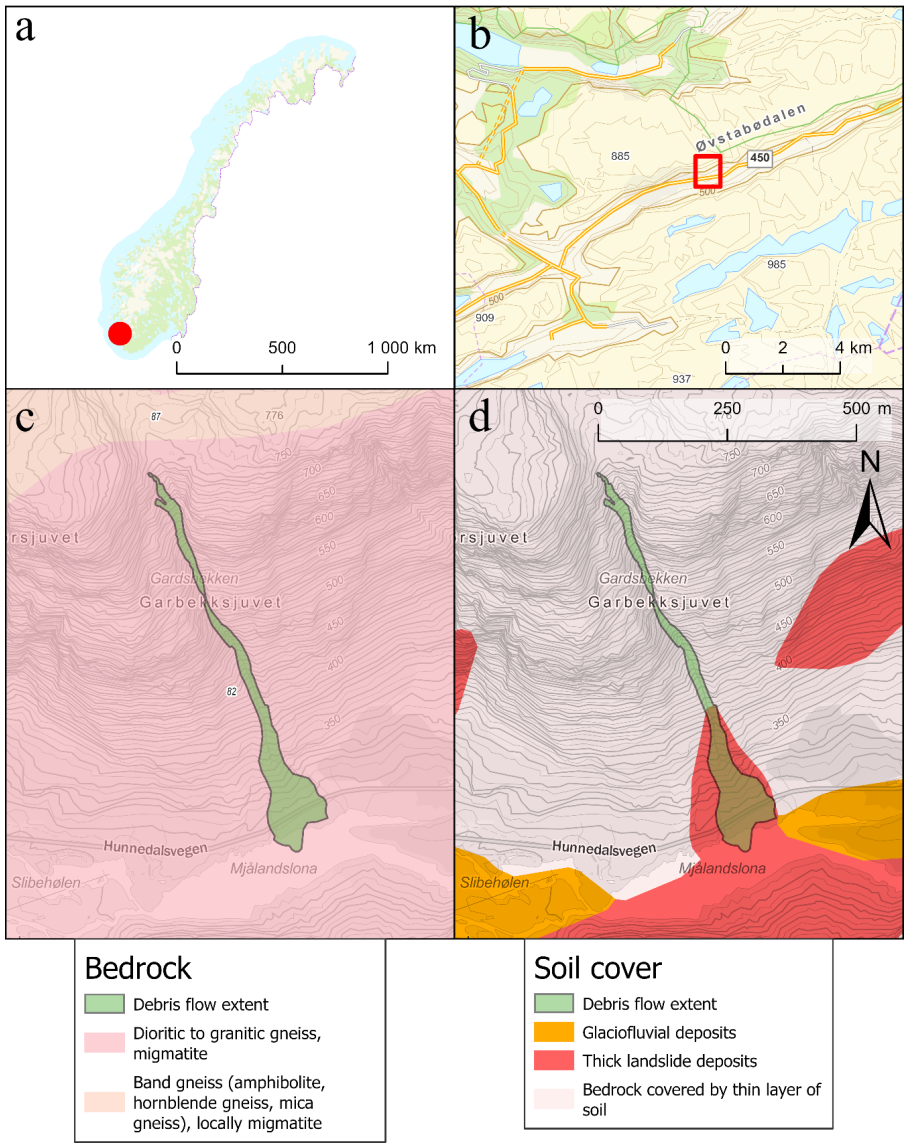

Figure 3.2 Maps of Hunnedalen: (a) Topographic map of Norway; (b) Topographic map of Hunnedalen area; (c) Geological map of Mjåland catchment; (d) Soil cover map of Mjåland catchment

Figure 3.3 shows a screenshot of the landslide report (nve.no): the landslide was reported to have occured at around 16:30 on 2nd June 2016 (notice that the event may have occurred earlier

compared to what is reported). The debris flow originated from a small landslide of approximately 2000 m^3. The initial landslide then entrained soil and boulders along the channel to grow to a final volume of approximately 20000 m^3. More details of the landslide event and dynamics are provided in *Paper I*.

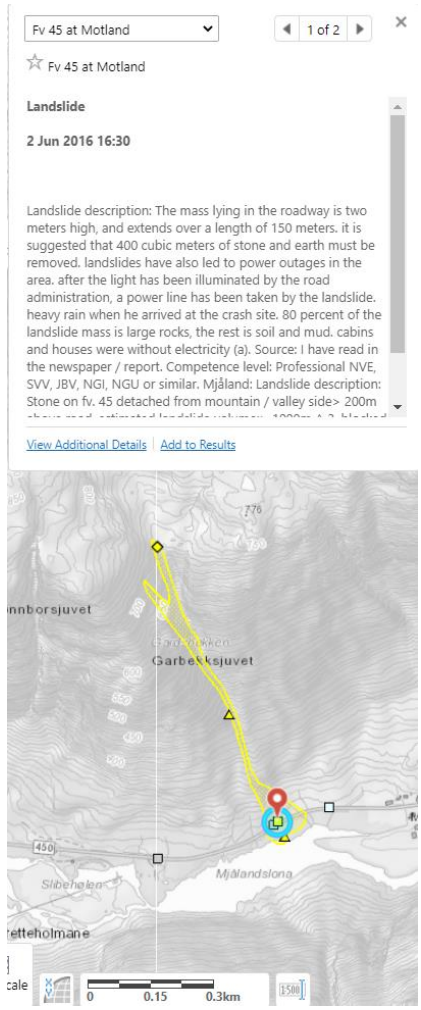

Figure 3.3 Landslide report (nve.no)

A basic analysis of the rainfall data is carried out here to preliminarily investigate the potential triggering factors of the initial landslide. The daily rainfall data in the 20 days before the event are shown in Figure 3.4. Rainfall data are taken from the weather station of Maudal, located at

approximately 6 km from the landslide. No rainfall is measured at this weather station the day before and on the day of the debris flow event (2nd June 2016). The daily rainfall amount in the weeks before the landslide is also quite low, which suggests that prolonged rainfall was not the cause of the debris flow.

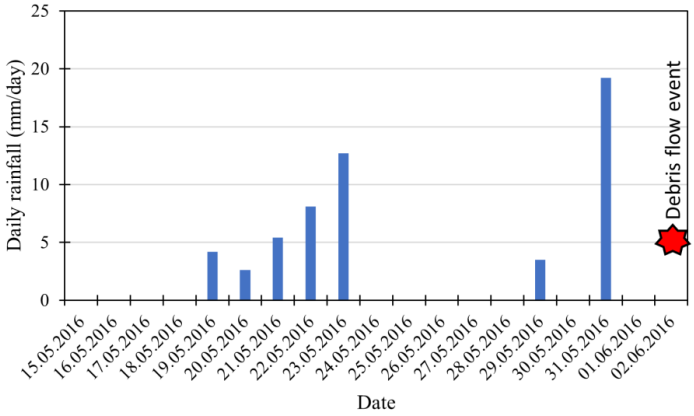

Figure 3.4 Daily rainfall measured at the weather station in Maudal (approximately 6 km from the landslide location) (data from xgeo.no)

To gain more insights on the local rainfall intensity, radar data by the Norwegian Meteorological Institute are analyzed. Figure 3.5 shows the hourly rainfall measured by radar in Mjåland on 2nd June 2016. A maximum rainfall of 5 mm/h is observed between h15:00 and h16:00, which is just before the landslide event at around h16. Figure 3.6 shows the spatial distribution of the hourly rainfall between h15:00 and h16:00 on 2nd June 2016. In the area around Mjåland, up to 20 mm/h are measured by the radar. Notice that radar data may be affected by errors and that the measured rainfall intensity depends on the spatial resolution of the radar data (in this case 1 km). Therefore, locally, rainfall may have been more intense compared to the measurements by the radar. The high rainfall intensity measured in the area around Mjåland therefore suggests that a short but intense rainfall may have been the triggering factor for the initial landslide.

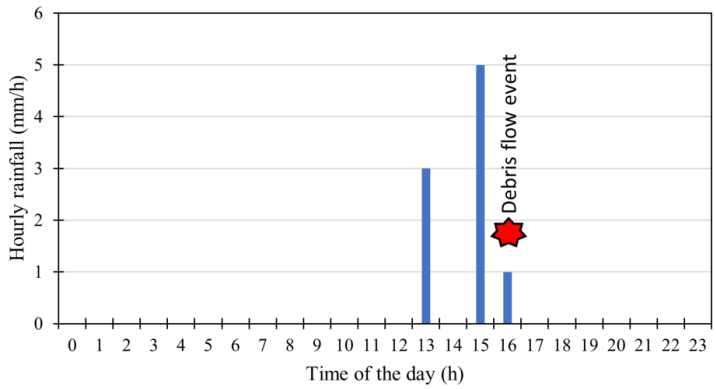

Figure 3.5 Hourly rainfall data measured by radar on 2nd June 2016 (data from https://github.com/metno/NWPdocs/wiki/Post-processed-products)

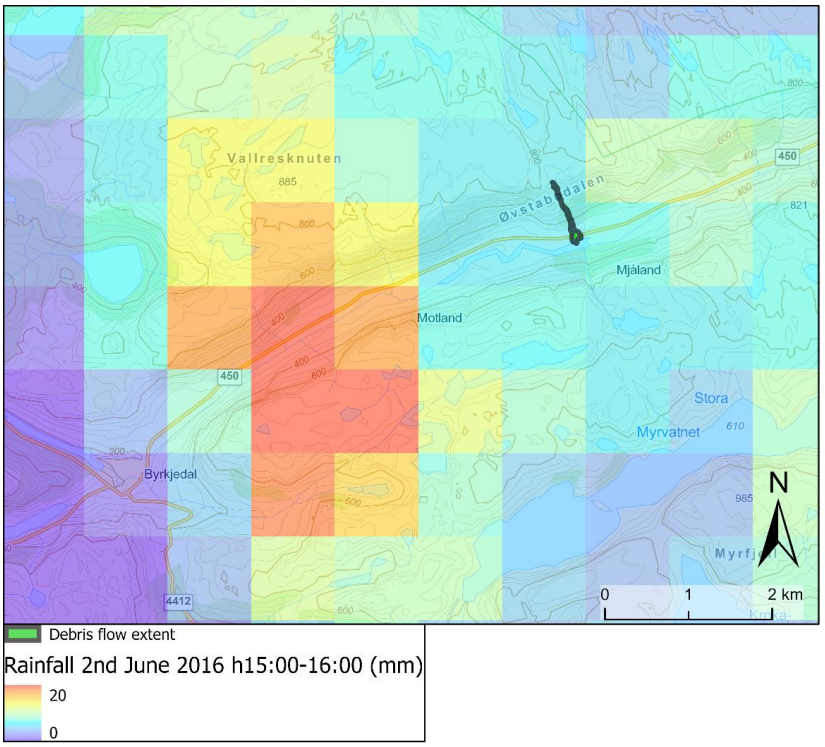

Figure 3.6 Spatial distribution of the hourly rainfall measured by radar from h15:00 to h16:00 on 2nd June 2016 in the area around Mjåland (data from https://github.com/metno/NWPdocs/wiki/Post-processed-products)

3.3. Paper I

Vicari, H., Nordal, S., Thakur, V. (2021). The Significance of Entrainment on Debris Flow Modelling: The Case of Hunnedalen, Norway. In: Barla, M., Di Donna, A., Sterpi, D. (eds) Challenges and Innovations in Geomechanics. IACMAG 2021. Lecture Notes in Civil Engineering, vol 126. Springer, Cham. https://doi.org/10.1007/978-3-030-64518-2_60

The significance of entrainment on debris flow modelling: the case of Hunnedalen, Norway

Hervé Vicari[1,*], Steinar Nordal[1] and Vikas Thakur[1]

[1] Department of Civil and Environmental Engineering, Norwegian University of Science and Technology
Høgskoleringen, 7A, 7034, Trondheim (Norway)
herve.vicari@ntnu.no

Abstract This paper studies the influence of entrainment on the runout behavior of a documented debris flow, in Hunnedalen (Norway), happened on 2nd June 2016. The steepness of the channel and the availability of sediments along the flow path caused the debris flow to grow from approximately 2000 m^3 to approximately 19000 m^3. This paper aims to back calculate this event, using a Voellmy rheology implemented in RAMMS:DF and including a debris flow entrainment model. Voellmy rheological parameters (friction coefficient μ and turbulence coefficient ξ) are back-calculated using the default parameters of the entrainment model in RAMMS:DF. The back-calculation aims to replicate available field data such as: the deposit shape and the total entrained volume. It is also shown how the total eroded volume is strongly affected by the choice of μ and ξ. Finally, the entrainment parameters are varied from their default value to understand their influence on entrainment magnitude.

Keywords: *debris flow, numerical modelling, entrainment, Voellmy rheology*

1 Introduction

Debris flows are a particular type of landslide, travelling at high velocities and for long distances along mountainous and torrential channels. Their travelling distance and destructive capacity can be increased due to entrainment of bed sediments during the flow along the channel.
Numerical models are useful instruments to study the dynamic of debris flows. Due to the large influence of the entrainment process on their behavior, it is important to include erosion in the numerical model (Frank et al., 2015).
Several software include such entrainment models. Among them, RAMMS:DF (Bartelt et al. 2013) implements an erosion model (Frank et al., 2015) calibrated on field observations (Berger et al., 2011). This model has already been applied to back-calculate some debris flow events (e.g. Frank et al., 2015, 2017). Frank et al. (2015) showed that such model predicts erosion values similar to those observed in the field. Frank et al. (2017) studied the influence of the erosion coefficients in the model and of the initial volume of the debris flow on the total eroded volume.

The present study focuses on the back-calculation of the Hunnedalen (Norway) debris flow, happened on 2nd June 2016, based on the deposition shape (estimated from satellite orthophotos and data collected after the event) and on the total eroded volume (estimated in the field). We therefore evaluated the sensitivity of the Voellmy's rheological parameters and of the erosion coefficients on the total eroded volume.

2 Description of the event and field study

The Mjåland catchment is located in the Hunnedalen valley, in Rogaland county (southern western Norway). The channel extends from 720 m a.s.l. to 300 m a.s.l., covering a planimetric longitudinal distance of approximately 750 m (Fig. 1a).

Fig. 1 Hunnedalen debris flow event on 2nd June 2016 (Courtesy: Multiconsult and Norwegian Public Roads Administration, NPRA) (a) and planimetric view of the area (b)

On 2nd June 2016, after a period of intense rainfalls, a landslide was triggered by mobilization of vegetated soft soil and talus cover, between 720 and 655 m a.s.l. This initial mass successively flowed down along the slope confined by the channel and was able to erode sediments and boulders for a volume 8 times bigger than the initial one. Many trees in the channel were also entrained by the debris flow. Finally, it deposited between 325 and 300 m a.s.l., covering the road for 150 m in extent and reaching, on the extreme right bank lobe, the river.
Field observations, carried out after the event (in June 2016, by Multiconsult) and successively (June 2019, by the author), allow to estimate the triggered, eroded and

deposited volumes (nomenclature is shown in Fig. 1b and in Table 1). The release area consisted of two main and distinct slides ("Source 1" with an estimated depth of 0.5 m and "Source 2" with an estimated depth of 1.5 m). This initial landslide volume was then able to erode the soil bed in the channel flowing downslope. Erosion happened in two sections of the channel: "Erosion 1", with an estimated average erosion depth of 1 m (this soil layer was completely eroded down to the bedrock level, which is now outcropping), and "Erosion 2" with an estimated average erosion depth of 1.2 m. The channel section between them, here called "Bedrock", was most likely not eroded during the event. Finally, the debris flow deposited in the zone indicated as "Deposition area", with an average thickness of 2 m.

Table 1 Estimated depth of source landslide, erosion sections along the channel and deposition fan. The volumes are computed as the product between the depth and the inclined area from the orthophoto

Zone	Depth (m)	Volume (m^3)
Source 1	0.5	231
Source 2	1.5	1898
Erosion 1	1	2938
Erosion 2	1.2	13840
Deposition	2	20380

3 RAMMS Debris Flow: theoretical aspects

In this study, RAMMS:DF (Bartelt et al., 2013) software is used. The model is based on a one-phase equivalent incompressible fluid with constant density. Mass and momentum balance equations are solved in a Eulerian reference system by the finite volume method. The stopping calculation criteria is based on the percentage of momentum (Bartelt et al., 2013).

The model uses a constant earth pressure coefficient (equal to 1) and implements a Voellmy rheology, as in Eq. (1), to express the total basal shear resistance (S):

$$S = \mu\rho gHcos\varphi + \frac{\rho gU^2}{\xi}. \quad (1)$$

Where ρ is the bulk density, g is the gravitational acceleration, φ is the slope angle, H is the mean flow height, U is the mean flow velocity, μ is the Coulomb apparent friction coefficient and ξ is the turbulence coefficient.

The debris flow entrainment model is described in Frank et al. (2015) and is based on field data from the Illgraben channel in Switzerland (Berger et al., 2011). The maximum erosion depth (e_m) is expressed by Eq. (2):

$$e_m = \begin{cases} 0 & \text{for } \tau < \tau_c \\ \frac{dz}{d\tau}(\tau - \tau_c) & \text{for } \tau \geq \tau_c \end{cases}. \quad (2)$$

Where τ is the shear stress at the base of the flow, τ_c is a critical shear stress and $dz/d\tau$ is an average potential erosion depth. Erosion rate is specified by the parameter dz/dt and is active when Eq. (2) is valid and until the erosion depth has reached the maximum erosion depth (Frank et al., 2015). Different values of the entrainment parameters ($dz/d\tau$, dz/dt, τ_c) can be used in RAMMS:DF.

4 Back-analysis of the Hunnedalen debris flow

4.1 Input data in RAMMS

Four ingredients are needed to run a simulation in RAMMS: topography of the area with a digital terrain model; release volume; rheology; erosion law.
A pre-event DTM is used for the simulation. The grid spacing corresponds to 2 m. A resolution of 5 m was also tested but judged too coarse; and a resolution of 0.5 m requires a too long calculation time. However, a 2 m resolution is considered sufficiently accurate and in literature, this grid spacing is often used.
The release volume corresponds to 2129 m^3 (the sum of "Source 1" and "Source 2" in Table 1). The release area has been defined based on the post-event orthophoto in GIS. Block release method is used, by subtracting the release depth (Table 1) to the initial DTM, which helps to keep the initial volume inside the channel (Frank et al., 2017).
The Voellmy rheology is used in RAMMS. The range of values investigated to simulate the Hunnedalen debris flow event is between 0.01 and 0.4 for the friction coefficient and between 100 and 800 m/s^2 for the turbulence coefficient. This range of values is often used in literature; for example, Bartelt et al. (2013) describe typical values of the friction coefficient between 0.05 and 0.4 and suggest values between 100 and 1000 m/s^2 for the turbulence coefficient. Furthermore, the lower values of ξ in this range are reported for granular flows, while the higher values are often found for muddy flows.
The back-calculation and the consequent analysis (chapters 4.2 and 4.3) are done by keeping the erosion parameters constant and equal to the default value in RAMMS: τ_c=1 kPa; $dz/d\tau$=-0.1 m/kPa and dz/dt=-0.025 m/s. This allows to understand the influence of the Voellmy parameters on the erosion magnitude. Furthermore, in the zone "Erosion 1", the maximum erodible depth is set to 1 m, to account for the known presence of the bedrock, which constitutes a boundary limit to the erosion process. In chapter 4.4, the erosion coefficients are varied from their default values, to understand their influence.
Finally, for all the simulations, it was decided to fix the stop parameter – which, in RAMMS, corresponds to the percentage of total momentum – equal to 10%: in many simulations, a lower value was not high enough to stop the flow and numerical diffusion happened. Even setting the stop parameter to 10%, in some cases (in particular for high values of μ), it was necessary to manually stop the program, as the percentage of total momentum started to oscillate around a constant value. It was however decided to not increase the stop parameter over 10% to avoid too early stoppage of the flow.

NOTE. τ is the slope-parallel gravity stress ($\tau=\rho g H \sin\varphi$)

4.2 Results of the back-calculation and discussion

The back-calculation aims at replicating the available data observed in the field: depositional shape and total eroded volume. The following values of the Voellmy rheology are tested: μ=0.01; 0.05; 0.1; 0.2; 0.3; 0.4 and ξ=100; 150; 200; 400; 800 m/s^2. Further values are successively tested to find the best-fit parameters of the debris flow event. Fig. 2 shows the dependency of the total eroded volume from the Voellmy rheological parameters (friction coefficient, μ, and turbulence coefficient, ξ).

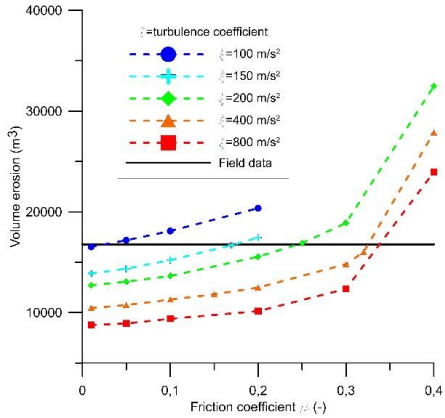

Fig. 2 Total erosion volume computed with RAMMS, with different values of Voellmy's rheological parameters

In particular, four couples of rheological parameters (μ=0.01, ξ=100 m/s^2; μ=0.17, ξ=150 m/s^2; μ=0.25, ξ=200 m/s^2; μ=0.32, ξ=400 m/s^2) are able to simulate the observed erosion volume (16778 m^3), but they are giving different deposition shapes (Fig. 3). The selection of the best-fit parameters, among them, can be therefore based on the similarity of the depositional shape to the observed one: simulations in Fig 3b and in Fig. 3c both produce acceptable results. A too low value of the friction coefficient (under 0.1, like in Fig. 3a) would in fact produce a too long runout and too thin deposits, while a too high value (above 0.3, like in Fig. 3d) would have the opposite effects. The turbulence coefficient, vice versa, has a lower influence on the deposition process (cf. Bartelt et al., 2013), but it can greatly vary the flow velocities along the channel: too high values of ξ (e.g. 800 m/s^2) would give unreasonably high velocities in this case study.

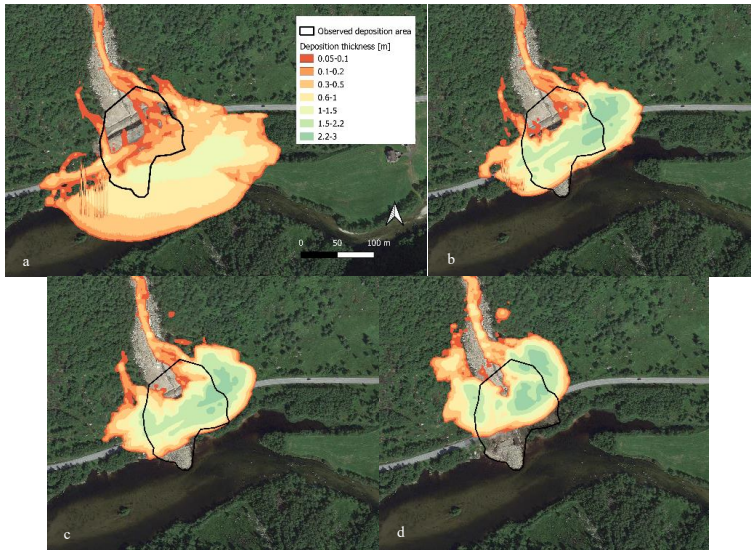

Fig. 3 Simulated deposition shapes for different values of Voellmy's rheological parameters: μ=0.01, ξ=100 m/s^2 (a); μ=0.17, ξ=150 m/s^2 (b); μ=0.25, ξ=200 m/s^2 (c); μ=0.32, ξ=400 m/s^2 (d)

Considering the available data, the best-fit parameters are considered to be: μ=0.17 and ξ=150 m/s^2. It is difficult however to precisely select them, as many field observations are missing (e.g. flow heights and velocities). Also, the depositional process in the simulation does not account for the presence of the trees, which might be important at low velocities (i.e. during deposition) to confine laterally the flow. The flow in the fan and in the flatter final zone is also influenced by the choice of the earth pressure coefficient. Gray et al. (1999) showed that the use of passive/active coefficients is fundamental to correctly simulate the deposit shape. In particular, when the flow reaches the fan, it can expand laterally (due to the loss of channel confinement) and is therefore subjected to a dilative motion in the cross-slope direction. Using an active earth pressure coefficient, in this direction, would reduce the lateral spreading. In the slope direction, vice versa, the flow would be subjected to a compressive motion, correspondent to a passive state.

4.3 Influence of Voellmy's parameters on erosion magnitude

As shown in Fig. 2, the Voellmy's rheological parameters greatly affect the total eroded volume. An increasing eroded volume is obtained for increasing values of μ and decreasing values of ξ: this might be due to how these two parameters influence, at any given location, the flow height – which affects the shear stress in Eq. (2) – and the duration of the flow – which is directly related to the erosion parameter *dz/dt*.

NOTE. Unfortunately, the paper contains a mistake in Fig. 3. The correct legend is as follows:

4.4 Influence of erosion parameters on erosion magnitude

In this section, the influence of the potential erosion depth ($dz/d\tau$, with values of -0.05; -0.1 and -0.2 m/kPa) and of the erosion rate (dz/dt, with values of -0.013; -0.025 and -0.05 m/s) on the total eroded volume is studied. The parametric study is performed by keeping constant the Voellmy's parameters to the best-fit values (μ=0.17 and ξ=150 m/s^2) and the critical shear stress to 1 kPa. In fact, Frank et al. (2017) showed that, for large initial volumes (higher than 10-50 m^3, in the Meretschibach catchement), the volume growth due to entrainment of bed sediments has a low sensitivity from the critical shear stress. Also, the slope angle in the Hunnedalen channel is high: Frank et al. (2015) suggest adjusting the critical shear stress for low slope channels (under 10°).
Fig. 4 shows the influence of the two erosion parameters: the eroded volume is clearly increasing with increasing values of the absolute values of $dz/d\tau$ and dz/dt.

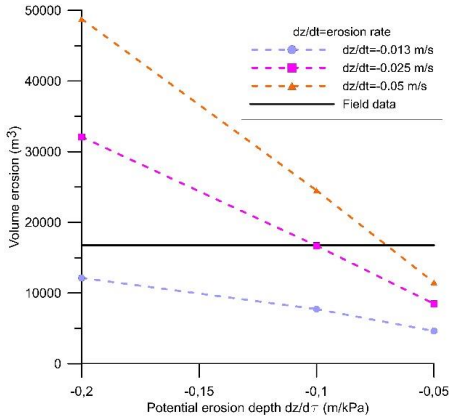

Fig. 4 Total erosion volume computed with RAMMS, for different values of the erosion parameters, with the best-fit Voellmy's rheological parameters (μ=0.17 and ξ=150 m/s^2)

This result demonstrates that it would be possible to back-calculate the eroded volume using different values of the erosion parameters (but changing the value of Voellmy's parameters found in Chapter 4.2). However, the simultaneous calibration of five parameters (two Voellmy's parameters and three erosion parameters) would be difficult in the absence of many field data, which is often the case for non-monitored debris flows.

5 Conclusions

The software RAMMS:DF was used to back-analyze the Hunnedalen debris flow (2nd June 2016). A Voellmy rheology is implemented in the software and an erosion model

is included. It was possible to find some values of the Voellmy parameters which are able to simulate the observed total erosion volume, when the default erosion coefficients in RAMMS are chosen. The simulated runout distance is similar to the field data; however, the simulated deposit area shows more lateral spreading.
The influence of the Voellmy's parameters on the eroded volume was shown. Further studies could evaluate the link between Voellmy's rheological parameters, flow characteristics (in particular: flow height and velocity and flow duration) and the eroded volume. This might allow a more physical explanation of the trends observed in Fig. 2.
Finally, it was shown that it is, in theory, possible to use different erosion parameters to back-calculate the total eroded volume. The back-analysis of a debris flow event can therefore be conducted by calibrating five parameters (two Voellmy's rheological parameters and three erosion coefficients): this task is however not easy in the absence of many field observations. RAMMS manual (Bartelt et al., 2013) therefore gives some brief suggestions for the choice of the erosion parameters (related to the bed compaction, saturation and the expected erosion depth). Adding new case studies in literature – and related back-calculations – on debris flow events can allow to address the choice of these parameters, based on the specific field conditions of the event and on physical data (e.g. type of bed material, quantitative data of bed compaction and saturation).

Acknowledgements The work is supported by SFI KLIMA2050 (www.klima2050.no). We are grateful to Agnes Selma Haker (NPRA) and Ashenafi Lulseged Yifru (NTNU) for their help during the field survey in June 2019.

References

Bartelt, P., Bieler, C., Buehler, Y., Christen, M., Deubelbeiss, Y., Graf, C., McArdell, B., Salz, M., and Schneider, M. (2013) RAMMS – rapid mass movements simulation, A numerical model for debris flows in research and practice, user manual v1.7.0, Debris Flow. Manuscript update: November 2017, WSL Institute for Snow and Avalanche Research SLF, avail- able at: https://ramms.slf.ch/ramms/downloads/RAMMS_DBF_Manual.pdf (last access: 01 December 2019).

Berger, C., McArdell, B. W., and Schlunegger, F. (2011). Direct measurement of channel erosion by debris flows, Illgraben, Switzerland. *Journal of Geophysical Research: Earth Surface* 116(1), 1–18.

Frank, F., Mcardell, B. W., Huggel, C., and Vieli, A. (2015). The importance of entrainment and bulking on debris flow runout modeling: examples from the Swiss Alps. *Nat. Hazards Earth Syst. Sci.* 15, 2569–2583.

Frank, F., Mcardell, B. W., Oggier, N., Baer, P., Christen, M., and Vieli, A. (2017). Debris-flow modeling at Meretschibach and Bondasca catchments, Switzerland: sensitivity testing of field-data-based entrainment model. *Nat. Hazards Earth Syst. Sci.* 17, 801–815.

Gray, J. M. N. T., Wieland, M., and Hutter, K. (1999). Gravity-driven free surface flow of granular avalanches over complex basal topography. *Proc. R. Soc. Lond. A.* 455. 1841-1874.

3.4. Summary and limitations of the back-calculation of entrainment using RAMMS

The Hunnedalen debris flow was back-calculated in *Paper I* using RAMMS::DF software and an empirical entrainment model. The numerical model allowed to simulate the runout distance and to approximately capture the deposition shape by calibrating the Voellmy parameters. The parameters of the Voellmy model and of the entrainment model were observed to influence the total entrainment volume. However, several values of the entrainment parameters could back-calculate the total entrainment volume. Indeed, the entrainment model is empirical and does not include the physical processes affecting entrainment.

A first drawback of the empirical entrainment model is that the entrainment rate is assumed to be constant ($E = -dz/dt$), which does not respect conservation of momentum for the entrained bed layer (more details will be provided in the Supplementary Material of *Paper II*). Furthermore, the empirical entrainment model does not account for the shearing action of the debris flow onto the bed and for the development of resisting stresses within the erodible bed, which might eventually become weaker by development of excess pore pressures. Finally, it is practically and theoretically challenging to use a depth-averaged model such as RAMMS to simulate the flow interaction with mitigation barriers.

Therefore, to progress the knowledge on entrainment and its mitigation with flexible barriers, large-scale flume model tests are carried out (Chapter 4). A more advanced numerical method, the Material Point Method will then be introduced (Chapter 5) to back-calculate the test results and to attempt to capture the physical processes during entrainment by explicitly modelling the erodible bed material through an adequate constitutive model. Boulders can also be modelled with the Material Point Method, which offers the possibility to directly study their influence on entrainment and on the flow dynamics.

Chapter 4

4. Physical flume modelling

The large-scale flume model in Hong Kong

Coupled measurements of entrainment and flow dynamics in nature have been limited in the past, which has therefore hindered a holistic understanding of the entrainment process. Furthermore, the influence of mitigation structures such as flexible barriers on the debris flow entrainment has not been studied yet. Flume tests are an effective tool to simulate debris flows interacting with an erodible bed and with flexible barriers, allowing to measure quantitatively the flow dynamics in a controlled laboratory environment. However, the debris flow dynamics and entrainment are influenced by scaling effects (Iverson 2015). To reduce scaling effects, the largest feasible flume facility should be used. Hence, the large-scale 28 m-long flume model built by Ng et al. (2019) was used to study debris flows interacting with an erodible bed and with flexible barriers. In this work, the original flume model was modified to include an erodible bed.

Measuring entrainment is however challenging, as the variations of the bed thickness may be masked by deposition of debris material on top. Several techniques to measure erosion have been studied in this work and implemented in a small-scale flume model to test their effectiveness. Appendix A provides a summary of the instrumentation solutions which have been tested to measure entrainment. Among these solutions, a new technique, called "erosion columns", provided the best results, as it allowed to measure the entrainment depth and differentiate it from deposition. The erosion columns were therefore implemented in the large-scale flume model and will be described more in detail in *Paper II*.

Details of the flume model and instrumentation are reported in *Paper II* and Appendix B. Appendix C provides information on the measured bed parameters before the tests. *Paper II* presents the flume test results and their interpretation.

4.1. Paper II

Vicari, H., Ng, C.W.W., Nordal, S., Thakur, V., De Silva, W.A.R.K., Liu, H., Choi, C.E. 2021. The Effects of Upstream Flexible Barrier on the Debris Flow Entrainment and Impact Dynamics on a Terminal Barrier. Canadian Geotechnical Journal, Just-IN: 1–37. https://doi.org/10.1139/cgj-2021-0119.

Pagination not final (cite DOI) / Pagination provisoire (citer le DOI)

Canadian Science Publishing

ARTICLE

The effects of upstream flexible barrier on the debris flow entrainment and impact dynamics on a terminal barrier

Hervé Vicari, Charles W.W. Ng, Steinar Nordal, Vikas Thakur, W.A. Roanga K. De Silva, Haiming Liu, and Clarence E. Choi

Abstract: The destructive nature of debris flows is mainly caused by flow bulking from entrainment of an erodible channel bed. To arrest these flows, multiple flexible barriers are commonly installed along the predicted flow path. Despite the importance of an erodible bed, its effects are generally ignored when designing barriers. In this study, three unique experiments were carried out in a 28 m long flume to investigate the impact of a debris flow on both single and dual flexible barriers installed in a channel with a 6 m long erodible soil bed. Initial debris volumes of 2.5 and 6 m^3 were modelled. For the test setting adopted, a small upstream flexible barrier before the erodible bed separates the flow into several surges via overflow. The smaller surges reduce bed entrainment by 70% and impact force on the terminal barrier by 94% compared to the case without an upstream flexible barrier. However, debris overflowing the deformed flexible upstream barrier induces a centrifugal force that results in a dynamic pressure coefficient that is up to 2.2 times higher than those recommended in guidelines. This suggests that although compact upstream flexible barriers can be effective for controlling bed entrainment, they should be carefully designed to withstand higher impact forces.

Key words: landslide, debris flow, flexible barrier, entrainment, flume.

Résumé : La nature destructrice des coulées de débris est principalement causée par le gonflement du débit résultant de l'entraînement d'un lit de canal érodable. Pour arrêter ces coulées, de multiples barrières flexibles sont généralement installées tout au long de la trajectoire prévue des coulées. Malgré l'importance d'un lit érodable, ses effets sont généralement ignorés lors de la conception des barrières. Dans cette étude, trois expériences uniques ont été réalisées dans un canal de 28 m de long pour étudier l'impact d'une coulée de débris sur des barrières flexibles simples et doubles installées dans un canal avec un lit de sol érodable de 6 m de long. Des volumes initiaux de débris de 2,5 et 6 m^3 ont été modélisés. Dans le cadre de l'essai adopté, une petite barrière flexible en amont du lit érodable sépare l'écoulement en plusieurs poussées par surverse. Les poussées plus petites réduisent l'entraînement du lit de 70 % et la force d'impact sur la barrière terminale de 94 % par rapport au cas sans barrière flexible en amont. Cependant, les débris qui débordent de la barrière flexible déformée en amont induisent une force centrifuge qui entraîne un coefficient de pression dynamique jusqu'à 2,2 fois supérieur à ceux recommandés dans les lignes directrices. Cela suggère que, bien que les barrières flexibles compactes en amont puissent être efficaces pour contrôler l'entraînement du lit, elles doivent être conçues avec soin pour résister à des forces d'impact plus élevées. [Traduit par la Rédaction]

Mots-clés : glissement de terrain, coulée de débris, barrière flexible, entraînement, canal d'écoulement.

1. Introduction

Debris flows may increase in scale by entraining bed material along the flow path (Hungr et al. 2005; Iverson and Ouyang 2015). Entrainment occurs when a debris flow shears a soil bed (Medina et al. 2008; Iverson 2012; Iverson and Ouyang 2015) and generates excess pore pressures, which reduces the shear resistance of the bed (Hungr et al. 2005; Iverson et al. 2011). Over recent decades, flexible barriers have been increasingly used to mitigate debris flow hazards (Wendeler et al. 2008). One of the design functions of installing multiple flexible barriers in a channel is to reduce bed entrainment. However, there is a dearth of literature on the use of flexible barriers for controlling channel bed entrainment. Instead, the emphasis of the existing work in the literature on impact dynamics is placed on non-erodible beds (Ng et al. 2017; Song et al. 2018). To improve mitigation measures for controlling entrainment, the effects of flow–bed-barrier interaction need to be elucidated.

Some research work has been carried out to reveal the interactions between multiple barriers installed in a channel (Kwan

Received 13 March 2021. Accepted 22 September 2021.

H. Vicari, S. Nordal, and V. Thakur. Norwegian University of Science and Technology (NTNU), Department of Civil and Environmental Engineering, Trondheim, Norway.
C.W.W. Ng,* W.A.R.K. De Silva, and H. Liu. Hong Kong University of Science and Technology (HKUST), Department of Civil and Environmental Engineering, Hong Kong SAR, P.R. China.
C.E. Choi. University of Hong Kong, Department of Civil Engineering, Hong Kong SAR, P.R. China.
Corresponding author: Clarence E. Choi (email: cechoi@hku.hk).
*C.W.W. Ng served as an Editor in Chief at the time of manuscript review and acceptance; peer review and editorial decisions regarding this manuscript were handled by W.A. Take.

Pagination not final (cite DOI) / Pagination provisoire (citer le DOI)

Fig. 1. (*a*) Cross section of 28 m long flume and instrumentation layout (U refers to ultrasonic sensors; E refers to erosion column; cell 1 measures simultaneously normal and shear stress; and cell 2 measures normal stress and pore pressure; L1 and L2 refer to the locations 3.4 and 12.5 m from gate, respectively); (*b*) cross-section of cell 1 (triaxial cell). $\sigma_{f,bot}$, basal normal stress; $\tau_{f,bot}$, basal shear stress.

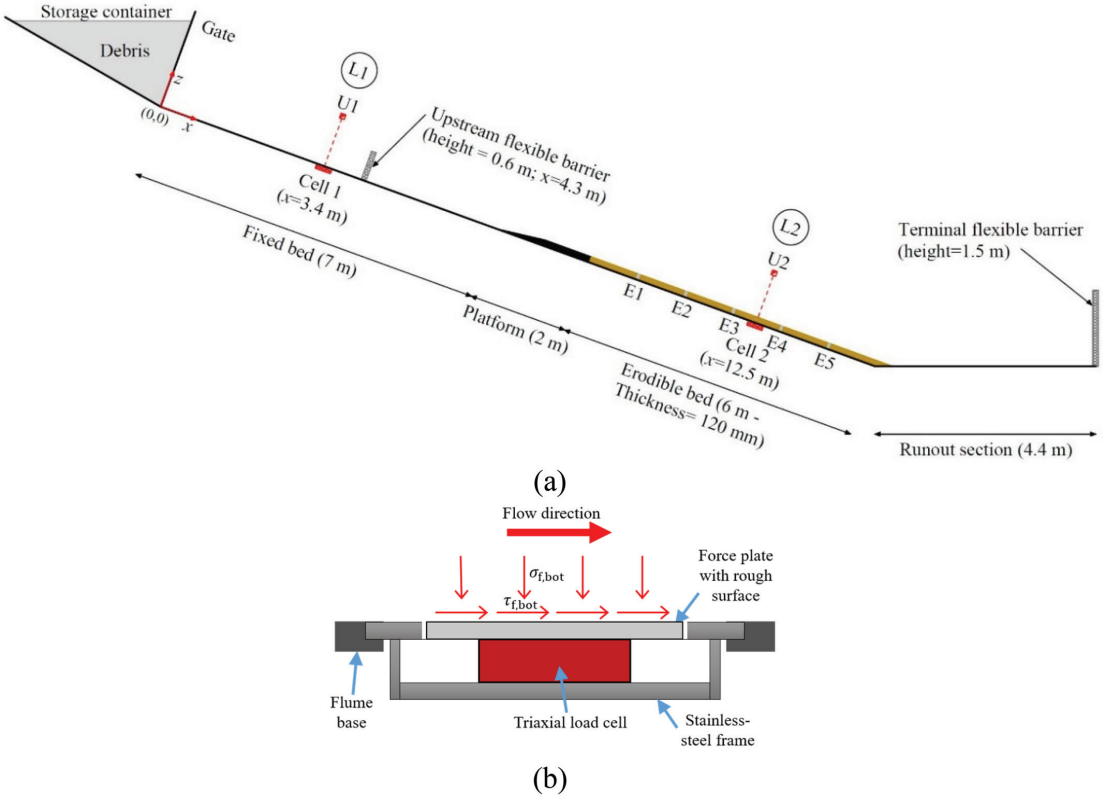

et al. 2015; Ng et al. 2019). Ng et al. (2020) proposed and evaluated an analytical framework for the design of multiple rigid barriers on non-erodible beds. They concluded that multiple barriers enable the progressive reduction in debris flow volume and dissipation of energy during successive sequences of impacts, overflow, and landing. The reduced velocities and volume after interacting with each barrier results in lower impact forces exerted on downstream barriers. However, the aforementioned work focused on the impact dynamics of rigid barriers installed in channels with non-erodible beds. The deformation of a flexible barrier attenuates the impact force and alters overflow dynamics (Ng et al. 2020), which can affect the entrainment process between barriers.

Shen et al. (2019) carried out numerical simulations using a depth-averaged model to investigate the influence of a series of successive rigid check dams on reducing entrainment. Their results showed that a series of dams can minimise flow bulking by creating a cascading effect. However, check dams are fundamentally different compared to flexible barriers. Rigid check dams are designed to impound static material behind them and the filled dams are not cleaned. Instead, a series of filled check dams serves to stabilise the terrain to minimise further erosion. In contrast, flexible barriers are designed to take both dynamic and static impact loading, and they need to be cleaned after each event. Also, flexible barriers deform during impact and are expected to reduce in height after impact, thereby altering overflow dynamics. With the emergence of flexible barriers for debris flow mitigation, the fundamental mechanisms of interaction between a debris flow and flexible barriers on erodible beds is an important topic that requires further investigation.

The main scientific challenges that have limited progression towards a rational basis for leveraging flexible barriers to control channel bed entrainment include: (*i*) the poor temporal predictability of natural debris flows, which has hindered our understanding of the fundamental flow–bed–barrier mechanisms of interactions; and (*ii*) the nonlinear dynamic scaling of debris flows caused by the interplay between the solid and fluid phases (Iverson 2015). The nonlinear scaling necessitates the largest testing facilities feasible. In this study, a series of unique flume tests were carried out in a 28 m long flume to model up to 6 m^3 of initial debris material impacting single and dual flexible barriers installed in a channel with an erodible bed.

2. Flume experiments

2.1. Model setup

As aforementioned, the largest test facilities feasible are required to address the scaling issues pertaining to the timescale for pore pressure diffusion (Iverson 2015). The scale of the flume experiments in this study is among the largest of its kind in the world. Figure 1*a* shows a cross section of the 28 m long flume (Ng et al. 2019) that was used to carry out experiments in this study. The

Published by Canadian Science Publishing

Fig. 2. (*a*) Upstream flexible barrier (looking downstream in channel); (*b*) terminal flexible barrier (looking upstream in channel); (*c*) top view of deflected flexible barrier cable and calculation of impact force (F) from measurements of cable force (T), horizontal force (T_H), and deflection angle of cable (ψ).

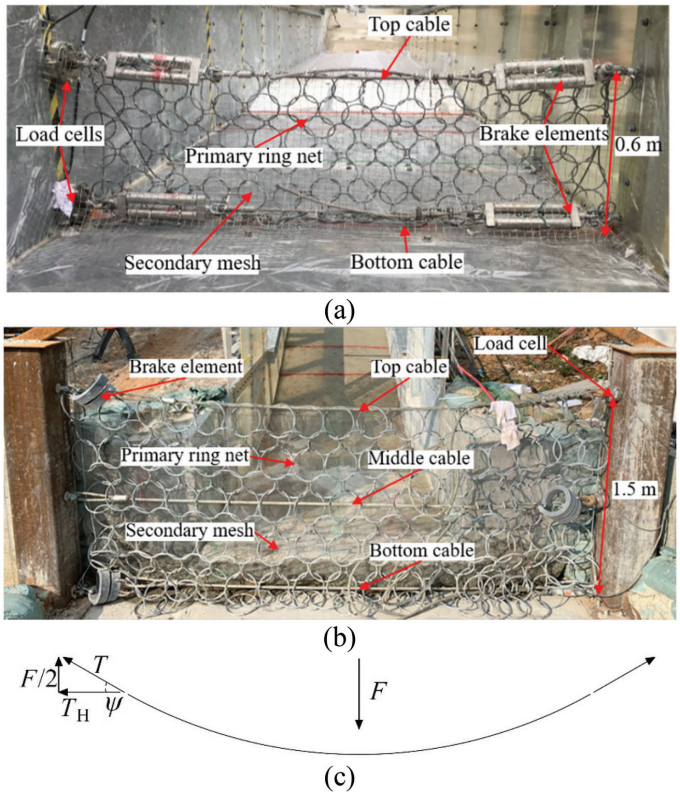

channel has a rectangular cross section with a width of 2 m and depth of 1 m. The side walls are transparent on one side of the channel to enable the flow and impact kinematics to be observed. A storage container, that is 5 m in length, is inclined at 30° at the upper end of the channel. The container can store up to 10 m^3 of debris material. A double gate system is used to retain the debris material inside the storage container. The gate is secured and released by a mechanical arm that is controlled by an electric motor. The main channel is 15 m long and is inclined at 20°. An erodible bed with a thickness of 120 mm was prepared along the last 6 m of the inclined section. The erodible bed is prepared on top of a 5 mm thick metallic mesh to increase the channel bed roughness to hold the erodible bed in place. A rigid platform with an inclined length of 2 m was used to allow the debris flow to smoothly transition from the fixed bed to the erodible one. The transition consists of two parts. The first part forms an angle of 7° with respect to the inclined channel for an inclined distance of 1 m. The second part is 120 mm in thickness and runs parallel to the inclined channel. At the end of the inclined section is a horizontal 4.4 m runout section.

Figure 2*a* shows the upstream flexible barrier, which is installed orthogonally to the channel bed just 4.3 m downstream from the gate. The barrier is 0.6 m in height and 2 m in width. The primary ring of the barrier net consists of 100 mm diameter rings made using four windings of high yield strength steel wires that are 2 mm in diameter. The primary ring net is suspended by the top and bottom cables. The ring net is laterally anchored to the side of the flume using two smaller cables. The top and bottom load bearing steel cables with 12 mm diameter are equipped with brake elements to replicate the load–displacement behaviour of prototype barriers (Ng et al. 2017). The brake elements simplify the loading response of a prototype barrier using a bilinear curve (Ng et al. 2020). In addition to the primary ring net, a secondary mesh with 25 mm square openings made of stainless-steel wire with a diameter of 1 mm are connected to the main cables to retain the debris material.

The terminal flexible barrier is installed at the end of the runout section (Fig. 2*b*). The terminal barrier is 1.5 m in height and 4 m in width. The barrier is supported by three load bearing steel cables with 16 mm diameter, which are connected to a steel frame. Braking devices are installed on each cable. The primary ring net consists of 200 mm diameter rings made using four windings of steel wires that are 2 mm in diameter. The secondary mesh has 25 mm square openings made of steel wires that are 1 mm in diameter.

2.2. Instrumentation

A laser sensor, U1, and an ultrasonic sensor, U2, (model: Keyence IL600/IL1000 and Banner TUB30X) were mounted above the centreline of the flume bed to measure the flow depth at inclined distances of 3.4 and 12.5 m from the gate, respectively

Published by Canadian Science Publishing

Pagination not final (cite DOI) / Pagination provisoire (citer le DOI)

Fig. 3. Side schematic showing working principle of an erosion column: (*a*) initial placement of erosion column; (*b*) erosion column installed inside erodible bed with bolt still in place; (*c*) erosion column inside erodible bed with bolt removed; (*d*) side schematic of erosion column after each test, with erodible bed material and nuts entrained and debris material deposited on top.

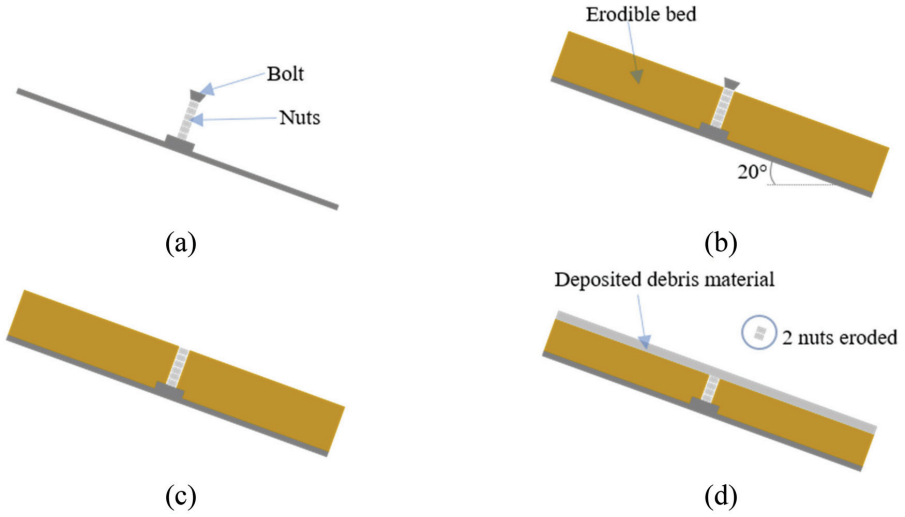

(Fig. 1*a*). The resolution of the sensors is ±1 mm. An unmanned aerial vehicle with an on-board video camera (model: UAV DJI Phantom 3) was used to capture aerial videography of each test. By knowing the distance between reference lines marked on the flume bed and the time between frames, the frontal velocity could be calculated. High-speed cameras (model: Mikotron EoSens 4CXP) were also used to capture the kinematics of the debris flow, at 300 fps and with a resolution of 2336 × 1712 pixels, over the erodible bed and the impact dynamics on the flexible barriers. Basal instrumentation cells were installed along the flume bed to measure the normal and shear stresses, and changes in pore pressures at the base of the flow. Details of the instrumentation cells are discussed in Ng et al. (2019). Figure 1*b* shows the cross section of the instrumentation cell 1 located directly underneath depth sensor U1. Cell 1 is instrumented to simultaneously measure the normal and shear stresses at the base of the flow using a triaxial load cell (model: sensor ME K3D160). The triaxial load cell is rigidly connected to a force plate roughened by epoxy and sand. Cell 2 is located underneath depth sensor U2, which is instrumented to measure the normal stress and pore pressures at the base of the erodible bed. Henceforth in the text, the location of 3.4 and 12.5 m from the gate is represented by L1 and L2, respectively. L1 is located prior to the upstream flexible barrier and L2 is located in the erodible bed section (Fig. 1*a*).

The cables of the flexible barriers were equipped with tension load cells to measure the cable forces. For both top and bottom cables of the upstream flexible barrier, a through-hole load cell is used (model: Omega LSHD-50k). The load cell is fixed to the wall of the flume and measures the horizontal component of the cable force (T_H). For the terminal flexible barrier, the top and middle cables are also connected to a through-hole load cell (model: TML TCLK-50 kNA), which is fixed to the frame of the terminal flexible barrier to measure the horizontal component of the cable force (T_H). As for the bottom cable of the terminal barrier, an in-line load cell is used (model: TML TCLP-100kNB). The in-line load cell deflects in the cable direction and therefore measures the cable force (T). Figure 2*c* shows the top view of a deflected cable of a flexible barrier. The impact force (F) is orthogonal to the barrier. The measurements of the cable loads (T and T_H) and deflection angles (ψ) can be used to deduce the impact force (F) (Ng et al. 2017).

For the top and bottom cables of the upstream barrier and for the top and middle cables of the terminal barrier that use through-hole load cells to measure T_H, the impact force F can be calculated as follows:

$$F = 2T_H \tan\psi \quad (1)$$

while, for the bottom cable of the terminal barrier that uses in-line load cells that measure T, the impact force F can be calculated as follows:

$$F = 2T \sin\psi \quad (2)$$

A data logger (model: NI cDAQ-9137) with a sampling rate of 2 kHz was used to record the measurements of cell 1, cell 2, U1, U2, and of the cable forces.

2.3. Entrainment depth measurement

A unique method of erosion columns (Fig. 3), similar to that proposed by Berger et al. (2011), was used to differentiate deposition from entrainment. This allowed the entrainment depth to be measured. The columns were installed in the erodible bed prior to its construction. A total of five rows of erosion columns were installed at increments of 1 m along the centreline of the channel. Each erosion column consists of 21 nuts. A single nut is 5 mm in height and has an inner diameter of 6 mm. To align the erosion column each nut is threaded through a bolt with a diameter of 4 mm. Thus, the accuracy of this approach is equivalent to the thickness of a nut (±5 mm). The bolt is initially fixed to a plate attached to the base of the channel (Fig. 3*a*). The soil bed is then prepared around the erosion columns (Fig. 3*b*). Afterwards, the bolts are removed, and the nuts are free to be entrained with the erodible bed (Fig. 3*c*). After each test, the difference between the initial number and the remaining number of nuts are counted to determine the entrainment depth (Fig. 3*d*). The deposition depth is also measured at the end of each test. The deposition depths are

Published by Canadian Science Publishing

Table 1. Test program.

Test ID	Released flow volume (m^3)	Barrier configuration
V2.5-B1	2.5	Single flexible barrier (terminal)
V6-B1	6	Single flexible barrier (terminal)
V6-B2	6	Dual flexible barriers (upstream + terminal)

distinguished as the height of deposited material above the level of the remaining nuts.

2.4. Test program

Three experiments were carried out in the 28 m long flume. In each test an erodible bed was prepared at the same location along the inclined section. The first two tests were conducted using initial volumes of 2.5 and 6 m^3. In both of these tests, only a terminal flexible barrier was installed at the end of the runout zone. In the third experiment, an initial volume of 6 m^3 was used and an upstream flexible barrier was installed before the erodible bed at an inclined distance of 4.3 m from the gate (Fig. 1*a*). This position of the upstream flexible barrier should be installed to avoid overflow from directly landing on the erodible bed. Otherwise, scour may occur and undermine the stability and serviceability of the flexible barrier foundation. In the field, the channel bed may be protected from scour using geotextiles (e.g., Feiger and Wendeler 2019). A terminal barrier was also installed at the end of the runout zone for this third test. Table 1 gives a summary of the test program.

2.5. Modelling procedure

The debris flow material consists of a sand–gravel–clay mixture (Ng et al. 2019). The mixture comprises 36% gravel (2–20 mm), 61% sand (0.075–2 mm), and 3% fines (<0.075 mm) by mass. A solid concentration (C_s) of 70% was selected for the tests. The initial density of the debris mixture was 2155 kg/m^3. For the erodible bed, a sand–gravel–clay mixture was also used. However, the composition differed slightly from the debris material. The bed material consists of sand (0.075–2 mm, 63%), fine gravel (2–5 mm, 33%), and fines (<0.075 mm, 4%). The initial water content and void ratio of the erodible bed play an important role in the entrainment dynamics (Iverson et al. 2011). Excess pore pressures in the bed material can develop only if the water content is high enough to create continuous water networks to transmit pore pressures (Iverson et al. 2011). The target gravimetric water content was selected to be 15% because it avoided pre-mature bed failure, which would occur for high degree of saturation.

Before each experiment, the bed material was mixed to achieve a gravimetric water content of 15%. The mixture was then placed on the 6 m long erodible bed section. After bed preparation, soil samples were obtained from the bed to measure the gravimetric water content, which was approximately 15%, and electrical capacitance sensors (model: Decagon EC-5) were used to measure the volumetric water content, which was about 25%. From these water content measurements, the void ratio was calculated to be about 0.6. Afterwards, the gate was secured, and the storage tank was prepared with the debris mixture. The gates were then released to initiate dam-break.

3. Interpretation of test results

3.1. Observed flow and impact kinematics

Figure 4 shows the typical kinematics for an upstream flexible barrier for test V6-B2 where an upstream barrier is installed before the erodible bed and a terminal barrier is installed at the end of the runout zone. The interaction between the flow and the upstream flexible barrier is viewed through the transparent sidewall. The flume inclination of 20° is indicated in Fig. 4*a* as a reference. The time when the flow front impacts the upstream barrier is taken as $t = 0$ s (Fig. 4*a*). At $t = 0.12$ s (Fig. 4*b*), the top and bottom cables are deformed while the subsequent flow material is accumulated. The retained material, called a dead zone herein, forms a curved ramp for incoming flow to override. The curvature of the ramp is likely due to the deformation of the barrier. In contrast, a similar curvature is not reported for the dead zone forming behind a rigid barrier (Ng et al. 2019). The flow on top of the dead zone runs-up and resembles ($t = 0.35$ s) the vertical jet mechanism reported by Choi et al. (2015) for viscous flows or fast flows (Faug 2021). In contrast, a pileup mechanism is typically observed for slow moving flows (Wendeler et al. 2019). The jet eventually reaches its maximum height (Fig. 4*c*) and overflows the barrier at $t = 0.95$ s (Fig. 4*d*). This overflowing material forms the first surge that reaches the erodible bed after the upstream barrier. At the same time incoming flow is observed to follow a curvilinear trajectory as it overrides the dead zone. As the supply of debris material from the storage container diminishes, the launch angle of the overflow from the barrier crest changes from an upward angle to a downward angle towards the channel bed (Fig. 4*e*), which forms the second surge that flows downstream. Finally, the debris material comes to rest behind the upstream barrier at $t = 4.30$ s to form a final horizontal deposit (Fig. 4*f*).

The overflow was observed to form two distinct surges separated by about 1 s in duration. The first surge lands at an inclined distance of 4 m downstream from the upstream barrier. The second surge lands directly on top of the debris material on the flume bed from the first surge and is observed to decelerate. Figure 5 shows the impact kinematics on the terminal barrier for a volume of 6 m^3 impacting a single terminal barrier (test V6-B1) compared to a dual barrier system (test V6-B2). The volume and impact velocity of the flow that the terminal barrier in test V6-B1 arrests are larger and higher, respectively, than that for the terminal barrier in test V6-B2. Therefore, a distinct run-up mechanism is observed on the terminal barrier for test V6-B1 compared to a pileup mechanism for the terminal barrier in test V6-B2. Details on the measured impact forces are discussed later.

3.2. Flow depth and frontal velocity

Figure 6 shows the evolution of the measured flow depths at inclined distances of 3.4 m (L1) and 12.5 m (L2) from the gate measured using U1 and U2, respectively. The flow depth measurements for test V2.5-B1, test V6-B1, and test V6-B2 are compared. The $t = 0$ s in the abscissa shows the time that the flow front reaches the respective locations at L1 and L2. At L1 (Fig. 6*a*), the effects of scale on the flow depths are evident. More specifically, the maximum measured flow depth for the test with a smaller initial volume of 2.5 m^3 (test V2.5-B1) is about two times less than that for the larger volume of 6 m^3 (tests V6-B1 and V6-B2). Larger flow depths generate higher normal bed stress and have larger timescales for pore pressure diffusion (Iverson 2015). Furthermore, the flow depth profiles for tests V6-B1 and V6-B2 are initially similar in magnitude until impact occurs on the upstream barrier in test V6-B2. In test V6-B2, the presence of an upstream flexible barrier causes the flow depth to increase after $t = 2$ s as debris is arrested and accumulates behind the upstream barrier. At L2 (Fig. 6*b*), the measured flow depths for all three tests have noticeably decreased compared to those measured at L1 as the debris mass spreads along the channel (Ng et al. 2013). Moreover, a noticeable difference between the flow depth profiles due to scale is observed between the test conducted using the smaller initial volume of 2.5 m^3 (test V2.5-B1) and the larger initial volume of 6 m^3 (tests V6-B1 and V6-B2). The flow depth measurements for $t > 3$ s indicate the final change in the bed height, which decreased due to entrainment, but increased due to deposition of debris material.

Figure 7 shows a comparison of the measured frontal flow velocities ($\bar{v}_f$) along the channel for the three tests. The frontal flow velocities are measured using the video recordings from the top view of the flume during the flow propagation. For reference, theoretical velocity profiles calculated for a rigid block is shown. Based on the conservation of energy, the velocity of a rigid block can be calculated as:

Pagination not final (cite DOI) / Pagination provisoire (citer le DOI)

Fig. 4. Impact kinematics for upstream flexible barrier (test V6-B2): (*a*) t = 0 s; (*b*) t = 0.12 s; (*c*) t = 0.35 s; (*d*) t = 0.95 s; (*e*) t = 1.50 s; (*f*) t = 4.30 s.

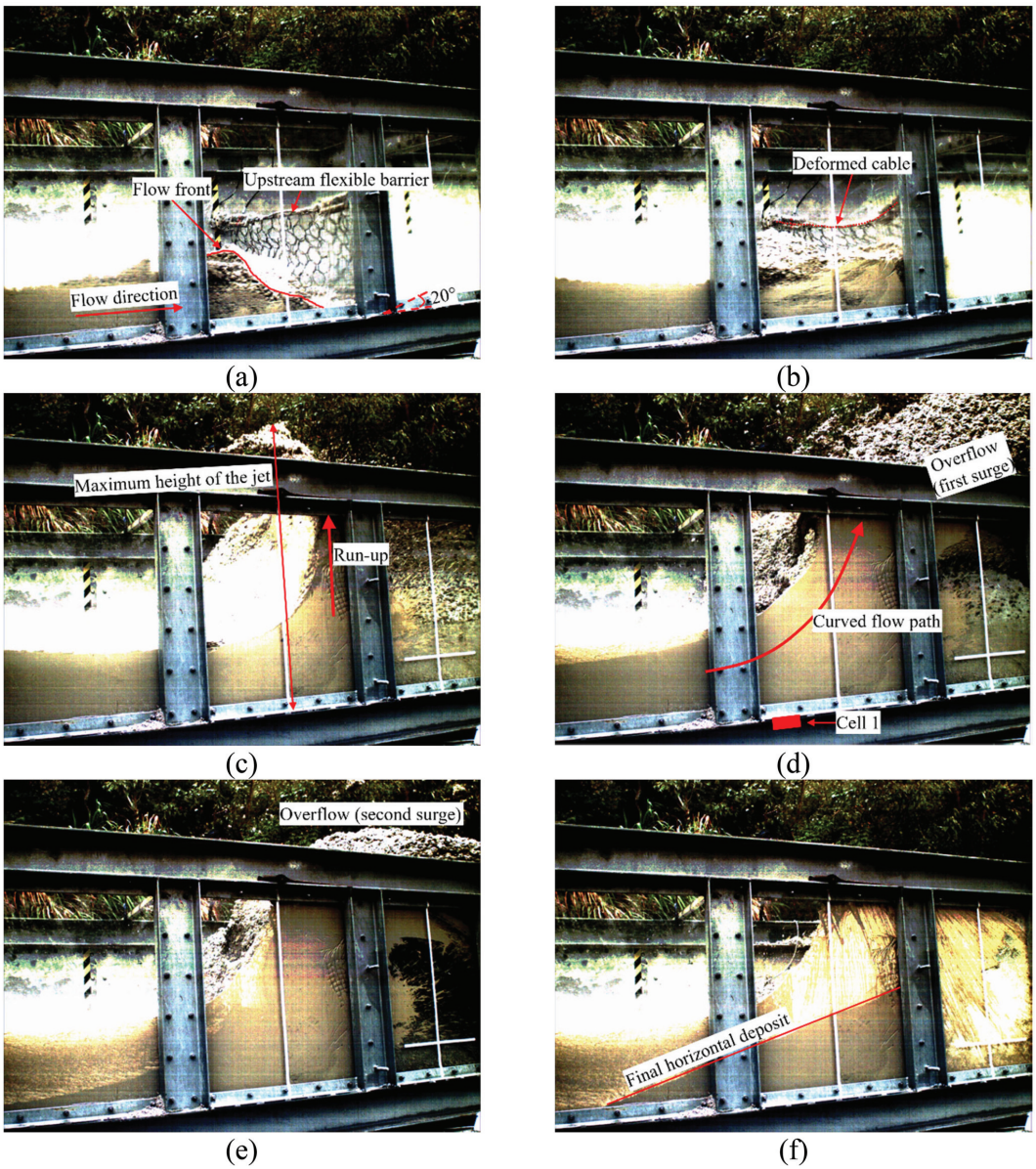

$$v_b(x) = \sqrt{2g\left[x\sin(\theta) + h_0 - x\cos(\theta)\overline{\mu}_{f,bot}\right]} \quad (3)$$

where g is the acceleration due to gravity, x is the distance along the flume from the gate, θ is the slope angle, h_0 (= 1.13 m) is the initial height of the center of mass of the flow, and $\overline{\mu}_{f,bot}$ is the apparent friction coefficient at the base of the block. A frictionless block corresponds to $\overline{\mu}_{f,bot}$ = 0, which as expected, overestimates the flow velocities. The measured debris flow front in each test accelerates over the fixed bed section and decelerates over the erodible bed because of a higher basal friction. Generally, the velocity increase is governed by the conversion of potential energy into kinetic energy (Sassa 1988). Thus, the frontal velocities in tests V6-B1 and V6-B2 are higher than in test V2.5-B1, because of the larger initial volume, which results in a higher potential

Published by Canadian Science Publishing

Pagination not final (cite DOI) / Pagination provisoire (citer le DOI)

Fig. 5. Observed impact mechanism from front of terminal barrier: (*a*) run-up impact mechanism for test V6-B1; and (*b*) pileup impact mechanism for test V6-B2.

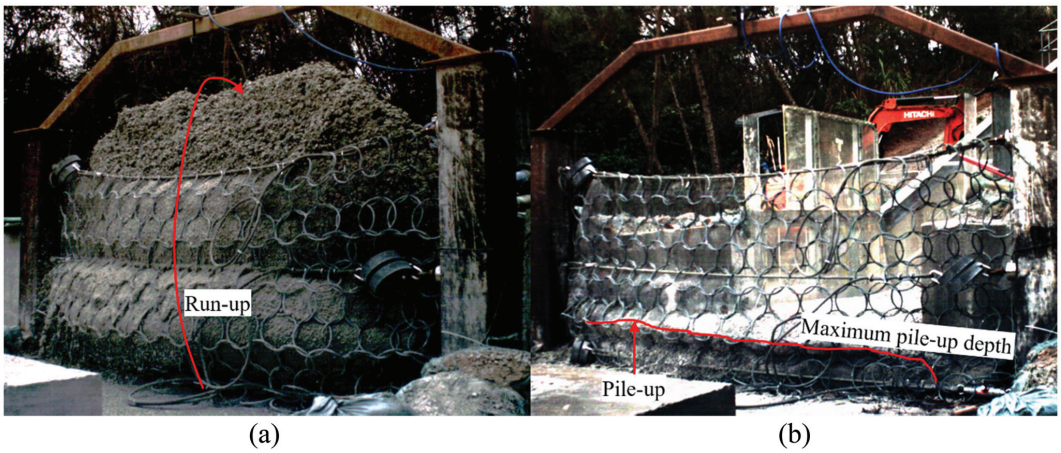

Fig. 6. Flow depth measurements: (*a*) 3.4 m downstream from gate (L1); (*b*) 12.5 m downstream from gate (L2).

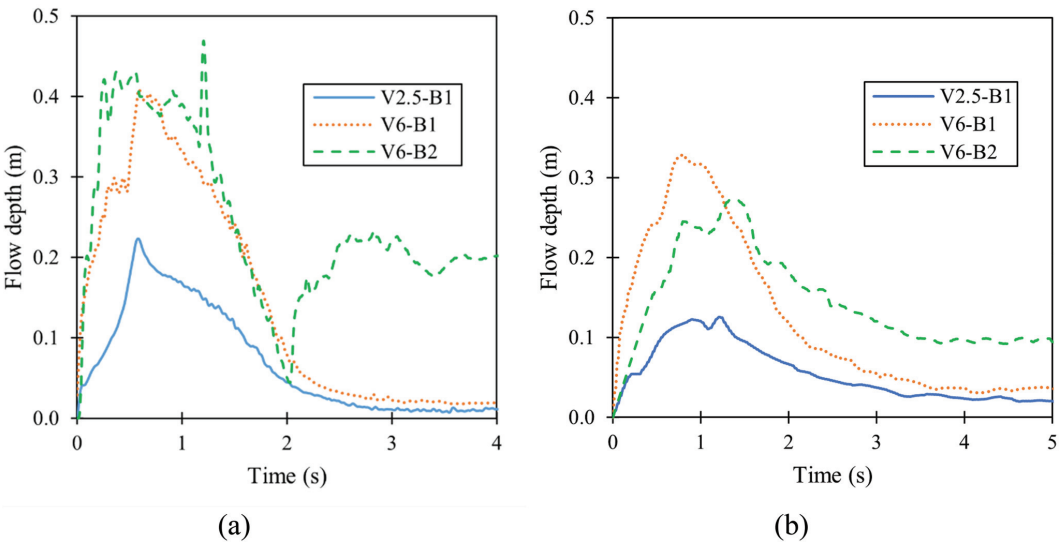

energy when the debris mass is released. In reality, friction is dissipating energy at the base of the flow to decelerate the flow. Thus, a frictional block that considers energy dissipation (third term on the right hand side of eq. 3) would provide a more realistic comparison with the measured flow velocities. If an apparent basal friction coefficient of $\overline{\mu}_{f,bot} = 0.16$ is assumed, then the calculated and measured velocites for test V6-B1 over the fixed bed section show reasonable agreement. An explanation for the choice of this value of $\overline{\mu}_{f,bot}$ will be discussed later when examining the role of basal stresses on the entrainment dynamics.

3.3. Measured entrainment

Figure 8 shows the measured entrainment depths using the erosion columns placed at the centreline of the channel for the three tests. The entrainment magnitudes range from 5 to 105 mm (maximum depth that can be measured using erosion columns). For each experiment, the maximum entrained depth is observed near the start of the bed and the entrained depth generally decreases along the flow direction of the erodible bed. A similar entrainment pattern was observed in experimental results reported by Haas and van Woerkom (2016), who adopted a similar test configuration to study entrainment. One possible explanation for the maximum entrainment occurring near the start of the erodible bed is because the thickness of the erodible bed decreases during entrainment, while the height of the rigid platform remains unchanged, which causes the flow to dig into the erodible bed.

The entrained depths over the bed length in test V6-B2 are lower than the entrained depths of test V2.5-B1 and test V6-B1. The total

Published by Canadian Science Publishing

Pagination not final (cite DOI) / Pagination provisoire (citer le DOI)

Fig. 7. Comparison of frontal flow velocity (velocities for test V6-B2 not shown in middle because of presence of upstream barrier). The erodible bed section (from 9 to 15 m) is indicated.

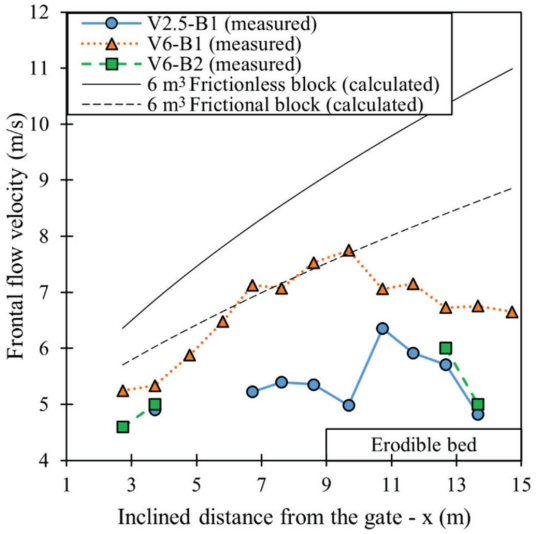

entrainment volume can be calculated by integrating the measured entrainment depths along the length of the erodible bed. As expected, the debris flow with an initial volume of 6 m^3 entrained a much higher volume (test V6-B1, measured entrained volume 0.9 m^3) compared to the test with an initial volume of 2.5 m^3 (test V2.5-B1, 0.5 m^3). In test V6-B2, the upstream flexible barrier retained a part of the initial volume (approximately 1.2 m^3) and the measured entrainment volume decreased to 0.3 m^3. By partially arresting the debris flow volume, flow bulking is reduced. Furthermore, deposition on the erodible bed is also observed for each test. The maximum deposition heights of 50, 90, and 130 mm were measured for test V2.5-B1, test V6-B1, and test V6-B2, respectively. The higher deposition measured on the erodible bed in test V6-B2 indicates that the influence of the upstream flexible barrier has altered the flow and impact dynamics.

3.4. Flow basal stresses

Figures 9*a* and 9*b* show the time-histories of the basal normal stress ($\sigma_{f,bot}$) and shear stress ($\tau_{f,bot}$) measured by cell 1 for tests V6-B1 and V6-B2, respectively. For test V2.5-B1, the instrumentation in cell 1 malfunctioned. Therefore, no basal stress measurements are shown for this test. The flow depths measured by U1, which is mounted directly above cell 1 are also shown for reference. In test V6-B1, the measured peak normal stress is 9.5 kPa, which occurs at about the same time as the peak flow depth, which is 0.4 m. The normal stress ($\sigma_{f,bot}$) can be compared to estimated theoretical value by assuming static equilibrium perpendicular to the channel bed and neglecting bed-normal accelerations (McArdell et al. 2007; Iverson et al. 2010):

$$(4) \qquad \sigma_{f,bot(calc)} = \rho g h_f \cos\theta$$

where ρ is bulk density and h_f is the flow depth. The bulk density of the flow can be taken as $\rho = \rho_s C_s + \rho_w(1 - C_s) = 2155$ kg/m^3 where density of the solid grain (ρ_s) is 2650 kg/m^3, density of water (ρ_w) is 1000 kg/m^3, and solid concentration (C_s) is 0.7. Based on eq. 4, the calculated normal stress is $\sigma_{f,bot(calc)} \cong 20 h_f$ kPa. It is worthwhile to note that in test V6-B1 the normal stress generally follows the same trend as the flow depth. Any differences in trend are likely due to not considering flow acceleration in the bed-normal direction, which may induce normal stresses that are higher than those under static conditions. Similarly, Iverson et al. (2010) reported higher measured normal stress on a smooth bed compared to calculated ones using eq. 4.

More interestingly, the maximum flow depths for tests V6-B1 and V6-B2 did not differ significantly. However, it is observed that in test V6-B2 (Fig. 9*b*) the measured normal stress reaches a peak value of 18.9 kPa, which is almost two times that measured in test V6-B1. The higher normal stress measured in test V6-B2 was caused by the presence of the upstream flexible barrier. After the flow impacts the upstream barrier, debris deposits accumulate on cell 1 (Fig. 4*d*). The deposits form a curved ramp due to the deformation of the barrier to enable subsequent debris material to overflow the upstream barrier following a curvilinear trajectory. The flow on top of the ramp-like deposit is curvilinear, of which the centrifugal component transmitted to the channel bed and the barrier. This component can be calculated as proposed by Hungr (1995) as follows:

$$(5) \qquad \sigma_c = \frac{\rho h_L \bar{v}_L^2}{R}$$

where h_L is the depth of the flow layer over the retained material (~0.2 m), $\bar{v}_L$ is the flow velocity of the layer travelling towards the flexible barrier (~5 m/s), and R is the radius of curvature (~0.9 m), which is approximated from the high-speed camera images (Fig. 4). The centrifugal stress from eq. 5 is estimated as 12 kPa. This centrifugal component can be added to the calculated static basal stress $\sigma_{f,bot(calc)} \cong 8$ kPa from eq. 4 to obtain a similar value as the maximum measured normal stress in test V6-B2.

In test V6-B1, the peak shear stress occurs at $t = 0.11$ s, which is earlier than the peak normal stress at $t = 0.59$ s. A similar result is also observed in test V6-B2. The delay between the measured shear and normal stresses can be explained by an unsaturated flow front characterised by low pore pressures. Similar observations were reported by Iverson et al. (2010).

McArdell et al. (2007) and Berger et al. (2011) measured the flow basal shear, normal stress and pore pressure of natural debris flows in the field (Illgraben channel, Switzerland) and McArdell et al. (2007) showed the shear stress at the base of the flow using a Mohr–Coulomb relationship. Iverson et al. (2010) also measured the basal normal stress and pore pressures and modelled the flow basal shear stress, assuming a frictional flow and also adopted a Mohr–Coulomb relationship. Estimates of the Savage and Friction numbers (Iverson 1997) for the flows modelled in this study (refer to online Supplementary material, Table S1[1]) suggest that collisional and viscous stresses are less important than the frictional stresses. The Savage number varies between 6×10^{-5} and 4×10^{-3}, which suggests frictional stresses to be dominant over collisional ones, as defined by the threshold of 0.1 reported by Savage and Hutter (1989). Furthermore, it is found that the Friction number of the flows in this study varies between 8×10^4 and 1×10^6, which is higher than the threshold for friction stresses to be dominant over viscous ones (1400 as defined by Iverson and LaHusen 1993). Assuming frictional behaviour is an appropriate idealisation, the basal shear stress can be expressed as follows:

$$(6) \qquad \tau_{f,bot} = \sigma'_{f,bot}\mu' = (\sigma_{f,bot} - p_{f,bot})\mu' = \sigma_{f,bot}(1 - \lambda_{f,bot})\mu'$$

where $\sigma'_{f,bot}$ is the basal effective stress normal to the bed, μ' is the effective friction coefficient of the debris material, $p_{f,bot}$ is the flow basal pore pressure. $\lambda_{f,bot}$ is the flow basal pore pressure

[1]Supplementary data are available with the article at https://doi.org/10.1139/cgj-2021-0119.

Published by Canadian Science Publishing

Pagination not final (cite DOI) / Pagination provisoire (citer le DOI)

Fig. 8. Measured entrainment depths along centreline of erodible bed.

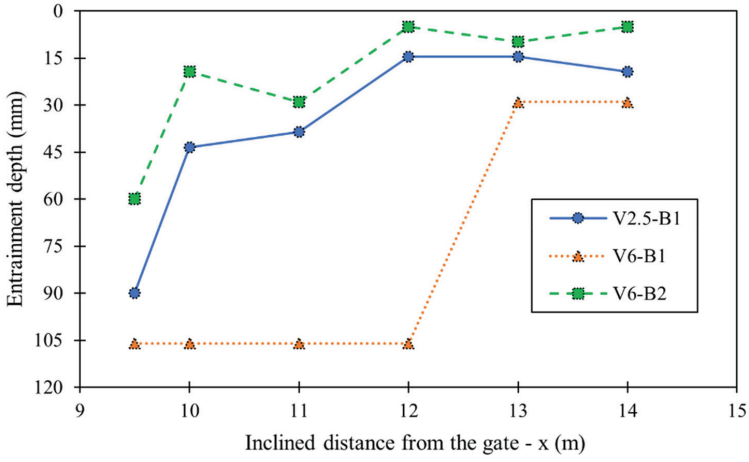

Fig. 9. Basal stress and flow depth measurements 3.4 m downstream from gate (L1): (*a*) test V6-B1; and (*b*) test V6-B2.

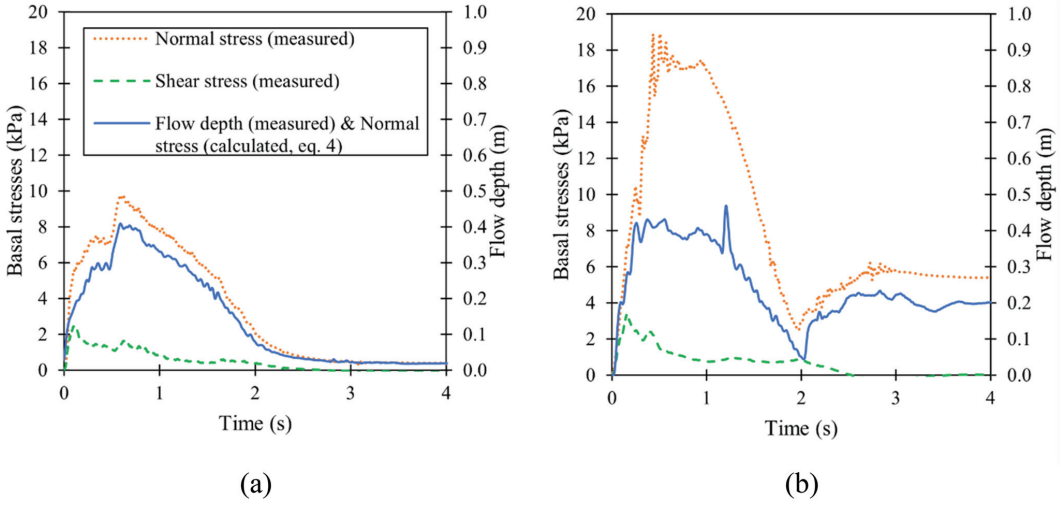

ratio, which indicates the degree of flow liquefaction: a value of 0 characterises a dry flow, while a value of 1 characterises a liquefied flow. The flow basal pore pressure ratio has a significant influence on the debris flow mobility (Iverson et al. 2010) and bed entrainment (Iverson 2012). The basal pore pressure ratio can be calculated using eq. 6, and measurements of the normal and shear stresses and the effective friction coefficient of the soil, which was measured as $\mu' = 0.89$ using direct shear test in the laboratory.

Figure 10 shows the calculated flow basal pore pressure ratio for tests V6-B1 and V6-B2 at L1. The flow basal pore pressure ratio gradually increases from 0.2 to about 0.9. McArdell et al. (2007) reported a flow basal pore pressure ratio of 0.8. Moreover, Iverson et al. (2010) reported a flow basal pore pressure ratio of 0.6 for sand–gravel flow mixtures and 1.0 for sand–gravel–mud mixtures. For both flow mixtures, the flow front was reported to be unsaturated with low excess pore pressures. The influence of the flow basal pore pressure ratio on flow mobility can be observed by considering the frictional block model discussed in Fig. 7. The average value of the basal pore pressure ratio, $\overline{\lambda}_{f,bot}$, is 0.82. Consequently, an average value of the apparent friction coefficient at the base of the flow can be defined as $\overline{\mu}_{f,bot} = (1 - \overline{\lambda}_{f,bot})\mu' = 0.16$. This value was used previously to describe the behaviour of the frictional block model using eq. 3. The high measured flow velocities (Fig. 7) likely resulted from a high degree of flow fluidisation, which significantly decreased the basal apparent friction. This analysis shows that perhaps an idealised frictional rheology may provide a first order approximation of debris flow mobility on non-erodible

Published by Canadian Science Publishing

Pagination not final (cite DOI) / Pagination provisoire (citer le DOI)

Fig. 10. Calculated flow basal pore pressure ratio for test V6-B1 and test V6-B2, 3.4 m downstream from gate (L1).

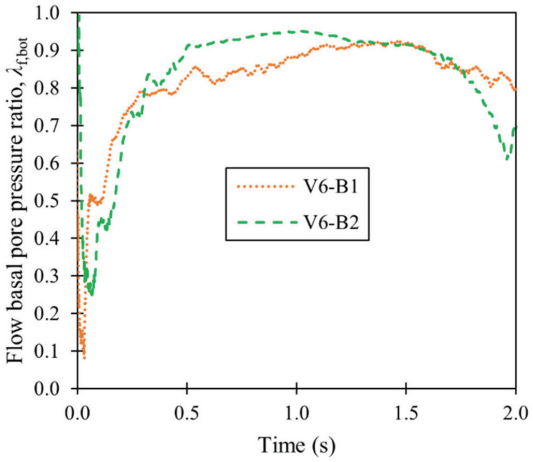

Fig. 11. Comparison of back-calculated entrainment rate 12.5 m downstream from gate (L2).

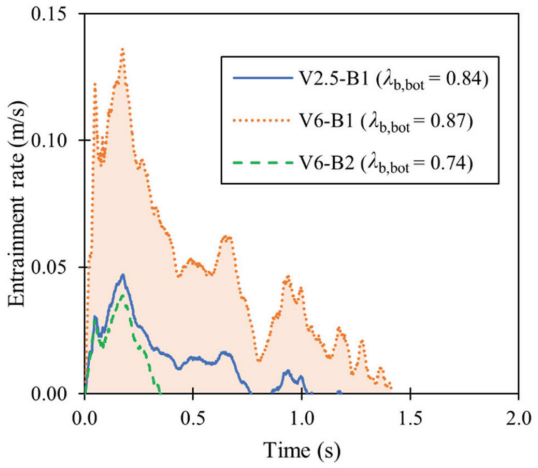

beds, but it may present difficulties in capturing flow mobility on erodible beds.

3.5. Entrainment rate

Figure 11 shows a comparison of the back-calculated entrainment rates at 12.5 m downstream from the gate (L2) for each test. The entrainment rate is the volume transfer per unit area at the flow–bed interface. The back-calculation method is described in this section. The total entrainment depth, z_b, can be calculated by integrating the entrainment rate with time:

$$(7) \qquad |z_b|_{(calc)} = \int_0^{t_{DF}} E\,dt$$

where t_{DF} is the debris flow duration and E is the entrainment rate. The entrainment rate can be expressed as follows (Iverson 2012, refer to online Supplementary material, Fig. S1[1]):

$$(8) \qquad E(t) = 2gh_f(t)\cos\theta\,\mu' \frac{\lambda_{b,top}(t) - \lambda_{f,bot}(t)}{\overline{v}_f}$$

where $\lambda_{b,top}$ (= $p_{b,top}/\sigma_{f,bot}$) is the pore pressure ratio at the top of the erodible bed, assuming $\sigma_{f,bot} = \sigma_{b,top}$. Equation 8 is used to calculate the entrainment depth in eq. 7 using measurements obtained at 12.5 m downstream from the gate (L2), notably the flow depth, the frontal flow velocity, and the flow basal pore pressure ratio. It is worthwhile to note that the flow basal pore pressure changes as the flow travels from L1 to L2. However, for simplicity, the value of $\lambda_{f,bot}$ is taken at L1 and is assumed to also be applicable at L2. To account for the different flow duration at L2 ($t_{L2} \cong 3$ s) compared to the flow duration at L1 ($t_{L1} \cong 2$ s), the time axis of $\lambda_{f,bot}$ (Fig. 10) is stretched, by a factor of 1.5, so that the maximum time becomes 3 s instead of 2 s. By doing so, the measurement of $\lambda_{f,bot}$ can be used in eq. 8 for the calculation at L2.

Obtaining $\lambda_{b,top}(t)$ would require multiple pore pressure and normal stress sensors placed at different depths in the erodible bed (e.g., McCoy et al. 2012). Given the difficulty of predicting or measuring the evolution of the bed pore pressure, Medina et al. (2008) and Shen et al. (2020) adopt a constant value of $\lambda_{b,top}$, which is back-calculated — through a trial-and-error approach — to make the computed entrainment converge to the observed entrainment measurements. Similarly, this approach was adopted by considering a constant value in time of $\lambda_{b,top}$. The magnitude of $\lambda_{b,top}$ for the three tests is unknown a priori, but is back-calculated using eq. 8 to match the calculated entrainment depth (eq. 7) with the measured entrainment depth at L2. Figure 11 shows the entrainment rates calculated by using eq. 8 with $\lambda_{b,top}$ = 0.84 for test V2.5-B1, $\lambda_{b,top}$ = 0.87 for test V6-B1, and $\lambda_{b,top}$ = 0.74 for test V6-B2 at 12.5 m downstream from the gate (L2). Indeed, assuming these particular values of the bed pore pressure ratio allows to match the theoretical entrainment depths (eq. 7 and the area under the entrainment rate curve for test V6-B1) with the measured entrainment depth at L2.

The difference in pore pressure generated at the base of the flow and the erodible bed governs entrainment (Iverson 2012). The volumetric water content of the erodible bed in this study was 25%. As aforementioned, bed pore pressures can only develop if the water content is high enough to create continuous water networks that are capable of transmitting pore pressures (Iverson et al. 2011). For example, in the experiments of Iverson et al. (2011), positive bed pore pressures close to liquefaction ($\lambda_{b,top} \cong 1$) were reported for volumetric water contents higher than 22%. The rapid loading applied on the erodible bed by the debris flow may have generated undrained conditions, which rapidly increase pore pressures in the bed. The undrained loading causes the bed pore pressures to be proportional to the normal stress (compression), implying that it may be reasonable to assume a constant value of $\lambda_{b,top}$. Furthermore, the shear stress transmitted by the flow to the erodible bed may cause shear deformation (Iverson et al. 2011), which may cause contractive behaviour of the loose bed (Iverson 2012) and generate excess pore pressures. Notwithstanding, it may still be reasonable to assume that the generation of pore pressures via shearing should be more significant compared to generation of pore pressure by compression of voids of the granular bed material, given the low excess pore pressure measured (approximately 1.4 kPa) at the base of the bed (cell 2) compared to a theoretical normal stress of 7 kPa (eq. 4). Pore pressures were likely only increasing locally at the sheared interface between the entrained and the stationary bed.

The calculated entrainment rate in test V6-B1 reaches a maximum value of 0.13 m/s. In contrast, the entrainment rate reaches a maximum value of 0.04 m/s in tests V2.5-B1 and V6-B2. The calculated entrainment rates are consistent with the fact that test V6-B1 led to the highest entrainment depth. Entrainment of the bed occurred within 0.4 s for test V6-B2, 1 s for test V2.5-B1, and 1.4 s for test V6-B1

Published by Canadian Science Publishing

Pagination not final (cite DOI) / Pagination provisoire (citer le DOI)

Fig. 12. Measured forces on terminal barrier: (*a*) test V2.5-B1; (*b*) test V6-B1; and (*c*) test V6-B2.

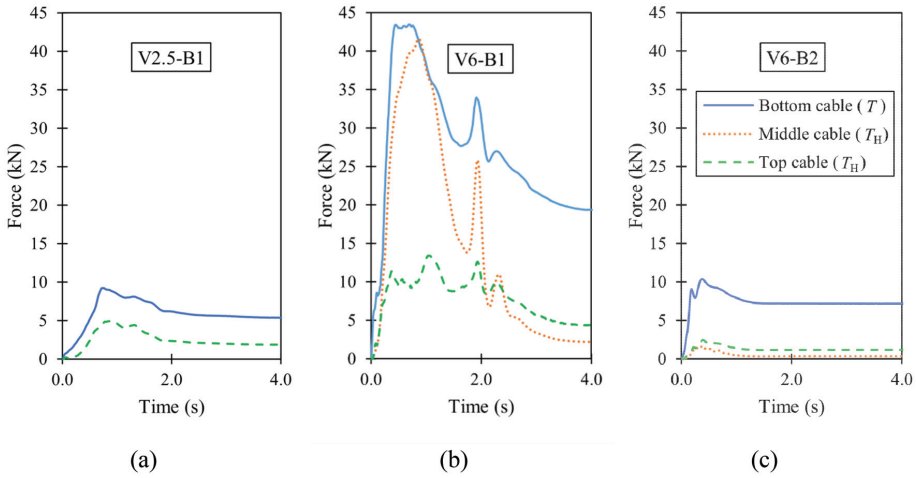

Table 2. Measured and calculated parameters for tests with initial volume of 6 m^3 impacting upstream and terminal barriers.

Test ID	Deflection angle bottom cable (°)	Deflection angle middle cable (°)	Deflection angle top cable (°)	Total peak impact force, F_T (kN)	Flow velocity (m/s)	Flow depth (m)	Back-calculated dynamic pressure coefficient α
V6-B1 (terminal barrier)	20	17	4	55	6.1	0.3	1.2
V6-B2 (terminal barrier)	8	3	2	3	4*	0.2*	0.2
V6-B2 (upstream barrier)	15	—	15	113	5.5	0.4	2.2

*Denotes second surge.

upon arrival of the flow front. The entrainment rate then becomes 0 or negative, which indicates deposition. The high positive entrainment rates up to t = 1 s imply that entrainment is dominant at the flow front, especially when the difference between $\lambda_{b,top}$ and $\lambda_{f,bot}$ is the highest. In fact, unsaturated flow front, characterised by low values of $\lambda_{f,bot}$, transmits higher basal shear stress and can entrain more bed material compared to the liquefied flow body. Higher entrainment at the flow front was also reported by Berger et al. (2011) in field measurements and Iverson et al. (2011) in their flume experiments. The rate of entrainment depends on the driving stresses caused by the flow and the resisting strength of the bed material. The driving stresses may be collisional or frictional in nature depending on the particle sizes involved (Song and Choi 2021). The resisting stress depends on the shear strength of the soil material involved and its water content (Song and Choi 2021). Also, the driving stresses may vary spatially and temporally within a debris flow. As such, the entrainment rate is case dependent and is expected to differ from event to event. Furthermore, deposition also occurs concurrently with entrainment. The entrainment depths in nature are often masked by the deposition so the elevation of steep creeks and riverbeds may even be higher than before a debris flow event.

The higher entrainment in test V6-B1, compared to test V2.5-B1, is mainly influenced by the larger flow depths recorded in test V6-B1. The larger flow depths generate higher shear stress at the flow–bed interface. It can be concluded that the initial flow volume has a significant influence on the flow depth and therefore on the entrainment magnitude. As expected, the entrainment process is scale dependent. In test V6-B2, despite a higher value of the flow depth compared to test V2.5-B1, the entrainment depth is the lowest compared to the other two tests. In test V6-B2, the bed pore pressure ratio, $\lambda_{b,top}$, is consistently lower than in test V6-B1, implying that only the first part of the flow, up to t = 0.4 s, entrains. In fact, the upstream flexible barrier changes the flow behaviour downstream, especially by reducing entrainment. Based on the two distinct overflow surges observed in test V6-B2, only the first overflow surge generated significant shear on the bed capable of increasing bed pore pressures and entraining bed material. In contrast, the second surge only flowed over the deposited material from the first surge and decelerated as it sheared the slower-moving debris material.

3.6. Impact dynamics

Figure 12 shows the measured cable force time histories for the top, middle, and bottom cables of the terminal barrier (T for the bottom cable and T_H for the middle and top cables) for the three tests. The t = 0 s indicates the time the flow front reaches the terminal barrier. The y-axis shows the cable force in kN while the x-axis shows the elapsed time in seconds. In general, for all three tests the peak cable force is reached within t = 1 s and gradually the loading attenuates to a residual static state. In comparison of the three cable force time histories, the bottom cable attains a higher peak and final force. Test V6-B1 shows the highest cable forces on the terminal barrier, while the magnitude of the cable forces in tests V2.5-B1 and V6-B2 are similar and lower than those measured in test V6-B1. A summary of the measured deflection angles of the cables are shown in Table 2. The deflection angle is measured at the end of the test. On the terminal barrier, the deflection angle is higher for the bottom and middle cables

Published by Canadian Science Publishing

because more loading is induced on them. The deflection angles on the terminal barrier are also much higher in test V6-B1 compared to test V6-B2, because the impact load was larger, and the cables deflected more.

The measured peak cable forces (T_H and T) (Fig. 12) and the measured cable deflection angles (ψ) (Table 2) are used to calculate the impact force (F) on each cable based on eqs. 1 and 2. Consequently, the total impact force (F_T) on the barrier is derived as the summation of the top, middle, and bottom cable impact force (F). The total peak impact forces, F_T, for the terminal barrier in tests V6-B1 and V6-B2 are 55 and 3 kN, respectively (Table 2). For comparison, the total peak impact force on the upstream barrier in test V6-B2 (113 kN) is also shown.

The total peak impact force is used by engineers for the design of flexible barriers to resist the debris flow impact. This peak impact force is generally estimated using the hydrodynamic equation (Kwan and Cheung 2012):

$$F_T = \alpha \rho \bar{v}_f^2 h_f w \quad (9)$$

where α is a dynamic pressure coefficient, $\bar{v}_f$ and h_f are the flow velocity and depth before impact, respectively (Table 2), and w is the width of the flow before impact (2 m). Wendeler et al. (2019) reports a value of α equal to 1.0 for debris flows impacting a flexible barrier in the field, but a range of values from 1.0 to 5.0 can be found in literature (Poudyal et al. 2019). The dynamic pressure coefficient α can be back-calculated as 2.2 for the upstream barrier in test V6-B2 and 1.2 and 0.2 for the terminal barrier in tests V6-B1 and V6-B2, respectively. The dynamic pressure coefficient is not calculated for test V2.5-B1 because the load cell for the middle cable malfunctioned during the test.

The value of α is higher for the upstream barrier (2.2) in test V6-B2 compared to that of the terminal barrier (1.2) for the test with only the terminal barrier (test V6-B1). The high value of α at the upstream barrier may have been caused by the centrifugal component of the force (Hungr 1995) from the curved layer flowing over the dead zone (Fig. 4*d*) and drag from overflow (Wendeler et al. 2019). Furthermore, the small barrier to flow depth ratio (1.5) may have limited energy dissipation internally in the flow, with higher force transferred to the upstream barrier.

More importantly, the value of α on the terminal barrier decreases significantly when the upstream flexible barrier is used (test V6-B2 compared to test V6-B1). A rational explanation for this reduction can be found by analysing the impact process on the terminal flexible barrier (Fig. 5). In test V6-B1, a higher volume (5.7 m^3) impacted the barrier with a higher flow velocity (6.1 m/s). A run-up impact mechanism therefore developed (Fig. 5*a*), which mobilised all three cables in the barrier. In contrast, in test V6-B2, the volume impacting the terminal barrier was much smaller and limited to the second surge (2.6 m^3), which was flowing over the deposit from the first surge. Furthermore, the velocity impacting the terminal barrier in test V6-B2 had decreased (4 m/s) due to the upstream barrier. The impact on the terminal barrier was therefore a pileup mechanism (Fig. 5*b*).

4. Conclusions

A series of unique physical experiments were conducted in a 28 m long flume to study the impact of a debris flow on both single and dual flexible barriers installed in a channel with a 6 m long erodible soil bed. Two different initial volumes of 2.5 and 6 m^3 were investigated. Based on the experimental results, the following conclusions for the settings adopted in this study may be drawn as follows:

1. A compact upstream flexible barrier (1.5h_f) with a design capacity of only 20% of the intial debris volume installed before an erodible bed reduces the peak discharge by creating several smaller overflowing surges. The formation of surges when interacting with the upstream barrier decreases entrainment by 70% and the impact force on the terminal barrier by 94% compared to the case without an upstream barrier. The design dynamic pressure coefficient α for the terminal barrier decreases from 1.2 to 0.2 in presence of the additional upstream barrier. This suggests that installing a compact upstream flexible barrier can lead to design optimisation for the terminal barrier.
2. Although the upstream barrier was successful in reducing entrainment and the impact force induced on the terminal barrier, the deformation of the upstream barrier upon impact formed a curved ramp-like deposit for subsequent flow to induce centrifugal force on the barrier. This barrier configuration unexpectedly led to a back-calculated dynamic pressure coefficient of 2.2, which is much higher than the recommended 1.5 in design guidelines. This finding suggests that the maximum deformation and orientation of a flexible barrier with respect to the channel requires further consideration as the overflow trajectory differs compared to rigid barriers.
3. Experimental results show that debris flow–bed–barrier interaction is a complex problem driven by the scale of the event. This is supported by the differences in flow depths, frontal velocities, entrainment depths and rates, and impact forces between the 2.5 and 6 m^3 tests. Furthermore, it is shown that not only is the scale important in determining the entrainment volume and impact forces, but the upstream barrier can reduce entrainment and the impact force on the terminal barrier. Evidently, debris flows in nature are much larger in scale and occur in successive surges. Further investigation of the spacing between barriers, barrier deformation, barrier height and slope are required to move towards a rational basis to leverage multiple flexible barriers to reduce the scale of, and mitigate, a debris flow event.

Author statements

Competing interests

The authors declare there are no competing interests.

Contributors statement

Hervé Vicari: conceptualization, investigation, formal analysis, methodology, visualization, writing — original draft. Charles W.W. Ng and Vikas Thakur: funding acquisition, project administration, supervision, writing — review and editing. Steinar Nordal: conceptualization, funding acquisition, supervision, writing — review and editing. W.A. Roanga K. De Silva and Haiming Liu: investigation, formal analysis, writing — review and editing. Clarence E. Choi: funding acquisition, investigation, formal analysis, methodology, project administration, supervision, writing — review and editing.

Funding statement

The authors of this paper would like to acknowledge Centre for Research Driven Innovation (CRI) KLIMA2050 and INTPART project "Landslide Mitigation of Urbanized Slopes for Sustainable Growth", funded by the Research Council of Norway. The authors are also grateful for the financial sponsorship from the Research Grants Council of Hong Kong (General Research Fund Grants 16212618, 16209717, 16210219, T22-603/15 N, and AoE/E-603/18). Clarence Choi would also like to acknowledge the support received from the start-up fund from the Department of Civil Engineering and the Faculty of Engineering at the University of Hong Kong. W.A.R.K. De Silva gratefully acknowledges the support of Hong Kong PhD Fellowship scheme (HKPFS) provided by the Research Grants Council (RGC) of Hong Kong Special Administrative Region (HKSAR).

Data availability

All data are available upon reasonable request.

Acknowledgements

The authors are grateful for the technical assistance related to model preparation and testing that was provided by the Norwegian University of Science and Technology (Frank Stæhli) and by the Hong Kong University of Science and Technology (Sunil Poudyal, Aastha Bhatta, Shengyi Lin).

References

Berger, C., McArdell, B.W., and Schlunegger, F. 2011. Direct measurement of channel erosion by debris flows, Illgraben, Switzerland. Journal of Geophysical Research: Earth Surface, **116**(1). doi:10.1029/2010JF001722.

Choi, C.E., Au-Yeung, S.C.H., Ng, C.W.W., and Song, D. 2015. Flume investigation of landslide granular debris and water runup mechanisms. Géotechnique Letters, **5**(1): 28–32. doi:10.1680/geolett.14.00080.

Faug, T. 2021. Impact force of granular flows on walls normal to the bottom: slow versus fast impact dynamics. Canadian Geotechnical Journal, **58**(1): 114–124. doi:10.1139/cgj-2019-0399.

Feiger, N., and Wendeler, C. 2019. Scour and erosion experience with flexible debris-flow nets. *In* Debris-Flow Hazards Mitigation: Mechanics, Monitoring, Modeling, and Assessment — Proceedings of the 7th International Conference on Debris-Flow Hazards Mitigation, Golden, Colo., 10–13 June 2019. Association of Environmental and Engineering Geologists, Special Publication 28. pp. 941–948.

Haas, T.D., and van Woerkom, T. 2016. Bed scour by debris flows: experimental investigation of effects of debris-flow composition. Earth Surface Processes and Landforms, **41**(13): 1951–1966. doi:10.1002/esp.3963.

Hungr, O. 1995. A model for the runout analysis of rapid flow slides, debris flows, and avalanches. Canadian Geotechnical Journal, **32**(4): 610–623. doi:10.1139/t95-063.

Hungr, O., McDougall, S., and Bovis, M. 2005. Entrainment of material by debris flows. *In* Debris-flow hazards and related phenomena. *Edited by* M. Jakob and O. Hungr. Springer, Berlin, Heidelberg. pp. 135–158. doi:10.1007/3-540-27129-5_7.

Iverson, R.M. 1997. The physics of debris flows. Reviews of Geophysics, **35**(3): 245–296. doi:10.1029/97RG00426.

Iverson, R.M. 2012. Elementary theory of bed-sediment entrainment by debris flows and avalanches. Journal of Geophysical Research: Earth Surface, **117**(3). doi:10.1029/2011JF002189.

Iverson, R.M. 2015. Scaling and design of landslide and debris-flow experiments. Geomorphology, **244**: 9–20. doi:10.1016/j.geomorph.2015.02.033.

Iverson, R.M., and LaHusen, R.G. 1993. Friction in debris flows: inferences from large-scale flume experiments. *In* Hydraulic Engineering 1993: Proceedings of the 1993 Conference on Hydraulics Division, San Francisco, Calif., 25–30 July 1993. American Society of Civil Engineers, New York, NY. Vol. 2. pp. 1604–1609.

Iverson, R.M., and Ouyang, C. 2015. Entrainment of bed material by Earth-surface mass flows: review and reformulation of depth-integrated theory. Reviews of Geophysics, **53**(1): 27–58. doi:10.1002/2013RG000447.

Iverson, R.M., Logan, M., LaHusen, R.G., and Berti, M. 2010. The perfect debris flow? Aggregated results from 28 large-scale experiments. Journal of Geophysical Research, **115**(F3): F03005. doi:10.1029/2009JF001514.

Iverson, R.M., Reid, M.E., Logan, M., Lahusen, R.G., Godt, J.W., and Griswold, J.P. 2011. Positive feedback and momentum growth during debris-flow entrainment of wet bed sediment. Nature Geoscience, **4**(2): 116–121. doi:10.1038/ngeo1040.

Kwan, J.S.H., and Cheung, R.W.M. 2012. Suggestion on design approaches for flexible debris resisting barriers. Discussion Note DN1/2012. The Government of Hong Kong Standards and Testing Division, Hong Kong, China.

Kwan, J.S.H., Koo, R.C.H., and Ng, C.W.W. 2015. Landslide mobility analysis for design of multiple debris-resisting barriers. Canadian Geotechnical Journal, **52**(9): 1345–1359. doi:10.1139/cgj-2014-0152.

McArdell, B.W., Bartelt, P., and Kowalski, J. 2007. Field observations of basal forces and fluid pore pressure in a debris flow. Geophysical Research Letters, **34**(7). doi:10.1029/2006GL029183.

McCoy, S.W., Kean, J.W., Coe, J.A., Tucker, G.E., and Staley, D.M. 2012. Sediment entrainment by debris flows: in situ measurements from the headwaters of a steep catchment. Journal of Geophysical Research Atmospheres, **117**: 1–25. doi:10.1029/2011JF002278.

Medina, V., Hürlimann, M., and Bateman, A. 2008. Application of FLATModel, a 2D finite volume code, to debris flows in the northeastern part of the Iberian Peninsula. Landslides, **5**(1): 127–142. doi:10.1007/s10346-007-0102-3.

Ng, C.W.W., Choi, C.E., and Law, R.P.H. 2013. Longitudinal spreading of granular flow in trapezoidal channels. Geomorphology, **194**: 84–93. doi:10.1016/j.geomorph.2013.04.016.

Ng, C.W.W., Song, D., Choi, C.E., Liu, L.H.D., Kwan, J.S.H., Koo, R.C.H., and Pun, W.K. 2017. Impact mechanisms of granular and viscous flows on rigid and flexible barriers. Canadian Geotechnical Journal, **54**(2): 188–206. doi:10.1139/cgj-2016-0128.

Ng, C.W.W., Choi, C.E., Majeed, U., Poudyal, S., and De Silva, W.A.R.K. 2019. Fundamental framework to design multiple rigid barriers for resisting debris flows. *In* Proceedings of the 16th Asian Regional Conference on Soil Mechanics and Geotechnical Engineering (16ARC), Taipei, Taiwan, 14–18 October 2019.

Ng, C.W.W., Choi, C.E., Liu, H., and Poudyal, S. 2020. Design recommendations for single and dual rigid and flexible debris flow resisting barriers with and without basal clearance. *In* Proceedings of the 5th World Landslides Forum, Kyoto, Japan. pp. 33–53.

Poudyal, S., Choi, C.E., Song, D., Zhou, G.G.D., Yune, C.Y., Cui, Y., et al. 2019. Review of the mechanisms of debris-flow impact against barriers. *In* Debris-Flow Hazards Mitigation: Mechanics, Monitoring, Modeling, and Assessment — Proceedings of the 7th International Conference on Debris-Flow Hazards Mitigation, Golden, Colo., 10–13 June 2019. Association of Environmental and Engineering Geologists, Special Publication 28. pp. 1027–1034.

Sassa, K. 1988. Special lecture: Geotechnical model for the motion of landslides. *In* Proceedings of 5th Symposium on Landslides, Lausanne, Switzerland, 10–15 July 1988. *Edited by* C. Bonnard. Balkema, Rotterdam. pp. 37–55.

Savage, S.B., and Hutter, K. 1989. The motion of a finite mass of granular material down a rough plane. Journal of Fluid Mechanics, **199**: 177–215. doi:10.1017/S0022112089000340.

Shen, W., Wang, D., Qu, H., and Li, T. 2019. The effect of check dams on the dynamic and bed entrainment processes of debris flows. Landslides, **16**(11): 2201–2217. doi:10.1007/s10346-019-01230-7.

Shen, P., Zhang, L., Wong, H.F., Peng, D., Zhou, S., Zhang, S., and Chen, C. 2020. Debris flow enlargement from entrainment: a case study for comparison of three entrainment models. Engineering Geology, **270**: 105581. doi:10.1016/j.enggeo.2020.105581.

Song, P., and Choi, C.E. 2021. Revealing the importance of capillary and collisional stresses on soil bed erosion induced by debris flows. Journal of Geophysical Research: Earth Surface, **126**(5): e2020JF005930. doi:10.1029/2020JF005930.

Song, D., Choi, C.E., Ng, C.W.W., and Zhou, G.G.D. 2018. Geophysical flows impacting a flexible barrier: effects of solid-fluid interaction. Landslides, **15**(1): 99–110. doi:10.1007/s10346-017-0856-1.

Wendeler, C., McArdell, B.W., Volkwein, A., Denk, M., and Gröner, E. 2008. Debris flow mitigation with flexible ring net barriers — field tests and case studies. WIT Transactions on Engineering Sciences, **60**: 23–31. doi:10.2495/DEB080031.

Wendeler, C., Volkwein, A., McArdell, B.W., and Bartelt, P. 2019. Load model for designing flexible steel barriers for debris flow mitigation. Canadian Geotechnical Journal, **56**(6): 893–910. doi:10.1139/cgj-2016-0157.

Supplementary material

The Effects of Upstream Flexible Barrier on the Debris Flow Entrainment and Impact Dynamics on a Terminal Barrier

Hervé Vicari, Charles W.W. Ng, Steinar Nordal, Vikas Thakur, W.A. Roanga K. De Silva, Haiming Liu, and Clarence E. Choi*
*Corresponding author (cechoi@hku.hk)

Affiliation:

H. Vicari, S. Nordal, V. Thakur: Norwegian University of Science and Technology (NTNU), Department of Civil and Environmental Engineering, Trondheim, Norway.
C.W.W. Ng, W.A.R.K. De Silva, H. Liu: Hong Kong University of Science and Technology (HKUST), Department of Civil and Environmental Engineering, Hong Kong.
C.E. Choi: University of Hong Kong, Department of Civil Engineering, Hong Kong.

1. Flow characterisation using dimensionless numbers

The Savage number is the ratio between collisional and friction stresses (Iverson 1997):

(S1) $$N_{\mathrm{Sav}} = \frac{\rho_s \delta^2 \dot{\gamma}^2}{(\rho_s - \rho_f) g \mu' h_f}$$

where $\rho_s = 2650$ kg/m^3 is the density of the solid grains, $\rho_f = 1100$ kg/m^3 is the fluid density, δ = 1 mm is the average grain diameter in the flow, $\mu' = 0.89$ is the effective friction coefficient of the soil, and $\dot{\gamma}$ is the shear rate of the flow, which can be approximated as the ratio between the average flow velocity and the flow depth (h_f).

The Friction number is the ratio between frictional and viscous stresses (Iverson 1997):

(S2) $$N_{\mathrm{fric}} = \frac{C_s}{1 - C_s} \frac{(\rho_s - \rho_f) g \mu' h_f}{\nu \dot{\gamma}}$$

where $C_s = 0.7$ is the solid concentration of the flow and $\nu = 10^{-3}\ Pa \cdot s$ is the viscosity of the fluid component. These two dimensionless numbers will depend on the flow parameters (velocity and flow depth), which are changing for each test and at the two locations of the flow depth sensors, specifically L1 (x = 3.4 m) and L2 (x = 12.5 m). The values of the Savage and Friction numbers are shown in Table S1.

Table S1. Summary of Savage and Friction numbers.

Location	L1 - 3.4 m			L2 - 12.5 m		
Test ID	V2.5-B1	V6-B1	V6-B2	V2.5-B1	V6-B1	V6-B2
Flow depth (m)	0.2	0.4	0.4	0.1	0.3	0.3
Flow velocity (m/s)	4.9	5.3	5.0	5.7	6.8	6.0
Savage number	4×10^{-4}	8×10^{-5}	6×10^{-5}	4×10^{-3}	3×10^{-4}	4×10^{-4}
Friction number	3×10^{5}	9×10^{5}	1×10^{6}	8×10^{4}	5×10^{5}	4×10^{5}

2. Calculation of entrainment rate

Iverson (2012) proposed a two-layer entrainment model (Fig. S1a). One layer represents the flow and one layer represents the erodible bed, which is on a rigid base. A Cartesian coordinate system is oriented with the *x* direction along the flow direction and the *z* direction orthogonal to the base of the bed.

Based on the conservation of momentum for the entrained bed layer (Fig. S1b), the entrainment rate, *E*, can be expressed as (Iverson 2012):

(S3) $$E = -\frac{\partial z_b}{\partial t} \cong -\frac{\Delta z_b}{\Delta t} = \frac{\tau_{f,bot} - \tau_{b,top}}{\rho v_{f,bot}}$$

where t is time, z_b is the distance from the rigid bed to the top of the boundary layer; $\tau_{f,bot}$ is the flow basal shear stress; $\tau_{b,top}$ is the bed resisting shear stress, ρ is the flow density and $v_{f,bot}$ is the basal flow velocity. The basal flow velocity is assumed to be proportional to the average flow velocity ($\overline{v_f}$) (Johnson et al. 2012) and given as follows:

(S4) $$v_{f,bot} = \frac{1}{2}\overline{v_f}$$

By combining eq. (S3) and eq. (S4), the entrainment rate can be expressed as:

(S5) $$E = 2\frac{\tau_{f,bot} - \tau_{b,top}}{\rho \overline{v_f}}$$

Finally, by modelling the flow and the bed as frictional materials and using a Mohr-Coulomb law, the entrainment rate can be expressed as:

(S6) $$E(t) = 2gh_f(t)cos\theta\mu' \frac{\lambda_{b,top}(t) - \lambda_{f,bot}(t)}{\bar{v}_f}$$

where g is the acceleration due to gravity; h_f is the flow depth; θ is the slope angle; μ' is the effective friction coefficient; $\lambda_{f,bot}$ is the flow basal pore pressure ratio; $\lambda_{b,top}$ is the bed pore pressure ratio. The pore pressure ratios are defined as the pore pressure (of the flow or the bed) divided by the total normal stress.

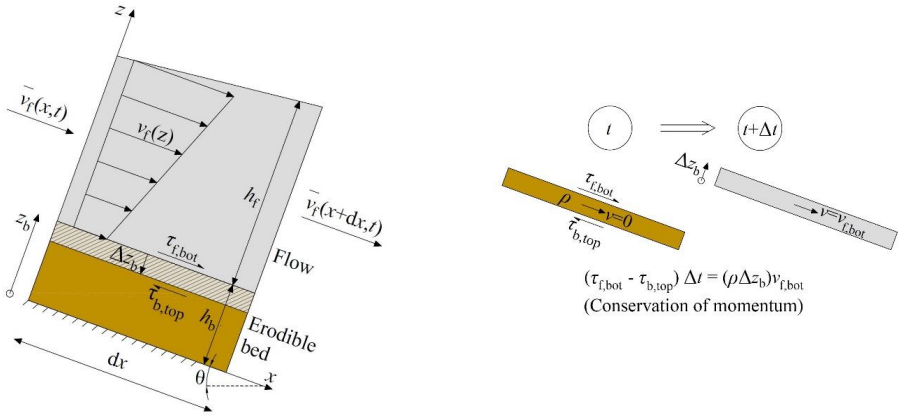

(a) (b)

Fig. S1. Schematic of two-layer entrainment model: (a) vertical section of debris flow travelling over erodible bed; (b) details of entrained bed layer.

References

Iverson, R.M. 1997. The Physics of Debris Flows. Reviews of Geophysics, **35**(3): 245–296. doi:10.1029/97RG00426

Iverson, R.M. 2012. Elementary theory of bed-sediment entrainment by debris flows and avalanches. Journal of Geophysical Research: Earth Surface, **117**(3): 1–17. doi:10.1029/2011JF002189.

Johnson, C.G., Kokelaar, B.P., Iverson, R.M., Logan, M., Lahusen, R.G., and Gray, J.M.N.T. 2012. Grain-size segregation and levee formation in geophysical mass flows. Journal of Geophysical Research: Earth Surface, **117**(1): 1–23. doi:10.1029/2011JF002185.

Chapter 5

5. MPM modelling

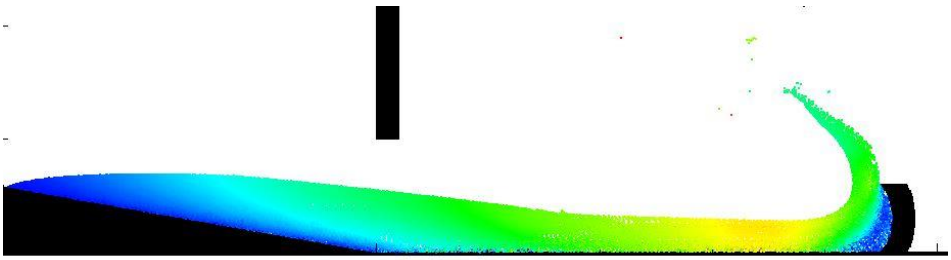

Numerical simulation using the Material Point Method

In *Paper II*, entrainment has been investigated using an analytical formulation, which allowed to analyze the influence of the flow basal shear stress and bed pore pressure development on the entrainment. However, entrainment could be back-calculated only at a specific location along the bed (where the flow depth was measured). Furthermore, it remains challenging to explain the observed entrainment pattern, where higher erosion was observed at the start of the erodible bed at the transition from the fixed rigid bed. As an alternative to the analytical formulation, a three-dimensional numerical model such as MPM can be applied to attempt to capture the entrainment pattern and mechanisms. MPM can also be applied to simulate the flow interaction with the flexible barrier.

The basics of the MPM algorithm are described in this chapter. *Paper III* then presents the back-calculation of the large-scale flume experiments. *Paper IV* is then presented, which attempts to simulate different entrainment cases, involving boulders.

5.1. Material Point Method (MPM)

MPM (Sulsky et al. 1994) is adopted in this research to model the debris flow behaviour, the entrainment process and the impact on the flexible barrier. The software Uintah (uintah.utah.edu) is used. MPM allows to compute the dynamic behaviour at large deformations of a continuum material, which is assumed to be equivalent to the two-phase debris flow.

To illustrate the basic principles of the numerical integration scheme, a simple case is considered, consisting of a 1-dimensional linear elastic material, which can move and deform along the z-direction (Figure 5.1a). This material is discretized into two material points, P1 and P2 (Lagrangian points), which carry the material properties (Figure 5.1b). The properties are transferred on a fixed mesh (Eulerian grid), which in this case consists of three nodes, N1, N2 and N3, where the computation of the dynamic behaviour is carried out. The function transferring the material properties to the nodes, and vice versa, is termed interpolation function (Figure 5.1c), which is here assumed to be linear. The material point method involves the following computational steps:

i. The material points at time t are carrying the state data, in terms of position (z_P), velocity (v_P), stress (σ_P). Figure 5.1d shows the particle velocities $v_{P1}(t)$ and $v_{P2}(t)$.
ii. The particle mass (M_P) is transferred to the nodes (M_N), through the interpolation functions (S_{P-N}):

$$\begin{aligned} M_{N1} &= M_{P1}S_{P1-N1} \\ M_{N2} &= M_{P1}S_{P1-N2} + M_{P2}S_{P2-N2} \\ M_{N3} &= M_{P2}S_{P2-N3} \end{aligned} \quad \textbf{5.1}$$

iii. The particle velocities (v_P) are transferred to the nodes (v_N) (Figure 5.1e):

$$\begin{aligned} v_{N1}(t) &= \frac{v_{P1}M_{P1}S_{P1-N1}}{M_{N1}} \\ v_{N2}(t) &= \frac{v_{P1}M_{P1}S_{P1-N2} + v_{P2}M_{P2}S_{P2-N2}}{M_{N2}} \\ v_{N3}(t) &= \frac{v_{P2}M_{P2}S_{P2-N3}}{M_{N3}} \end{aligned} \quad \textbf{5.2}$$

iv. The internal forces on the nodes are computed, based on the divergence of the stresses (Figure 5.1f):

$$\begin{aligned} F_{N1}(t) &= \frac{M_{P1}}{\rho_{P1}}\frac{dS_{P1-N1}}{dz}\sigma_{P1} \\ F_{N2}(t) &= \frac{M_{P1}}{\rho_{P1}}\frac{dS_{P1-N2}}{dz}\sigma_{P1} + \frac{M_{P2}}{\rho_{P2}}\frac{dS_{P2-N2}}{dz}\sigma_{P2} \\ F_{N3}(t) &= \frac{M_{P2}}{\rho_{P2}}\frac{dS_{P2-N3}}{dz}\sigma_{P2} \end{aligned} \quad \textbf{5.3}$$

where σ_P is the particle stress and $\frac{dS_P}{dz}$ is the gradient of the interpolation function.

v. The acceleration at each node is computed:

$$\begin{aligned} a_{N1}(t) &= \frac{F_{N1}(t)}{M_{N1}} + g \\ a_{N2}(t) &= \frac{F_{N2}(t)}{M_{N2}} + g \\ a_{N3}(t) &= \frac{F_{N3}(t)}{M_{N3}} + g \end{aligned} \quad \textbf{5.4}$$

where the acceleration due to gravity, g, is also accounted.

vi. The nodal velocities are then calculated using explicit forward Euler integration (Figure 5.1g):

$$\begin{aligned} v_{N1}(t+\Delta t) &= v_{N1}(t) + a_{N1}(t)\Delta t \\ v_{N2}(t+\Delta t) &= v_{N2}(t) + a_{N2}(t)\Delta t \\ v_{N3}(t+\Delta t) &= v_{N3}(t) + a_{N3}(t)\Delta t \end{aligned} \quad \textbf{5.5}$$

Boundary conditions (if any) are also applied at this stage on the relevant nodes.

vii. The computed nodal velocities are used to back calculate the velocities of the material points (Figure 5.1h):

$$v_{P1}(t+\Delta t) = v_{P1}(t) + S_{P1-N1}a_{N1}(t)\Delta t + S_{P1-N2}a_{N2}(t)\Delta t$$
$$v_{P2}(t+\Delta t) = v_{P2}(t) + S_{P2-N2}a_{N2}(t)\Delta t + S_{P2-N3}a_{N3}(t)\Delta t \quad \textbf{5.6}$$

viii. The particle strains are updated, based on the gradients of the nodal velocities:

$$\varepsilon_{P1}(t+\Delta t) = \varepsilon_{P1}(t) + \frac{dS_{P1-N1}}{dz}v_{N1}(t+\Delta t)\Delta t + \frac{dS_{P1-N2}}{dz}v_{N2}(t+\Delta t)\Delta t$$
$$\varepsilon_{P2}(t+\Delta t) = \varepsilon_{P2}(t) + \frac{dS_{P2-N2}}{dz}v_{N2}(t+\Delta t)\Delta t + \frac{dS_{P2-N3}}{dz}v_{N3}(t+\Delta t)\Delta t \quad \textbf{5.7}$$

ix. From the strain, the updated stress is calculated, based on the constitutive model (linear elastic, in this example):

$$\sigma_{P1}(t+\Delta t) = E\varepsilon_{P1}(t+\Delta t)$$
$$\sigma_{P2}(t+\Delta t) = E\varepsilon_{P2}(t+\Delta t) \quad \textbf{5.8}$$

x. The position of the material points is updated (Figure 5.1i):

$$z_{P1}(t+\Delta t) = z_{P1}(t) + S_{P1-N1}v_{N1}(t+\Delta t)\Delta t + S_{P1-N2}v_{N2}(t+\Delta t)\Delta t$$
$$z_{P2}(t+\Delta t) = z_{P2}(t) + S_{P2-N2}v_{N2}(t+\Delta t)\Delta t + S_{P2-N3}v_{N3}(t+\Delta t)\Delta t \quad \textbf{5.9}$$

xi. The nodes are reset to the initial position and the procedure is repeated.

To guarantee the stability of the numerical simulation, the propagation of an elastic wave in the time step Δt should not exceed the distance between two nodes. This is defined as the Courant-Friedrichs-Lewy condition:

$$\Delta z_{\text{wave}} < \Delta z_{N1-N2} \quad \textbf{5.10}$$

where Δz_{N1-N2} is the distance between two adjacent nodes (for instance N1 and N2) and Δz_{wave} is the distance of wave propagation, which can be expressed as:

$$\Delta z_{\text{wave}} = v_{\text{wave}}\Delta t \quad \textbf{5.11}$$

where v_{wave} is the wave velocity, as function of the Young's modulus (E) and density (ρ):

$$v_{\text{wave}} = \sqrt{E/\rho} \quad \textbf{5.12}$$

The combination of Eqs. 5.10, 5.11, 5.12 results in a condition for the time step:

$$\Delta t < \Delta z_{N1-N2}\sqrt{\rho/E} \quad \textbf{5.13}$$

Furthermore, additional conditions on the time step are depending on the actual nodal velocities (Jiang et al. 2017).

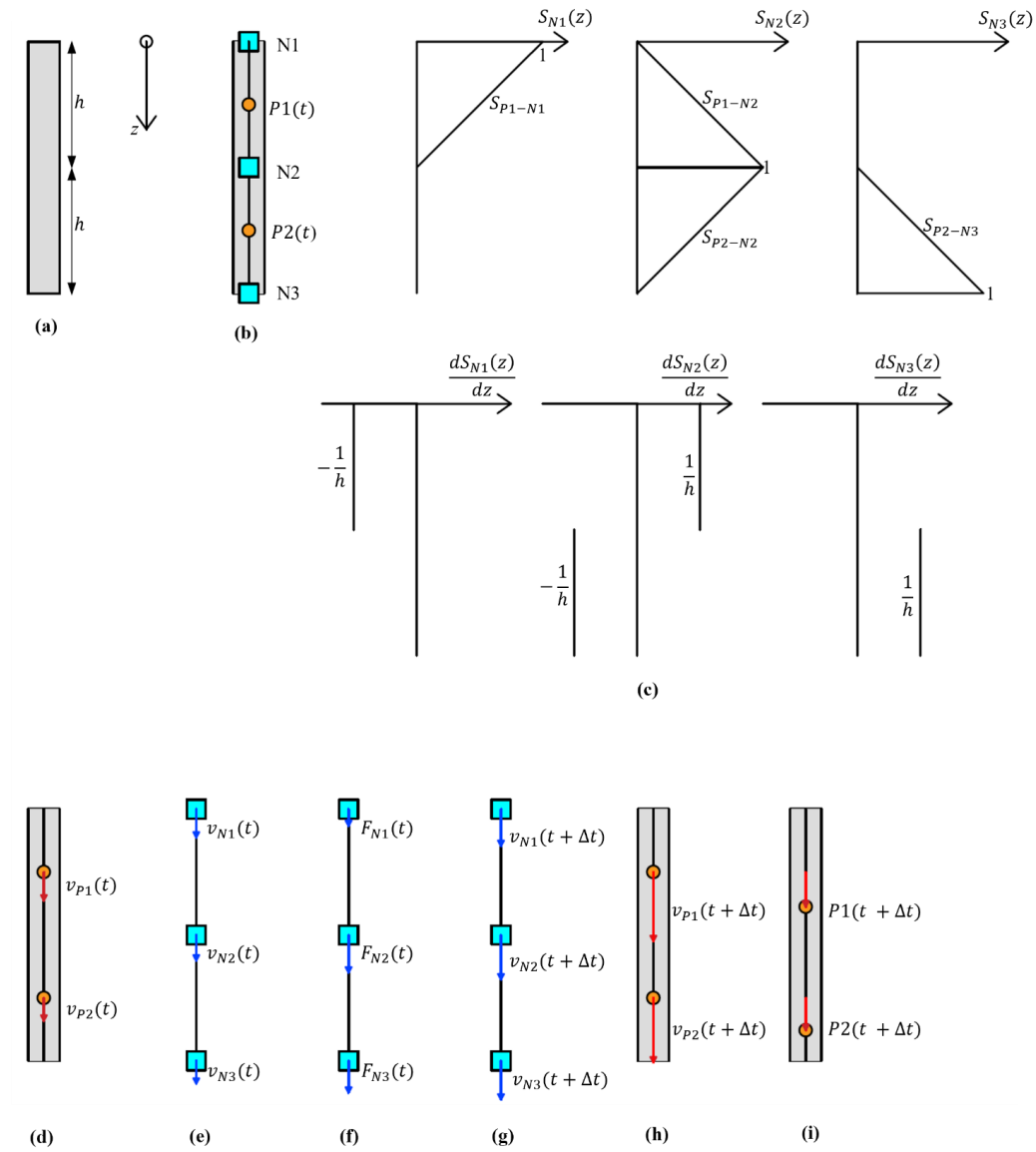

Figure 5.1 Overview of the material point method for the case of a 1-dimensional column: (**a**) 1-dimensional column with linear elastic material behaviour; (**b**) discretization of the column in material points (P1, P2) and creation of a grid of nodes (N1, N2, N3); (**c**) interpolation functions (S) and their derivatives (dS/dz); (**d**) particle velocities; (**e**) nodal velocities; (**f**) nodal forces; (**g**) updated nodal velocities; (**h**) updated particle velocities; (**i**) updated particle positions

In this research, the material point method coded in Uintah has been used. The algorithm is an improved version of the MPM described in Figure 5.1: in particular, the Generalized Interpolation Material Point (GIMP) (Bardenhagen and Kober 2004) is used. GIMP introduces a particle domain which makes the shape function of higher order than in MPM. Therefore, the gradient of the shape function in GIMP is linear rather than a step-function as in MPM. The adoption of GIMP can improve the stability of the calculation.

The model and the material constitutive models are described and applied in *Paper III*. In particular, the debris flow and erodible bed are modelled as elasto-plastic materials, with a Mohr-Coulomb yield criterion. The debris flow material properties are based on an apparent friction angle, which is calibrated to account for the influence of pore pressures on flow mobility. Regarding the erodible bed, a softening model is introduced (*Paper III*) to account for the progressive increase of excess pore pressures as the bed is sheared by the debris flow.

Paper III models a cross-section of the flume (i.e., a plane-strain problem) to reduce the computational costs. This implies that the shear resistance of the lateral flume walls on the debris flow is neglected. Indeed, the ratio between lateral (T_{lateral}) and basal (T_{basal}) shear forces can be calculated considering a frictional material behaviour:

$$\frac{T_{\mathrm{lateral}}}{T_{\mathrm{basal}}} \cong \frac{\frac{1}{2}\sigma_{\mathrm{b}} h_{\mathrm{f}} tan\varphi_{\mathrm{f-b}}}{\sigma_{\mathrm{b}} W tan\varphi_{\mathrm{f-b}}} = \frac{h_{\mathrm{f}}}{2W} \qquad \textbf{5.14}$$

where h_{f} is the flow depth and $W = 2\ m$ is the width of the flume, $\sigma_b W$ is the flow basal normal force (per unit length), $\frac{1}{2}\sigma_{\mathrm{b}} h_{\mathrm{f}}$ is the flow lateral normal force (assuming linear variations of the vertical stress with depth and a hydrostatic earth pressure coefficient), $\varphi_{\mathrm{f-b}}$ is the flow basal apparent friction angle. Considering an average flow depth of 0.3 m, the ratio between the shear forces is equal to $\frac{F_{\mathrm{lateral}}}{F_{\mathrm{basal}}} \cong 0.075$, which shows that the lateral shear forces are negligible compared to the basal shear force. Therefore, a 2D model can be regarded as a valid approximation to simulate the flow dynamics, at least on the centreline of the flume.

5.2. Paper III

Vicari, H., Tran, Q.A., Nordal, S., and Thakur, V.K.S. 2022. MPM modelling of debris flow entrainment and interaction with an upstream flexible barrier. Landslides. doi:10.1007/s10346-022-01886-8.

Original Paper

Landslides
DOI 10.1007/s10346-022-01886-8
Received: 18 October 2021
Accepted: 31 March 2022

Hervé Vicari · Quoc Anh Tran · Steinar Nordal · Vikas Thakur

MPM modelling of debris flow entrainment and interaction with an upstream flexible barrier

Abstract Flexible barriers may be installed upstream in debris flow channels to reduce entrainment of bed material. Simulating both the entrainment and the impact on a barrier by the same numerical tool remains challenging. For this purpose, a three-dimensional one-phase material point method (MPM) software is used herein to back-calculate two large-scale flume experiments. These experiments were conducted to measure the entrainment of an erodible bed and the impact on a flexible barrier. To simulate the entrainment of the wet bed, a Mohr–Coulomb softening model is introduced. In the model, the apparent friction angle of the bed material decreases as a function of the distortional strain, effectively reproducing the pore pressure increase observed in the experiments. From the tests and the numerical simulations, we identify two main mechanisms leading to entrainment: (i) the direct rubbing and colliding effect of the flow on to the bed and (ii) a significant bed shear strength reduction. Concerning the first mechanism, existing models only consider the rubbing of the bed surface by a shear stress parallel to the slope. However, we observe that a ploughing-type erosion occurs due to normal stresses acting on the bed in the flow direction. The additional ploughing explains why beds which are mechanically stronger than the flow can also be partly entrained. Larger entrainment volumes are found when the bed material loses shear strength due to pore pressure buildup that eventually leads to a self-propelled entrainment where the bed no longer has frictional strength to carry its own weight.

Keywords Landslide · Debris flow · Entrainment · Flexible barrier · Material point method · Flume

Introduction

Debris flows are one of the most hazardous types of landslides in Norway and other parts of the world and become more frequent due to an increase of precipitations from climate change. Its steep topography makes Norway susceptible to debris flow events. The events are often accompanied by significant bed entrainment (e.g. Breien et al. 2008). The initial debris flow volume is typically rather small, but the volume can extensively increase by entraining or accumulating soil, rocks, fluid and vegetation along the flow path (Hungr et al. 2005). The Centre for Research-based Innovation, Klima 2050 (Solheim et al. 2021), was created with the aim of reducing the risks associated with climate change and protecting critical infrastructures from landslides. A typical debris flow landslide took place in Hunnedalen (Norway) on 2nd June 2016 after a period of intense rainfall (Fig. 1a). The initial landslide volume was only about 2000 m^3, but following entrainment, it increased to 20,000 m^3 (Vicari et al. 2021b) and buried a regional road, FV 45, remarkably without causing injuries. Figure 1b shows a detail of the eroded flow channel (field survey in June 2019), with entrainment depths of more than 2 m.

To study the entrainment process and mitigation solutions, large-scale flume tests have been conducted (Vicari et al. 2021a) in a unique facility located in Hong Kong (Ng et al. 2019). The 28-m-long flume was designed to reduce scaling effects typical for debris flows (Iverson 2015). The experimental study of Vicari et al. (2021a) showed that an upstream flexible barrier (i.e. placed upstream of the erodible bed) can effectively reduce both entrainment and the impact on a terminal barrier. The experimental results will be briefly summarized in this paper. To gain more insights regarding the entrainment mechanisms and the impact on the barrier, a numerical study was suggested to back-calculate the experimental results. Among the several numerical methods described in the literature, an appropriate model should be selected to simulate both the interaction with the barrier and the entrainment. Typically, depth-averaged models are used to simulate the debris flow runout and entrainment (e.g. Medina et al. 2008; Pirulli and Pastor 2012; Pastor et al. 2014; Frank et al. 2015). However, depth-averaged numerical models cannot capture the vertical momentum redirection (Ng et al. 2020), which is typical of the interaction of a debris flow with a structure. Three-dimensional models have been successfully applied for this purpose (e.g. Kwan et al. 2015; Koo et al. 2018; Zhao et al. 2020; Cuomo et al. 2021; Lam and Wong 2021). However, only a few study entrainment using a three-dimensional model (Lee and Jeong 2018; Lee et al. 2019; Nikooei and Manzari 2020). Previous research has not focused on simulating both the entrainment of an erodible bed and the impact on a flexible barrier using the same numerical tool.

Gravity driven mass flows can entrain an erodible by two mechanisms: (i) transmission of basal stresses from the flow on to the erodible bed (Hungr et al. 2005), possibly followed by (ii) shear resistance decrease in the erodible bed by development of excess pore pressures (Sassa 1985). Concerning the first, the flow can transmit two types of basal stresses onto the erodible bed: a basal shear stress acting on a surface parallel to the flow direction, and a ploughing stress, which in principle is a normal stress acting on a surface perpendicular to the flow direction. Analytical solutions and models have previously been derived considering the transmission of shear stresses at the base (Iverson 2012; Issler 2014), but not ploughing stresses. Iverson (2012) obtained a formulation to evaluate the entrainment rate for a two-layer model (Fig. 2a). The upper layer (in red) represents the flow and the lower layer (in yellow) represents the erodible bed, resting on a rigid base. A Cartesian coordinate system is oriented with the x-direction along the flow direction and the z-direction orthogonal to the base of

Published online: 02 May 2022

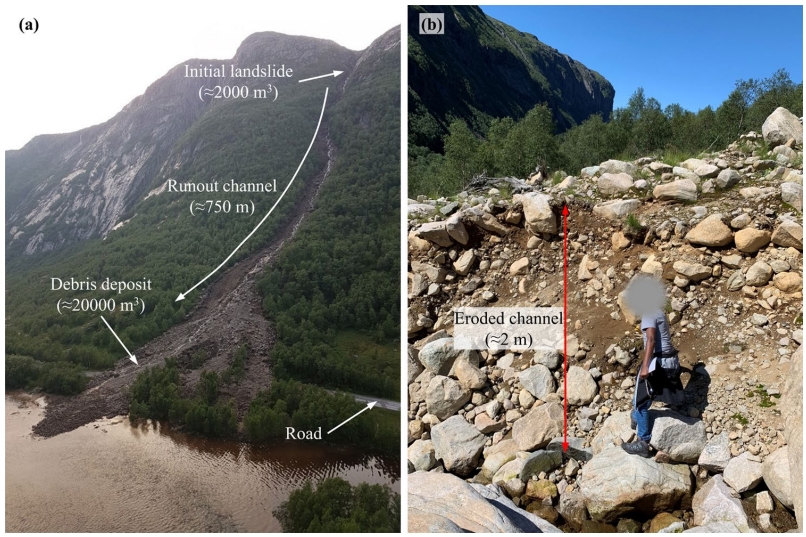

Fig. 1 Hunnedalen (Norway) debris flow on 2nd June 2016: (**a**) aerial photo after the event (courtesy: Multiconsult and Norwegian Public Roads Administration NPRA) (**b**) details of the eroded channel

the bed. A thin cross-hatched element of the bed with thickness Δz_b is about to be entrained in the flow. The stresses acting on the element are the upper contact shear stress from the debris flow onto the element (τ_{f-b}) while the bed resisting shear stress (τ_b) acts from below. This bed resisting shear stress can be modelled to decrease as a consequence of the development of excess pore pressures. By considering momentum conservation for the (cross-hatched) entrained bed layer (Fig. 2b), the entrainment rate can be expressed as:

$$E \cong \frac{\Delta z_b}{\Delta t} = \frac{\tau_{f-b} - \tau_b + \rho_b g \Delta z_b \sin\theta}{\rho_b v_f(z_b)} \quad (1)$$

where E is the entrainment rate, t is time, z_b is the distance from the rigid bed to the top of the boundary layer, ρ_b is the erodible bed density, θ is the slope angle, g is the acceleration due to gravity and $v_f(z_b)$ is the flow velocity at z_b. Compared to Iverson (2012) formulation, Eq. (1) also includes the slope-parallel gravitational term $\rho_b g \Delta z_b sin\theta$, to account for a finite thickness of the entrained bed layer Δz_b.

Equation (1) only models the shear stress (τ_{f-b}) acting on the planar x-parallel boundary of the entrained bed layer Δz_b, neglecting the ploughing basal stresses. On the other hand, three-dimensional models (hereon, this term is used to distinguish from depth-averaged models) can capture both basal shear stress and ploughing stress (Nikooei and Manzari 2020) and take complex and non-regular geometrical boundaries into account. In a three-dimensional model, the entrainment simply happens as a consequence of bed failure and the subsequent transport by flow. Bed failure needs to be controlled by an adequate constitutive model. For instance, Nikooei and Manzari (2020) considered an elasto-plastic behaviour with a Mohr–Coulomb criterion. In their study, however, a dry bed with constant friction was considered, which is quite inconsistent with the case of rainfall induced debris flows. A wet bed, instead, is expected to develop excess pore pressures as a consequence of the action of the debris flow (Sassa 1985; Hungr et al. 2005; Iverson et al. 2011; Iverson 2012), leading to strength reduction and ultimately to entrainment. Lee and Jeong (2018) and Lee et al. (2019) introduced a shear strength reduction law to

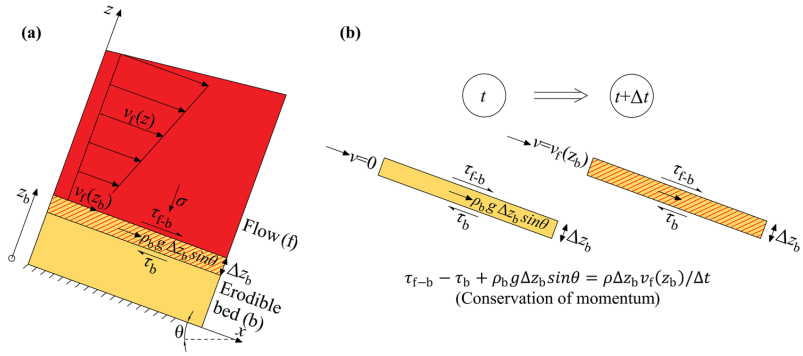

Fig. 2 Schematic of two-layer entrainment model: (**a**) vertical section of a debris flow travelling over an erodible bed (**b**) details of the entrained bed layer

allow the bed material to transform from a solid behaviour to a viscous one. Experiments carried out by Vicari et al. (2021a) pointed towards a frictional-type debris flow (Iverson 1997). An appropriate constitutive model to account for frictional shear strength reduction of the bed will therefore be introduced in this work to study the mechanisms leading to entrainment. The constitutive model is implemented into the generalized interpolation material point method (MPM) because of its ability to simulate large deformations, the coupled soil-structure interaction (e.g. impact on barriers) and the entrainment. The MPM was coded in the open-source Uintah computational framework. MPM in Uintah has previously been validated by simulations of penetration problems (Tran et al. 2017a), the quickness tests (Tran et al. 2017b), sensitive clay landslides (Tran and Sołowski 2019) and flow impact on rigid barrier (Seyedan and Solowski 2017) all compared with experimental results in laboratory or field. In this study, we model the debris flow experiments almost as a plane strain problem (a narrow 3D model to save computational cost) and the flexible barrier as a curved rigid barrier. A model to capture entrainment from a wet erodible bed is implemented in MPM inspired by field measurements of pore pressures and behaviouristic observations.

Physical and numerical model

Description of the large-scale flume tests

Large-scale flume experiments were conducted by Vicari et al. (2021a) to study the entrainment process by a debris flow and the impact on barriers. Figure 3 shows the 28-m-long flume (Ng et al. 2019) that was used to perform the two tests addressed herein with an initial volume of 6 m^3. The flume is 2 m wide and is delimited by two 1-m-tall lateral walls. The debris flow is released by mechanically opening the 1-m-tall door of the storage container, which is inclined at 30°. The debris can then flow over a 15-m-long channel, which is inclined at 20°. An upper 9-m-long fixed bed section ends in a very gentle wedge-shaped 2-m-long transition zone (denoted platform in Fig. 3a) which sends the flow on to the erodible bed. The wet, partly saturated erodible bed has a thickness of 120 mm and was prepared over the last 6 m of the 20° inclined channel. A steel grid provides high friction under the 120-mm erodible bed. An upper flexible barrier is installed 4.3 m from the release gate in one of two tests presented. The flowing mass is finally retained by a terminal flexible barrier, which is positioned at the end of a 4.4-m-long horizontal runout section. The debris material comprises 36% gravel, 61% sand and 3% fines and has a solid concentration of 70% by volume. The erodible bed comprises of 33% of fine gravel, 63% of sand and 4% fines and has an initial gravimetric water content of 15% in a loose state.

In each test, an ultrasonic sensor was mounted at location U1 (3.4 m from the gate) to measure the flow depth. An unmanned aerial vehicle was used to track the position of the flow front and calculate the frontal flow velocity. Furthermore, a load cell was installed at the base of the flume at U1 to simultaneously measure the flow basal normal stress and shear stress (Cell 1). Another load cell (Cell 2) was placed at the base of the flume at 12.5 m from the gate, measuring the normal stress and pore pressures under the erodible bed. Finally, a novel technique, called 'erosion columns', was developed to measure entrainment depths along the erodible bed section and distinguish them from deposition. Some key measurements of flow depth, flow velocity, entrainment depth, basal stress and pore pressure will be presented together with the calibration of the numerical model. The interested reader is referred to Vicari et al. (2021a) for additional information on the flume experiments.

Table 1 shows a summary of the two flume experiments each with an initial volume of 6 m^3. In the first experiment (V6-B1), the primary aim is to study the entrainment process, and therefore only a terminal barrier (height of 1.5 m) was installed at the end of the channel to stop and retain the debris flow. In the second test (V6-B2), an additional upstream flexible barrier (height of 0.6 m) was installed at 4.3 m from the gate in order to study the impact process on the flexible barrier for a well-defined flow, not disturbed by entrainment. The present work aims at back-calculating these two experiments using MPM, with a particular focus on interaction with the upstream barrier and on entrainment. First, measured flow in the upper section of the channel as well as the observed behaviour during impact is used to calibrate the parameters of the debris flow material in the MPM model. With these parameters locked the entrainment with no upstream barrier is then studied separately. During simulations of the entrainment, the focus is on identifying properties and parameters for the erodible bed.

Description of the MPM model

The material point method (MPM) based on continuum mechanics is well-suited to solve dynamic large deformation problems. Compared to the finite element method in which the integration points are fixed in the deformed mesh, the MPM allows the integration points, or namely material points, to move freely in the background mesh (Fig. 4). This provides the capability to model the large deformation of solid mechanics for history-dependent materials. Later, Bardenhagen and Kober (2004) proposed the generalized interpolation material point method (GIMP), which greatly improves the robustness and the accuracy of the original MPM. In this paper, GIMP version of material point method is used exclusively as coded in the open-source Uintah computational framework. All the numerical implementations can be found at the open-source platform GitHub (github.com/QuocAnh90/Uintah_NTNU) to replicate the numerical simulations in this paper.

To model the frictional-type debris flow of the flume tests (Vicari et al. 2021a), an elasto-plastic model, with a Mohr–Coulomb yield criterion, is selected both for the flowing debris material and erodible bed. In general, the Mohr–Coulomb criterion can be expressed as:

$$\tau = c + \left(\sigma - p_w\right) \tan \varphi' = c + \sigma(1 - \lambda) \tan \varphi' = c + \sigma \tan \varphi \qquad (2)$$

where τ is the shear stress, σ is the normal stress, p_w is the pore pressure, c is the cohesion, φ' is the effective friction angle and $\lambda = p_w/\sigma$ is defined as the pore pressure ratio (Iverson and Denlinger 2001). Stresses are positive in compression. φ is the apparent friction angle (Pirulli and Pastor 2012; Kwan et al. 2019) defined by Eq. (2) as:

$$\tan \varphi = (1 - \lambda) \tan \varphi' \qquad (3)$$

In the present work, the flow and erodible bed materials are modelled as one-phase materials, which corresponds to using apparent friction in Eq. (2). This implies that the apparent friction angle implicitly accounts for the effect of pore pressures, if $\lambda > 0$ is used. The one-phase approach is the state of the art for

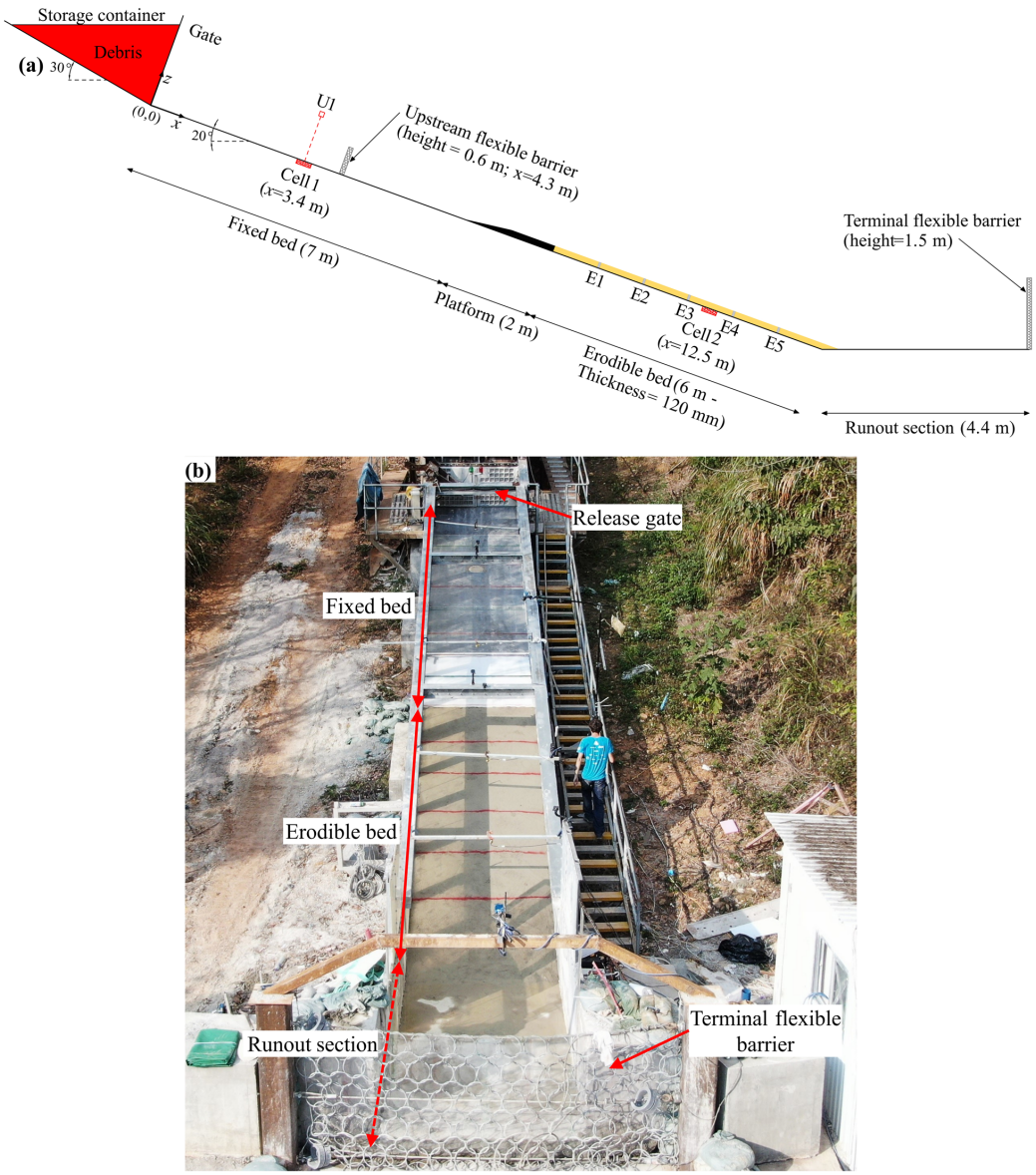

Fig. 3 Flume model: (**a**) cross-section with instrumentation layout (U refers to ultrasonic sensor; E refers to the erosion column; Cell 1 measures flow basal normal and shear stresses; and Cell 2 measures normal stress and pore pressure at the base of the bed) (**b**) aerial photo of the flume

debris flow numerical modelling (Kwan et al. 2015, 2019; Koo et al. 2018; Zhao et al. 2020; Lam and Wong 2021) and is the most commonly used in engineering practice (e.g. Frank et al. 2015). The dilatancy angle is set to zero in the simulations.

The yield criterion for the debris flow (f) material is expressed with the following notation:

$$\tau_f = c_f + \sigma \tan \varphi_f \quad (4)$$

where c_f is the internal cohesion and φ_f is the internal apparent friction angle of the flowing debris. Since the pore pressure evolution in the flow cannot be computed explicitly, φ_f needs to be calibrated to simulate the observed debris flow mobility (Koo et al. 2018; Zhao

Table 1 Test program, key flow characteristics and key parameters addressed by numerical modelling

Test ID	Barrier configuration	Flow characteristics and numerical modelling
V6-B1	Single flexible barrier (terminal)	• Measured flow depth and velocity on the fixed bed → back-calculation of the debris flow parameters • Measured entrainment → calibration of the entrainment model
V6-B2	Dual flexible barriers (upstream + terminal)	• Impact dynamics on the upstream barrier → back-calculation of the debris flow parameters

et al. 2020; Lam and Wong 2021) and impact kinematics with the barrier (Kwan et al. 2015, 2019; Lam and Wong 2021).

The contact shear stresses between the debris flow (f) and the flume base (b) are also modelled using Mohr–Coulomb's law:

$$\tau_{f-b} = \sigma \tan \varphi_{f-b} \tag{5}$$

where φ_{f-b} is the flow basal apparent friction angle between the debris flow and the flume base. The contact algorithm described by Bardenhagen et al. (2001) has been implemented to model the contact stresses. For simplicity, Eq. (5) is also pragmatically used to model the contact shear stress between the debris flow (f) and the erodible bed (b), where (b) then refers to bed rather than base. This simplification may be made since the yield criterion of erodible bed will control the behaviour if entrainment takes place during a slide.

The yield criterion of the erodible bed (b) is expressed as:

$$\tau_b = c_b + \sigma \tan \varphi_b \tag{6}$$

where c_b is the internal cohesion and φ_b is the internal apparent friction angle of the erodible bed. The bed pore pressures and therefore the apparent friction angle of the bed are expected to change in time in function of the shearing imposed by the debris flow (Iverson 2012). A softening model is used in this study (Fig. 5) to simulate the shear resistance reduction resulting from increase in pore pressures for increasing distortional strain (Iverson 2012; George and Iverson 2014). This is inspired by the field observations reported in Vicari et al. (2021a). Simplifying to plane strain and incompressible bed material, the increment of distortional strain in the bed can be expressed as:

$$\delta\varepsilon_d = \frac{1}{\sqrt{3}}\sqrt{4\delta\varepsilon_z^2 + \delta\gamma_{xz}^2} \tag{7}$$

where $\delta\varepsilon_z$ is the normal strain increment in the z-direction and $\delta\gamma_{xz}$ is the shear strain increment. The bed is initially considered to be in a solid state, with zero pore pressures: the effective friction angle (φ'_b) is therefore implemented, remaining constant until the accumulated distortional strain in the erodible bed reaches a threshold value defined by ε_{d0}. The friction coefficient is thereafter reduced linearly from an initial value tan φ'_b to a final value tan φ_{bR} (where φ_{bR} is the bed residual apparent friction angle). The residual value of φ_{bR} is reached at ε_{dR} and kept for distortional strains larger than ε_{dR}. The correspondent bed pore pressure ratio can be calculated according to Eq. (3) providing the red dashed line in Fig. 5. The bed pore pressure is zero for $\varepsilon_d < \varepsilon_{d0}$; it then increases linearly until ε_{dR} and remains constant at the final value $\lambda_{bR} = 1 - \frac{\tan\varphi_{bR}}{\tan\varphi'_b}$ for $\varepsilon_d > \varepsilon_{dR}$. By using this softening model, the erodible bed is therefore stable prior to the arrival of the debris flow, but it will yield and move significantly if the apparent friction angle of the bed becomes sufficiently low.

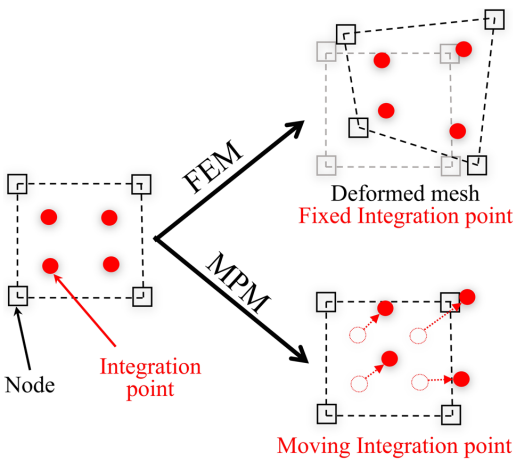

Fig. 4 Comparison of FEM and MPM methods

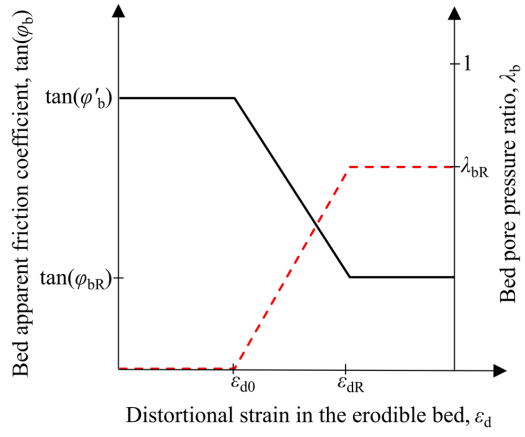

Fig. 5 Softening model for the erodible bed: bed apparent friction coefficient (solid black) and correspondent bed pore pressure ratio (dotted red)

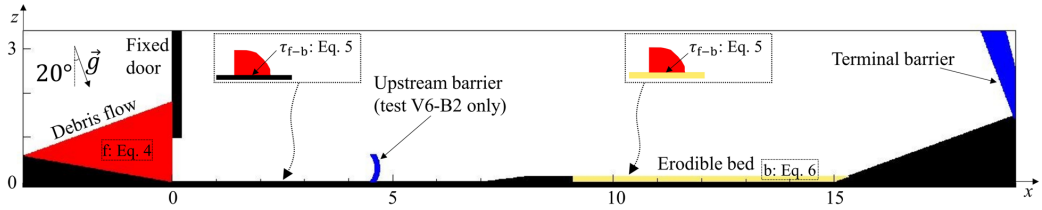

Fig. 6 Geometry of the model in MPM, materials and contacts (*f* refers to the debris flow material, *b* refers to the erodible bed, *f-b* refers to the base of the flow)

Calibration of the numerical model

Flume model, test setup and calibration procedure

Figure 6 shows the 2D model used for the simulations with MPM to simulate tests V6-B1 and V6-B2. The flume base is for convenience modelled as horizontal and therefore the gravity is tilted 20° to the vertical direction. We focus only on what happens along a longitudinal cross-section downward along the centreline of the real flume, i.e. in a way a plane strain problem is considered. The plane strain model is actually a narrow 3D model, made narrow to reduce the computational cost. The mesh size of 0.02 m in any direction is sufficiently low to guarantee the numerical convergence of the computations. This corresponds to the total number of the mesh elements equal to 192,033 and the total number of the material points is equal to 768,132. Numerical simulations have been performed using a high-performance computer (Sigma2 Betzy) using 8 nodes and a total of 1024 CPUs running in parallel. With these parameters, the simulation of 10 s of flow required about 7 h of computation time.

The numerical model is calibrated with regard to the observed flow behaviour, the impact dynamics on the upstream barrier and the entrainment. Table 2 shows a summary of the debris and bed parameters used for the calibration. The debris and bed materials, as defined by Eqs. (4), (5) and (6), are shown in Fig. 6. The calibration is performed in two steps: (i) the debris flow parameters (c_f, φ_f,φ_{f-b}) are calibrated based on measured data from the flume test and on the impact on the upstream flexible barrier; (ii) the erodible bed parameters (φ_{bR},ϵ_{d0},ϵ_{dR}) are calibrated to simulate the measured entrainment. The selection and discussion of the parameters values in Table 2 and detailed calibration results are provided in the next sections.

Table 2 Summary of the debris and bed material parameters

Material parameter	Value	Remarks
Debris flow (*f*)		
Flow density	2155 kg/m^3	Calculated from the debris mixture
Shear modulus	0.2 MPa	Calibrated, not influencing the results
Poisson's ratio	0.49	
Flow basal apparent friction, φ_{f-b}	9°	Measured in the experiments
Flow internal apparent friction, φ_f	15°	Calibrated
Flow internal cohesion, c_f	500 Pa	
Erodible bed (*b*)		
Bed density	1920 kg/m^3	Measured
Shear modulus	15 MPa	Typical value
Poisson's ratio	0.49	
Debris flow-erodible bed contact apparent friction, φ_{f-b}	9°	Measured in the experiments
Bed internal cohesion, c_b	100 Pa	Low value, fixed to avoid premature bed failure
Bed internal effective friction, φ'_b	42°	Measured through direct shear test
Bed internal residual apparent friction, φ_{bR}	22.5° (range: 6.5°–42°)	Calibrated
ϵ_{d0}	0.033 (range: 0.033–0.067)	
ϵ_{dR}	0.100 (range: 0.067–0.133)	

Modelling the debris flow behaviour

In this section, the debris material (*f*) parameters (Table 2) are discussed and calibrated. The flow density of 2155 kg/m^3 was calculated from the debris flow mixture used in the experiments. A low value of the elastic shear modulus (0.2 MPa) together with a Poisson's ratio of 0.49 was selected to consider the high-water content of the flow. These stiffness parameters were found to have a negligible influence on the flow behaviour, since the flow rapidly reaches large deformations, in which the plastic behaviour from the Mohr–Coulomb yield criterion dominates over the elastic behaviour.

The flow basal apparent friction angle (φ_{f-b}) was calculated and selected based on the measurements from Cell 1 of the basal normal (σ) and shear (τ_{f-b}) stresses in Test V6-B1, as shown in Fig. 7 (the flow depth is also shown for comparison with the normal stress). As the flow depth increases, the normal stress also increases almost proportionally. The flow basal shear stress is actually not directly proportional to the normal stress, as a result of different magnitudes of pore pressures along the flow (Vicari et al. 2021a). Correspondingly, the flow basal apparent friction angle from Eq. (5) (Fig. 8), φ_{f-b}, decreases in time from approximately 35° to 5°. The result is consistent with a typical distribution of pore pressures in a debris flow (Iverson et al. 2010). The debris flow front is unsaturated and carries lower pore pressures, which increases the basal shear resistance and therefore the apparent friction angle. The flow body behind the front is observed to be liquefied, and therefore carrying higher pore pressures, which results in a much lower basal shear stress and friction angle. From Fig. 8, the average value of the basal apparent friction angle versus time is calculated equal to 9°, which is the value assumed for the numerical simulations. The influence of choosing a constant friction angle in time will be discussed later.

The flow internal apparent friction angle (φ_f) and cohesion (c_f) are the two parameters that need to be calibrated to simulate the debris flow behaviour, in terms of velocity and flow depth (e.g. Koo et al. 2018; Zhao et al. 2020). Based on the sensitivity analysis, the parameters $c_f = 500Pa$ and $\varphi_f = 15°$ were selected as they provide a good agreement in terms of flow velocity. Figure 9 shows the measured frontal flow velocity in test V6-B1 compared to the computed one with the selected flow parameters from Table 2. The debris flow front is observed to accelerate over the fixed bed section because of the conversion of potential energy into kinetic energy. The measured debris flow front is then observed to decelerate at the beginning of the erodible bed area and to move steadily over the final part of the erodible bed. The deceleration may be due to the higher friction of the entrained bed material (we will discuss the calibration of the erodible bed parameters in more detail later). The numerical simulations can capture the trend and magnitude of the flow velocity well.

Figure 10 shows the comparison of the measured flow depth at 3.4 m from the gate (U1) with the simulation using the parameters in Table 2. The result from the numerical simulation differs from the measurement: the computed flow duration is longer, and the computed maximum flow depth of 0.3 m is lower compared to measured 0.4 m. All the simulations performed, changing the values of c_f, φ_f, φ_{f-b} and the stiffness parameters, did not have significant influence on the flow duration and on the maximum flow depth. The difference between simulated and measured flow depth may be due to modelling an instantaneous release of the debris flow, without considering a finite time for opening the gate (George and Iverson 2014). Furthermore, the assumption of a constant flow basal apparent friction may affect the debris flow duration. This will be addressed in the 'Discussion' section.

Modelling the debris flow impact kinematics on the upstream flexible barrier

Since a 2D model is used in this study to reduce the computational cost, an exhaustive model of the flexible barrier—i.e. considering the deformability of the cables and net (e.g. Leonardi et al. 2016; Kwan et al. 2019; Li et al. 2020; Zhao et al. 2020)—cannot be implemented. Instead, the upstream flexible barrier (test V6-B2)

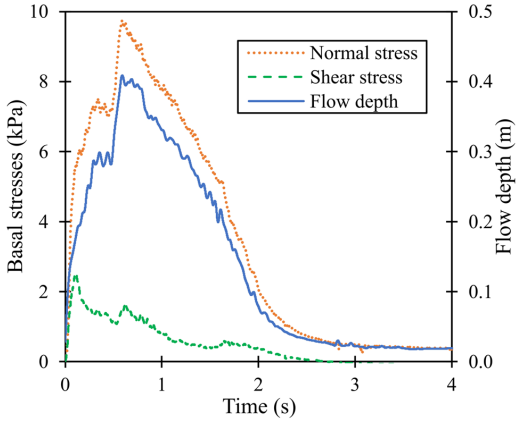

Fig. 7 Measured flow depth and basal shear and normal stress at 3.4 m from the gate for experiment V6-B1 (no upstream barrier)

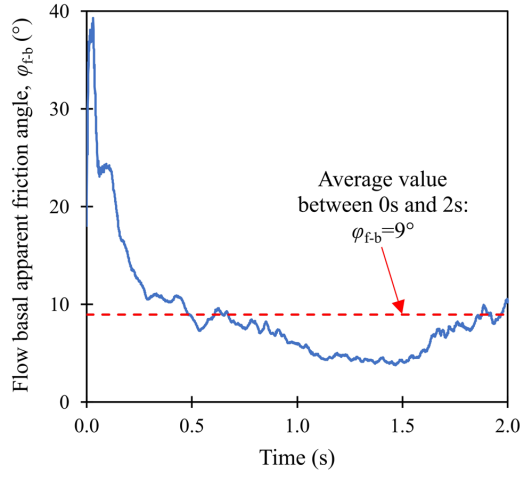

Fig. 8 Calculated flow basal apparent friction angle at 3.4 m from the gate for experiment V6-B1 (no upstream barrier) and the constant average value φ_{f-b} used in simulations

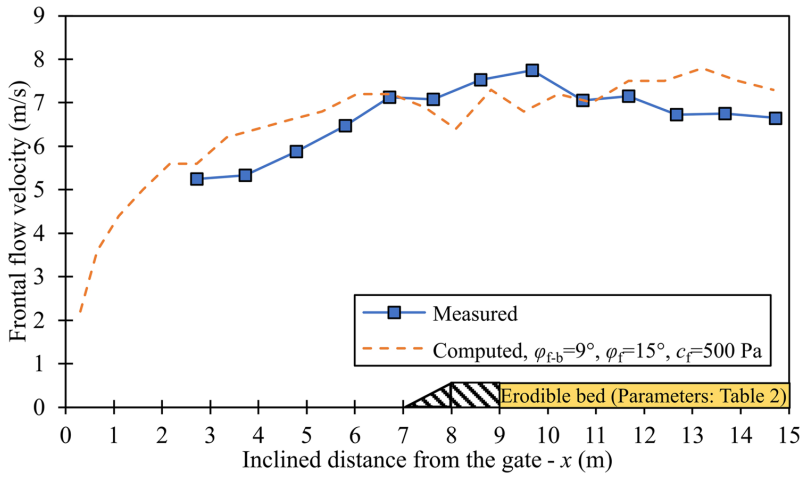

Fig. 9 Frontal flow velocity for test V6-B1 (no upstream barrier) and comparison with the numerical simulation

in this numerical study is simplified to a rigid constraint. However, to capture the fundamental effect of the deformability of a flexible barrier on flow redirection (Wendeler et al. 2019; Vicari et al. 2021a), the barrier is modelled with a curvature corresponding to its final deformed shape (deflection of 0.1 m, Fig. 6).

Figure 11a shows the impact run-up mechanism on the upstream flexible barrier observed in the experiment V6-B2, where a dead zone formed behind the barrier and the flow was redirected upwards reaching a maximum run-up height of 1.5 m orthogonal to the channel (Vicari et al. 2021a) (video from the experiment shown in Online Resource 1). Figure 11b shows the run-up mechanism for the numerical simulation using $c_f = 500Pa$ and $\varphi_f = 15°$ (video shown in Online Resource 2), while Fig. 11c shows the numerical simulation using $c_f = 500Pa$ and $\varphi_f = 30°$ (video shown in Online Resource 3). Both simulations exhibit a run-up mechanism which overpasses the barrier height. However, the maximum run-up height is significantly different: the simulation with $\varphi_f = 15°$ results in a run-up of 1.5 m, which is similar to that observed in the experiment, while the simulation with $\varphi_f = 30°$ underestimates the jet height (1.2 m). The frictional dissipation during the run-up happens on the surface indicated in Fig. 11b (dot red line), which separates the stationary debris material leaning towards the barrier (on the right, with almost nil velocity), namely the dead zone, to the debris material flowing upwards (on the left). Interestingly, the volume of the dead zone is higher for the simulation with $\varphi_f = 30°$ (Fig. 11c), which shows that frictional energy dissipation and velocity reduction are the factors limiting the run-up height, as also observed by Kwan et al. (2019).

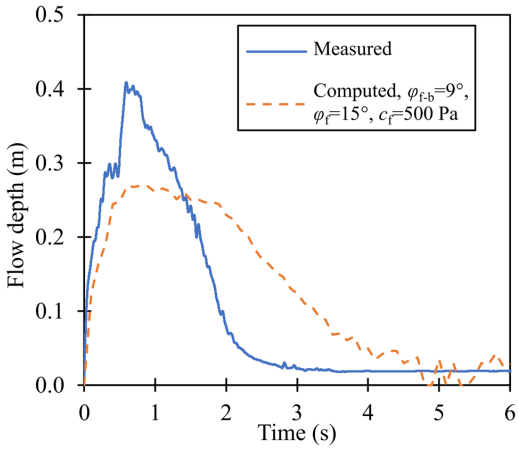

Fig. 10 Measured flow depth at 3.4 m from the gate for test V6-B1 (no upstream barrier) and comparison with the numerical simulation

For comparison, a simulation has also been performed using a straight rigid barrier (Fig. 11d) and the parameters $c_f = 500\ Pa$ and $\varphi_f = 15°$ (video shown in Online Resource 4). In this case, the rectilinear barrier cannot redirect the flow backwards as observed in the experiment and the run-up height is overestimated (1.9 m). Therefore, it can be concluded that the curved barrier implemented in the 2D model is a more satisfactory approximation of a flexible barrier to simulate the kinematics of the flow-barrier interaction. Such 2D model may be very useful to perform faster simulations compared to a 3D geometrical model. Furthermore, it can be observed that the curvature effect of a flexible barrier is a favourable feature to limit the run-up height and overflow.

Given the similarity between the numerical simulation of the impact mechanism with the observed one, $c_f = 500Pa, \varphi_f = 15°$ and $\varphi_{f-b} = 9°$ are considered to be the best-fit parameters to simulate the debris flow behaviour. The values are quite similar to the ones calibrated by Lam and Wong (2021) ($\varphi_f = 12°$ and $\varphi_{f-b} = 10°$) to simulate debris flows, with a slightly lower solid concentration of 60%, in the same flume model considered in this study. This similarity confirms the validity of our back-calculation for the flow behaviour and impact with the upstream barrier. Therefore, these calibrated debris flow parameters (Table 2) will be used consistently in the next sections, which focus on the calibration of the erodible bed parameters for the back-calculation of entrainment.

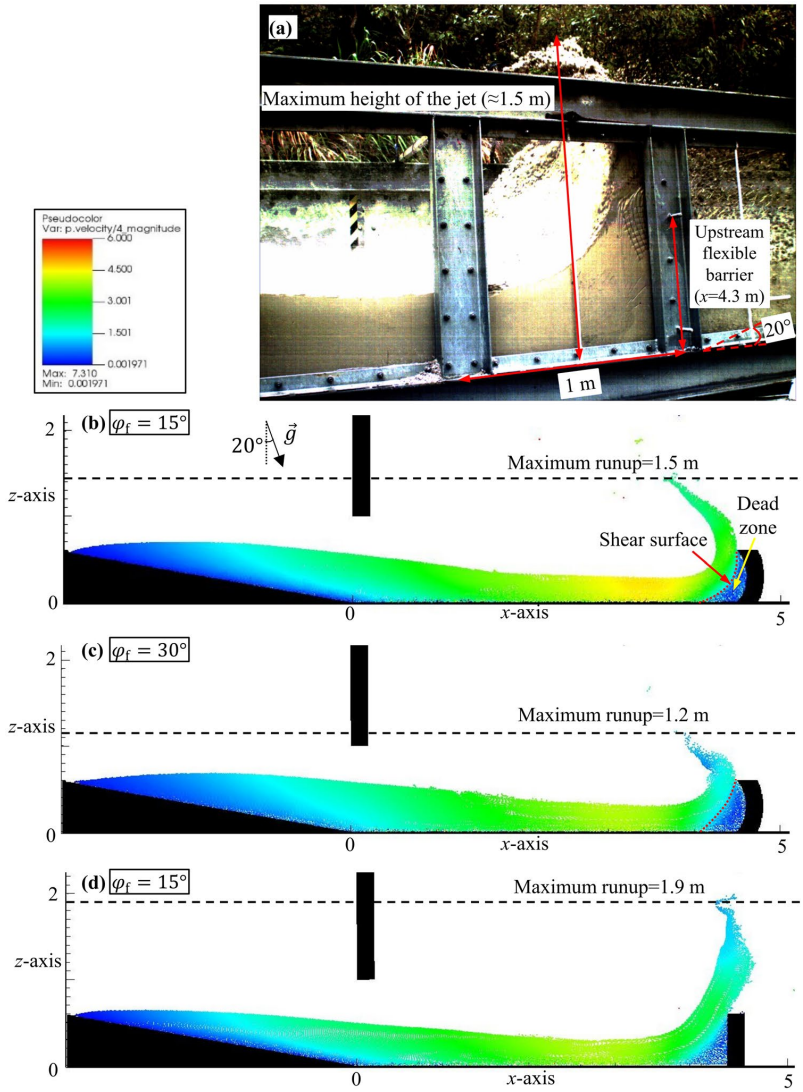

Fig. 11 Comparison of run-up mechanism on the upstream barrier in test V6-B2: (**a**) observed impact mechanism in test V6-B2 (with upstream barrier) (**b**) numerical simulation with $\varphi_f = 15°$ using a curved barrier (**c**) numerical simulation with $\varphi_f = 30°$ using a curved barrier (**d**) numerical simulation with $\varphi_f = 15°$ using a rectilinear barrier

Modelling the entrainment volume

In this section, the erodible bed material (b) parameters (Table 2) are back-calculated to simulate entrainment measured in test V6-B1 (no upstream barrier) (an aerial video from the experiment is shown in Online Resource 5). The bed density was calculated from the bed composition equal to 1920 kg/m^3. The elastic shear modulus is chosen equal to 15 MPa, corresponding to a moderately compacted, thin loose sand and gravel layer. The Poisson's ratio is chosen equal to 0.49 to model the fast entrainment phenomenon, which is likely to produce undrained conditions (Iverson et al. 2011). The contact apparent friction angle between the debris flow and the erodible bed (φ_{f-b}) is fixed to 9°, corresponding to the average estimate obtained from Cell 1 (Fig. 8). A low value of the bed cohesion (c_b) of 100 Pa is assigned to limit the bed deformation prior to entrainment. The internal apparent friction angle of the erodible bed (φ_b) is modelled according to the softening model presented in Fig. 5. Initially, the apparent friction angle is set equal to the bed effective friction angle of 42° (measured through direct shear test), which represents the partly saturated bed lacking positive pore pressures. As shearing of the bed occurs, the apparent friction angle is decreased to a final value of φ_{bR}. A parametric study is carried out to study the influence of φ_{bR}, ε_{d0} and ε_{dR} on the entrainment volume. The angle φ_{bR} is varied between 6.5° and 42°. The distortional strain ε_{d0} is varied between 0.033 and 0.067 and ε_{dR} between 0.067 and 0.133, which represent typical values (Lee et al. 2019).

Figure 12 shows the measured entrainment volume in test V6-B1 (0.9 m^3) and the results of the numerical simulations, with different values of φ_{bR}, ε_{d0} and ε_{dR}. The bed residual pore pressure ratio, λ_{bR}, is obtained from Eq. (3) and shown on the top horizontal axis. The entrainment volume increases for decreasing values of φ_{bR}, or equivalently for increasing values of λ_{bR}, which illustrates how bed shear strength reduction, due to pore pressure generation, increases entrainment (Iverson et al. 2011; Iverson 2012). It can also be observed that the entrainment volume is inversely proportional to ε_{d0} and ε_{dR}, which have a retarding effect on the onset of entrainment. However, the influence of ε_{d0} and ε_{dR} on the entrainment volume is lower compared to the parameter φ_{bR}.

The grid size affects the accuracy of the MPM simulations. Therefore, we performed a sensitivity analysis of the grid size presented in Fig. 12 (Fig. 13). The simulations with a grid size of 0.01 m compute a slightly smaller entrainment volume than the simulations with a grid size of 0.02 m. The minimum erodible thickness in a MPM simulation is equal to half the grid size, or one material point (cf. Figure 4). Therefore, in the simulations with the 0.02 m grid size, the entrainment of an additional 0.01-m-thick layer would result in a higher entrainment than the simulations with the 0.01-m grid size. In general, the simulations with a grid size of 0.02 m produced quite similar results compared to the simulations with a 0.01-m grid size. The back-calculated value of the bed residual apparent friction angle would be similar using the two grid sizes. A simulation with a grid size of 0.01 m required approximately 40 h of computation. Therefore, a grid size of 0.02 m was selected in this study for the sake of the computational cost. By using the 0.02-m grid size, the minimum erodible thickness (0.01 m) is still small compared to the high entrainment measured in test V6-B1. Li et al. (2021) showed that a 0.5 m grid size was sufficiently small to model in MPM a real snow avalanche event, where entrainment was neglected. However, if entrainment should also be modelled in MPM, the grid size should be sufficiently small compared to the expected entrainment depth in the field. Hence, a quite small grid size may be needed to simulate entrainment, even in real-scale debris flows, at the cost of very high computation time.

Using a grid size of 0.02 m, the set of parameters $\varphi_{bR} = 22.5°$, $\varepsilon_{d0} = 0.033$ and $\varepsilon_{dR} = 0.100$ provides the best fit with the measured entrainment volume (Fig. 12). The video of this numerical simulation is shown in Online Resource 6. The measured (test V6-B1) and computed spatial entrainment depth profiles are compared in Fig. 14. The measured entrainment depth is higher at the beginning of the erodible bed ($x < 11$ m) and it decreases downstream, which is probably due to the stability effect given by the soil wedge leaning on the horizontal runout section. Furthermore, the fixed height of the platform may have caused the flow to plough the erodible bed at $x < 11$ m, as shown by the video in Online Resource 7. The numerical simulation

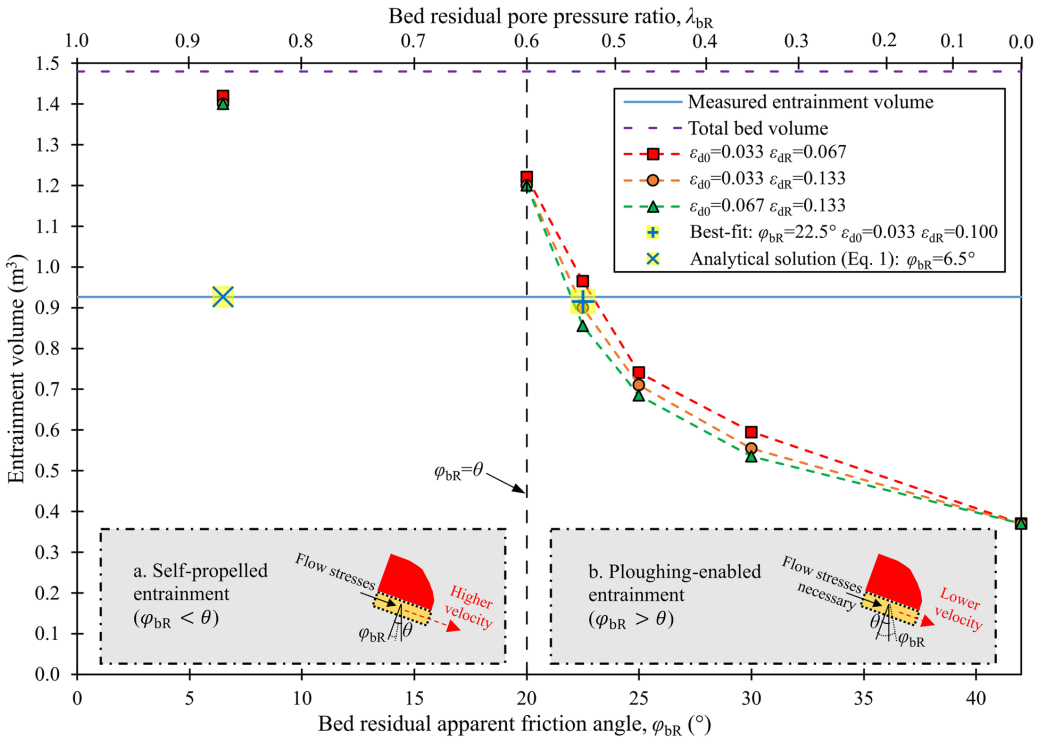

Fig. 12 Measured and computed entrainment volumes for test V6-B1 (no upstream barrier). See Fig. 5 for explanation of the parameters varied

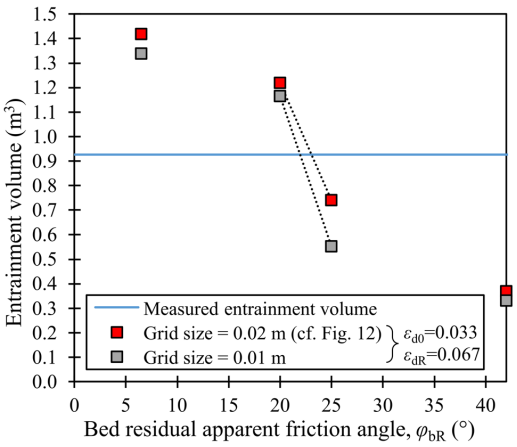

Fig. 13 Computed entrainment volumes for test V6-B1 using different grid sizes

can capture the spatial variations of entrainment depth and shows a good agreement with the experimental observation. The capability of the three-dimensional model used in this study to compute the internal mechanics and stability of the whole erodible bed is clearly an advantage compared to depth-averaged models, where entrainment would be calculated only based on the boundary shear stresses (cf. Eq. (1)).

Figure 15a shows a detail of the entrainment process for the simulation with the best-fit parameters. When the debris material flows over the erodible bed, it exerts a shear stress on the planar bed surface parallel to the x-axis. Since entrainment had already happened in some parts of the bed upstream, but less further down, the flow can also impact the bed by a normal stress in the direction of the x-axis. The entrainment process therefore is a combination of basal shear, on the planar surface parallel to the x-axis, and ploughing, roughly on the surface parallel to the z-axis. The stresses that are acting on the bed layer are exemplified in Fig. 15b. In addition to the shear stresses τ_{f-b} and τ_b discussed in Fig. 2, the flow transmits a normal stress σ_{f-b} (referred as ploughing stress) at the boundary between flow and bed on the surface parallel to the z-axis, while the normal stress σ_b is the reaction inside the erodible bed. The stress σ_{f-b} is a dynamic loading from the debris flow, while the stress σ_b is a passive static pressure. It can be expected that the resulting stress from σ_{f-b} and σ_b is positive in the x-direction, which increases the destabilizing effect on the erodible bed layer and erosion by ploughing may occur.

The existence of the additional ploughing stress by the debris flow implies that the back-calculated value of the bed residual apparent friction angle in MPM ($\varphi_{bR} = 22.5°$) is different compared to the back-calculation using the analytical solution which considers basal shear stress only (Eq. (1)). Indeed, Eq. (1) requires, for entrainment to happen, that the flow basal apparent friction angle (φ_{f-b}) from the flow on to the bed is higher than the bed residual apparent friction angle (φ_{bR}). The application of Eq. (1) would lead to $\varphi_{bR} = 6.5°$. However, we show that the entrainment volume computed in MPM with $\varphi_{bR} = 6.5°$ would be too high compared to the measured entrainment volume, because of the existence of the ploughing stresses. In general, the analytical solution of Eq. (1) (only basal shear τ_{f-b}) may still be valid when the topography of the bed remains approximately uniform and planar and therefore the ploughing stresses may be neglected. However, the three-dimensional MPM model, which also considers ploughing, becomes especially important if the topography of the bed changes significantly from the initial planar topography, as for example observed in the initial part of the erodible bed ($x < 11$ m).

Estimation of the pore pressures in the erodible bed

By using Eq. (3), the back-calculated bed residual apparent friction angle, $\varphi_{bR} = 22.5°$, corresponds to a pore pressure ratio $\lambda_{bR} = 0.5$ in correspondence of the evolving entrainment layer (approximately 0.01–0.02 m below the evolving upper surface of the erodible bed). Since this pore pressure ratio is higher than 0, it is suggested that the development of excess pore pressures at the bed-flow interface was a fundamental mechanism for entrainment to happen. In comparison, the simulation with $\varphi_{bR} = \varphi'_b = 42°$, i.e. without pore pressures generated in the bed ($\lambda_{bR} = 0$), shows a too low entrainment volume.

To gain more insights into the mechanisms of pore pressure development in the erodible bed, the measurements of the normal stress and pore pressure, in test V6-B1 at the base of the erodible bed (Cell 2), are shown in Fig. 16. Prior to entrainment ($t < 1$ s), the vertical normal stress is approximately 2.8 kPa, corresponding to the static weight of the erodible bed, while pore pressure is 0 kPa because the bed is initially unsaturated. When the debris material flows over the erodible bed, the normal stress increases to a maximum value of approximately 9 kPa and pore pressure increases to a maximum value of 1.5 kPa. The normal stress then decreases ($t > 4$ s) to 4.6 kPa, which is higher than the initial value of 2.8 kPa simply because significant debris material is deposited. Pore pressures remained approximately constant, which is likely due to limited dissipation in undrained conditions.

The bed pore pressure ratio λ_b at the base of the bed can be calculated as the ratio between the measured pore pressure and

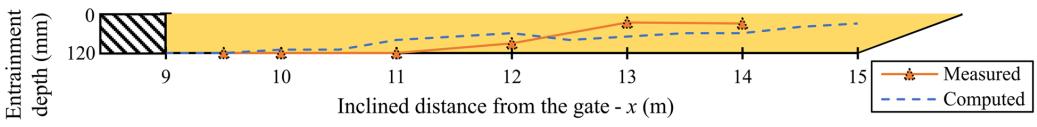

Fig. 14 Entrainment profile measured in test V6-B1 (no upstream barrier) and computed ($\varphi_{bR} = 22.5°$, $\varepsilon_{d0} = 0.033$ and $\varepsilon_{dR} = 0.100$)

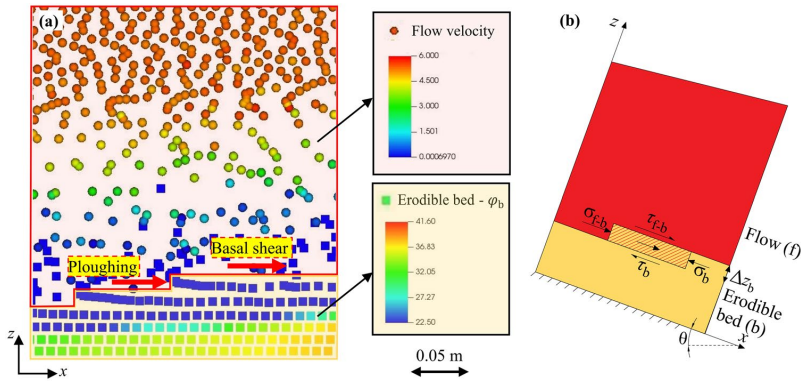

Fig. 15 Details of the entrainment process: (**a**) simulation with $\varphi_{bR} = 22.5°$, $\varepsilon_{d0} = 0.033$ and $\varepsilon_{dR} = 0.100$, observed at $x \approx 10$ m, 2 s after the flow front arrival (**b**) schematics of the eroded bed layer and stresses acting on it

the normal stress (Fig. 17). The ratio λ_b increases from 0 to a maximum value of 0.25 (continuous blue line). This implies that, at the base of the erodible bed, the soil material, which has not been entrained, develops a lower pore pressure ratio, without reaching the residual state ($\lambda_{bR} = 0.5$). This result may be understood considering the field observations from Mccoy et al. (2012) who only recorded an increase in pore pressure when the entrainment front was at a distance lower than 0.05 m from the pore pressure sensor. The limited transmission of pore pressures along the depth of the erodible bed shows that pore pressure generation in an initially unsaturated erodible bed may be mainly due to a shearing effect, which qualitatively confirms the validity of Fig. 5 to model pore pressure ratio increase as a function of the cumulated distortional strain.

Figure 17 also shows the computed λ_b using Eq. (3) at the base of the bed, for the numerical simulations with $\varphi_{bR} = 22.5°$ and for different combinations of ε_{d0} and ε_{dR}. λ_b is inversely proportional to ε_{d0} and ε_{dR}. Using $\varepsilon_{d0} = 0.067$ would even result in null pore pressures at the base of the bed. The best fit is obtained using $\varepsilon_{d0} = 0.033$ and $\varepsilon_{dR} = 0.100$. The parameters ε_{d0} and ε_{dR} of the proposed model therefore control how deep and how fast friction reduction (i.e. pore pressure increase) is transmitted into the erodible bed.

Discussion

Two entrainment behaviours

It appears from the numerical simulations and experimental observations that entrainment resulted from the following succession of mechanisms: (i) the debris flow overrides the erodible bed transmitting a basal shear stress (i.e. τ_{f-b}), which (ii) causes the development of excess pore pressures, which in turn (iii) lead to a shear

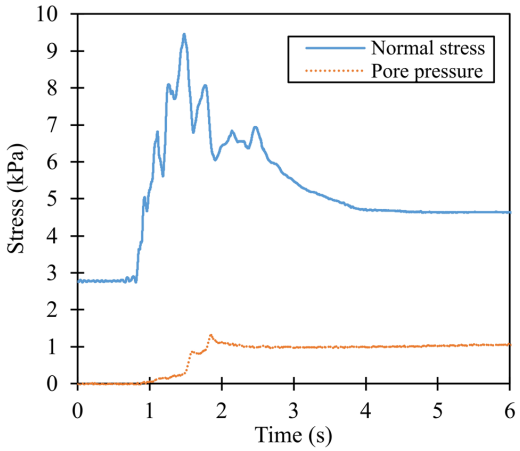

Fig. 16 Measured normal stress and pore pressure at the base of the erodible bed at 12.5 m downstream from the gate (Cell 2) for test V6-B1 (no upstream barrier)

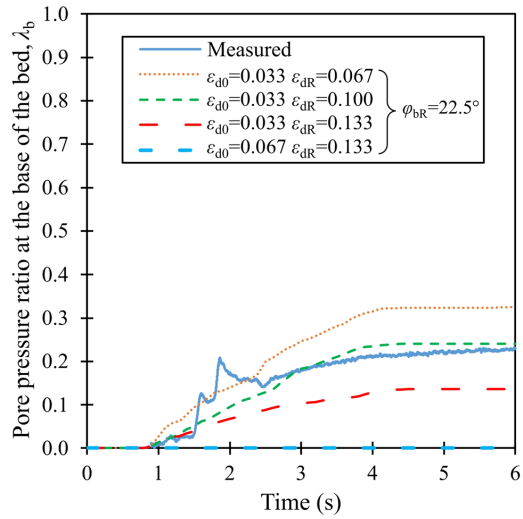

Fig. 17 Calculated and computed pore pressure ratio at the base of the erodible bed at 12.5 m downstream from the gate (Cell 2) for test V6-B1 (no upstream barrier)

strength (i.e. τ_b) reduction of the bed layer; (iv) at the same time, the debris flow exerts basal shear (τ_{f-b}) and ploughing stress (σ_{f-b}) on the bed which destabilize it and promote entrainment. In other words, entrainment is caused by a combination of stresses from the debris flow and bed shear strength reduction. Based on whether bed shear strength loss or transmission of flow basal stresses is dominant, it is reasonable to distinguish between two types of entrainment behaviours (Fig. 12):

(a) We suggest calling the first one a self-propelled entrainment. In this behaviour type, the strength reduction (event iii) dominates and the entrainment accelerates when the current apparent friction angle of the bed (φ_{bR}) is reduced to the slope angle (θ) or less. At this stage, the whole softened bed is unstable and moves downslope simply due to gravity. The movement is further accelerated by the contact stresses from the debris on top. The reduction in strength is considered to be an effect of pore pressure build up. This type of entrainment behaviour catches large volumes and causes a very fast motion, as observed in the case of very wet beds by Iverson et al. (2011).

(b) The second may be denoted ploughing-enabled entrainment. If the reduction of the bed shear strength (event iii) is less significant, a ploughing-enabled behaviour may dominate. In this case, the residual apparent friction angle of the bed is larger than the slope angle, $\varphi_{bR} > \theta$. The bed is then stable under gravity alone and entrainment can only happen if sufficiently high ploughing stresses are transmitted by the debris flow on to the bed below to destabilize it (event iv). Such ploughing-enabled entrainment has been reported for high values of the apparent friction angle of the bed. Entrainment is for instance observed experimentally in the case of dry beds which do not develop excess pore pressures (Mangeney et al. 2010; de Haas and van Woerkom 2016). This entrainment is definitely caused by the stresses from the debris flow. The high shear strength of the erodible bed leads to lower entrainment depths and lower velocities are observed for ploughing-enabled entrainment.

Some additional comments are appropriate regarding the curve in Fig. 12. In the ploughing-enabled entrainment zone of the plot, a small variation in the residual apparent bed friction, φ_{bR}, makes a huge difference in entrainment volume. The entrainment volume increases almost exponentially as the residual apparent bed friction approaches the slope angle θ. For a residual apparent bed friction less than the slope angle, the whole bed layer may become unstable (if sufficiently sheared by the debris flow). In the latter case, the entrainment volume is determined by how much volume passes into the residual state, which is controlled by the parameters ε_{d0} and ε_{dR}. If the entire bed liquifies by reaching the residual state, the volume in our test would be 1.48 m^3 (i.e. the total volume of bed material placed in the flume). We observe that we approach this limiting condition for low residual apparent friction.

Limitations of the one-phase model

A one-phase model has been used in this study to model the debris flow, and conventionally this implies that the flow apparent friction angle is constant, as the pore pressure ratio λ is assumed constant in time and space. This assumption is also made herein. However, debris flows are usually characterized by evolving magnitude of pore pressures, which has a significant influence on the basal friction, as shown in Fig. 8. The debris flow front is usually carrying lower pore pressures and is followed by a more liquefied body (McArdell et al. 2007; Iverson et al. 2010). The decreasing basal friction from the front to the tail of the flow may have an influence on the flow depth and velocity (Iverson 1997): a higher frictional resistance at the debris flow front may create a 'moving dam' pushed by the more liquefied flow body (Iverson et al. 2010). Therefore, the real debris flow duration is expected to be shorter compared to a debris flow with constant friction, since the tail of the flow can in reality move faster compared to the flow front. However, in the numerical simulations using a constant basal friction, the flow front and tail have the same basal resistance and therefore the flow duration is longer, and the maximum flow depth is smaller compared to the measurements (Fig. 10). In recent years, two-phase numerical models have been developed (e.g. George and Iverson 2014; Cuomo et al. 2021; Tayyebi et al. 2021), which allow to model the evolution of pore pressure in space and time and its effect on the flow mobility. Future developments of our MPM simulations should involve implementing a two-phase flow. By better capturing the pore pressure distribution in the flow, the flow dynamics (in terms of flow depth and velocity) could be improved.

It may be particularly important to use a two-phase model to simulate the flow interaction with the flexible barrier. Indeed, a flexible barrier may allow the fluid part to pass through the permeable mesh. At the same time, the permeability of the flexible barrier would impose a zero-pore pressure boundary condition on the static dead zone impounding against the flexible barrier, which could alter the run-up process. On the other hand, the airborne jet generated from the run-up may result in an increase in porosity (Cuomo et al. 2021), which could lead to a faster dissipation of excess pore pressures. The collision of the jet at landing may also cause a porosity increase and fast dissipation of excess pore pressures. Depending on which mechanism is dominant, either fluid passing through the mesh or dissipation of excess pore pressures during overflow, the debris flow downstream of the flexible barrier may be characterized by respectively lower or higher shear resistance than the original debris flow before impact on the barrier. For instance, in test V6-B2 (Vicari et al. 2021a), the debris flow was observed to significantly decelerate downstream of the flexible barrier, which is likely due to pore pressure dissipation. The one-phase model used in this study failed in modelling the flow behaviour downstream of the flexible barrier for test V6-B2: in this case, a two-phase model would be needed.

The pore pressure distribution within the debris flow may also affect the entrainment process. Lower pore pressures at the flow front followed by the more liquefied body may have consequences for entrainment. Indeed, the flow front may transmit higher shear stress to the erodible bed at the front, increasing entrainment, while the flow body and tail may transmit lower shear stress, with a reduced entrainment (Vicari et al. 2021a). On the other hand, regarding the erodible bed, despite being modelled as a one-phase material, the softening model introduced in Fig. 5 allows to mimic the evolution of pore pressures due to bed shearing. Thus, despite this model being semi-empirical and requiring the calibration of

the bed parameters, it allows to effectively simulate bed entrainment and to estimate the magnitude of the bed pore pressure ratio involved during the entrainment process.

Conclusions

The large-scale flume experiments by Vicari et al. (2021a) were back-calculated using a three-dimensional MPM numerical model to simulate the debris flow behaviour, impact on a flexible barrier and entrainment of a wet erodible bed. A narrow 3D longitudinal cross-section along the slope of the flume was modelled in the MPM, in order to reduce the computational time. The debris flow and bed were modelled as one-phase materials with an elasto-plastic model and a Mohr–Coulomb yield criterion. The apparent friction angle of the flow was calibrated to back-calculate the flow velocity and run-up impact dynamics on the upstream flexible barrier. We simplified the complexity of the flexible barrier to a rigid constraint, to be able to simulate the flexible barrier in a 2D geometrical model. The barrier is drawn with a curved shape, correspondent to the final curvature of the barrier. We observe that the run-up impact mechanism on the barrier can be well captured. We confirm that flexible barriers allow to reduce the run-up height compared to rigid rectilinear barriers, and that they may be beneficial to reduce the debris volume flowing downstream.

A softening model was implemented to model the friction reduction of the erodible bed, due to the increase in pore pressures, by coupling pore pressure increase to the distortional strain development. The introduced model is based on three parameters: the bed residual apparent friction angle, mainly controlling the total entrainment volume, and two thresholds for the distortional strain, which regulate the depth and speed of the pore pressure increase in the bed (or, equivalently, the shear strength reduction). We show that entrainment can happen because of bed shear strength reduction and due to the basal stresses transmitted by the flow. Our MPM model can account for both shear and ploughing basal stresses exerted by the debris flow on the erodible bed. In particular, the capability of MPM to also model the ploughing stresses, which have often been neglected in previous entrainment models, finally allows to explain why beds which are stronger than the flow can be entrained. The resulting entrainment behaviour for this type of flows and beds is referred as ploughing-enabled. This behaviour seems to be characterized by limited entrainment depths. On the other hand, if the bed pore pressure increase is high, the shear strength of the bed may become sufficiently low for the bed to fail under gravity alone. The additional shear and ploughing stresses transmitted by the debris flow then cause rapid and large entrainment. We suggest referring to this second behaviour as self-propelled entrainment.

The three-dimensional MPM model and the bed softening model introduced in this work were proved to be effective in simulating the debris flow entrainment. The introduced model may be particularly suited to analyse the complexity of natural debris flow events, where ploughing may especially occur for a non-uniform bed topography with concave and convex inflexions and varying geometry sideways. Furthermore, the boulders which are transported by the flow may in further MPM developments be incorporated to simulate how boulders may collide the bed and plough it. Finally, the three-dimensional model may allow to model secondary entrainment processes such as the instability of the channel banks. Depth-averaged models clearly cannot capture all these complex phenomena. A three-dimensional model is needed. The entrainment model introduced in this paper uses principles that have a potential towards a more holistic simulation of the entrainment process as seen in natural debris flow events.

Acknowledgements

The computations were performed on High-Performance Computing resources provided by UNINETT Sigma2 - the National Infrastructure for High-Performance Computing and Data Storage in Norway.

Funding

Open access funding provided by NTNU Norwegian University of Science and Technology (incl St. Olavs Hospital - Trondheim University Hospital). The authors of this paper would like to acknowledge Centre for Research Driven Innovation (CRI) KLIMA2050 and INTPART project 'Landslide mitigation of Urbanized Slopes for Sustainable Growth', funded by the Research Council of Norway. The author H. Vicari received support from the Centre for Research Driven Innovation (CRI) KLIMA2050 funded by the Research Council of Norway. The author Q. A. Tran received support from the European Union's Horizon 2020 research and innovation program under the grant agreement 101022007.

Code availability

Instructions for replicating the numerical results in this paper are given at the open-source platform GitHub (github.com/QuocAnh90/Uintah_NTNU). Also, the open-source code is shared in this platform for interested users to take up and make use of the results.

Declarations

Competing interests The authors declare no competing interests.

References

Bardenhagen SG, Guilkey JE, Roessig KM et al (2001) An improved contact algorithm for the material point method and application to stress propagation in granular material C. Comput Model Eng Sci 2:509–522. https://doi.org/10.3970/cmes.2001.002.509

Bardenhagen SG, Kober EM (2004) The generalized interpolation material point method C. Comput Model Eng Sci 5:477–495
Breien H, De Blasio FV, Elverhøi A, Høeg K (2008) Erosion and morphology of a debris flow caused by a glacial lake outburst flood, Western Norway. Landslides 5:271–80 https://doi.org/10.1007/s10346-008-0118-3
Cuomo S, Di Perna A, Martinelli M (2021) MPM hydro-mechanical modelling of flows impacting rigid walls. Can Geotech J
de Haas T, van Woerkom T (2016) Bed scour by debris flows: experimental investigation of effects of debris-flow composition. Earth Surf Process Landforms 41:1951–1966. https://doi.org/10.1002/esp.3963
Frank F, McArdell BW, Huggel C, Vieli A (2015) The importance of entrainment and bulking on debris flow runout modeling: examples from the Swiss Alps. Nat Hazards Earth Syst Sci 2569–2583. https://doi.org/10.5194/nhess-15-2569-2015
George DL, Iverson RM (2014) A depth-averaged debris-flow model that includes the effects of evolving dilatancy. II. Numerical predictions and experimental tests. Proceedings of The Royal Society A Mathematical Physical and Engineering Sciences 470. https://doi.org/10.1098/rspa.2013.0820
Hungr O, McDougall S, Bovis M (2005) Entrainment of material by debris flows. Debris-Flow Hazards Relat Phenom. https://doi.org/10.1007/3-540-27129-5_7
Issler D (2014) Dynamically consistent entrainment laws for depth-averaged avalanche models. J Fluid Mech 759:701–738
Iverson RM (1997) The physics of debris flows. Rev Geophys 35:245–296. https://doi.org/10.1029/97RG00426
Iverson RM (2012) Elementary theory of bed-sediment entrainment by debris flows and avalanches. J Geophys Res Earth Surf 117:1–17. https://doi.org/10.1029/2011JF002189
Iverson RM (2015) Scaling and design of landslide and debris-flow experiments. Geomorphology 244:9–20. https://doi.org/10.1016/j.geomorph.2015.02.033
Iverson RM, Denlinger RP (2001) Flow of variably fluidized granular masses across three-dimensional terrain 1. Coulomb Mixture Theory J Geophys Res 106:537–552
Iverson RM, Logan M, LaHusen RG, Berti M (2010) The perfect debris flow? Aggregated results from 28 large-scale experiments. J Geophys Res 115:F03005. https://doi.org/10.1029/2009JF001514
Iverson RM, Reid ME, Logan M et al (2011) Positive feedback and momentum growth during debris-flow entrainment of wet bed sediment. Nat Geosci 4:116–121. https://doi.org/10.1038/ngeo1040
Koo RCH, Kwan JSH, Lam C et al (2018) Back-analysis of geophysical flows using three-dimensional runout model. Can Geotech J 55:1081–1094. https://doi.org/10.1139/cgj-2016-0578
Kwan JSH, Koo RCH, Ng CWW (2015) Landslide mobility analysis for design of multiple debris-resisting barriers. Can Geotech J 52:1345–1359. https://doi.org/10.1139/cgj-2014-0152
Kwan JSH, Sze EHY, Lam C (2019) Finite element analysis for rockfall and debris flow mitigation works. Can Geotech J 56:1225–1250. https://doi.org/10.1139/cgj-2017-0628
Lam HWK, Wong AL (2021) Experimental and numerical study of dynamic soil debris impact load on reinforced concrete debris-resisting barriers. Landslides 18:955–966. https://doi.org/10.1007/s10346-020-01529-w
Lee K, Jeong S (2018) Large deformation FE analysis of a debris flow with entrainment of the soil layer. Comput Geotech 96:258–268. https://doi.org/10.1016/j.compgeo.2017.11.008
Lee K, Kim Y, Ko J, Jeong S (2019) A study on the debris flow-induced impact force on check dam with- and without-entrainment. Comput Geotech 113
Leonardi A, Wittel FK, Mendoza M et al (2016) Particle-Fluid-Structure Interaction for Debris Flow Impact on Flexible Barriers. Comput Civ Infrastruct Eng 31:323–333. https://doi.org/10.1111/mice.12165
Li X, Sovilla B, Jiang C, Gaume J (2021) Three-dimensional and real-scale modeling of flow regimes in dense snow avalanches. Landslides. https://doi.org/10.1007/s10346-021-01692-8
Li X, Zhao J, Kwan JSH (2020) Assessing debris flow impact on flexible ring net barrier: A coupled CFD-DEM study. Comput Geotech 128
Mangeney A, Roche O, Hungr O et al (2010) Erosion and mobility in granular collapse over sloping beds. J Geophys Res Earth Surf 115:1–21. https://doi.org/10.1029/2009JF001462
McArdell BW, Bartelt P, Kowalski J (2007) Field observations of basal forces and fluid pore pressure in a debris flow. Geophys Res Lett 34:2–5. https://doi.org/10.1029/2006GL029183
Mccoy SW, Kean JW, Coe JA et al (2012) Sediment entrainment by debris flows: In situ measurements from the headwaters of a steep catchment. J Geophys Res. https://doi.org/10.1029/2011JF002278
Medina V, Hürlimann M, Bateman A (2008) Application of FLATModel, a 2D finite volume code, to debris flows in the northeastern part of the Iberian Peninsula. Landslides 5:127–142. https://doi.org/10.1007/s10346-007-0102-3
Ng CWW, Choi CE, Majeed U et al (2019) Fundamental framework to design multiple rigid barriers for resisting debris flows. 16th Asian Regional Conference on Soil Mechanics and Geotechnical Engineering ARC pp. 1–11
Ng CWW, Wang C, Choi CE et al (2020) Effects of barrier deformability on load reduction and energy dissipation of granular flow impact. Comput Geotech. https://doi.org/10.1016/j.compgeo.2020.103445
Nikooei M, Manzari MT (2020) Studying effect of entrainment on dynamics of debris flows using numerical simulation. Comput Geosci 134. https://doi.org/10.1016/j.cageo.2019.104337
Pastor M, Blanc T, Haddad B et al (2014) Application of a SPH depth-integrated model to landslide run-out analysis. Landslides 11:793–812. https://doi.org/10.1007/s10346-014-0484-y
Pirulli M, Pastor M (2012) Numerical study on entrainment of bed material into rapid landslides. Géotechnique 62:959–972. https://doi.org/10.1680/geot.10.P.074
Sassa K (1985) The mechanism of debris flow. In: Proceedings of the 11th International Conference on Soil Mechanics and Foundation Engineering, San Francisco. pp 1173–1176
Seyedan S, Solowski WT (2017) Estimation of granular flow impact force on rigid wall using material point method. 5th International Conference on Particle-Based Methods - Fundamentals and Applications pp. 648–658
Solheim A, Strout JM, Piciullo L et al (2021) Reducing the risk from climate induced hazards to buildings and infrastructure; KLIMA 2050 - a centre for research-based innovation. In: 14th Congress Interpraevent pp. 1–3
Tayyebi SM, Pastor M, Stickle MM (2021) Two-phase SPH numerical study of pore-water pressure effect on debris flows mobility: Yu Tung debris flow. Comput Geotech 132
Tran Q-A, Solowski W, Karstunen M, Korkiala-Tanttu L (2017a) Modelling of fall-cone tests with strain-rate effects. In: Procedia Engineering
Tran QA, Sołowski W (2019) Generalized Interpolation Material Point Method modelling of large deformation problems including strain-rate effects – application to penetration and progressive failure problems. Comput Geotech 106:249–265. https://doi.org/10.1016/j.compgeo.2018.10.020
Tran QA, Solowski W, Thakur V, Karstunen M (2017b) Modelling of the quickness test of sensitive clays using the generalized interpolation material point method
Vicari H, Ng CWW, Nordal S et al (2021a) The effects of upstream flexible barrier on the debris flow entrainment and impact dynamics on a terminal barrier. Can Geotech J Just-IN:1–37. https://doi.org/10.1139/cgj-2021-0119
Vicari H, Nordal S, Thakur VKS (2021b) The significance of entrainment on debris flow modelling: the case of Hunnedalen, Norway. In: Challenges and Innovations in Geomechanics: Proceedings of the 16th International Conference of IACMAG
Wendeler C, Volkwein A, McArdell BW, Bartelt P (2019) Load model for designing flexible steel barriers for debris flow mitigation. Can Geotech J 56:893–910. https://doi.org/10.1139/cgj-2016-0157
Zhao L, He JW, Yu ZX et al (2020) Coupled numerical simulation of a flexible barrier impacted by debris flow with boulders in front. Landslides 17:2723–2736. https://doi.org/10.1007/s10346-020-01463-x

Supplementary information The online version contains supplementary material available at https://doi.org/10.1007/s10346-022-01886-8.

Hervé Vicari (✉) · **Quoc Anh Tran** · **Steinar Nordal** · **Vikas Thakur**
Department of Civil and Environmental Engineering, Norwegian University of Science and Technology (NTNU), Trondheim, Norway
Email: herve.vicari@ngi.no

5.3. Paper IV

Vicari, H., Tran, Q.A., Nordal, S., Thakur, V. 2021. MPM simulations of debris flow entrainment, modelling boulders explicitly. Submitted at the conference Geohazards 8 (Québec city).

This paper is not yet published and is therefore not included.

Chapter 6

6. Additional analysis and discussion on the flow behavior

UAV to record the debris flow

In this chapter, the flow dynamics over the fixed bed is analyzed in relation to *Paper II*. The significance of debris flow pore pressures on the flow mobility is discussed. A simple block-model to capture flow velocity is addressed. The flow behavior modelled in MPM (presented in *Paper III*) is further discussed in reference to the soil parameters. The limitations of the one-phase model approach are summarized.

6.1. Flow classification

To classify the type of flow behavior, the Savage and Friction numbers are calculated, according to Eqs. 2.1 and 2.4 respectively. The two dimensionless numbers are calculated at the two locations along the flume where flow depth and velocity are both measured, specifically L1 (x = 3.4 m) and L2 (x = 12.5 m). The values of the Savage and Friction numbers are shown in Table 6.1. The Savage number varies between 6×10^{-5} and 4×10^{-3}, which suggests frictional stresses to be dominant over collisional ones, as defined by the threshold of 0.1 reported by Savage and Hutter (1989). The Friction number varies between 8×10^{4} and 1×10^{6}, which is higher than the threshold for friction stresses to be dominant over viscous ones (1400 as defined by Iverson and LaHusen 1993). The flow behaviour is therefore idealized as frictional. The classification of the debris flow as frictional is supported qualitatively by the videos taken during the debris flow test (Supplementary file 1), where the flow is moving without significant mixing and collisions. The flow does not appear to be dilated. Hence, enduring frictional contacts between solid particles are plausible. Frictional behaviour is also typically observed in natural debris flows (Iverson and Denlinger 2001).

Some remarks on the calculated values of the Savage and Friction numbers are necessary:

- The pore pressure is assumed hydrostatic for the calculation of the frictional stresses in Eqs. 2.1 and 2.4. Higher pore pressures may however arise within the debris flow, which may cause higher value of N_{Sav} and lower value of N_{fric}. The pore pressure distribution at the base of the flow will be discussed in the next section.
- The shear rate $\dot{\gamma}$ is calculated using Eq. 2.3, which implies a combination of shear and basal slip. However, there is not enough experimental evidence to well constrain the values of the basal and surface flow velocities (Particle Image Velocimetry technique (e.g., Sanvitale and Bowman 2017) is not applicable due to the mud covering the soil particles). The

qualitative analysis of the experimental video (Supplementary file 1) and the results of the MPM analysis (discussed later) may point towards a lower value of $\dot{\gamma}$ compared to the calculation from Eq. 2.3, as the velocity may be nearly constant along the flow depth (plug flow). However, even assuming $\dot{\gamma} \to 0$ in Eqs. 2.1 and 2.4, the flow should be classified as frictional, as $N_{\mathrm{Sav}} \to 0$ and $N_{\mathrm{fric}} \to \infty$.

- (Sanvitale and Bowman 2017) showed that different values of the Savage number may be calculated for the different grain sizes in the debris flow mixture: the coarser grains of the mixture (higher δ) have higher values of N_{Sav}, while the finer grains (lower δ) have lower values of N_{Sav}. For the calculation of the Savage number of the experiments (*Paper II*), it is however preferred to calculate a unique average value of the Savage number for the whole mixture, using the average value of the grain size (δ =1 mm). Indeed, in the experiments, the soil was well graded. Therefore, coarse particles may collide with other coarse particles but also with finer particles surrounding them (Figure 2.2c). Nevertheless, the flow front may instead be dominated by coarser particles only, due to segregation.

Based on the above calculations and discussions of the Savage and Frictional numbers, the flow is assumed to be dominated by friction.

Table 6.1 Calculation of Savage and Friction numbers

Location	L1 - 3.4 m			L2 - 12.5 m		
Test ID	V2.5-B1	V6-B1	V6-B2	V2.5-B1	V6-B1	V6-B2
Flow depth (m)	0.2	0.4	0.4	0.1	0.3	0.3
Flow velocity (m/s)	4.9	5.3	5.0	5.7	6.8	6.0
Savage number*	4×10^{-4}	8×10^{-5}	6×10^{-5}	4×10^{-3}	3×10^{-4}	4×10^{-4}
Friction number*	3×10^{5}	9×10^{5}	1×10^{6}	8×10^{4}	5×10^{5}	4×10^{5}

*The following values of the material parameters were used: $C_{\mathrm{s}} = 0.7$, $\rho_{\mathrm{s}} = 2650\ \mathrm{kg/m^3}$, $\rho_{\mathrm{w}} = 1100\ \mathrm{kg/m^3}$, $\delta = 1\ mm$ (average grain size), $\mu' = 0.89$, $\eta_{\mathrm{w}} = 10^{-3}\ Pa \cdot s$. $\dot{\gamma}$ is calculated using Eq. 2.3

6.2. Measurement of the flow basal stresses

The development of pore pressures in a debris flow significantly affects the frictional shear resistance inside and at the base of the debris flow. In turn, the shear resistance may regulate the flow velocity, runout, entrainment processes and impact on the barriers. To gain more insights onto the flow dynamics, Cell 1 was placed at the base of the flume (3.4 m from the gate) to measure the flow basal normal (σ) and shear ($\tau_{\mathrm{f-b}}$) stresses. The measurement of these basal stresses (*Paper*

II) allows to quantify the pore pressure ratio at the base of the flow λ_{f-b}, or equivalently, the flow basal apparent friction angle φ_{f-b}. Indeed, by modelling the basal shear resistance with a Mohr-Coulomb model, the relationship between shear and normal stress can be expressed as follows:

$$\tau_{f-b} = (\sigma - p_w)tan\varphi' = \sigma(1 - \lambda_{f-b})tan\varphi' = \sigma tan\varphi_{f-b} \quad \textbf{6.1}$$

where φ' is the effective friction angle of the debris material and p_w is the pore pressure at the base of the flow.

The pore pressure ratio is a measure of the degree of liquefaction of the debris flow, since it is the ratio between the generated pore pressure and the normal stress. The apparent friction angle is directly influencing the mobility of the debris flow, as it reduces the shear resistance to account for the effect of pore pressures in a total-stress model (last member of Eq. 6.1). The two quantities are related through the following relationship, which is derived from Eq. 6.1:

$$tan\varphi_{f-b} = (1 - \lambda_{f-b})tan\varphi' \quad \textbf{6.2}$$

In *Paper II*, the interpretation for the flow mobility and entrainment was based on λ_{f-b} (Figure 6.1a). The average value in time of the flow basal pore pressure ratio is calculated as $\lambda_{f-b} = 0.82$. In *Paper III*, instead, the interpretation of the flow mobility was based on φ_{f-b} (Figure 6.1b). The average value in time of the flow basal apparent friction angle is calculated as $\varphi_{f-b} = 9°$.

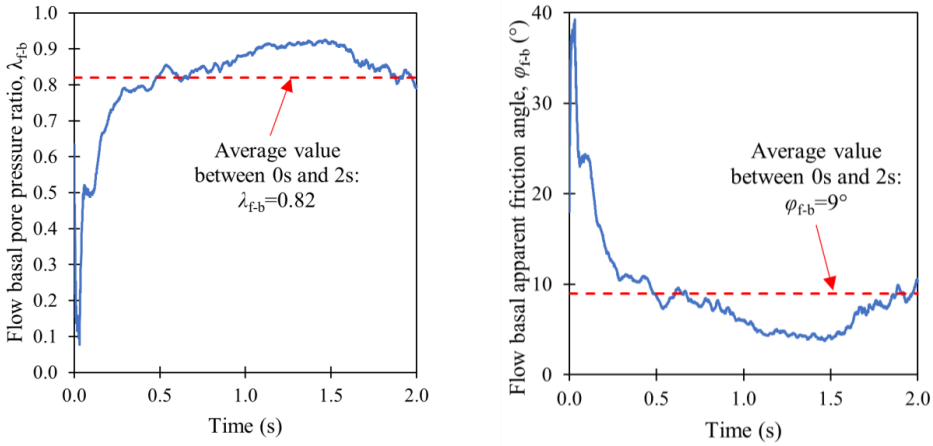

a **b**

Figure 6.1 (**a**) Flow basal pore pressure ratio; and (**b**) flow basal apparent friction calculated for test V6-B1 from the measurement of the flow basal stresses

High value of λ_{f-b}, close to 1, is observed, which indicates a significant degree of liquefaction of the debris flow. Pore pressure generation within the debris flow may be particularly significant at the onset of motion, just after opening the gate (George and Iverson 2014). Indeed, the change in shape of the debris flow during release may induce initially high shear rates, therefore causing pore pressure increase within the contractive debris flow material. The initial excess pore pressures may have persisted in time after debris flow initiation. To attempt to quantify the persistence of excess pore pressures, the pore pressure number N_P can be calculated according to Eq. 2.5. The following values of the flow parameters are used: $L = 20\,m$; $h_f = 0.3\,m$. The flow material parameters are more uncertain, as they may vary during the flow compared to a static case. A range of parameters is used for the calculation in Eq. 2.5, which may be representative for loose well graded sand: D_f between $1\ MPa$ and $20\ MPa$; k_f between $10^{-12}\ m^2$ and $10^{-10}\ m^2$; η_w between $10^{-3}\ Pa \cdot s$ and $5 \cdot 10^{-3}\ Pa \cdot s$. Using these values, the pore pressure number is calculated to possibly belong to a wide range, between 0.003 and 32. The lower limit would suggest that excess pore pressure persisted during all the flow duration, while the upper limit would indicate quicker dissipation of excess pore pressures. Figure 6.2a shows the debris flow deposit just 2 minutes after the test, while Figure 6.2b shows the same deposit 37 minutes after the test. In Figure 6.2b, unlike in Figure 6.2a, free excess water is observed to have leaked towards the surface of the debris deposit. This observation may suggest a slow diffusion process (consolidation) leading to the dissipation of the excess pore pressures. Therefore, it may be reasonable to hypothesize persistence of excess pore pressures during all the flow duration.

Furthermore, Eq. 2.5 shows that N_P strongly depends on the flow depth. During the debris flow motion, the flow front is thinner and therefore pore pressures may dissipate quickly, which would correspond to a higher value of N_P; the flow body is instead thicker and therefore N_P is lower. Faster pore pressure dissipation at the flow front is evident from Figure 6.1a, where the flow basal pore pressure ratio is lower at the beginning of the flow (correspondent to the flow front), while it increases afterwards (in the flow body). Furthermore, the creation of a coarser flow front, due to grain size segregation, may increase the debris permeability and therefore may accelerate the dissipation of excess pore pressures. The flow front is therefore characterized by higher frictional resistance (Figure 6.1b) because it is carrying lower pore pressures.

Figure 6.2 Photos of the deposit on the horizontal runout section, after test V2.5-B1: (a) approximately 2 minutes after the test; (b) approximately 37 minutes after the test. The red dot in the two figures is a reference drawn at the same location

6.3. A variable-friction two-blocks model

To improve the understanding of the influence of the variable basal friction on the flow dynamics, it is useful to analyse the distribution of the basal friction along the flow mass. The measurement of the flow depth at L1 (i.e., at the same location of Cell 1, where the flow basal stresses are measured) is shown in Figure 6.3a. Therefore, the cumulated volume which has flown at section L1 from time *t=0 s* (time of flow front arrival) to a generic time *t* can be calculated as:

$$V_{\mathrm{f}}(t) = W \int_0^t h_{\mathrm{f}}(t)\overline{v}_{\mathrm{f}}(t)dt \qquad \textbf{6.3}$$

where W is the width of the flume (the hypothesis that the flow depth is constant along a cross-section of the flume is made); $h_{\mathrm{f}}(t)$ is the flow depth at time t; $\overline{v}_{\mathrm{f}}(t)$ is the depth-averaged flow velocity of the column $h_{\mathrm{f}}(t)$. If we introduce the hypothesis that $\overline{v}_{\mathrm{f}}(t)$ is time independent (i.e.

constant along the longitudinal length of the flowing mass), the cumulated flow volume can be simplified as:

$$V_{\mathrm{f}}(t) = W\overline{v}_{\mathrm{f}}\int_0^t h_{\mathrm{f}}(t)\,dt \qquad \textbf{6.4}$$

where $\overline{v}_{\mathrm{f}}$ is taken equal to the measured frontal flow velocity at L1 (5.3 m/s, Figure 6 in *Paper II*). Under this hypothesis, $V_{\mathrm{f}}(t)$ can be easily calculated, as shown in Figure 6.3b. Interestingly, at the end of the flow (*t=2 s*), the calculated cumulated flow volume is equal to 5.6 m^3, which is very similar to the total volume used in the test (6 m^3). This implies that the assumption of a constant flow velocity $\overline{v}_{\mathrm{f}}$, along the length of the debris flow, may be regarded as approximately valid. Nevertheless, a thin debris flow layer at the tail of the debris flow (*t>2* s) appeared to flow at a lower velocity compared to the flow front and body.

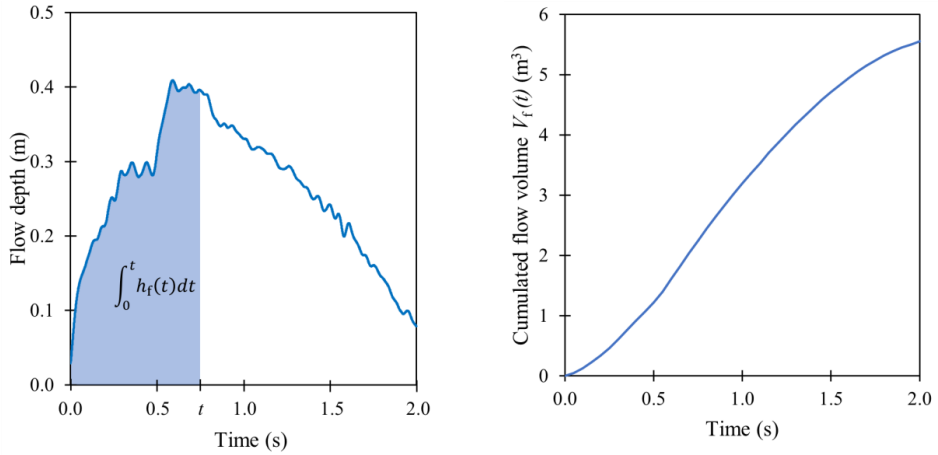

a **b**

Figure 6.3 (**a**) Flow depth measurement for test V6-B1 at L1 (x=3.4 m) and (**b**) cumulated flow volume

A constant velocity for both the flow front and body may appear contradictory with the experimental observation from Figure 6.1b, where the flow front has higher basal friction than the flow body and would therefore be expected to travel slower than the body. However, this contradiction can be explained by idealizing the flow mass as the combination of two deformable blocks, as shown in Figure 6.4. The flow front (indicated as V_1) represents the high frictional initial

part of the debris flow (here assumed for *t<0.25 s*). It has a volume V_1=0.5 m^3 (obtained from Eq. 6.4, with *t=0.25 s*) and an average basal apparent friction angle: $\bar{\varphi}_1 = 22°$. The flow body (V_2) represents the low friction body of the debris flow (*0.25 s<t<2 s*), with an approximate volume V_2=5.1 m^3 and an average basal apparent friction angle: $\bar{\varphi}_1 = 7°$. The forces acting on each of these blocks are exemplified in Figure 6.4b,c: $G_{1,2} = \rho_f V_{1,2} g sin\theta$ is the gravitational force in the slope-parallel direction; $T_{1,2} = \rho_f V_{1,2} g cos\theta tan\bar{\varphi}_{1,2}$ is the basal frictional resistance; $P_{1,2} = \pm\frac{1}{2} K \rho_f g h_f^2 cos\theta W$ is the earth pressure force which is exerted between the bodies 1 and 2 (where K is the earth pressure coefficient; h_f is the flow depth taken at *t=0.25 s*). Therefore, the equation of motion for bodies 1 and 2 can be expressed as:

$$\frac{dv_1}{dt} = gsin\theta - gcos\theta tan\bar{\varphi}_1 + \frac{1}{2}\frac{K g h_f^2 cos\theta W}{V_1} \quad \textbf{6.5}$$

$$\frac{dv_2}{dt} = gsin\theta - gcos\theta tan\bar{\varphi}_2 - \frac{1}{2}\frac{K g h_f^2 cos\theta W}{V_2} \quad \textbf{6.6}$$

Recalling the observation that the flow velocity can be assumed constant along the flowing mass, i.e., $v_1 = v_2 = \bar{v}_f$ and therefore $\frac{dv_1}{dt} = \frac{dv_2}{dt}$, Eqs. 6.5 and 6.6 combine as:

$$tan\bar{\varphi}_1 = tan\bar{\varphi}_2 + \frac{1}{2} K h_f^2 W \left(\frac{1}{V_1} + \frac{1}{V_2}\right) \quad \textbf{6.7}$$

Eq. 6.7 results in the inequality: $tan\bar{\varphi}_1 > tan\bar{\varphi}_2$. This implies that, in order to have a constant flow velocity along the flow extent, the flow front (V_1) must have a higher basal friction than the flow body (V_2). Instead, if the flow front and the flow body had the same basal friction ($\bar{\varphi}_1 = \bar{\varphi}_2 = \bar{\varphi}_{f-b} = 9°$), then the flow front would move faster compared to the flow body (cf. Eqs. 6.5 and 6.6) and the flow would spread more longitudinally, implying that the maximum flow depth would be smaller compared to the maximum one observed in the experiment ($h_f = 0.4\ m$). This explains the reason why the MPM model (*Paper III*), where a constant basal friction ($\bar{\varphi}_{f-b} = 9°$) is used, computes a lower flow depth compared to the experimental observation (Figure 6.5).

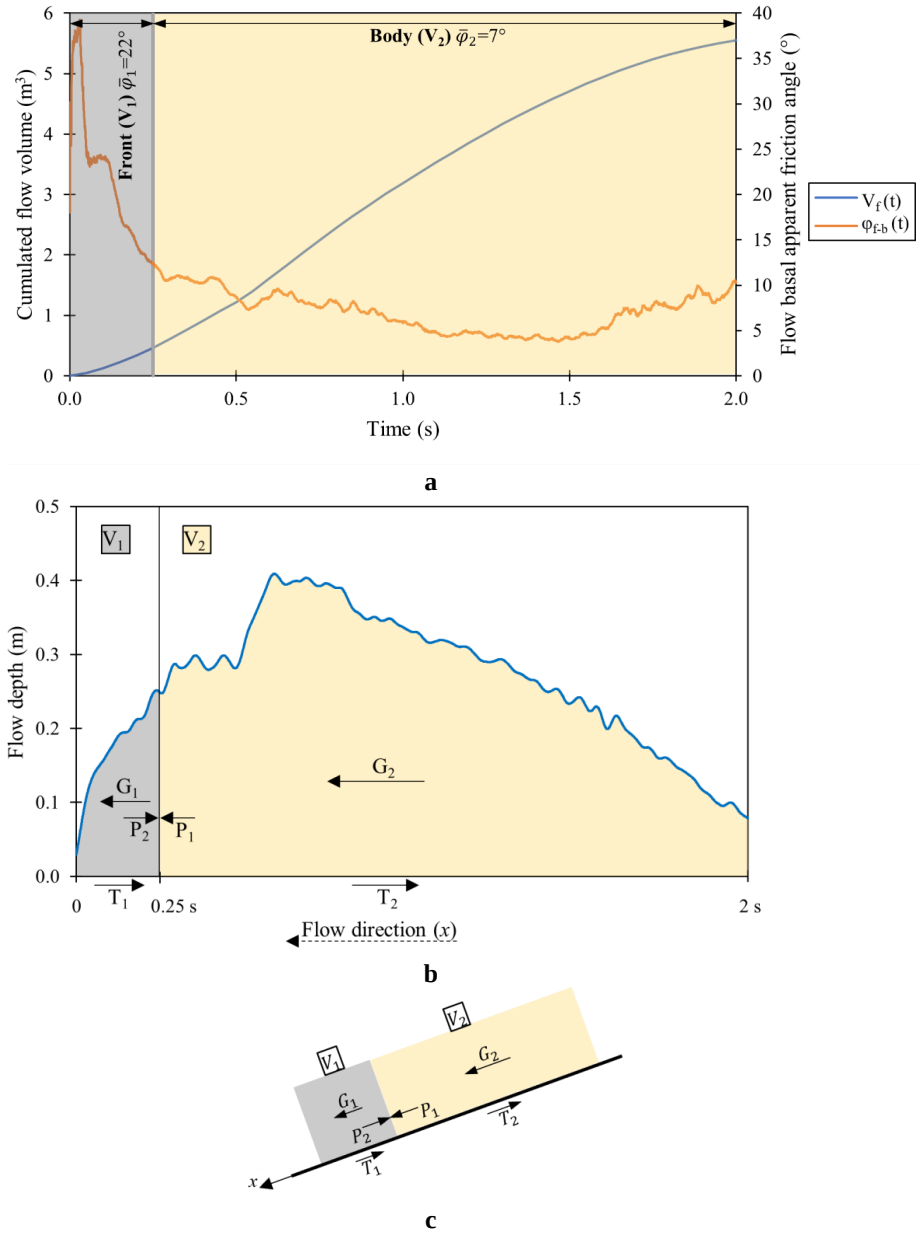

Figure 6.4 Two-blocks (front-body) model with variable friction: (**a**) calculation of volumes V_1 and V_2 and basal frictions $\bar{\varphi}_1$ and $\bar{\varphi}_2$; (**b**) forces acting on the two blocks; (**c**) sketch of the two blocks

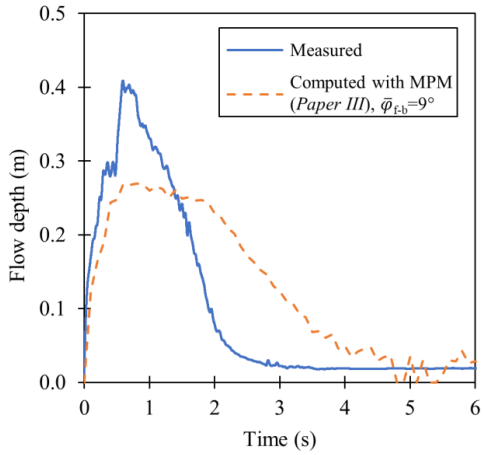

Figure 6.5 Comparison of the flow depth measured in test V6-B1 at L1 with the flow depth computed with MPM using $\bar{\varphi}_{f-b}$=9° (Result from *Paper III*)

6.4. The block model on the fixed bed

Flow velocity is among the most important parameters in debris flow dynamics, as it is directly related to the runout distance and to impact forces and run-up on obstacles, such as terminal walls, barriers and buildings. The flow velocity is related to the conversion of the potential energy of the initial landslide mass into kinetic energy, as the mass is flowing to lower elevations. This conversion of energies is however limited by frictional energy dissipation within the flow. The simplest model to capture the evolution of the flow velocity is a block flowing along a fixed bed (Figure 6.6). The momentum conservation for the block with mass *m* and moving at a velocity *v* can be expressed as follows:

$$m\frac{\Delta v}{\Delta t} = G - T_{\mathrm{f-b}} \qquad \textbf{6.8}$$

where G is the gravitational force in the slope direction:

$$G = mgsin\theta \qquad \textbf{6.9}$$

and $T_{\mathrm{f-b}}$ is the block basal frictional force:

$$T_{\mathrm{f-b}} = mgcos\theta tan\varphi_{\mathrm{f-b}} \qquad \textbf{6.10}$$

As the spatial variations of the flow basal apparent friction angle cannot be captured by a simple block model, the average value of φ_{f-b} must be used. By inserting Eqs. 6.9 and 6.10 into Eq. 6.8, the evolution of the velocity of the block can be expressed as:

$$v\frac{\Delta v}{\Delta x} = g(sin\theta - cos\theta tan\varphi_{f-b}) \qquad \textbf{6.11}$$

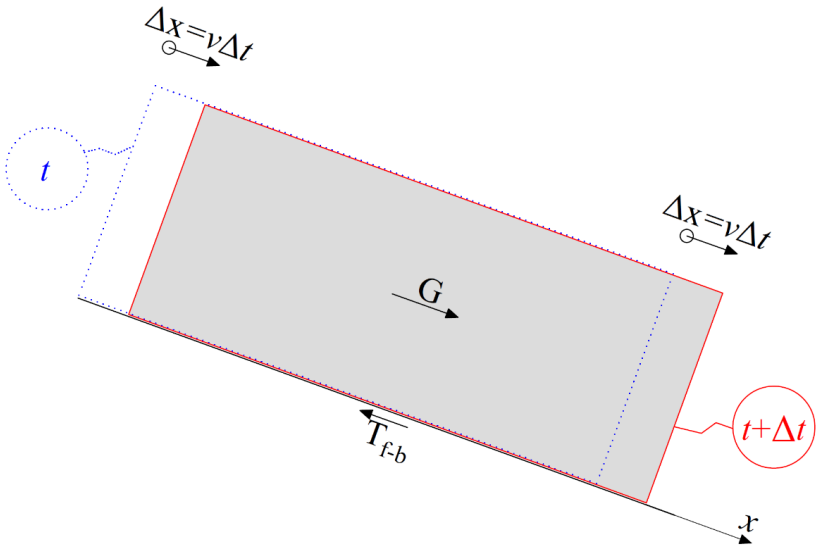

Figure 6.6 Frictional rigid block model moving on a fixed bed

Eq. 6.11 is valid when the height of the block is not varying significantly in time and therefore not affecting the potential energy of the block. However, in the experiments modelled in this study, the release volume is located at a higher elevation (Figure 1a in *Paper II*) from the fixed base of the channel; as the gate is opened, the initial volume then deforms, acquiring a lower flow depth. Therefore, to derive the evolution of the block flow velocity along the channel, it is more convenient to consider the conservation of energy of the block (Figure 6.7). The reference system for the specific energy (energy per unity of weight) (ε=0) is set in correspondence of the center of mass of the block when it is at a certain position x along the channel. In this reference system, the initial specific energy of the debris flow, before starting the experiment (i.e., at x=0 m), corresponds to the specific potential energy only:

$$\varepsilon_0 = \varepsilon(x=0) = xsin\theta - \frac{\bar{h}_f}{2}cos\theta + h_0 \quad \textbf{6.12}$$

The specific energy of the block, at a certain position *x* along the channel, is given by its specific potential energy (null, for the chosen reference system) and specific kinetic energy:

$$\varepsilon(x) = \frac{\bar{v}_f^{\,2}}{2g} \quad \textbf{6.13}$$

As the material flows for a certain distance *x*, energy is dissipated by basal friction:

$$\Delta\varepsilon(x) = \varepsilon_0 - \varepsilon(x) = \int_0^x cos\theta \cdot tan\varphi_{f-b}\, dx = cos\theta \cdot tan\varphi_{f-b} \cdot x \quad \textbf{6.14}$$

Therefore, by inserting Eqs. 6.12 and 6.13 into 6.14, the flow velocity at *x* can be derived as:

$$v(x) = \sqrt{2g\left(\varepsilon_0 - \Delta\varepsilon(x)\right)} = \sqrt{2g\left(xsin\theta + h_0 - \frac{\bar{h}_f}{2}cos\theta - xcos\theta tan\varphi_{f-b}\right)} \quad \textbf{6.15}$$

If $\Delta\varepsilon = 0$, Eq. 6.15 would be equivalent to $v(x) = \sqrt{2g\varepsilon_0}$, which expresses the free fall velocity of a frictionless debris flow. Velocity is however limited by frictional energy dissipation, through the term $\Delta\varepsilon$. Notice that Eq. 6.15 is similar to Eq. 3 in *Paper II*, which however neglected the specific potential energy of the flow (from the base of the flume) at position *x* (i.e., the term $\frac{\bar{h}_f}{2}cos\theta$).

Figure 6.8 shows the measured flow velocity for test V6-B1. The theoretical velocity profile for a rigid block is also calculated according to Eq. 6.15. In the equation, the average flow height is calculated as: $\bar{h}_f = \frac{1}{t_{DF}}\int_0^{t_{DF}} h_f(t)dt$, which is equal to 0.26 m (from the flow depth measurement at L1). Two reference lines are shown in the plot: the velocity of the frictionless block is calculated using $\varphi_{f-b} = 0°$; the velocity of the frictional block is calculated using $\bar{\varphi}_{f-b} = 9°$, which corresponds to the average value in time of the measured flow basal apparent friction angle. The frictional block model provides an accurate prediction of the measured flow velocity along the fixed bed section (x<9 m) but gives a poor estimation of the velocity along the erodible bed. The block model will be extended to the entrainment case in the next chapter.

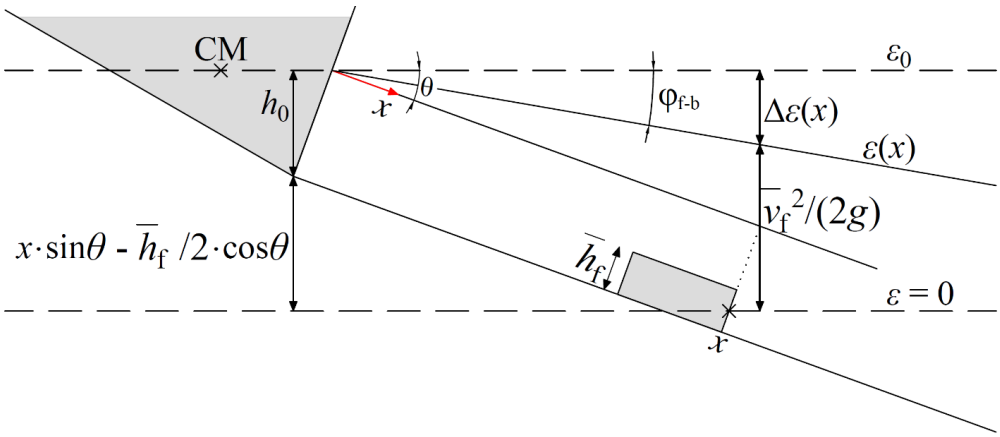

Figure 6.7 Conservation of energy for a frictional block model moving on a fixed bed. Notice that to simplify the drawing, mass graphically appears not to be conserved (the shaded triangle should have the same area as the shaded rectangle)

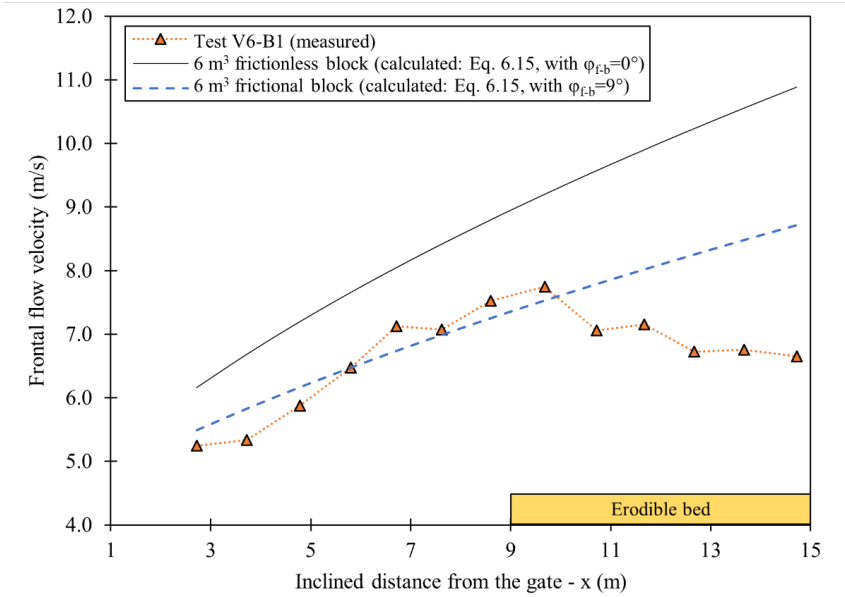

Figure 6.8 Measured and calculated frontal flow velocity for test V6-B1 and calculated velocity using the block model on a fixed bed

6.5. MPM model

As presented in *Paper III*, the MPM one-phase model is calibrated using a constant basal friction equal to $\bar{\varphi}_{\mathrm{f-b}} = 9°$. Using a one-phase model implies that the computed flow depth is lower compared to the measured flow depth for the real two-phase debris flow modelled in the flume experiments (cf. Chapter 6.3 and Figure 6.5). Regarding the flow velocity, using a constant basal friction provides a good estimate of the velocity variations along the flume, as demonstrated by the analysis using the block model (cf. Chapter 6.4). However, MPM is a continuum method which is significantly different from the rigid block model. Indeed, the flowing mass can deform internally in MPM. The frictional parameters of the debris flow are observed to govern the internal behavior of the debris flow in MPM, as the debris flow reaches large deformations (*Paper III*). It is observed that the internal frictional parameters have an influence on the flow behavior during the release stage, as the debris flow has to change in shape and therefore it deforms internally. This implies that shearing occurs internally, as shown in Figure 6.9a, which refers to the initiation of the debris flow (dam-break). The velocity of the computed debris flow along the flume is therefore dependent also on the internal strength parameters (other than the basal friction), which regulate the velocity after dam-break. As discussed in *Paper III*, the strength parameters are back-calculated to provide a good agreement with the measured flow velocity: from the sensitivity analysis in MPM, the values $c_{\mathrm{f}} = 500\ Pa$ and $\varphi_{\mathrm{f}} = 15°$ are found.

As the debris material in MPM starts flowing downstream on the fixed bed section, it acquires the typical elongated shape of debris flows, with an approximate flow depth of 0.3 m (Figure 6.9b). The computed debris flow is now moving as a deformed block, without significant internal shearing, as the computed flow velocity is observed to be approximately constant along the flow depth (Figure 6.9b). Indeed, by approximating the debris flow as an infinite slope, the safety factor at a point just above the base of the flow can be calculated as:

$$FS = \frac{c_{\mathrm{f}} + \rho_{\mathrm{f}} g h_{\mathrm{f}} cos\theta tan\varphi_{\mathrm{f}}}{\rho_{\mathrm{f}} g h_{\mathrm{f}} sin\theta} \qquad \textbf{6.16}$$

Using $h_{\mathrm{f}} \cong 0.25\ m$ and the best-fit strength parameters ($c_{\mathrm{f}} = 500\ Pa$ and $\varphi_{\mathrm{f}} = 15°$), one obtains $FS = 1.01$, which implies that no failure, and therefore no internal shearing, occurs in the moving mass, in agreement with the observed constant velocity profile along the flow depth. The fact that the mass is not shearing internally, but only at the base, qualitatively agrees with the observed flow

behavior (Supplementary file 1), where the debris flow seems to be sliding at the base, without any apparent mixing and shearing inside the mass.

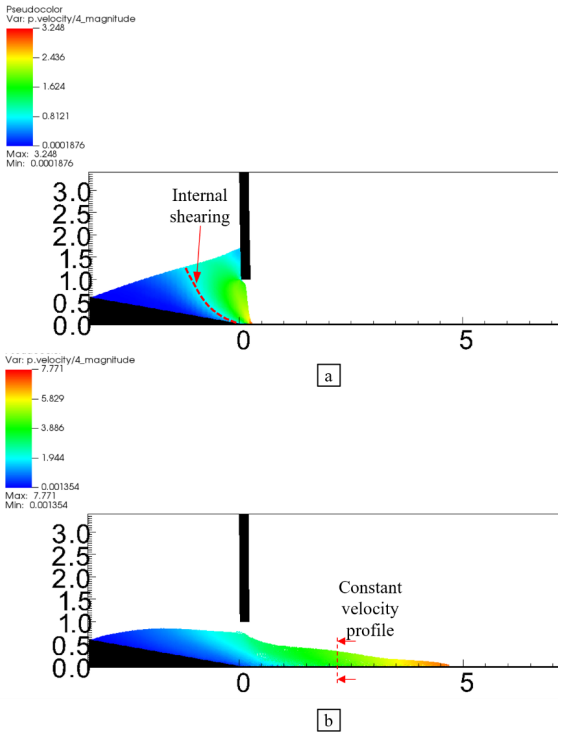

Figure 6.9 Computed flow behaviour with MPM, using $c_f = 500\ Pa$ and $\varphi_f = 15°$: (**a**) dam-break initiation of the debris flow (t=0.3 s after gate opening); (**b**) flow over the fixed bed (t=1 s)

6.5.1. Summary of frictional parameters to model debris flows

Previous studies have also modelled debris flows using three-dimensional numerical models, similar to MPM, and assuming one-phase elasto-plastic Mohr-Coulomb model. Table 6.2 shows a summary of the calibrated flow apparent friction parameters in previous studies. Obviously, the parameters back-calculated for each case study will strongly depend on the water content of the modelled debris flow and on the consequent magnitudes of pore pressures in the flow, which directly influence the apparent friction parameters. The parameters calibrated in MPM to model the debris flow experiments are well within the range of calibrated values in other studies. Table 6.2 may be used as a reference by practitioners.

Table 6.2 Apparent frictional flow parameters calibrated using one-phase three-dimensional numerical models

Study	Numerical model and case study	Calibrated apparent frictional flow parameters
(Kwan et al. 2015)	ALE – Yu Tung road debris flow (2008)	$\varphi_{\mathrm{f-b}} = 8°$ $\varphi_{\mathrm{f}} = 15°$ $c_{\mathrm{f}} = 1000\ Pa$ *
(Koo et al. 2018)	ALE – Several debris flow events in Hong Kong	$\varphi_{\mathrm{f-b}} = 8° - 20°$ $\varphi_{\mathrm{f}} = 15° - 30°$ (depending on the water content in the flow) *
(Kwan et al. 2019)	ALE – Illgraben and Veltheim field tests on impact on flexible barrier	$\varphi_{\mathrm{f-b}} = 12°$ $\varphi_{\mathrm{f}} = 15°$
(Lam and Wong 2021)	ALE – HKUST flume	$\varphi_{\mathrm{f-b}} = 10°$ $\varphi_{\mathrm{f}} = 12°$
Paper III	MPM – HKUST flume	$\varphi_{\mathrm{f-b}} = 9°$ (measured) $\varphi_{\mathrm{f}} = 15°$ $c_{\mathrm{f}} = 500\ Pa$

*Additional turbulent damping is used to limit high flow velocities

Chapter 7

7. Additional analysis and discussion on the entrainment behavior

Installing the instrumentation to measure entrainment

Different entrainment approaches have been used in the papers to simulate entrainment:

i. Depth-averaged modelling with RAMMS, with empirical entrainment rate (*Paper I*)
ii. Analytical solution for the entrainment rate (*Paper II*)
iii. MPM with softening model for the erodible bed (*Paper III*)
iv. MPM modelling of a boulder entrained at the debris flow front (*Paper IV*)

In this chapter, the entrainment modelling approaches are compared. Approaches ii and iii are discussed in relation to the back-calculation of the large-scale flume experiment. Additional details on the influence of the upstream flexible barrier on entrainment are also provided. The challenges related to modelling entrainment in natural debris flows are presented, through qualitative comparison of approaches i and iv.

7.1. Analysis of entrainment in the flume experiments

Figure 7.1 shows the spatial entrainment depths along the erodible bed section for the three experiments performed in the large-scale flume model, which are obtained by interpolating the entrainment depths measured with the erosion columns. In each test, the erosion depths are observed to significantly change in the longitudinal flow direction (*x*-axis). The erosion depth is higher at the start of the erodible beds and then decreases downstream. This entrainment pattern is discussed in *Paper III*. The variations of the erosion depth in the cross-section (*y*-axis) are significantly lower compared to the variations in the *x*-direction, which justifies the assumption of modelling a plane-strain problem in *Paper III*. Still, the observed entrainment variability in the *y*-direction may be due to some local variations of the flow depth and velocity.

Table 7.1 compares the volume of debris flow over the erodible bed (for tests V2.5-B1 and V6-B1 it corresponds to the initial debris volume; for test V6-B2, the volume retained by the upstream flexible barrier was subtracted from the initial release volume) with the total entrainment volume, obtained by integrating the entrainment depths (Figure 7.1) along the flume extent. Entrainment is scale-dependent, as the entrained volume in test V6-B1 is higher than in test V2.5-B1. This is in agreement with field studies (e.g., Rickenmann and Weber 2003). However, in test V6-B2, the upstream flexible barrier is significantly reducing entrainment, even if the volume of debris flowing over the erodible bed is in between the two tests without the upstream flexible

barrier. The reason for this entrainment reduction is explained in *Paper II* and will be further detailed in the next section 7.1.3.

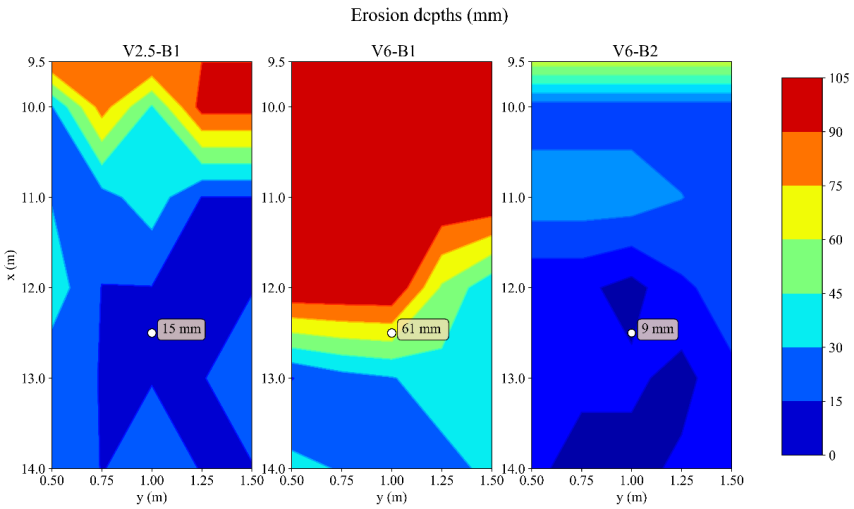

Figure 7.1 Contour map of the erosion depths in the three tests. *x* is the inclined distance from the gate and *y* is the distance from the right-side wall of the flume

The correlation between flow volume and entrainment volume is too simplistic to explain the mechanisms of the entrainment process, such as the stresses transmitted by the flow onto the bed and pore-pressure development in the erodible bed. Therefore, to gain more insights into the entrainment mechanisms, two modelling approaches were followed. In *Paper II*, an existing analytical entrainment rate model was applied, with the aim of back-calculating the pore-pressure ratio in the erodible bed to match with the measured entrainment depth. In *Paper III* instead, entrainment was modelled for the first time using MPM. This required introducing a softening model for the erodible bed, whose parameters were back-calculated to match with the measured entrainment volume. In particular, the back-calculation in *Paper II* is referred to the entrainment measured at *x=12.5 m* on the centerline of the flume, as the analytical formulation requires the flow depth as an input (in this case FD2, positioned exactly at *x=12.5 m*). Vice versa, the back-calculation approach used in *Paper III* considers the full extent (along the *x*-axis) of the flume: in this case, the entrainment depths are averaged at each cross-section of the flume (Figure 13 in *Paper III*). In chapter 7.1.1., the two approaches will be compared critically, highlighting the

advantages and drawbacks of each method. In chapter 7.1.2., a block model will be defined to capture the flow mobility on the erodible bed section. In chapter 7.1.3., a qualitative explanation will be given to explain the reduction of entrainment with an upstream flexible barrier, based on the observed kinematics of the flow-flexible barrier-erodible bed interaction.

Table 7.1 Comparison of the entrainment volume with the volume of debris flowing over the erodible bed for the three tests

Test ID	Volume flowing over the erodible bed (m^3)	Entrainment volume (m^3)
V2.5-B1	2.5	0.5
V6-B1	6	0.9
V6-B2	4.8	0.3

7.1.1. Comparison of analytical solution and MPM model

In this section, test V6-B1 is considered as it was back-calculated using both approaches. Two different approaches have been followed to back-calculate test V6-B1.

Analytical entrainment rate model (Iverson 2012) (*Paper II*)

Figure 7.2a qualitatively illustrates the debris flow, which is considered to exert the flow basal shear stress τ_{f-b} on the erodible bed layer, which in turn develops a resisting shear stress τ_b. The bed surfaces, on which the shear stresses act, are considered to be planar and parallel to the flow direction. A basal scour entrainment mechanism is therefore modelled. An analytical equation for the entrainment rate can hence be found, based on the conservation of momentum for the entrained bed layer (derivation shown in *Paper II*) and on analytical formulations for the shear stresses.

In *Paper II*, τ_{f-b} is modelled with a Mohr-Coulomb model:

$$\tau_{f-b}(t) = \sigma(t) tan\varphi_{f-b}(t) \quad \textbf{7.1}$$

where $\sigma(t)$ is the normal total stress acting at the base of the flow, which is evaluated as the normal component of the static weight at the debris flow base:

$$\sigma(t) = \rho_f g h_f(t) cos\theta \quad \textbf{7.2}$$

The measurement of the flow depth $h_f(t)$ at L2 (x=12.5 m) is used in Eq. 7.2 to calculate the time dependent normal stress. Therefore, the time dependent variations of the flow basal shear stress

can also be calculated (Eq. 7.1), using the flow basal apparent friction angle $\varphi_{\mathrm{f-b}}(t)$ from Figure 6.1b.

In *Paper II*, τ_{b} is also expressed using a Mohr-Coulomb model:

$$\tau_{\mathrm{b}}(t) = \sigma(t) tan\varphi_{\mathrm{b}} \qquad \textbf{7.3}$$

The bed apparent friction angle φ_{b} in Eq. 7.3 is dependent on the bed pore pressure ratio (λ_{b}): $tan\varphi_{\mathrm{b}} = tan\varphi'(1-\lambda_{\mathrm{b}})$. A constant value in time of φ_{b} is used in *Paper II*, as the mechanisms for pore pressure generation by shearing of the erodible bed cannot be derived analytically for the thin entrained bed layer. Therefore, φ_{b} is back-calculated, in the approach used in *Paper II*, to find the measured total erosion depth (z_{b}). The total erosion depth is found by integrating the entrainment rate in time and using Eqs. 7.1, 7.2, 7.3:

$$\begin{aligned} z_{\mathrm{b}} &= \int_0^{t_{\mathrm{DF}}} E(t)dt = \int_0^{t_{\mathrm{DF}}} \frac{\tau_{\mathrm{f-b}}(t) - \tau_{\mathrm{b}}(t)}{\rho_{\mathrm{b}} v_{\mathrm{f,bot}}} dt \\ &= \int_0^{t_{\mathrm{DF}}} \rho_{\mathrm{f}} g h_{\mathrm{f}}(t) cos\theta \frac{tan\varphi_{\mathrm{f-b}}(t) - tan\varphi_{\mathrm{b}}}{\rho_{\mathrm{b}} \bar{v}_{\mathrm{f}}/2} dt \end{aligned} \qquad \textbf{7.4}$$

where $v_{\mathrm{f,bot}}$ is the basal flow velocity (assumed half of the average flow velocity $\bar{v}_{\mathrm{f}}$, cf. *Paper II*). The only unknown parameter in Eq. 7.4 is φ_{b}. By trial and error, the value of $\varphi_{\mathrm{b}} = 6.5°$ is found for test V6-B1 (or equivalently $\lambda_{\mathrm{b}} = 0.87$, cf. *Paper II*). Indeed, using $\varphi_{\mathrm{b}} = 6.5°$, the measured entrainment depth $z_{\mathrm{b}} = 61\ mm$ (for test V6-B1) is correctly calculated from Eq. 7.4. In the other experiments (V2.5-B1 and V6-B2), different flow depths $h_{\mathrm{f}}(t)$ and flow velocities $\bar{v}_{\mathrm{f}}$ are measured at L2. Hence, different values of φ_{b} are back-calculated (cf. *Paper II*).

It is observed in *Paper II* that the spatial variations of the flow basal apparent friction $\varphi_{\mathrm{f-b}}(t)$ can affect the spatial distribution of entrainment. As discussed in Chapter 6, the flow front has higher apparent basal friction, which results in a higher entrainment rate (cf. Figure 11 in *Paper II*). Instead, the flow body has lower apparent basal friction and hence lower entrainment rates, which may also be negative indicating deposition at the tail of the debris flow (cf. Figure 11 in *Paper II*). Higher entrainment at the flow front and lower entrainment in the flow body has previously been reported by (Berger et al. 2011, Iverson et al. 2011).

The calculated entrainment rate varies between 0 m/s and 0.15 m/s (Figure 11 in *Paper II*), and the average entrainment rate (in time) is approximately 0.02 m/s. This range of values has similar

order of magnitude of the entrainment rate parameter $\frac{dz}{dt}$ used for the back-calculation in *Paper I*, where values between 0.013 m/s and 0.05 m/s are suggested in the RAMMS model (Figure 4 in *Paper I*). The similitude between the results from the analytical model and the parameter in the empirical entrainment model suggests that both models may at least capture approximate entrainment depths.

Despite the analytical model of the entrainment rate being able to explain the basic physics of the entrainment process (notably, the change in momentum of the entrained layer due to application of a destabilizing force by the debris flow), it is based on too idealized geometrical and load conditions, which may limit its capability to correctly simulate entrainment.

In particular, the analytical formulation can only model a basal scour mechanism, as it only accounts for shear stresses parallel to the bed surface (specifically $\tau_{\mathrm{f-b}}$ and τ_{b}, as schematized in Figure 7.2a). The flow is also idealized to move parallel to the bed surface, therefore only shearing the bed. In reality, the internal motion of a debris flow is rather three-dimensional (e.g., Choi and Goodwin 2021) and the erodible bed may not be planar during the whole entrainment process. These limitations of the analytical formulation therefore did not allow to give a satisfactory explanation for the reasons for the higher entrainment observed at the start of the erodible bed (after the fixed bed platform) and lower entrainment observed at the downstream side of the erodible bed.

Another limitation of the analytical model is that the erodible bed internal stress state and pore pressures are not modelled explicitly. Indeed, only a final state of the shear strength of the bed (τ_{b}) is captured, correspondent to a reduced shear strength of the bed which mechanically allows entrainment (e.g., $\varphi_{\mathrm{b}} = 6.5°$, or equivalently $\lambda_{\mathrm{b}} = 0.87$). In reality, the bed was initially (prior to the debris flow) unsaturated and carrying much lower pore pressures, which kept it stable on the $20°$ inclined slope.

MPM model (*Paper III*)

MPM solves the three-dimensional momentum conservation equations, without introducing hypothesis on the flow direction (unlike a depth-averaged model) and without the need to derive a formulation for the entrainment rate. Instead, in MPM the internal stress states of the flow and

erodible bed are considered by modelling them as continuum materials with an elasto-plastic model. Entrainment happens when the bed fails internally. Figure 7.2b shows the idealized entrainment configuration, where the debris flow exerts both shearing (τ_{f-b}) and ploughing (σ_{f-b}) stresses onto the erodible bed layer. In turn, the bed develops internal stresses τ_b and σ_b.

In *Paper III*, a one-phase approach is used for the debris flow material. The average value of the flow basal apparent friction ($\varphi_{f-b} = 9°$) is used. This is a limitation compared to the analytical model in *Paper II*, where the spatial variations of the basal friction were considered.

Regarding the erodible bed, a one-phase apparent model is used, which is based on the concept exemplified in Figure 2.6d. A softening model is used to simulate the reduction of bed shear strength (Figure 5 in *Paper III*). The internal apparent friction angle of the erodible bed (φ_b) is made decrease with the distortional strain, to mimic the development of excess pore pressures as the bed is sheared by the debris flow. The parameters of this model therefore need to be calibrated to compute the measured entrainment volume, as the final (residual) pore pressure generated in the bed is unknown a priori. For test V6-B1, the bed residual apparent friction is back-calculated as $\varphi_{bR} = 22.5°$. The higher value compared to the back-calculation with the analytical formulation is because MPM also models ploughing type of stresses, as detailed in *Paper III*.

Therefore, the MPM model can potentially simulate all the stages leading to entrainment: (i) the debris flow overrides the bed and transmit a basal shear stress, which (ii) causes the development of excess pore pressures in the bed, which in turn (iii) decrease the bed shear resistance; (iv) the combination of the action from the debris flow and the reduced bed resistance can cause the failure, i.e. entrainment, of a bed layer. Most importantly, contrary to the analytical entrainment model, MPM is a three-dimensional model, which therefore can evaluate all the stresses transmitted by the debris flow onto the erodible bed (Figure 7.2b). The evolution of pore pressures, through the softening model, is also captured, which allows to have a stable bed, with null apparent pore pressures, before entrainment and an increase in apparent pore pressures during the entrainment process. Furthermore, MPM considers the internal stress state of the erodible bed, which allows to model the spatial variations of entrainment. Indeed, the high entrainment at the start of the erodible bed is because the debris flow is ploughing the bed from the elevated position of the platform. Instead, the end of the erodible bed was more stable, as the bed is leaning on the flat horizontal runout section. Limited entrainment was therefore measured and computed.

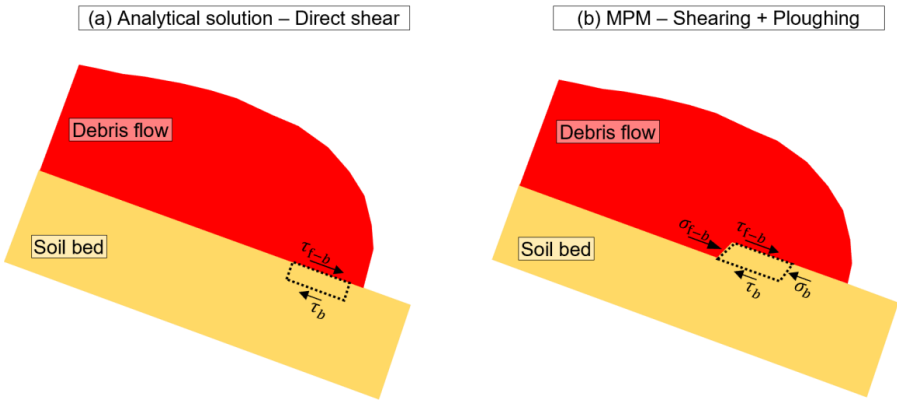

Figure 7.2 Schematics of the entrainment process: (a) in the analytical model considering direct shear of the erodible bed layer; (b) in the MPM model considering both basal scour and ploughing

7.1.2. Summary of frictional parameters for the erodible bed

Table 7.2 shows a summary of the bed pore pressure ratio (λ_b) measured and computed in other studies and in this work. The bed pore pressure ratio provides an indication of the degree of liquefaction, which is reached in the erodible bed during entrainment. Pore pressures in the erodible bed are due to both the initial saturation of the bed and to the development of excess pore pressures due to the shearing action from the debris flow. The bed apparent friction angle (φ_b) is also indicated, which is found from: $tan\varphi_b = (1 - \lambda_b)tan\varphi'$. The development of excess pore pressures in the erodible bed is strongly related to the initial water content of the erodible bed. In their experiments, Reid et al. (2011) reported variations of λ_b between 0.1 and 0.85 for increasing initial bed water contents. The back-calculation of test V6-B1 results in $\lambda_b = 0.87$. The back-calculation using MPM results in $\lambda_b = 0.53$ at the top of the bed, while lower values are computed (and measured) at the base of the bed ($\lambda_b = 0.22$). Fundamentally, the results from MPM show that significant variations of pore pressures may occur within the erodible bed. The higher pore pressures occur at the top of the bed, as the shearing action from the debris flow is the highest.

Table 7.2 Bed pore pressure ratio and bed apparent friction measured in different studies

Study	Bed pore pressure ratio, λ_{bR}	Bed apparent residual friction, φ_{bR}	Comment
(Iverson et al. 2011, Reid et al. 2011)	0.1	-	- Moderately wet bed (volumetric water content=18%). - Measured at the base of the 0.12 m-thick bed
	0.85	-	- Very wet bed (volumetric water content=25%). - Measured at the base of the 0.12 m-thick bed (however, following entrainment the bed thickness decreased to almost 0 m)
Paper II **(test V6-B1)**	0.87	6.5°	- At the evolving flow-erodible bed interface - Back-calculated using Iverson (2012) formula
Paper III **(test V6-B1)**	0.53	22.5°	- At the evolving flow-erodible bed interface - Back-calculated in MPM
	0.22	35°	- Measured at the base of the 0.12 m-thick bed

7.1.3. The block model with entrainment

As detailed in Chapter 6.4, the frictional block model of Eq. 6.15 valid on the fixed bed cannot explain the velocity trend measured on the erodible bed section. Indeed, three additional key aspects should be considered to model the flow dynamics on the erodible bed: (i) account for the change in flow momentum due to entrainment (Iverson 2012) and (ii) deposition; (iii) account for the change in basal friction due to entrainment (Iverson 2013). A block model over an erodible bed is considered in Figure 7.3. The momentum conservation for the flow block can be expressed as:

$$\frac{\Delta(mv)}{\Delta t} = G - T_b \qquad \textbf{7.5}$$

where T_b is the basal friction of the flow + entrained bed layer (Δz_b) landslide block. The variation of momentum can further be expressed as:

$$\frac{\Delta(mv)}{\Delta t} = m\frac{\Delta v}{\Delta t} + v\frac{\Delta m}{\Delta t} = m\frac{\Delta v}{\Delta t} + v\frac{\Delta m_e - \Delta m_d}{\Delta t} \quad \textbf{7.6}$$

Compared to Eq. 6.8, Eq. 7.6 contains the additional term related to the variation in mass (Δm) of the debris flow, which may be added by entrainment (Δm_e) or lost by deposition (Δm_d).

In the case of test V6-B1, significant entrainment and deposition were both observed (*Paper II*). It can be estimated that the entrainment of the erodible bed (approximately 0.9 m^3 along the whole bed) was approximately equal to the deposition of debris material from the tail of the flow (approximately 1 m^3 along the whole bed). Therefore, $\Delta m_e = \Delta m_d$ is considered as an approximation.

The effect of entrainment therefore does not appear on the left-hand side of Eq. 7.5. However, the fundamental distinction to the non-entrainment case (Eq. 6.8) derives from the basal shear force: the correct shear resistance to be used for the flow + entrained bed layer system is represented by the basal friction of the entrained bed layer (Iverson 2013) (cf. Figure 7.3). Therefore, T_{b}, instead of $T_{\mathrm{f-b}}$, needs to be used in the momentum conservation equation. Under these assumptions, Eq. 7.5 reduces to:

$$m\frac{\Delta v}{\Delta t} = G - T_{\mathrm{b}} \quad \textbf{7.7}$$

The slope-parallel gravitational force can be expressed as:

$$G = mgsin\theta \quad \textbf{7.8}$$

and the basal shear force is expressed using a Mohr-Coulomb model with the bed apparent friction φ_{b}:

$$T_{\mathrm{b}} = mgcos\theta tan\varphi_{\mathrm{b}} \quad \textbf{7.9}$$

Eq 7.7 therefore reduces to:

$$\frac{\Delta v}{\Delta t} = gsin\theta - gcos\theta tan\varphi_{\mathrm{b}} \quad \textbf{7.10}$$

If an infinitesimal increment of Δt is considered, i.e., $\Delta t \rightarrow dt$, Eq. 7.10 can be expressed as:

$$v\frac{dv}{dx} = gsin\theta - gcos\theta tan\varphi_{\mathrm{b}} \quad \textbf{7.11}$$

which can be solved from *x*=9 m (start of the erodible bed), using the initial condition for the flow velocity at *x*=9 m ($v(x = 9\ m)$ obtained from Eq. 6.15):

$$\int_{v(x=9\ m)}^{v(x)} vdv = \int_{x=9\ m}^{x} (gsin\theta - gcos\theta tan\varphi_b)dx \qquad \textbf{7.12}$$

which results in the flow velocity evolution along the erodible bed:

$$v(x) = \sqrt{v(x = 9m)^2 + 2(x - 9)(gsin\theta - gcos\theta tan\varphi_b)} \qquad \textbf{7.13}$$

By using the back-calculated bed residual apparent friction angle from the MPM simulations ($\varphi_b = 22.5°$), Eq. 7.13 can be plotted along the erodible bed section (green line in Figure 7.4), which fits quite well with the measured velocity. This result fundamentally shows that the increase of the basal friction applied at the base of the block, from the fixed bed section ($\varphi_{f-b} = 9°$) to the erodible bed section ($\varphi_b = 22.5°$), is the cause for the measured decrease in flow velocity along the erodible bed.

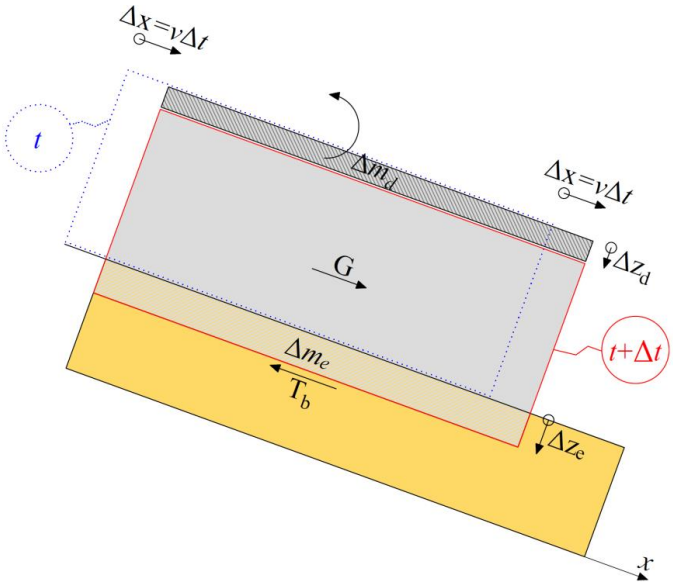

Figure 7.3 Frictional rigid block moving on an erodible bed

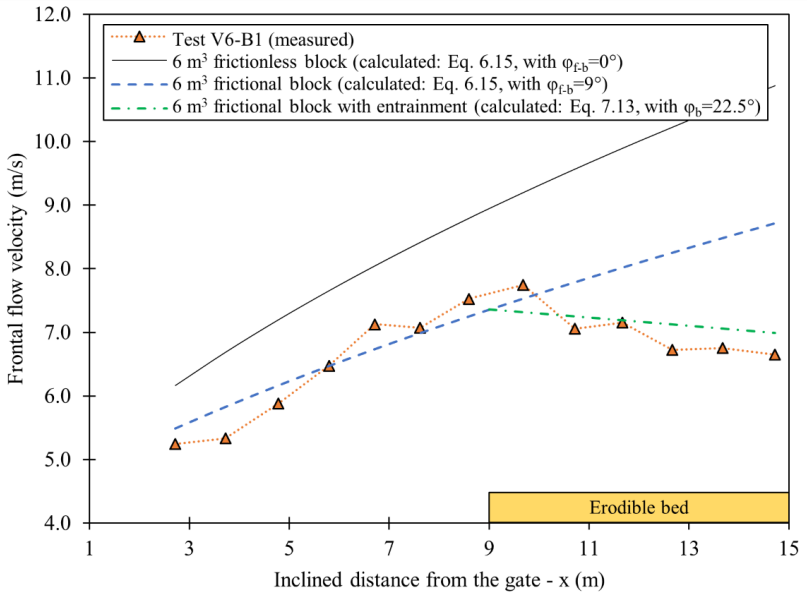

Figure 7.4 Measured frontal flow velocity for test V6-B1 and calculated velocity using the frictional block with entrainment

7.1.4. Influence of the upstream flexible barrier on entrainment

The impact kinematics of the flow on the upstream flexible barrier for test V6-B2 has been described in *Paper II* (Figure 4). In this chapter, additional information is provided regarding the landing process after impact on the upstream barrier, and the consequent change in flow dynamics which caused a decrease of entrainment compared to test V6-B1.

Figure 7.5 shows the landing dynamics after the flow impacts the upstream flexible barrier in test V6-B2. The time when the flow impacts the upstream flexible barrier is taken as t=0 s (Figure 7.5a). At t=0.73 s (Figure 7.5b) the flow runs up on the flexible barrier. At t=1.42 s (Figure 7.5c) the flow lands over the fixed bed and platform. The impact on the fixed bed causes the formation of a splash which creates a dilated flow. The dilated flow is due to the collisional impact of the debris flow at landing, which causes a volume expansion. At t=2.03 s (Figure 7.5d) a first debris flow surge is seen to flow downstream over the erodible bed section. As more material overflows from the upstream flexible barrier, a second flow surge forms (Figure 7.5e), which overrides the material deposited from the first flow surge (Figure 7.5f). The formation of two distinct flow surges is also documented by the video taken at the terminal flexible barrier (Supplementary file 2), where

the first flow surge stops immediately before the terminal flexible barrier (Figure 7.6a), while the second flow surge, arriving 3.28 s later, impacts the terminal barrier (Figure 7.6b).

The observed landing kinematics in test V6-B2 can explain qualitatively the reasons for the reduced entrainment compared to test V6-B1. An interpretation can be made based on videos of the experiment (e.g., Supplementary file 2). Figure 7.7 shows the interpretation of the landing and entrainment mechanisms in test V6-B2, which is also discussed in *Paper II*. The first debris flow surge, generated from the overflow from the upstream flexible barrier, lands at approximately 3-4 m from the barrier (Figure 7.7a). The collision of the flow on the fixed bed during landing causes the debris flow material to jump upwards, in a direction orthogonal to the flume base (Figure 7.7b); part of the material is also redirected upstream parallel to the flume base. This causes the creation of an elongated debris flow after landing, which appears dilated (lower bulk density). This material then starts flowing downstream, with the formation of a first flow surge (Figure 7.7c), which appears quite thin and slow. The first flow surge is mainly depositing all along the erodible bed, without generating significant entrainment. The dominance of deposition over entrainment may have been due to the landing over the platform, which consequently causes the flow to jump upwards (normal to the flume), without being able to scour or plough the erodible bed. The slow flow motion may also have contributed to the dominance of deposition over entrainment. After the flow of the first surge commenced, the remaining debris material left upstream of the erodible bed started flowing downstream, generating a second surge over the deposited debris (Figure 7.7d). Shearing therefore occurred along the interface between the second flow surge and the deposit, which limited the shearing transmitted onto the erodible bed. Therefore, pore pressures in the erodible bed and entrainment remained limited. An attempt has been made to model the low observed entrainment with the analytical model (*Paper II*), by adopting a smaller value of the bed pore pressure ratio, because of the lower shearing from the debris flow. Instead, the MPM model was not able to correctly simulate the landing mechanics and the formation of the two flow surges. Modelling these complex phenomena may require the use of a two-phase model, considering the evolution of pore pressures in the debris flow body. Indeed, the creation of a dilated flow during overflow and after landing may have accelerated the dissipation of excess pore pressures within the debris flow. Lower excess pore pressures would therefore decrease the flow velocity and increase deposition.

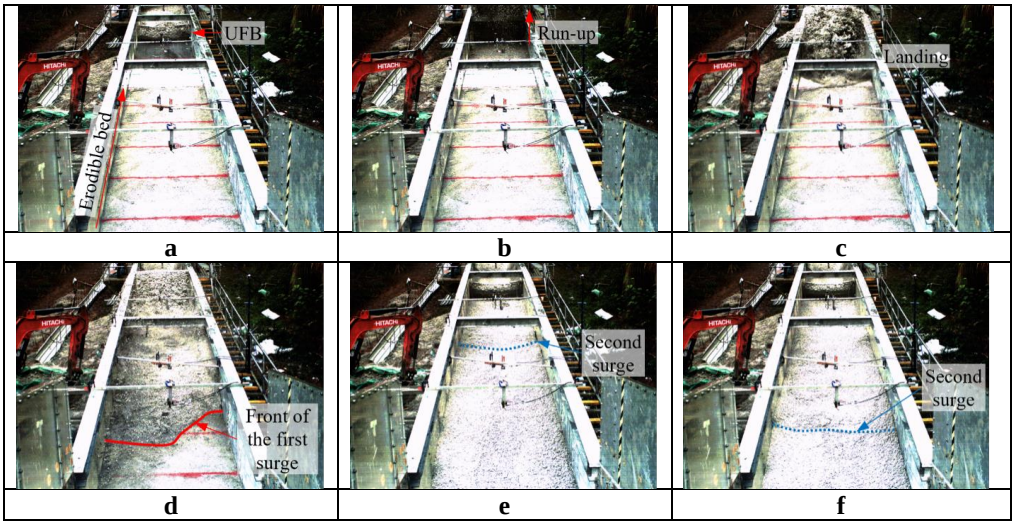

Figure 7.5 Landing process after the impact with the upstream flexible barrier (test V6-B2): (**a**) t=0 s; (**b**) t=0.73 s; (**c**) t=1.42 s; (**d**) t=2.03 s; (**e**) t=3.19 s; (**f**) t=3.59 s

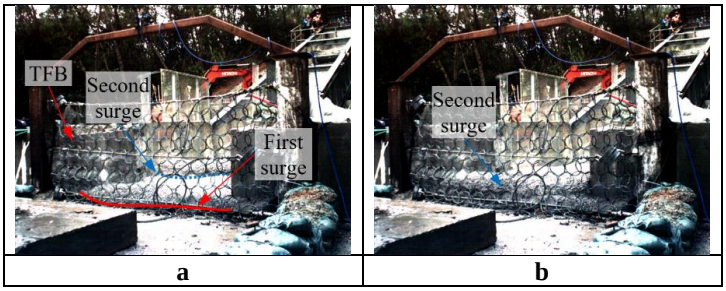

Figure 7.6 Impact on the terminal flexible barrier for test V6-B2: (**a**) first flow surge; (**b**) second surge

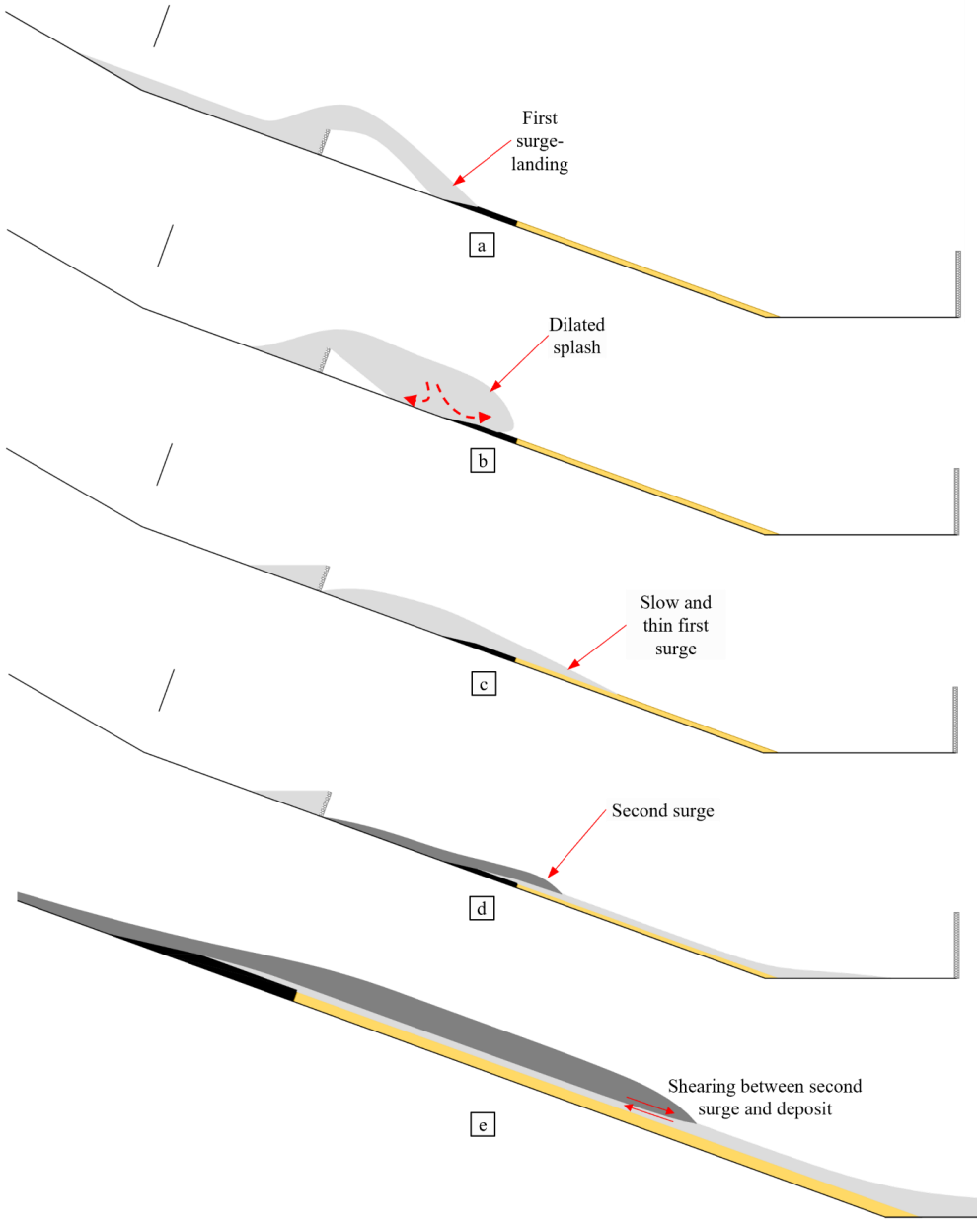

Figure 7.7 Qualitative sketch of the landing mechanism from the upstream flexible barrier with formation of two flow surges: (**a**) Landing of the first surge (t≈1.4 s); (**b**) Creation of a dilated splash from the landing process (t≈1.5 s); (**c**) First surge overriding the erodible bed (t≈1.8 s); (**d**) Formation of a second flow surge (t≈3.3s); (**e**) Detail of the second flow surge shearing the deposit only (t≈3.7 s)

7.2. Investigating different entrainment scenarios observed in nature

In *Paper II*, entrainment has been experimentally modelled according to a simplified configuration: the erodible bed topography was smooth (rectilinear); the slope angle was constant; the bed soil was homogeneous and the water content in the bed was approximately the same on the whole bed. Furthermore, the bed material was only constituted of soil and fluid, without the inclusion of macroscopically large boulders. Simple conditions must indeed be assumed in physical modelling, whose goal is to grasp the basic physical principles of entrainment. The simple initial and boundary conditions of the bed made it possible to back-calculate entrainment either using an analytical entrainment rate formulation (*Paper II*) or by modelling the soil as a continuum in MPM (*Paper III*).

However, in nature the initial conditions of the bed may be more complex. Figure 7.8 shows the Hunnedalen release area and channel. The topography appears quite irregular, with many boulders laying on the slope and mixed with finer soil. It is also likely that the bed water content before the debris flow event in 2016 may have been heterogeneous, since the soil properties controlling water infiltration (e.g., soil permeability) may have varied quite significantly along the channel extent and along the bed thickness. The complexity of the bed conditions hinders the application of the analytical entrainment rate formula in *Paper II*, which is based on the hypothesis of a homogeneous soil bed without boulders. For this reason, it was preferred to back-calculate the Hunnedalen debris flow event using the empirical entrainment model in RAMMS, which assumes a constant entrainment rate. Furthermore, the extent of the Hunnedalen debris flow event was significant (750 m), and the flow volume was large (20000 m^3 after entrainment). For computational reasons, a depth-averaged model is therefore preferred instead of a three-dimensional model such as MPM.

Figure 7.8 Hunnedalen channel (photos from field visit in June 2019): (a) Soil material in the release areas; (b) Boulders along the channel

The empirical entrainment model in RAMMS allowed to back-calculate the observed entrainment volume in Hunnedalen (Figure 2 in *Paper I*), through calibration of the Voellmy model parameters. However, RAMMS does not allow to capture some physical processes of entrainment, and in particular: (i) the transmission of shearing and ploughing stresses by the debris flow and the progressive development of bed excess pore pressures (cf. *Paper III*); (ii) the frontal entrainment of boulders along the flow path. To progress towards more realistic modelling of entrainment as observed in natural debris flows, simulations were performed in MPM to study the entrainment of a wet soil bed (*Paper III*) and the entrainment of large boulders (*Paper IV*). Based on the field survey of the Hunnedalen channel in 2019, it can be hypothesized that the entrainment of boulders may have been quite significant in the debris flow event of 2016. It is therefore worthwhile to investigate the influence of frontal boulder entrainment on the debris flow dynamics. In particular, boulders can be modelled explicitly in MPM. The computation of a boulder laying on the slope and being hit by a debris flow shows a significant deceleration of the debris flow (Figure 6 in *Paper IV*). Boulders entrained at the flow front may therefore reduce the debris flow mobility.

In RAMMS, instead, the frontal boulder entrainment cannot be modelled explicitly. Therefore, to account for the influence of boulders on the flow mobility in RAMMS, a strategy may be to artificially increase the friction coefficient of the debris flow. A 2D conceptual model is assumed as in Figure 7.9, where a boulder of mass m_{B} is pushed by the debris flow front. The debris flow region behind the boulder is idealized as a rigid block of mass m_{f}. Figure 7.9a shows the forces acting on the debris flow and on the boulder, specifically: the slope-parallel gravity force; the basal frictional resistance and the earth pressures exerted between the debris flow and the boulder. Therefore, the equations of motion for the debris flow (f) and the boulder (B) can be expressed as:

$$\frac{dv_{\mathrm{f}}}{dt} = gsin\theta - gcos\theta tan\varphi_{\mathrm{f-b}} - \frac{P}{m_{\mathrm{f}}} \qquad \textbf{7.14}$$

$$\frac{dv_{\mathrm{B}}}{dt} = gsin\theta - gcos\theta tan\varphi_{\mathrm{B}} + \frac{P}{m_{\mathrm{B}}} \qquad \textbf{7.15}$$

where $\varphi_{\mathrm{f-b}}$ is the flow basal apparent friction and φ_{B} is the friction angle acting at the base of the boulder. Notice that Eqs. 6.5 and 6.6 only model the situation when the boulder is transported at the flow front. The initial mobilization due to the debris flow impact is not considered. The initial entrainment of the boulder is however simulated and discussed in *Paper IV*.

It is hypothesized that the boulder and the debris flow travel downslope with the same velocity ($v_\mathrm{f} = v_\mathrm{B}$), and therefore the flow does not overtake the boulder (as observed in the MPM simulation, Figure 7 in *Paper IV*). The hypothesis of equal velocities is exactly valid for the flow column immediately behind the boulder, but it may also be applicable for a wider flow region behind the boulder. Eqs. 6.5 and 6.6 can therefore be combined to generate a new form of the equation of motion for the debris flow, mathematically equivalent to Eq. 6.5:

$$\frac{dv_\mathrm{f}}{dt} = gsin\theta - gcos\theta \frac{m_\mathrm{f} tan\varphi_{\mathrm{f-b}} + m_\mathrm{B} tan\varphi_\mathrm{B}}{m_\mathrm{f} + m_\mathrm{B}} \qquad \textbf{7.16}$$

Eq. 7.16 may also be interpreted as the equation of motion of an equivalent debris flow block, which does not model explicitly the boulder at the flow front (Figure 7.9b). In this case, the influence of the frontal boulder is instead accounted by using a modified flow basal friction $\varphi^\mathrm{B}_{\mathrm{f-b}}$ equal to:

$$tan\varphi^\mathrm{B}_{\mathrm{f-b}} = \frac{m_\mathrm{f} tan\varphi_{\mathrm{f-b}} + m_\mathrm{B} tan\varphi_\mathrm{B}}{m_\mathrm{f} + m_\mathrm{B}} \qquad \textbf{7.17}$$

It is observed in Eq. 7.17 that $\varphi^\mathrm{B}_{\mathrm{f-b}} > \varphi_{\mathrm{f-b}}$, if $\varphi_\mathrm{B} > \varphi_{\mathrm{f-b}}$. This is usually verified as the debris flow is typically liquefied implying a low value of $\varphi_{\mathrm{f-b}}$ (for instance $\varphi_{\mathrm{f-b}} = 9°$ in the flume experiments), while the boulder basal friction φ_B is higher as is not mediated by pore pressures. Eq. 7.16 therefore indicates that a boulder entrained at the flow front slows down the flow compared to a flow without a boulder at the flow front.

The main implication of Eq. 7.17 is that the effect of a boulder entrained at the flow front may be considered in RAMMS even if boulders cannot be modelled explicitly. The boulder influence can indeed be introduced by using $tan\varphi^\mathrm{B}_{\mathrm{f-b}}$ in the Voellmy model. The back-calculated friction for the Hunnedalen case ($\mu = 0.17$, Figure 3b in *Paper I*) may therefore at least partially embed the influence of frontal boulder entrainment (cf. Figure 7.8b). Obviously, the flow dynamics in nature may have been more complex compared to the idealization in Figure 7.9, as boulders may have limited dimensions and be overtaken and englobed within the debris flow. The boulder may also have different shapes and roll or bounce instead of sliding. Finally, only the frontal part of the debris flow may be decelerated by the boulder at the front, which implies that m_f is the frontal flow mass. Hence, the friction coefficient $tan\varphi^\mathrm{B}_{\mathrm{f-b}}$ should theoretically only be applied to the debris flow front.

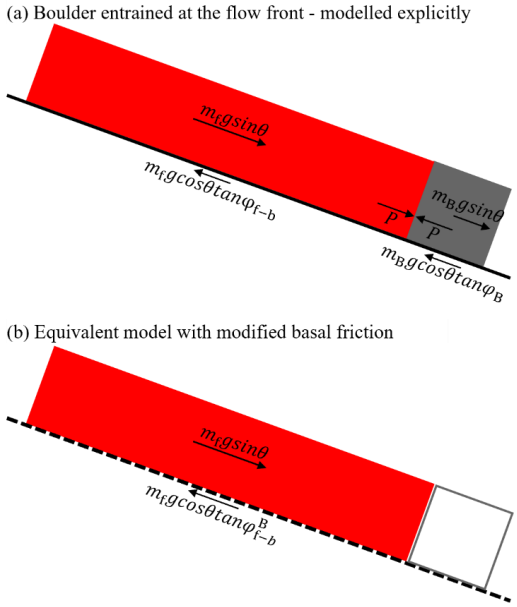

Figure 7.9 Analytical models of boulder entrained and transported at the front of a debris flow

A mass flow made of several boulders may be dominated by collisions between the boulders (e.g., Choi and Goodwin 2021). Therefore, boulders may collide an erodible soil bed, generating significant erosion. This is for example shown in the MPM simulation of one single bouncing boulder (Figure 9 in *Paper IV*), where a small debris flow is generated from the point of impact. The inclusion of boulders in a debris flow may create a boulder-rich debris flow. This type of flow has for instance been studied by (Li and Zhao 2018), who however did not model entrainment. Modelling a boulder rich debris flow may be especially important to simulate natural debris flows, like in the Hunnedalen case. However, the extension of the MPM model to full-scale catchments will be conditioned by future improvements of computational performances.

Chapter 8

8. Additional analysis and discussion on the flow interaction with multiple flexible barriers

Flexible barrier after a flume test

In this chapter, the impact mechanics on the flexible barriers observed in the experiments is further analyzed. The impact kinematics on the upstream and terminal flexible barriers is discussed. The dynamic pressure coefficient to calculate the impact forces is discussed and compared to other studies. A block model is introduced to back-calculate the measured run-up height.

8.1. Run-up kinematics on the flexible barriers

The high-speed cameras positioned along the flume recorded the impact of the debris flow on the flexible barriers. The maximum run-up heights are shown in *Paper II* (Figure 4c for test V6-B2 on the upstream flexible barrier; Figure 5a for test V6-B1 on the terminal flexible barrier; Figure 5b for test V6-B2 on the terminal flexible barrier). The maximum run-up heights are also sketched in Figure 8.1. The impact mechanisms may be categorized as run-up and pile-up, as follows:

I. **Run-up impact mechanism on the compact flexible barrier** (Supplementary file 3). Figure 8.1a shows a sketch of the run-up mechanism on the upstream flexible barrier for test V6-B2. As the debris flow was stopped by the upstream barrier, static debris (referred as dead zone) impounded against the flexible barrier to form a curved ramp for incoming debris material to overflow. This dead zone could extend from the base to the crest of the barrier, given the low barrier height-flow depth ratio ($\frac{H_B}{h_f}$ =1.5). Therefore, the flow was observed to overflow the barrier following a curved flow path which created a centrifugal force component on both the flume base and the flexible barrier. Cell 1 measured this additional centrifugal stress, as described in Figure 9b of *Paper II*, and high values of the impact cable forces were recorded (Table 2 in *Paper II*). The impact forces on the flexible barrier will be further discussed in this chapter.

II. **Run-up impact mechanism on the tall terminal flexible barrier** (Supplementary file 4). Figure 8.1b shows the run-up mechanism on the terminal flexible barrier for test V6-B1. Given the high flow velocity and large flow volume, a run-up mechanism was observed also on the terminal flexible barrier. However, compared to case I, the flow was mainly redirected vertically, without forming a curved flow path overflowing the barrier. The

vertical run-up mechanism was due to the high barrier-flow depth ratio ($\frac{H_B}{h_f}$ =5), which limited the formation of a static deposit extending to the crest of the barrier.

III. **Pile-up impact mechanism on the terminal flexible barrier** (Supplementary file 2). Figure 8.1c shows the pileup mechanism on the terminal flexible barrier for test V6-B2. As described in Chapter 7, the upstream flexible barrier split the debris flow into two surges. The first surge was observed to decelerate after landing and stop immediately before the terminal flexible barrier. The second surge was flowing over the deposit from the first surge. Only the second surge impacted the terminal flexible barrier with a reduced volume and velocity (*Paper II*). This resulted in a pileup impact mechanism on the terminal flexible barrier, where the runup height was limited due to the low energy of the second surge. Therefore, the upstream flexible barrier had a substantial effect on the successive impact on the terminal flexible barrier in test V6-B2, which was significantly different from the impact observed in test V6-B1.

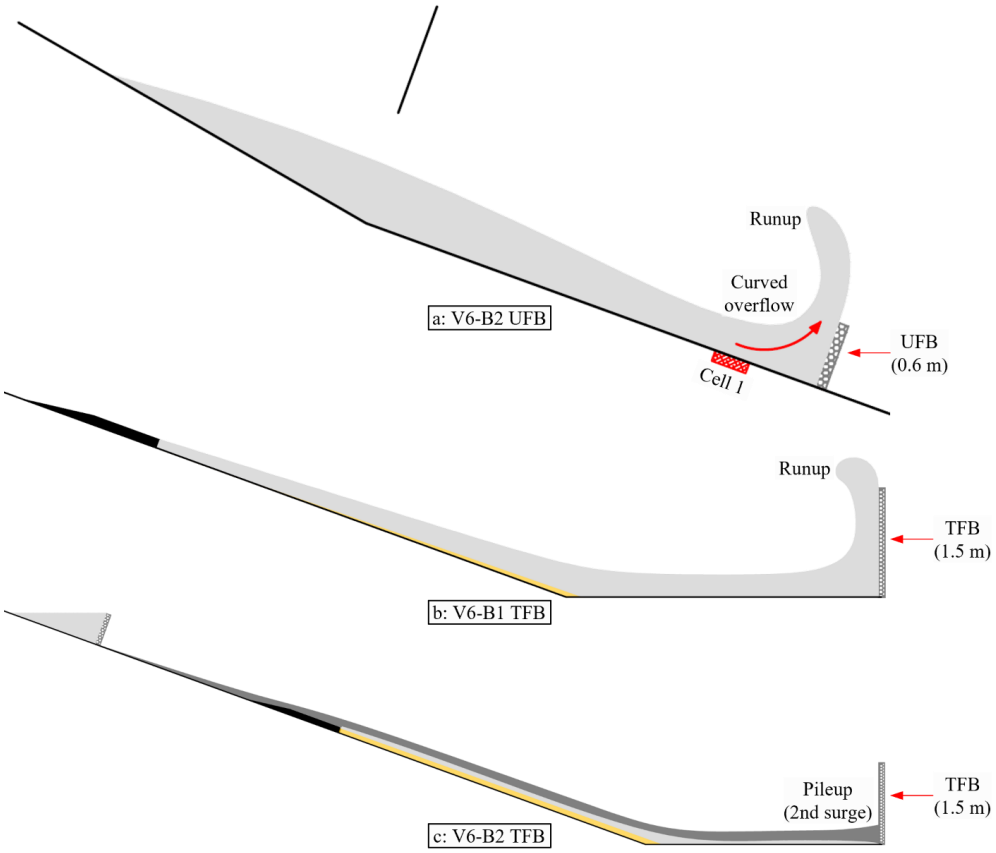

Figure 8.1 Schematics of the impact mechanisms on the flexible barriers for: (**a**) upstream flexible barrier (UFB) in test V6-B2; (**b**) terminal flexible barrier (TFB) in test V6-B1; (**c**) terminal flexible barrier in test V6-B2

8.2. Impact force on the flexible barriers

The measured cable forces (T and T_{H}) on the terminal flexible barrier are shown in Figure 12 of *Paper II*. The impact force orthogonal to the barrier (F), on each cable, is obtained through Eqs. 1 and 2 of *Paper II* (Figure 2c). Therefore, the total impact force on the barrier, F_{T}, is obtained as the sum of the impact forces on each cable. For the upstream flexible barrier, the total impact force is calculated as:

$$F_{\mathrm{T}} = 2T_{\mathrm{H,bc}} tan\psi_{\mathrm{bc}} + 2T_{\mathrm{H,tc}} tan\psi_{\mathrm{tc}} \qquad \textbf{8.1}$$

where ψ is the deflection angle of the cable, "bc" refers to the bottom cable and "tc" to the top cable.

For the terminal flexible barrier, the total impact force is calculated as:

$$F_{\mathrm{T}} = 2T_{\mathrm{bc}} sin\psi_{\mathrm{bc}} + 2T_{\mathrm{H,mc}} tan\psi_{\mathrm{mc}} + 2T_{\mathrm{H,tc}} tan\psi_{\mathrm{tc}} \qquad \textbf{8.2}$$

where "mc" refers to the middle cable. Notice that for the bottom cable, $sin\psi$ is used instead of $tan\psi$ because a different type of load cell has been used (cf. *Paper II*).

The total impact force (F_{T}) on the upstream and terminal flexible barriers are shown in Figure 8.2. The terminal flexible barrier in test V6-B1 was subjected to a run-up impact type. A more gentle pile-up impact was instead observed on the terminal flexible barrier in test V6-B2. Therefore, the total impact force on the terminal barrier is higher in test V6-B1 compared to test V6-B2. The impact of the debris flow on the upstream flexible barrier in test V6-B2 was also a run-up mechanism. As discussed previously and in *Paper II*, the curved flow path caused the transmission of additional centrifugal forces on the upstream flexible barrier, which caused the total impact force to be the highest.

For each test, the total peak impact force can be determined (Figure 8.2): 55 kN for the terminal barrier in test V6-B1; 3 kN for the terminal barrier in test V6-B2; 113 kN for the upstream barrier in test V6-B2. To analytically model the impact force, the hydrodynamic model is used (Eq. 2.17), which is justified by the high calculated values of the Froude number before impact on the barriers (Fr between 2.8 and 3.6). The dynamic pressure coefficient α is hence back-calculated, using Eq. 2.17 and the measured values of the flow velocity and depth (Table 2 in *Paper II*), as: 1.2 for the terminal barrier in test V6-B1; 0.2 for the terminal barrier in test V6-B2; 2.2 for the upstream barrier in test V6-B2.

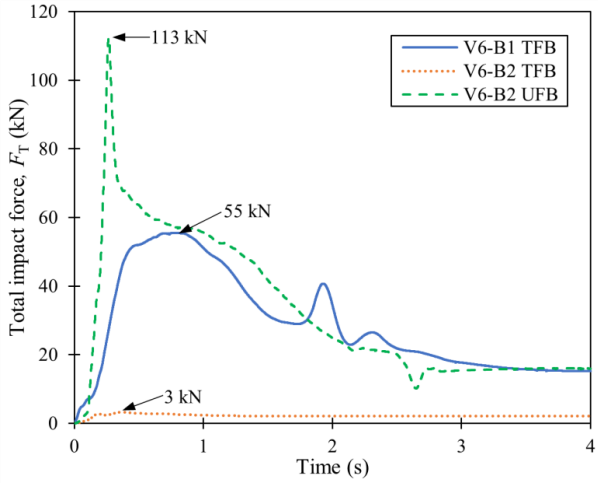

Figure 8.2 Total impact force on the terminal and upstream flexible barriers

8.2.1. Summary of dynamic pressure coefficient α on flexible barriers

Table 8.1 shows the dynamic pressure coefficient calculated in different studies for flows impacting flexible barriers. Values ranging from 0.2 to 2.2 have been reported for different flow types and impact mechanisms.

Floods have typical values between 0.2 and 1.4 (Ng et al. 2017, Song et al. 2018), depending on the viscosity of the fluid. The lower value is associated to less viscous flows, while the higher value characterizes very viscous flows.

(Kwan and Cheung 2012, Song et al. 2018, Wendeler et al. 2019) reported typical α values for wet debris flows between 0.7 and 2, which were observed for run-up impact mechanisms. The impact in test V6-B2 on the upstream barrier is characterized by $\alpha = 2.2$, while the impact in test V6-B1 on the terminal barrier has $\alpha = 1.2$. These two tests also exhibited a run-up mechanism, but were characterized by different values of the normalized barrier height H_B/h_f. The terminal barrier has a high value of $H_B/h_f = 5$, similar to the tests by (Song et al. 2018), and is characterized by a lower value of α. The upstream barrier has instead a low value of $H_B/h_f = 1.5$ and is characterized by a higher value of α. The results from *Paper II* therefore suggest that the normalized barrier height H_B/h_f can influence significantly α and therefore the impact force. Indeed, in the case of the upstream flexible barrier, the flow could not dissipate much energy by internal shearing, because all the flow thickness impacted the whole barrier height in block (all

together). Furthermore, the curved overflow caused additional centrifugal stresses to be transmitted onto the upstream flexible barrier. The influence of the normalized barrier height on the impact force needs to be further investigated in future research.

(Song et al. 2018) reported a value of α = 0.2 for dry granular flows, which impact the flexible barrier with a pile-up mechanism. Similarly, in test V6-B2, on the terminal flexible barrier, a pile-up mechanism was observed, and similarly α = 0.2 has been calculated. This result shows that an upstream flexible barrier can reduce α and the impact force on a terminal barrier, by splitting the flow into multiple surges, which transition to a pile-up mechanism on the terminal barrier.

Table 8.1 Dynamic pressure coefficient α for flexible barriers impacted by debris flows, as calculated in different studies. UFB refers to the upstream flexible barrier; TFB refers to the terminal flexible barrier

Study	α	Type of flow	Comment
(Kwan and Cheung 2012)	2	Debris flow	Design guidelines in Hong Kong
(Ng et al. 2017)	0.4-0.8	Dry sand	Pile-up impact mechanism
	1.2-1.4	Viscous flow (high viscosity)	Run-up impact mechanism
(Song et al. 2018)	0.7-1.3	Debris flows with different solid concentrations	Run-up impact mechanism
	0.2	Dry granular flow	Pile-up impact mechanism
	0.2	Flood (low viscosity of the fluid)	
(Wendeler et al. 2019)	0.1-1.0	Mud flow	Laboratory tests
	0.7-2.0	Debris flow	Field tests
***Paper II* (V6-B2 – UFB)**	2.2	Debris flow	Run-up impact mechanism Low value of H_B/h_f
***Paper II* (V6-B1 – TFB)**	1.2	Debris flow	Run-up impact mechanism High value of H_B/h_f
***Paper II* (V6-B2 – TFB)**	0.2	Debris flow	Pile-up impact mechanism

8.3. Back-calculation of the run-up height

Flexible barriers may be designed to completely stop a debris flow and to avoid overtopping. Hence, the determination of the run-up height upon impact is an important problem. In this thesis, three approaches have been used to model the run-up: (i) flume experiments (*Paper II* and section 8.1); (ii) MPM model (*Paper III*); (iii) block model (described afterwards, section 8.3.2).

8.3.1. Back-calculation of the run-up height on the upstream barrier using MPM

Paper III describes the back-calculation with MPM of the run-up on the upstream flexible barrier for test V6-B2. To reduce the computational cost, a plane strain model was adopted. Therefore, the flexible barrier was modelled as a rigid constraint in the channel with a curvature correspondent to the final deflected shape (deflection at the center of the ring net equal to 0.1 m). To back-calculate the runup height of 1.5 m, a sensitivity analysis was performed on the debris flow parameters (internal apparent friction angle, φ_f, and cohesion, c_f). The best-fit parameters were back-calculated as: $\varphi_f = 15°$ and $c_f = 500\ Pa$ (Figure 11b in *Paper III*). It is observed that the computed run-up height on the upstream flexible barrier reduces with the internal apparent friction angle of the debris flow. Indeed, a higher value of φ_f is associated to a higher shear resistance exerted on the overflowing debris.

8.3.2. A block model to evaluate run-up

To verify and discuss the significance of the back-calculated debris flow parameters in MPM, a simple block model is used to model the run-up on a flexible barrier (Figure 8.3). The frontal part of the debris flow has an average flow depth $\bar{h}_f$ just before impact (Figure 8.3a). After impact, the flow reaches a maximum run-up height H_R (Figure 8.3b). It is assumed that during the run-up process the block tilts by 90° but maintains the same initial shape (Figure 8.3a and Figure 8.3b). The mass of the run-up block is therefore calculated as:

$$m_R = \rho_f \bar{h}_f H_R W \qquad \textbf{8.3}$$

where $W = 2\ m$ is the width of the flume.

The specific energy of the center of mass of this block can be calculated, for the situations before (ε_1) and after (ε_2) impact. The specific energy is the total energy divided by the weight of the block, $m_R g$. The reference height for the energy is taken at the base of the barrier. Before impact, the center of mass of the block has specific energy given by the sum of the specific potential energy and the specific kinetic energy (Figure 8.3a):

$$\varepsilon_1 = \frac{\bar{h}_f}{2} cos\theta + \frac{H_R}{2} sin\theta + \frac{v_f^2}{2g} \qquad \textbf{8.4}$$

where v_f is the flow velocity before impact. After impact the block has null kinetic energy. Hence, the specific energy of the center of mass of the block after impact is given by its vertical height (Figure 8.3b):

$$\varepsilon_2 = \frac{H_R}{2} cos\theta + \frac{\bar{h}_f}{2} sin\theta \quad \textbf{8.5}$$

The dissipated specific energy during the run-up process is therefore given by:

$$\Delta\varepsilon = \varepsilon_1 - \varepsilon_2 \quad \textbf{8.6}$$

Table 8.2 shows the measured flow parameters and the calculations of the specific energies ε_1 and ε_2 for the upstream flexible barrier (UFB) in test V6-B2 and the terminal flexible barrier (TFB) in test V6-B1. Notice that the average flow depth of the block is evaluated as $\bar{h}_f = \frac{1}{t_R}\int_0^{t_R} h_f(t)dt$, where $h_f(t)$ is the measured flow depth before impact (cf. *Paper II*) and t_R is the time at which the maximum run-up on the barrier is observed. Based on the analysis of the videos of the experiments, the following values of the flow depth are used: for the UFB in test V6-B2, $t_R \cong 0.35\ s$ and hence $\bar{h}_f = 0.2\ m$; for the TFB in test V6-B1, $t_R \cong 1\ s$ and hence $\bar{h}_f = 0.3\ m$. The flow velocities v_f are assumed equal to the frontal flow velocities measured in the tests (Table 2 in *Paper II*). Using the measured flow parameters, the specific energies and the dissipated specific energy (Eq. 8.6) are calculated as shown in the first part of Table 8.2. Approximately 1.1 m of specific energy is dissipated during the impact process on the flexible barriers.

To quantitatively model this energy loss, two dissipation mechanisms are considered in the block model:

i. Frictional shearing of the run-up material against the barrier (Figure 8.3c). It is hypothesized that the frictional dissipation is mainly happening at the contact of the debris flow with the barrier, which has height H_B. Hence, the dissipated specific energy by frictional shearing is given by:

$$\Delta\varepsilon_{T//} = \frac{\bar{F}_{T//} H_B}{m_R g} \quad \textbf{8.7}$$

where $\bar{F}_{T//}$ is the shear force acting on the run-up block at the contact with the barrier. This shear force may be calculated using the Mohr-Coulomb criterion:

$$\bar{F}_{T//} = c_f W H_B + \bar{F}_T tan\varphi_f \quad \textbf{8.8}$$

where $\bar{F}_{\mathrm{T}}$ is the average total impact force on the barrier during the run-up process, which is calculated as the average in time of the total impact force ($F_{\mathrm{T}}(t)$) from Figure 8.2: $\bar{F}_{\mathrm{T}} = \frac{1}{t_{\mathrm{R}}}\int_0^{t_{\mathrm{R}}} F_{\mathrm{T}}(t)dt$. The cohesion and friction parameters are assumed based on the MPM back-calculation (*Paper III*): $c_{\mathrm{f}} = 500\ Pa$ and $\varphi_{\mathrm{f}} = 15°$.

ii. The flexible barrier deforms upon impact (Figure 8.3d) and therefore dissipates energy. The dissipated specific energy by barrier deformation is given by:

$$\Delta\varepsilon_{\mathrm{B}} = \frac{\bar{F}_{\mathrm{T}}\Delta_{\mathrm{B}}}{m_{\mathrm{R}}g} \qquad \textbf{8.9}$$

where Δ_{B} is the average deformation of the flexible barrier in the slope-parallel direction. A value $\Delta_{\mathrm{B}} \cong 0.1\ m$ is observed in the tests.

Hence, the dissipated specific energy is approximately equal to:

$$\Delta\varepsilon \cong \Delta\varepsilon_{\mathrm{T}//} + \Delta\varepsilon_{\mathrm{B}} \qquad \textbf{8.10}$$

The second part of Table 8.2 shows the calculation of the dissipation specific energies $\Delta\varepsilon_{\mathrm{T}//}$ and $\Delta\varepsilon_{\mathrm{B}}$. Their sum, $\Delta\varepsilon$ (Eq. 8.10), is equal to 0.9 m, which is approximately equal to the "measured" specific energy variation from Eq. 8.6. This equality shows that the block model accounting for energy dissipation can approximately capture the run-up mechanism on flexible barriers. The frictional energy dissipation is the main dissipation mechanism, as it accounts for 60% to 80% of the total energy dissipation. The energy dissipated by friction increases with the Mohr-Coulomb parameters c_{f} and φ_{f}, which therefore reduce the run-up height. This result is qualitatively in agreement with the results from the MPM simulations (Figure 11 in *Paper III*) and with the numerical simulations by (Kwan et al. 2019), which showed that an increase in friction reduces the run-up. The energy dissipation due to the deformation of the flexible barrier is also contributing to dissipation of energy. The deformability of flexible barriers is therefore favorable in reducing the runup height. The run-up height may be further limited by the curvature effect of the flexible barrier which redirects the flow upstream. This effect could be effectively captured by the MPM simulations (Figure 11 in *Paper III*).

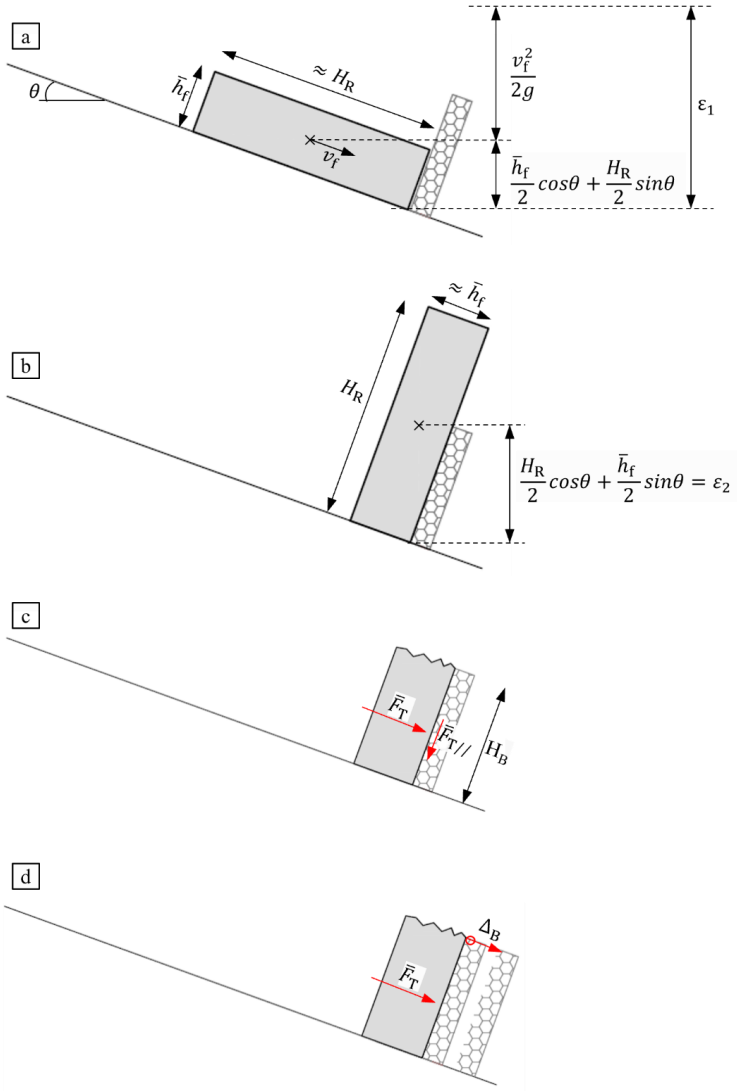

Figure 8.3 Energy conservation for the run-up on flexible barriers: **a** initial energy, just before impact; **b** final energy, at maximum run-up (notice that the block has the same volume of the initial block in **a**); **c** dissipation of energy during the runup due to frictional shearing; **d** dissipation of energy due to the deformation of the flexible barrier

Table 8.2 Measurement and calculation of the specific energies of the block model before and after impact on the flexible barriers (UFB indicates the upstream flexible barrier and TFB indicates the terminal flexible barrier)

Parameter	Impact on UFB (test V6-B2)	Impact on TFB (test V6-B1)
Measured run-up		
Slope angle, θ	20°	0°
Height of the barrier, H_B (m)	0.6	1.5
Average flow depth of the flow front, $\bar{h}_f$ (m)	0.2 *	0.3 **
Average flow velocity of the flow front, v_f (m/s)	5.5	6.1
Initial specific energy, ε_1 (m) (Eq. 8.4)	1.9	2.0
Measured run-up height, H_R (m)	1.5	1.9
Final specific energy, ε_2 (m) (Eq. 8.5)	0.7	1.0
$\Delta\varepsilon = \varepsilon_1 - \varepsilon_2$ (m) (Eq. 8.6)	1.2	1.1
Calculation of the energy dissipation		
Average impact force (calculated from Figure 8.2), $\bar{F}_T$ (kN)	42 *	40 **
Calculated shear force during run-up on the barrier, $\bar{F}_{T//}$ (kN) † (Eq. 8.8)	12	12
Specific energy dissipated by friction, $\Delta\varepsilon_{T//}$ (m) (Eq. 8.7)	0.6	0.7
Specific energy dissipated by deformation of the barrier, $\Delta\varepsilon_B$ (m) ‡ (Eq. 8.9)	0.3	0.2
Specific energy dissipated, $\Delta\boldsymbol{\varepsilon}$ (m) (Eq. 8.10)	0.9	0.9

* $t_R = 0.4\ s$ is used for the calculation; ** $t_R = 1\ s$ is used for the calculation; † $c_f = 500\ Pa$ and $\varphi_f = 15°$ are used in the calculations; ‡ $\Delta_B = 0.1\ m$ is used in the calculation

Chapter 9

9. Summary and conclusions

Flexible barrier installed in the field

9.1. Summary

The entrainment mechanisms of a debris flow interacting with channel bed materials (soil, fluid and boulders) are not fully understood yet. Previous entrainment models are often empirical, which therefore hinder the holistic understanding of the physical processes involved in the debris flow entrainment of an erodible bed. Novel measurements and numerical modelling techniques of the entrainment process are needed to progress towards a more rational understanding of entrainment. Furthermore, the role of mitigation solutions such as flexible barriers on the entrainment has not been elucidated yet.

In this PhD, a large-scale flume is used to physically model entrainment and the impact of a debris flow on multiple flexible barriers. The Material Point Method is used to numerically simulate the debris flow behavior, entrainment, and the impact on the flexible barriers. The main contributions from this PhD thesis are:

- A technique to measure entrainment in flume experiments is developed.
- Large-scale flume experiments are performed to study the entrainment of a wet soil bed by a debris flow. The flow basal stresses have been measured to explain the observed flow mobility and the entrainment mechanisms.
- Entrainment is modelled for the first time using the Material Point Method. A softening model for the erodible bed is introduced to capture the shear strength reduction in the erodible bed. Entrainment mechanisms are identified.
- The entrainment of large boulders at the debris flow front is modelled explicitly for the first time using the Material Point Method. The influence of a boulder entrained at the flow front on the flow mobility is analyzed.
- Analytical, empirical, and numerical solutions to back-calculate entrainment are applied and compared in relation to different case studies. The limits of applicability of each model are highlighted.
- Multiple (dual) flexible barriers are investigated, through physical flume modelling. The influence of an upstream flexible barrier on entrainment is also studied for the first time. The impact forces in the dual barrier configuration are analyzed.

9.2. Conclusions

Debris flows typically grow in volume by entraining channel bed materials along the flow path. The Hunnedalen (Norway) debris flow event in 2016 was taken as a refence because the initial volume increased 10 times due to entrainment. A field survey after the debris flow event showed that both wet soil bed and boulders were entrained by the debris flow. Numerical simulations of the Hunnedalen (Norway) debris flow were therefore performed to back-calculate entrainment. An existing empirical entrainment model was used within a depth-averaged software. The simulation results showed that the entrainment parameters are not well constrained and cannot capture the physical processes during entrainment. Therefore, large-scale flume experiments were carried out to study the entrainment mechanisms of an erodible wet soil bed.

A novel technique was developed to measure entrainment in the flume model, specifically to differentiate entrainment from deposition of debris flow on top. Tests were therefore carried out with different release volumes, which showed that flow velocities and entrainment are scale dependent. The flow basal normal and shear stresses were measured, which suggested a significant degree of liquefaction at the base of the debris flow. Hence, the flow mobility was enhanced. Based on the measurements of the flow basal stresses and using an analytical entrainment rate equation, the highly frictional flow front was associated to higher entrainment, while the more liquefied flow body and tail were associated to lower entrainment and deposition. However, the simple analytical model could not capture the physical processes during entrainment, in particular the progressive reduction of the bed shear strength. Also, a characteristic entrainment pattern was observed in all the experiments, with higher entrainment just after the transition from the superelevated fixed bed. This spatial distribution of entrainment was however difficult to explain.

The Material Point Method was therefore used to back-calculate the flume experiments. A softening model was used for the erodible bed, which allowed to simulate the progressive reduction of the bed shear strength due to pore pressure development as the bed is sheared. Using this softening model, the bed was initially stable, but it was eventually destabilized due to the shearing and colliding action of the debris flow. The entrainment volume was computed to be inversely proportional to the final residual bed shear strength. The interaction of the flow with the erodible bed was observed to be a combination of basal scour (shearing on surfaces parallel to the flow direction) and ploughing (collision on surfaces normal to the flow direction). The ploughing stresses have been neglected in previous entrainment models but are fundamental to explain the

entrainment of beds which are mechanically stronger than the debris flow (ploughing-enabled entrainment behavior). As MPM is a three-dimensional model, it can simulate flow velocity components normal to the topography. Therefore, the MPM simulations could capture the higher entrainment at the start of the erodible bed, which was due to the flow digging and ploughing the bed from the superelevated fixed bed. It is advised to employ three-dimensional software (instead of depth-averaged software) to model channel beds characterized by significant variations of the topography and transitions between fixed and erodible beds.

The observations in the Hunnedalen channel hinted at the importance of studying a special case of entrainment: boulders resting in the channel and being hit and entrained by the debris flow front. Using the Material Point Method, these boulders could be modelled explicitly. The simulations showed the importance of considering the "frontal boulder entrainment", which is computed to decrease the flow mobility. Instead, it would be challenging to simulate this entrainment case in depth-averaged models. Nevertheless, a simple analytical equation is derived where the friction coefficient at the base of the flow is artificially increased to implicitly consider a boulder at the flow front.

Flexible barriers were assessed in this work to mitigate debris flows and entrainment. In all the large-scale flume tests, a terminal flexible barrier was placed at the end of the flume. In one test, an additional compact flexible barrier was placed upstream of the erodible bed. This flexible barrier split the flow into thinner surges, which decreased both the entrainment downstream and the impact force on the terminal barrier, compared to the test without the upstream barrier. Therefore, multiple flexible barriers are more effective than a single terminal barrier to progressively reduce the debris flow thickness, velocity, and entrainment, and increase deposition. A series of compact flexible barriers placed in the upstream part of a debris flow channel may therefore avoid excessive flow bulking due to entrainment, and therefore decrease the debris flow runout.

9.3. Future work

This thesis presented large-scale flume experiments to study entrainment of a wet soil bed and to quantify the influence of multiple flexible barriers on debris flow entrainment. Cost and time constraints allowed to test only one combination of the bed water content and composition. Future studies may attempt to model different bed conditions. Only one location of the upstream flexible

barrier was tested. Furthermore, the slope angle could not be changed, and the choice of the upstream barrier height was constrained by the height of the lateral channel walls. Future studies should therefore investigate the effects of different upstream barrier heights, spacings and slope angles on the entrainment reduction. The additional studies may allow to define empirical laws to design the characteristics of a flexible barrier to control debris flow entrainment.

The debris flow and the erodible bed were modelled in MPM as one-phase materials. This showed some limitations in simulating the flow depth along the flume as the spatial variations of the flow basal friction are not modelled. A two-phase model may allow to better simulate the debris flow behavior.

Some preliminary trials were carried out to simulate in MPM the upstream flexible barrier and debris flow entrainment simultaneously. However, the trials were unsuccessful, as the numerical model failed in simulating the landing after overflow and the creation of two flow surges. A two-phase model may serve this purpose, as it may better capture the pore pressure distribution in the debris flow and simulate deposition of the first flow surge after landing.

To design flexible barriers to leverage entrainment in nature, full-scale experiments will be needed. Alternatively, numerical modelling should be applied to real debris flow cases. In this thesis, the Hunnedalen debris flow event was considered, but it could only be modelled using the depth-averaged RAMMS model with an empirical entrainment law. However, a depth-averaged model cannot simulate the interactions flow-flexible barrier and the landing dynamics. These interactions are better captured using a three-dimensional model, such as the MPM used in this study. However, higher computational power will be needed to simulate larger debris flows as observed in nature.

This thesis also set a starting point for the comprehension of some characteristic entrainment situations observed in nature, such as transitions between fixed beds (e.g., bedrock) and erodible soil beds, and the frontal boulder entrainment. In natural debris flow events, the entrainment of boulders can generate a boulder enriched debris flow, which is a mixture of both soil, fluid, and boulders. This important case should be modelled in future using MPM, also to study its interaction with a wet soil bed.

References

References

Barbolini, M., Biancardi, A., Cappabianca, F., Natale, L., and Pagliardi, M. 2005. Laboratory study of erosion processes in snow avalanches. Cold Regions Science and Technology, **43**(1–2): 1–9. doi:10.1016/j.coldregions.2005.01.007.

Bardenhagen, S.G., and Kober, E.M. 2004. The generalized interpolation material point method. CMES - Computer Modeling in Engineering and Sciences, **5**(6): 477–495.

Berger, C., Mcardell, B.W., Fritschi, B., and Schlunegger, F. 2010. A novel method for measuring the timing of bed erosion during debris flows and floods. **46**: 1–7. doi:10.1029/2009WR007993.

Berger, C., McArdell, B.W., and Schlunegger, F. 2011. Direct measurement of channel erosion by debris flows, Illgraben, Switzerland. Journal of Geophysical Research: Earth Surface, **116**(1): 1–18. doi:10.1029/2010JF001722.

Bowman, E.T., Laue, J., Imre, B., and Springman, S.M. 2010. Experimental modelling of debris flow behaviour using a geotechnical centrifuge. Canadian Geotechnical Journal, **47**(7): 742–762. doi:10.1139/T09-141.

Breien, H., De Blasio, F. V., Elverhøi, A., and Høeg, K. 2008. Erosion and morphology of a debris flow caused by a glacial lake outburst flood, Western Norway. Landslides, **5**(3): 271–280. doi:10.1007/s10346-008-0118-3.

Canelli, L., Ferrero, A.M., Migliazza, M., and Segalini, A. 2012. Debris flow risk mitigation by the means of rigid and flexible barriers - Experimental tests and impact analysis. Natural Hazards and Earth System Science, **12**(5): 1693–1699. doi:10.5194/nhess-12-1693-2012.

Castanon-Jano, L., Blanco-Fernandez, E., Castro-Fresno, D., and Ballester-Muñoz, F. 2017. Energy Dissipating Devices in Falling Rock Protection Barriers. Rock Mechanics and Rock Engineering, **50**(3): 603–619. doi:10.1007/s00603-016-1130-x.

Cheung, A.K.C., Yiu, J., Lam, H.W.K., and Sze, E.H.Y. 2018. Advanced numerical analysis of landslide debris mobility and barrier interaction. HKIE Transactions Hong Kong Institution of Engineers, **25**(2): 76–89. doi:10.1080/1023697X.2018.1462106.

Choi, C.E., and Goodwin, G.R. 2021. Effects of interactions between transient granular flows and macroscopically rough beds and their implications for bulk flow dynamics. Canadian Geotechnical Journal, **58**(12): 1943–1960. doi:10.1139/cgj-2020-0160.

Christen, M., Kowalski, J., and Bartelt, P. 2010. RAMMS: Numerical simulation of dense snow avalanches in three-dimensional terrain. Cold Regions Science and Technology, **63**(1–2): 1–14. doi:10.1016/j.coldregions.2010.04.005.

Coussot, P., and Meunier, M. 1996. Recognition, classification and mechanical description of debris flows. Earth-Science Reviews, **40**(3–4): 209–227. doi:10.1016/0012-8252(95)00065-8.

DeNatale, J.S., Iverson, R.M., Major, J.J., LaHusen, R.G., Fiegel, G.L., and Duffy, J.D. 1999. Experimental testing of flexible barriers for containment of debris flows. *In* US Geol. Surv. Open File Rep., 99.

Frank, F., McArdell, B.W., Huggel, C., and Vieli, A. 2015. The importance of entrainment and bulking on debris flow runout modeling: examples from the Swiss Alps. Natural Hazards and Earth System Sciences, **15**(11): 2569–2583. doi:10.5194/nhess-15-2569-2015.

Frank, F., Mcardell, B.W., Oggier, N., Baer, P., Christen, M., and Vieli, A. 2017. Debris-flow modeling at Meretschibach and Bondasca catchments , Switzerland : sensitivity testing of field-data-based entrainment model. : 801–815.

Ghasemi, A., Kaitna, R., Fritton, P., Blankenship, B.T., Feng, Q., Densmore, A., de Haas, T., and Hill, K.M. 2019. Erosion by experimental debris flows: Particle size effects. Debris-Flow Hazards Mitigation: Mechanics, Monitoring, Modeling, and Assessment - Proceedings of the 7th International Conference on Debris-Flow Hazards Mitigation,: 10–17.

Haas, T. de, and Woerkom, T. van. 2016. Bed scour by debris flows: experimental investigation of effects of debris-flow composition. Earth Surface Processes and Landforms, **41**(13): 1951–1966. doi:10.1002/esp.3963.

Hanssen-Bauer, I., Førland, E.J., Haddeland, I., Hisdal, H., Lawrence, D., Mayer, S., Nesje, A., Sandven, S., Sandø, A.B., Sorteberg, A., and Ådlandsvik, B. 2017. Climate in Norway 2100 – a knowledge base for climate adaptation. *In* Norwegian Environmental Agency, report no. 1/2017.

Hungr, O., Evans, S.G., Bovis, M.J., and Hutchinson, J.N. 2001. A review of the classification of landslides of the flow type. Environmental and Engineering Geoscience, **VII**(3): 221–238. doi:10.2113/gseegeosci.7.3.221.

Hungr, O., Leroueil, S., and Picarelli, L. 2014. The Varnes classification of landslide types, an

update. Landslides, **11**(2): 167–194. doi:10.1007/s10346-013-0436-y.

Hungr, O., McDougall, S., and Bovis, M. 2005. Entrainment of material by debris flows. Debris-flow Hazards and Related Phenomena,: 135–158. doi:10.1007/3-540-27129-5_7.

Hussin, H.Y., Quan Luna, B., van Westen, C.J., Christen, M., Malet, J.-P., and van Asch, T.W.J. 2012. Parameterization of a numerical 2-D debris flow model with entrainment : a case study of the Faucon catchment , Southern French Alps. Natural Hazards and Earth System Science,: 3075–3090. doi:10.5194/nhess-12-3075-2012.

Issler, D. 2014. Dynamically consistent entrainment laws for depth-averaged avalanche models. Journal of Fluid Mechanics, **759**: 701–738.

Issler, D., Gauer, P., and Barbolini, M. 2000. Continuum models of particle entrainment and deposition in snow drift and avalanche dynamics. Models of Continuum Mechanics in Analysis and Engineering. Proceedings of a conference held at the Technische Universität Darmstadt, September 30 to October 2, 1998, (January): 58–80.

Iverson, R.M. 1997. The physics of debris flows. Reviews of Geophysics, **35**(3): 245–296. doi:10.1029/97RG00426;

Iverson, R.M. 2012. Elementary theory of bed-sediment entrainment by debris flows and avalanches. Journal of Geophysical Research: Earth Surface, **117**(3): 1–17. doi:10.1029/2011JF002189.

Iverson, R.M. 2013. Discussion of Numerical study on the entrainment of bed material into rapid landslides. Geotechnique, **63**(10): 887–888. doi:10.1680/geot.12.D.007.

Iverson, R.M. 2015. Scaling and design of landslide and debris-flow experiments. Geomorphology, **244**: 9–20. Elsevier B.V. doi:10.1016/j.geomorph.2015.02.033.

Iverson, R.M., and Denlinger, R.P. 2001. Flow of variably fluidized granular masses across three-dimensional terrain 1. Coulomb mixture theory. Journal of Geophysical Research, **106**: 537–552.

Iverson, R.M., and George, D.L. 2014. A depth-averaged debris-flow model that includes the effects of evolving dilatancy. I. Physical basis. Proceedings of the Royal Society A: Mathematical, Physical and Engineering Sciences, **470**(2170). doi:10.1098/rspa.2013.0819.

Iverson, R.M., Logan, M., LaHusen, R.G., and Berti, M. 2010. The perfect debris flow? Aggregated results from 28 large-scale experiments. Journal of Geophysical Research,

115(F3): F03005. doi:10.1029/2009JF001514.

Iverson, R.M., and Ouyang, C. 2015. Entrainment of bed material by Earth-surface mass flows: Review and reformulation of depth-integrated theory. Rev. Geophys., **53**: 27–58. doi:10.1002/2013RG000447.Received.

Iverson, R.M., Reid, M.E., Logan, M., LaHusen, R.G., Godt, J.W., and Griswold, J.P. 2011. Positive feedback and momentum growth during debris-flow entrainment of wet bed sediment. Nature Geoscience, **4**(2): 116–121. doi:10.1038/ngeo1040.

Jiang, C., Schroeder, C., and Teran, J. 2017. An angular momentum conserving affine-particle-in-cell method. Journal of Computational Physics, **338**: 137–164. Elsevier Inc. doi:10.1016/j.jcp.2017.02.050.

Johnson, C.G., Kokelaar, B.P., Iverson, R.M., Logan, M., Lahusen, R.G., and Gray, J.M.N.T. 2012. Grain-size segregation and levee formation in geophysical mass flows. Journal of Geophysical Research: Earth Surface, **117**(1): 1–23. doi:10.1029/2011JF002185.

Koo, R.C.H., Kwan, J.S.H., Lam, C., Goodwin, G.R., Choi, C.E., Ng, C.W.W., Yiu, J., Ho, K.K.S., and Pun, W.K. 2018. Back-analysis of geophysical flows using three-dimensional runout model. Canadian Geotechnical Journal, **55**(8): 1081–1094. doi:10.1139/cgj-2016-0578.

Kwan, J.S.H., and Cheung, R.W.M. 2012. Supplementary technical guidance on design of rigid debris resisting barriers. Technical Note No. TN 2/2012.

Kwan, J.S.H., Koo, R.C.H., and Ng, C.W.W. 2015. Landslide mobility analysis for design of multiple debris-resisting barriers. Canadian Geotechnical Journal, **52**(9): 1345–1359. doi:10.1139/cgj-2014-0152.

Kwan, J.S.H., Sze, E.H.Y., and Lam, C. 2019. Finite element analysis for rockfall and debris flow mitigation works. Canadian Geotechnical Journal, **56**(9): 1225–1250. doi:10.1139/cgj-2017-0628.

Lam, H.W.K., and Wong, A.L. 2021. Experimental and numerical study of dynamic soil debris impact load on reinforced concrete debris-resisting barriers. Landslides, **18**(3): 955–966. Landslides. doi:10.1007/s10346-020-01529-w.

Lee, K., and Jeong, S. 2018. Large deformation FE analysis of a debris flow with entrainment of the soil layer. Computers and Geotechnics, **96**(November): 258–268. Elsevier. doi:10.1016/j.compgeo.2017.11.008.

Lee, K., Kim, Y., Ko, J., and Jeong, S. 2019. A study on the debris flow-induced impact force on check dam with- and without-entrainment. Computers and Geotechnics, **113**(April): 103104. Elsevier. doi:10.1016/j.compgeo.2019.103104.

Leonardi, A., Wittel, F.K., Mendoza, M., Vetter, R., and Herrmann, H.J. 2016. Particle-Fluid-Structure Interaction for Debris Flow Impact on Flexible Barriers. Computer-Aided Civil and Infrastructure Engineering, **31**(5): 323–333. doi:10.1111/mice.12165.

Li, X., and Zhao, J. 2018. A unified CFD-DEM approach for modeling of debris flow impacts on flexible barriers. International Journal for Numerical and Analytical Methods in Geomechanics, **42**(14): 1643–1670. doi:10.1002/nag.2806.

Li, X., Zhao, J., and Kwan, J.S.H. 2020. Assessing debris flow impact on flexible ring net barrier: A coupled CFD-DEM study. Computers and Geotechnics, **128**(May): 103850. Elsevier Ltd. doi:10.1016/j.compgeo.2020.103850.

Mangeney, A., Roche, O., Hungr, O., Mangold, N., Faccanoni, G., and Lucas, A. 2010. Erosion and mobility in granular collapse over sloping beds. Journal of Geophysical Research: Earth Surface, **115**(3): 1–21. doi:10.1029/2009JF001462.

Maricar, F., Hashimoto, H., Ikematsu, S., and Miyoshi, T. 2011. Effect of Two Succesive Check Dams on Debris Flow Deposition. Italian Journal of Engineering Geology and Environment,: 1073–1082. doi:10.17654/JPJBDec2015_099_115.

Mccoy, S.W., Kean, J.W., Coe, J.A., Tucker, G.E., and Staley, D.M. 2012. Sediment entrainment by debris flows: In situ measurements from the headwaters of a steep catchment. Journal of Geophysical Research, **117**(June 2014). doi:10.1029/2011JF002278.

McDougall, S., and Hungr, O. 2005. Dynamic modelling of entrainment in rapid landslides. Canadian Geotechnical Journal, **42**(5): 1437–1448. doi:10.1139/t05-064.

Medina, V., Hürlimann, M., and Bateman, A. 2008. Application of FLATModel, a 2D finite volume code, to debris flows in the northeastern part of the Iberian Peninsula. Landslides, **5**(1): 127–142. doi:10.1007/s10346-007-0102-3.

Ng, C.W.W., Choi, C.E., Koo, R.C.H., Goodwin, G.R., Song, D., and Kwan, J.S.H. 2018. Dry granular flow interaction with dual-barrier systems. Geotechnique, **68**(5): 386–399. doi:10.1680/jgeot.16.P.273.

Ng, C.W.W., Choi, C.E., Liu, H., and Poudyal, S. 2020a. Design recommendations for single and

dual rigid and flexible debris flow resisting barriers with and without basal clearance. *In* World Landslides Forum. Kyoto. pp. 33–53.

Ng, C.W.W., Choi, C.E., Majeed, U., Poudyal, S., and de Silva, W.A.R.K. 2019. Fundamental framework to design multiple rigid barriers for resisting debris flows. 16th Asian Regional Conference on Soil Mechanics and Geotechnical Engineering, ARC 2019, (Lo 2000): 1–11.

Ng, C.W.W., Majeed, U., Choi, C.E., and De Silva, W.A.R.K. 2021. New impact equation using barrier Froude number for the design of dual rigid barriers against debris flows. Landslides, **18**(6): 2309–2321. doi:10.1007/s10346-021-01631-7.

Ng, C.W.W., Song, D., Choi, C.E., Liu, L.H.D., Kwan, J.S.H., Koo, R.C.H., and Pun, W.K. 2017. Impact mechanisms of granular and viscous flows on rigid and flexible barriers. Canadian Geotechnical Journal, **54**(2): 188–206. doi:10.1139/cgj-2016-0128.

Ng, C.W.W., Wang, C., Choi, C.E., De Silva, W.A.R.K., and Poudyal, S. 2020b. Effects of barrier deformability on load reduction and energy dissipation of granular flow impact. Computers and Geotechnics, **121**(July 2019). doi:10.1016/j.compgeo.2020.103445.

Nikooei, M., and Manzari, M.T. 2020. Studying effect of entrainment on dynamics of debris flows using numerical simulation. Computers and Geosciences, **134**. doi:https://doi.org/10.1016/j.cageo.2019.104337.

Poudyal, S., Choi, C.E., Song, D., Zhou, G.G.D., Yune, C.Y., Cui, Y., Leonardi, A., Busslinger, M., Wendeler, C., Piton, G., Moase, E., and Strouth, A. 2019. Review of the mechanisms of debris-flow impact against barriers. Debris-Flow Hazards Mitigation: Mechanics, Monitoring, Modeling, and Assessment - Proceedings of the 7th International Conference on Debris-Flow Hazards Mitigation,: 1027–1034.

Pudasaini, S.P., and Hutter, K. 2007. Avalanche dynamics: Dynamics of rapid flows of dense granular avalanches. Springer.

Reid, M.E., Iverson, R.M., Logan, M., Lahusen, R.G., Godt, J.W., and Griswold, J.P. 2011. Entrainment of bed sediment by debris flows : results from large-scale experiments. : 367–374. doi:10.4408/IJEGE.2011-03.B-042.

Remaître, A., W. J. Van Asch, T., Malet, J.P., and Maquaire, O. 2008. Influence of check dams on debris-flow run-out intensity. Natural Hazards and Earth System Science, **8**(6): 1403–1416. doi:10.5194/nhess-8-1403-2008.

Rickenmann, D. 1999. Empirical relationships for Debris Flow. Natural hazards, **19**(47): 47–77.

Rickenmann, D., and Weber, D. 2003. Erosion by debris flows in field and laboratory experiments. Debris-Flow Hazards Mitigation: Mechanics, Prediction, and Assessment,: 883–894.

Sanvitale, N., and Bowman, E.T. 2017. Visualization of dominant stress-transfer mechanisms in experimental debris flows of different particle-size distribution. Canadian Geotechnical Journal, **54**(2): 258–269. doi:10.1139/cgj-2015-0532.

Sassa, K. 1985. The mechanism of debris flow. *In* Proceedings of the 11th International Conference on Soil Mechanics and Foundation Engineering, San Francisco. pp. 1173–1176.

Schürch, P., Densmore, A.L., Rosser, N.J., and McArdell, B.W. 2011. Dynamic controls on erosion and deposition on debris-flow fans. Geology, **39**(9): 827–830. doi:10.1130/G32103.1.

Solheim, A., Strout, J.M., Piciullo, L., Kalsnes, B.G., Eidsvig, U.K., Capobianco, V., Heyerdahl, H., Harbitz, C.B., and Cepeda, J.M. 2021. Reducing the risk from climate induced hazards to buildings and infrastructure; KLIMA 2050 - A centre for research-based innovation. *In* 14th Congress INTERPRAEVENT 2021. pp. 1–3.

Song, D., Choi, C.E., Ng, C.W.W., and Zhou, G.G.D. 2018. Geophysical flows impacting a flexible barrier: effects of solid-fluid interaction. Landslides, **15**(1): 99–110. doi:10.1007/s10346-017-0856-1.

Song, D. ri, Zhou, G.G.D., Choi, C.E., and Zheng, Y. 2019. Debris flow impact on flexible barrier: effects of debris-barrier stiffness and flow aspect ratio. Journal of Mountain Science, **16**(7): 1629–1645. doi:10.1007/s11629-018-5314-6.

Sovilla, B., Burlando, P., and Bartelt, P. 2006. Field experiments and numerical modeling of mass entrainment in snow avalanches. **111**(August 2005): 1–16. doi:10.1029/2005JF000391.

Sulsky, D., Chen, Z., and Schreyer, H.L. 1994. A particle method for history-dependent materials. Computer Methods in Applied Mechanics and Engineering, **118**(1–2): 179–196. doi:10.1016/0045-7825(94)90112-0.

Takahashi, T. 2014. Debris flow: mechanics, prediction and countermeasures. CRC Press, London.

Varnes, D.J. 1978. Slope movement types and processes. *In* Schuster RL, Krizek RJ (eds) Landslides, analysis and control, special report 176: Transportation research board, National Academy of Sciences. Washington, DC. pp. 11–33.

Vicari, H., Ng, C.W.W., Nordal, S., Thakur, V., De Silva, W.A.R.K., Liu, H., and Choi, C.E.

2021a. The Effects of Upstream Flexible Barrier on the Debris Flow Entrainment and Impact Dynamics on a Terminal Barrier. Canadian Geotechnical Journal, **Just-IN**: 1–37. doi:10.1139/cgj-2021-0119.

Vicari, H., Nordal, S., Thakur, V. (2021). The Significance of Entrainment on Debris Flow Modelling: The Case of Hunnedalen, Norway. In: Barla, M., Di Donna, A., Sterpi, D. (eds) Challenges and Innovations in Geomechanics. IACMAG 2021. Lecture Notes in Civil Engineering, vol 126. Springer, Cham. https://doi.org/10.1007/978-3-030-64518-2_60

Vicari, H., Tran, Q.A., Nordal, S., and Thakur, V.K.S. 2022. MPM modelling of debris flow entrainment and interaction with an upstream flexible barrier. Landslides. doi:10.1007/s10346-022-01886-8.

Wang, G., and Sassa, K. 2003. Pore-pressure generation and movement of rainfall-induced landslides: Effects of grain size and fine-particle content. Engineering Geology, **69**(1–2): 109–125. doi:10.1016/S0013-7952(02)00268-5.

Wendeler, C., McArdell, B.W., Volkwein, A., Denk, M., and Gröner, E. 2008. Debris flow mitigation with flexible ring net barriers - Field tests and case studies. WIT Transactions on Engineering Sciences, **60**: 23–31. doi:10.2495/DEB080031.

Wendeler, C., and Volkwein, A. 2015. Laboratory tests for the optimization of mesh size for flexible debris-flow barriers. Natural Hazards and Earth System Sciences, **15**(12): 2597–2604. doi:10.5194/nhess-15-2597-2015.

Wendeler, C., Volkwein, A., McArdell, B.W., and Bartelt, P. 2019. Load model for designing flexible steel barriers for debris flow mitigation. Canadian Geotechnical Journal, **56**(6): 893–910. doi:10.1139/cgj-2016-0157.

Yifru, A.L. 2020. Investigation of a screen structure for mitigating debris-flows along coastal roads. Norwegian University of Science and Technology.

Zhao, L., He, J.W., Yu, Z.X., Liu, Y.P., Zhou, Z.H., and Chan, S.L. 2020. Coupled numerical simulation of a flexible barrier impacted by debris flow with boulders in front. Landslides, **17**(12): 2723–2736. doi:10.1007/s10346-020-01463-x.

Appendices

Appendix A – Development and testing of instrumentations to measure entrainment

When debris material flows over an erodible bed, it can cause its entrainment, i.e., its failure and displacement. The simplest method to measure the entrainment depth would be to measure the difference between the initial bed elevation and the final one (after the experiment, or after the debris flow event). This technique is often used to measure the total entrainment volume in debris flows in the field, by subtracting the digital terrain model before and after the debris flow event (e.g. Schürch et al. 2011). Similarly, Ghasemi et al. (2019), in small-scale experiments, measured the total change in mass of the erodible bed. The limitation of these methods is that they calculate the total change in bed thickness (or mass) due to both entrainment and deposition from the debris flow on top. Therefore, they provide a non-conservative measure of entrainment.

A better technique to measure entrainment, without including deposition, should therefore focus on the internal kinematics of the bed, allowing to monitor internal failure of the bed at different depths from the surface. Several solutions have been tested in this work, using the small-scale 5m-long flume model built by Yifru (2020). The original flume was modified to allow the insertion of a box (Figure A1) in which an erodible bed could be built. The box is placed at 4.1 m from a release cylinder.

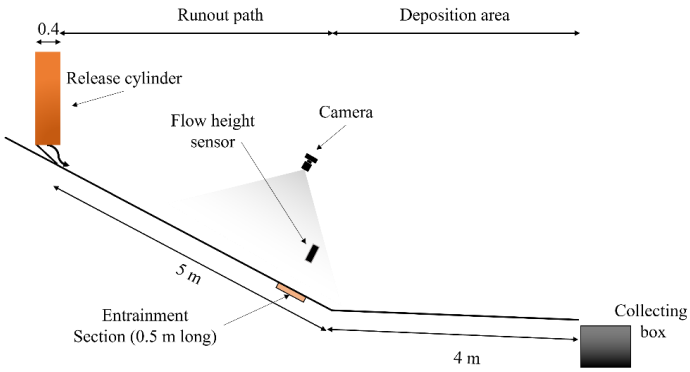

Figure A1 Cross-section of the small-scale flume model with the entrainment section

The solutions which have been attempted to measure entrainment are the following:

- ***Measuring the flow depth***. Figure A2 shows a typical flow depth measurement during a test. The initial value (0 mm) indicates the upper surface of the erodible bed, prior to debris flow arrival. The flow depth then increases to the maximum flow depth. It then decreases

to a negative value, which indicates that entrainment is surely happening, which might however also be a combination with flowing or deposited debris material. Indeed, it is possible to observe some fluctuations. Finally, the displacement increases, which indicates deposition. As discussed previously, this technique does not allow to separate entrainment from deposition on top of the erodible bed.

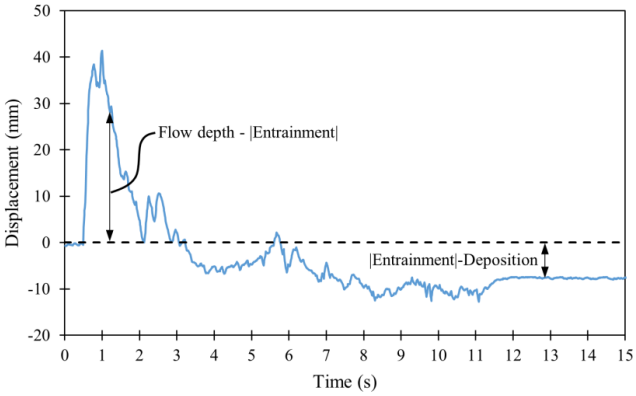

Figure A2 Measurement of the flow depth in the small-scale flume at the entrainment section

- ***Inclusion of colored gravel layers*** inside the erodible bed. The bed was prepared in layers (Figure A3): erodible bed material, covered by a layer of blue gravel, covered by a layer of erodible bed material, covered by red gravel, covered by a layer of erodible bed material. By excavating the bed after the experiment, it is possible to check whether the colored layers are still in place. The method is a simplification of the one used by Haas and Woerkom (2016). The issue of implementing this method is related to obtaining regular surfaces between the layers, with known depth from the surface. Furthermore, it was challenging to determine, after the experiment, whether the colored gravel was entrained or was in the original position.

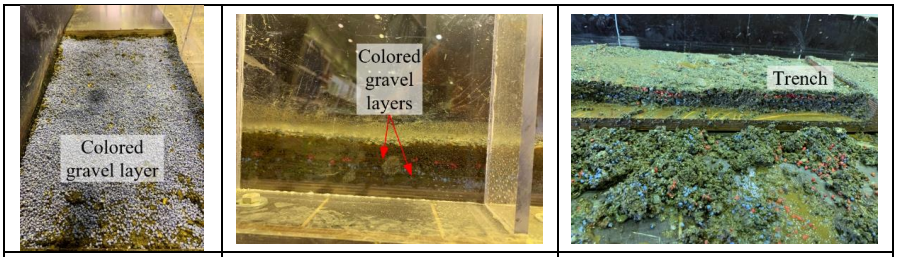

Figure A3 Inclusion of colored gravel layer in the erodible bed to determine entrainment depth

- ***Breaking cables*** (Figure A4). A trench is excavated in a cross-section of the erodible bed at a known depth, where a cable is inserted and then covered with bed material. The cable has a plug and is connected in a circuit. If the plug becomes disconnected, due to failure of the bed, then the circuit gets open and the electronic signal changes. The time at which the circuit becomes open is recorded. The issue with this method was that the plug was mechanically too strong to become unplugged and did not break consistently. On the other hand, a mechanically weaker plug may have caused the circuit to break before conducting the test. This solution was abandoned.

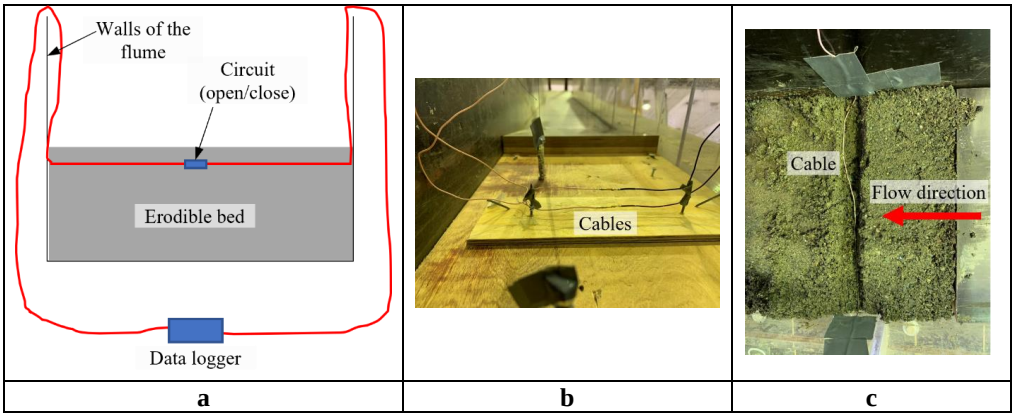

Figure A4 Insertion of a breaking cable in the erodible bed to determine entrainment: (a) Sketch of the setup; (b) Cables inserted into the flume and (c) covered with soil

- ***Erosion columns***. Figure A5a shows the small-scale flume model, whose base was cut to allow the insertion of a manufactured box (Figure A5b). The box has 9 holes, where the erosion column can be screwed through a bolt (Figure A5c). 13 nuts of 3 mm thickness are connected through a bolt, each with a height of 3 mm (total height of 0.04 m). The erodible bed is then prepared, and the bolts are unscrewed (Figure A5d) and the box is inserted into the flume. The test is then performed by releasing the debris flow from a cylinder placed at the top of the channel (Figure A5e). Finally, the box is extracted, and the erodible bed is excavated around each erosion column to count the number of nuts left in place (Figure A5f). The purpose of the flume experiments in the small-scale flume was to test the feasibility of this method to measure entrainment depths. A reference test was carried out using a slope angle of 30°, an initial volume of 25 L of a sand + gravel soil with 60% solid concentration. The erodible bed was prepared with 5% gravimetric water content. Three repetitions were carried out for this reference test. The average erosion depth, calculated on the 9 erosion column, is shown in Table A1: the result of entrainment was consistent. The erosion column methodology was effective, simple to be applied and reliable. This method was therefore chosen to be used in the large-scale flume model in Hong Kong. The methodology used for the large-scale experiments is described with more details in *Paper II*.

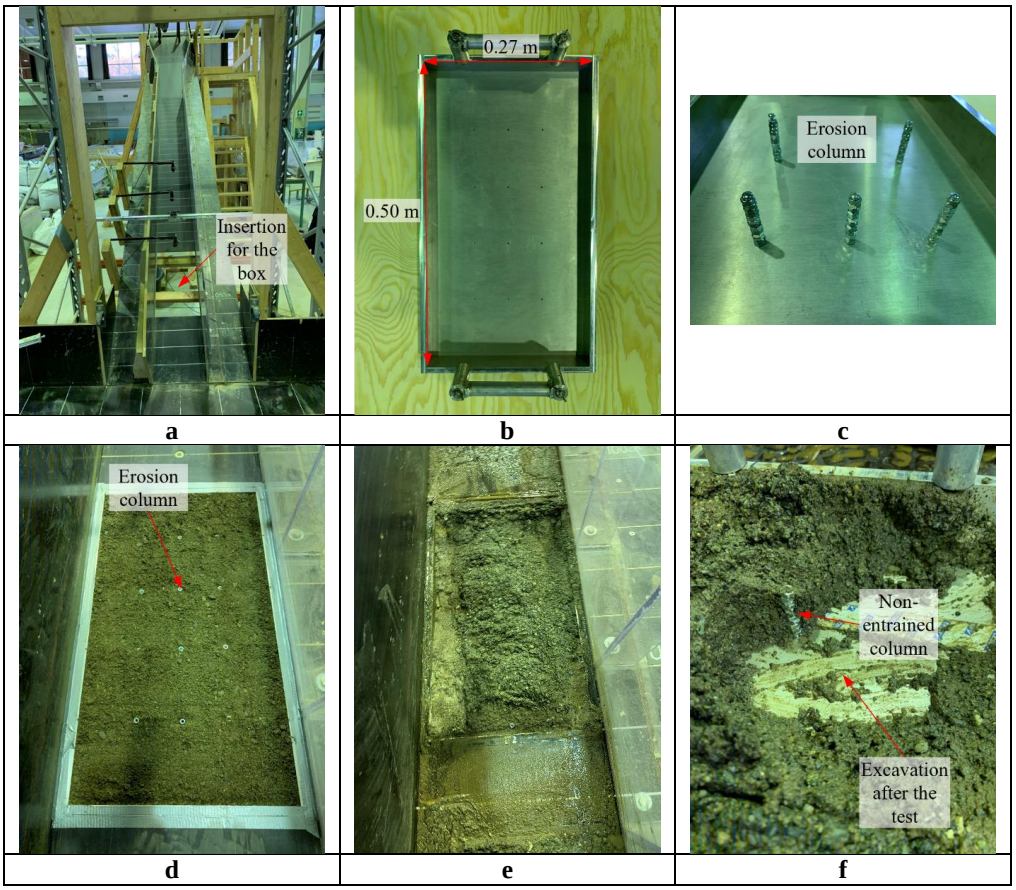

Figure A5 Erosion columns tested in the small-scale flume model. (**a**) flume; (**b**) box for the erodible bed; (**c**) erosion columns screwed at the base of the box; (**d**) box filled with the erodible bed and bolts which have been unscrewed; (**e**) entrainment and deposition on the box after the test; (**f**) manual excavation of the erodible bed around the erosion columns to count the number of remining nuts

Table A1 Average entrainment depth for each repetition of the reference test in the small-scale flume model

Repetition	Average entrainment depth (mm)
1	11.50
2	11.25
3	11.00

Appendix B – Instrumentation for the large-scale flume tests and test procedure

Erosion columns

Figure B1 shows photos of the erosion columns used in the large-scale flume model in Hong Kong.

Figure B1 Erosion columns placed in the large-scale flume in Hong Kong: (**a**) 5 rows of erosion columns installed at a longitudinal spacing of 1 m; 5 erosion columns installed on each row with a mutual spacing of 25 cm (50 cm from the channel sides); (**b**) removal of the bolt, (**c**) measurement of the erosion and deposition depths after the debris flow test

Flow depth sensors

The flow depth is measured orthogonally to the channel base using an ultrasonic and/or laser sensor anchored to a beam, which is fixed to the channel lateral walls (Figure B2a). Each flow depth sensor was calibrated before the test. The sensor was installed at fixed varying distances from a target. The voltage measured from the sensor was plotted against the distance between the laser and the target (Figure B2b), which allows to draw a conversion curve from voltage to distance.

Cameras and UAV

High speed cameras (model: Mikotron EoSens 4CXP) and Go-Pro cameras (model: GoPro Hero 5) were used to capture the details of the kinematics of the debris flow and its interaction with the flexible barriers and the erodible bed. An unmanned aerial vehicle with an on-board video camera (model: UAV DJI Phantom 3) was used to capture an aerial video of each test. The video results were then exported in the software Tracker to determine the flow velocity, by tracking the flow front, based on the known distance (Calibration stick) between reference lines marked on the flume bed (Figure B3).

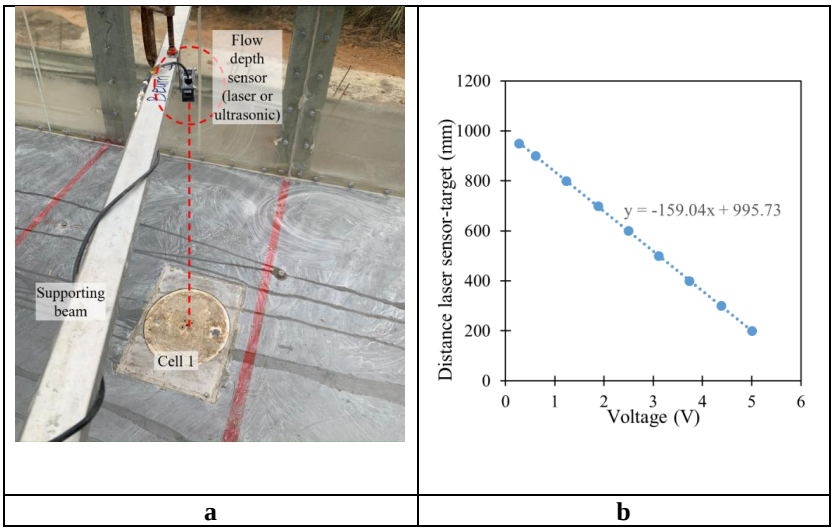

Figure B2 (a) Laser sensor measuring the flow depth normal to the flume base; (b) Typical calibration curve

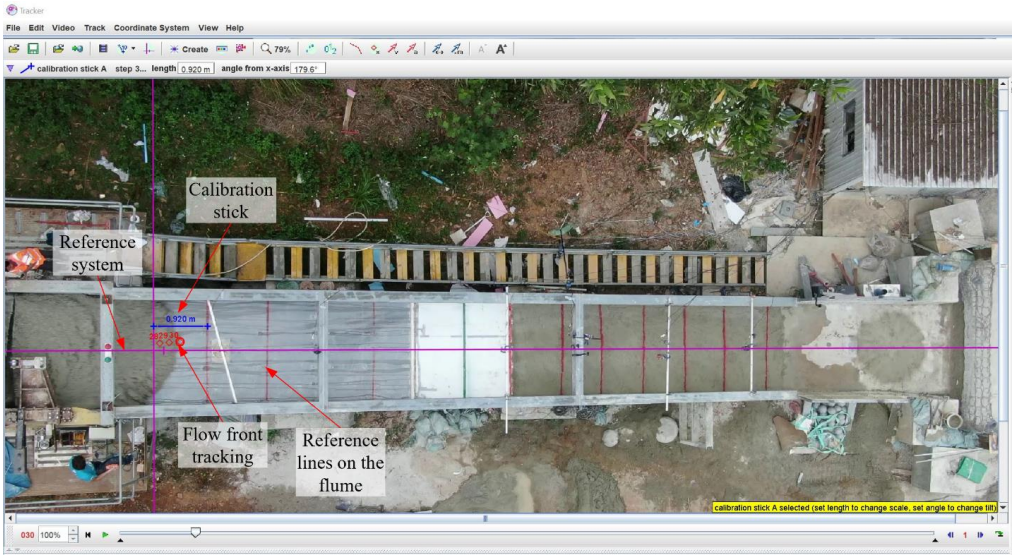

Figure B3 Tracking the flow front in Tracker from an aerial video of the flume test

Cell 1

Cell 1 is located at 3.4 m from the release gate and positioned at the base of the fixed bed to measure the flow basal normal and shear stresses. Cell 1 is referred as triaxial load cell (model number ME K3D160), since it measures the forces along three orthogonal axes. The surface plate attached to the cell was roughened by epoxy and sand, to replicate the flow basal friction along the erodible bed.

The calibration of Cell 1 is shown in Figure B4. Loads, with a known mass m, were applied on the surface of Cell 1. Therefore, for each load, the normal force (orthogonal to the slope) was calculated as $mgcos\theta$ and the shear force (along the slope direction) was calculated as $mgsin\theta$. The normal and shear stresses are therefore calculated as the ratio between the force and the area of the plate (A=*0.078* m^2):

$$\sigma = \frac{mgcos\theta}{A} \quad \textbf{B1}$$

$$\tau = \frac{mgsin\theta}{A} \quad \textbf{B2}$$

Corresponding to each load (and therefore each calculated stress), the voltage is measured by the sensors in Cell 1. The calibration coefficients are therefore found by plotting the measured voltage and the calculated stresses (Figure B4).

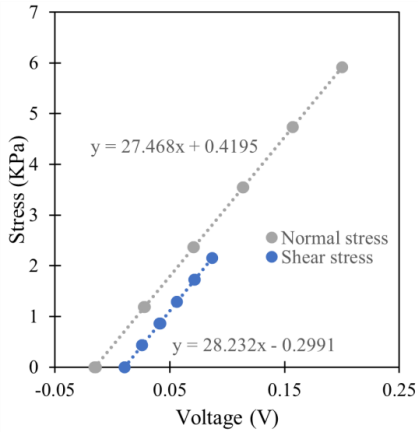

Figure B4 Calibration curve for Cell 1

Cell 2

Cell 2 is positioned at the base of the erodible bed, at 12.5 m from the release gate (Figure B5a). Cell 2 is equipped with a normal stress sensor and a pore pressure sensor. The normal stress sensor was calibrated in an analogous manner as described for Cell 1. The pore pressure sensor was calibrated by using a pipe connected to the pore pressure chamber and positioned vertically. The pipe was filled with water, at increasing heights. By measuring the height of the water column and the voltage, the calibration curve was determined (Figure B5b).

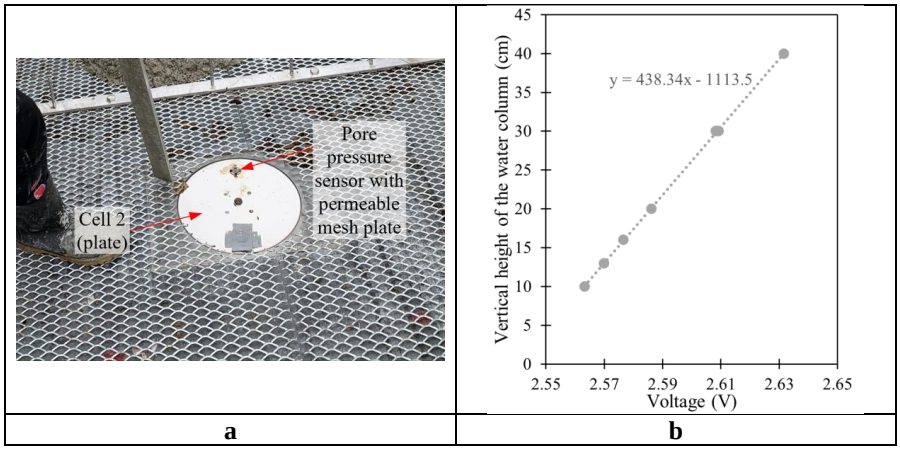

Figure B5 (a) Cell 2 with pore pressure sensor; (b) Typical calibration curve of the pore pressure sensor

Load cells - Flexible barriers

The load cells are fixed to the channel lateral walls in the case of the upstream barrier, and to the frame of the terminal barrier, and connected to the cables to measure the cable forces. The load cells were calibrated through a tensile test (Figure B6a), by measuring the tensile load applied by the machine and the correspondent voltage (Figure B6b).

The cables of the upstream and terminal flexible barrier and the cables of the primary ring nets have a nominal Young's modulus equal to 100 GPa.

Energy brakers are connected to the cables and used to dissipate debris flow energy and replicate the typical trilinear stiffness of a flexible barrier. The force-displacement curves were obtained by performing a tensile test and are shown in Figure B7.

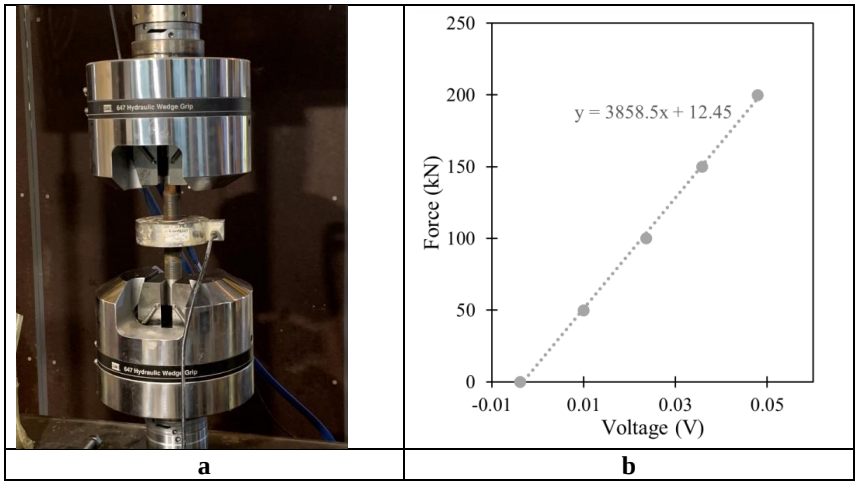

Figure B6 (a) Calibration of the load cell of the flexible barrier (tensile test); (b) Typical calibration curve

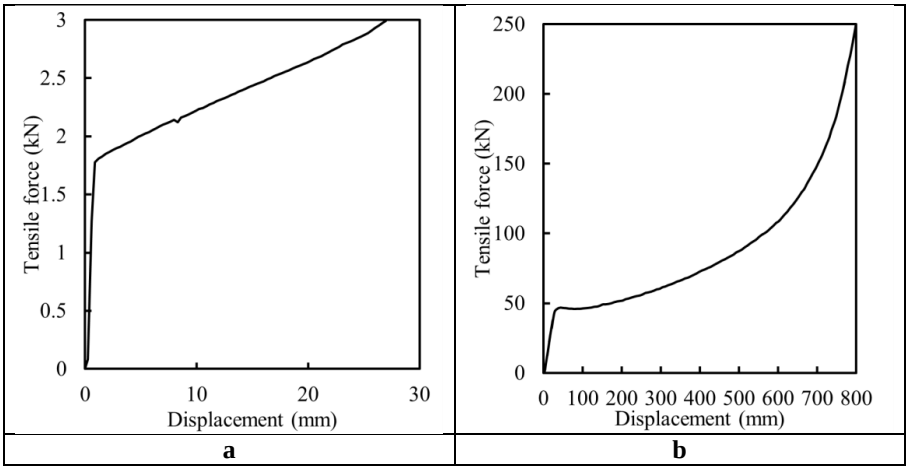

Figure B7 Result of the tensile test on the energy brakers (test performed by Sunil Poudyal): (a) energy braker for the upstream flexible barrier; (b) energy braker for the terminal flexible barrier

Test procedure

The original flume model Ng et al. (2019) has been modified to study the entrainment by debris flows and the interaction with flexible barriers. A fixed platform was built between 7 m and 9 m from the gate to gradually increase the elevation to the 0.12 m thickness of the erodible bed. A 5 mm-thick rough metallic mesh was anchored at the base of the erodible bed to hold the erodible bed in place and avoid it sliding. The erosion columns were fixed through a bolt on a metallic slat, anchored to the flume base (Figure B8a). In test V6-B2, the upstream flexible barrier was also installed at 4.3 m from the gate.

Before each test, the erodible bed material was transported to the flume with a concrete truck, which pre-mixed the soil at a target gravimetric water content of 15% (refer to Appendix B for the details on the erodible bed parameters). The material was then carried into the erodible bed section by using an excavator and layered on the base by using shovels and avoiding compacting the material (Figure B8b). The material was levelled to create the 0.12 m thick bed (Figure B8c). After complete placement of the erodible bed, the bolts of the erosion columns were then removed from a hammock (Figure B8d), to avoid standing on the erodible bed, which would compact and mobilize the soil bed. From the hammock, red lines were also sprayed on the erodible bed (Figure B8e), at a longitudinal spacing of 1 m, which serve as a reference for the video analysis. Finally, just before the test, samples were taken to determine the gravimetric water content of the erodible bed and the volumetric water content was measured. At the same time, the instrumentation, consisting of flow depth sensors and cameras was installed in several points along the flume. After preparation of the erodible bed, the release gate was closed mechanically. Two concrete trucks then transported the debris flow material, prepared at the target solid concentration of 70%. The debris material was discharged into the storage container (Figure B8f) through a chute. The UAV was flown, and data logger and cameras were triggered. The mechanical arm of the release gate was actioned to mechanically open the doors of the storage container, which triggered the debris flow by dam-break. After the test, data were saved and photos were taken. In correspondence of each erosion column, the nuts left in place were counted, by carefully excavating the debris deposit and erodible bed. The deposition depth was also measured at some locations.

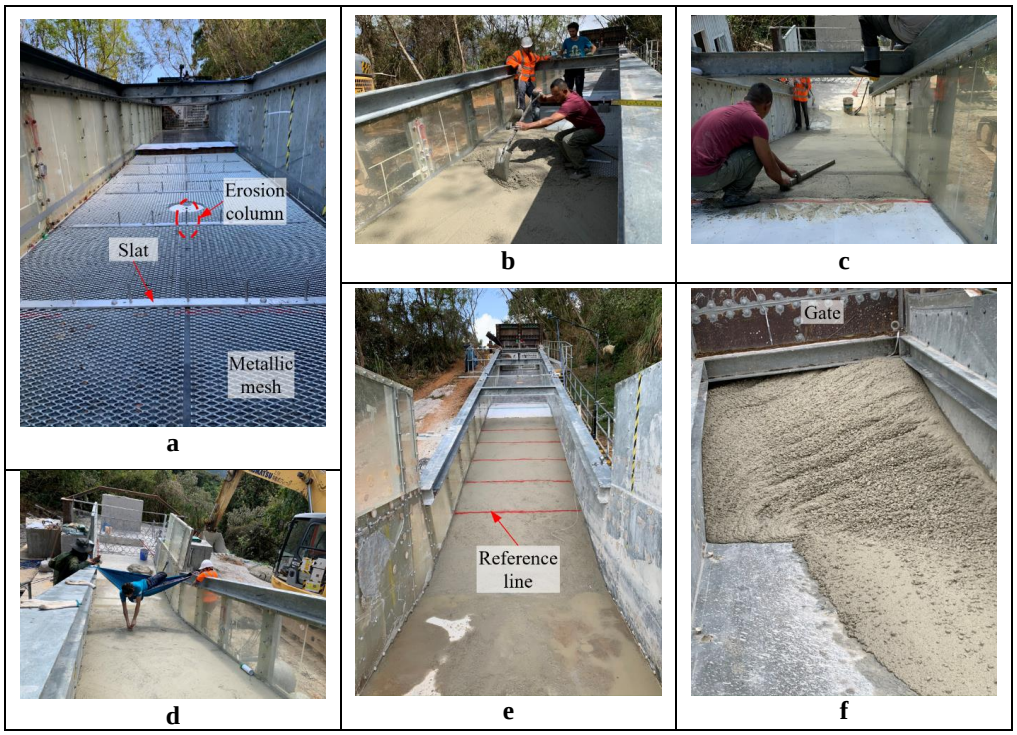

Figure B8 Procedure to perform the large-scale flume experiments: (**a**) erosion columns positioned; (**b**) (**c**) building the erodible bed; (**d**) removing the bolts of the erosion columns; (**e**) drawn reference lines on the erodible bed; (**f**) filling the release gate

Appendix C – Erodible bed soil characterization

Choice of the water content

The initial water content and void ratio of the erodible bed play an important role in the entrainment dynamics (Iverson et al. 2011). Excess pore pressures in the bed material can develop only if the water content is high enough to create continuous water networks to transmit pore pressures (Iverson et al. 2011, Reid et al. 2011). Therefore, the gravimetric water content was selected by investigating its effect on the void ratio and degree of saturation for the bed material adopted.

Different soil specimens of the bed material were prepared in a Proctor mold, with increasing gravimetric water content. The specimens were lightly compacted to ensure specimen uniformity and a loose condition. Based on the known gravimetric water content and total volume, the void ratio and the degree of saturation of the wet soil were determined (Figure C1). The target gravimetric water content was selected to be 15% because it avoided pre-mature bed failure, which would occur for high degree of saturations (>80%).

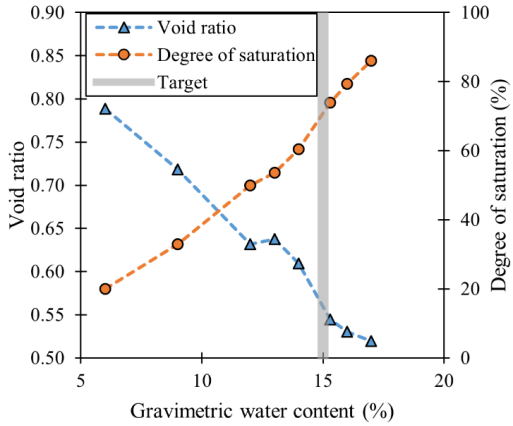

Figure C1 Relationship between gravimetric water content, void ratio and degree of saturation for erodible bed material

Before each experiment, the bed material was mixed to achieve a gravimetric water content of 15%. The mixture was then placed on the 6 m-long erodible bed section. After bed preparation,

soil samples were obtained from the bed to measure the gravimetric water content (using a drying oven), which was approximately 15% (Table C1).

Table C1 Gravimetric water content measured on the erodible bed soil

	Test V2.5-B1	**Test V6-B1**	**Test V6-B2**
	Measured gravimetric water content for samples		
	15.5%	14.9%	15.0%
	15.6%	15.2%	14.5%
	14.1%	14.8%	15.1%
	15.6%	15.7%	15.4%
	15.2%	15.0%	15.1%
	14.5%	15.2%	14.6%
	15.2%	15.3%	15.9%
	14.7%	14.9%	15.6%
	15.2%	15.2%	
		14.6%	
Average for test	**15.1%**	**15.1%**	**15.1%**

Before each experiment, an electrical capacitance sensor (model: Decagon EC-5) was used to measure the volumetric water content (calibration shown in Figure C2), which was about 25% (Table C2). From these measurements, the void ratio can be calculated as:

$$e = -1 + \frac{w\rho_s}{\vartheta_w \rho_w} \quad \textbf{C1}$$

where w is the gravimetric water content, ρ_s is the solid density (measured equal to 2630 kg/m^3) and ϑ_w is the volumetric water content. An average void ratio $e \cong 0.6$ is obtained. The degree of saturation is calculated as:

$$S_r = \frac{\rho_s w}{\rho_w e} \quad \textbf{C2}$$

An average degree of saturation $S_r \cong 65\%$ is obtained. Finally, the total density of the erodible bed is calculated as:

$$\rho_b = \frac{\rho_s(1+w)}{1+e} \quad \textbf{C3}$$

which is equal to 1920 kg/m^3.

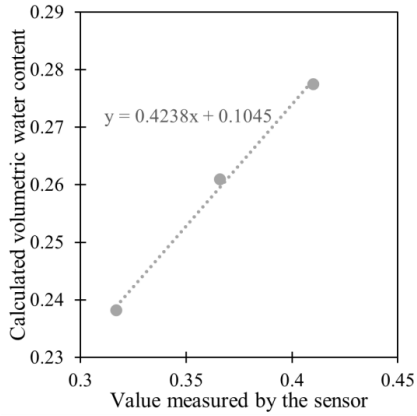

Figure C2 Calibration of volumetric water content sensor from soil samples

Table C2 Volumetric water content measured on the erodible bed soil

	Test V2.5-B1	**Test V6-B1**	**Test V6-B2**
	Measured volumetric water content		
	23.7%	25.5%	Not measured
	23.3%	24.6%	
	24.1%	25.3%	
	23.9%	24.9%	
	25.5%	25.0%	
	25.6%	25.5%	
	24.9%		
	24.5%		
Average for test	**24.4%**	**25.2%**	

Direct shear test

Direct shear tests were performed to determine the friction angle of dry erodible bed soil. Tests were performed at different normal stresses and measuring the shear stress at failure (Figure C3). This allows to determine the effective friction angle of the erodible bed, $\varphi'_b = 41.6°$.

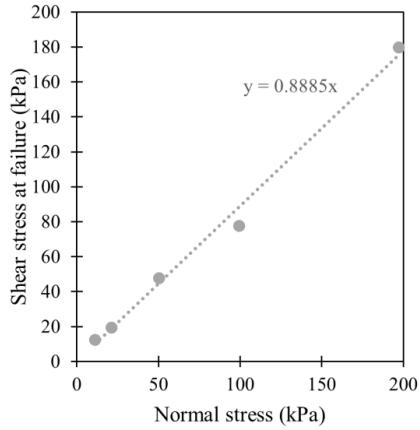

Figure C3 Direct shear tests on erodible bed dry soil samples

ISBN 978-82-326-5538-0 (printed ver.)
ISBN 978-82-326-5199-3 (electronic ver.)
ISSN 1503-8181 (printed ver.)
ISSN 2703-8084 (online ver.)

NTNU

Norwegian University of
Science and Technology